**Verena Kaltenhauser**

# *In situ* synthesis of metal sulphide / polymer nanocomposites in single junction and tandem solar cells

Zur Erlangung des akademischen Grades eines Doktors der technischen Wissenschaften

erreicht an der

Technischen Universität Graz

Betreuer:

Assoc. Prof. DI Dr. Gregor Trimmel

Institut für Chemische Technologie von Materialien

Technische Universität Graz

2013

*„Indess sie forschten, röntgten, filmten, funkten, entstand von selbst die köstlichste Erfindung: der Umweg als die kürzeste Verbindung zwischen zwei Punkten.“*

Erich Kästner

Deutsche Fassung:

Beschluss der Curricula-Kommission für Bachelor-, Master- und Diplomstudien vom 10.11.2008

Genehmigung des Senates am 1.12.2008

## EIDESSTATTLICHE ERKLÄRUNG

Ich erkläre an Eides statt, dass ich die vorliegende Arbeit selbstständig verfasst, andere als die angegebenen Quellen/Hilfsmittel nicht benutzt, und die den benutzten Quellen wörtlich und inhaltlich entnommenen Stellen als solche kenntlich gemacht habe.

Graz, am …… ……..

(Unterschrift)

Englische Fassung:

## STATUTORY DECLARATION

I declare that I have authored this thesis independently, that I have not used other than the declared sources / resources, and that I have explicitly marked all material which has been quoted either literally or by content from the used sources.

…… ……..

date (signature)

# Abstract

Nanocomposite or inorganic/organic hybrid solar cells consist of an organic semiconductor, usually a polymer, and inorganic semiconducting nanoparticles. They offer the potential to combine the advantages of conjugated polymers like roll to roll processing with the electrical and optical properties of inorganic semiconducting nanoparticles, which can be tuned by varying their size and shape due to the quantum confinement.

The first part of this thesis deals with the synthesis and characterization of metal xanthates as precursors for the preparation of polymer/metal sulphide nanocomposites and their application in solar cells. The main focus was set on Bi-, Pb-, Sb-, Ni-, Co-and In-xanthates which can be converted in their corresponding metal sulphides by temperature treatment. In the case of Bi-xanthate also a crystal structure could be determined. The emphasis was set on the investigation of the decomposition of the xanthates, which was performed by TGA measurements and high resolution mass spectroscopy, as well as on the detailed study of the properties of the metal sulphides and the polymer/metal sulphide nanocomposites. The crystal phase of the metal sulphides was analysed by XRD measurements. For Bi-, Pb-, Sb- and In-sulphides only one crystal phase was determined, whereas for Ni-and Co-sulphides more than one phase was assigned. Furthermore, for $Bi_2S_3$ nanocrystals TEM pictures were obtained, showing that nanorods have been formed upon *in situ* synthesis. In addition, photoluminescence quenching measurements were performed and solar cells with $Bi_2S_3$, PbS, $Sb_2S_3$ and $In_2S_3$ were prepared to check the suitability of novel metal xanthtates as precursors for metal sulphides as acceptor materials.

In the second part of this thesis, polymer/inorganic hybrid tandem solar cells were investigated. Tandem solar cells are two single cells on top of each other, offering the possibility of power conversion efficiency enhancement. For this purpose, different recombination layers were elaborated. Tandem devices with open circuit voltages reaching nearly the sum of the individual cells have been realized. Furthermore, in order to prove the stability of the morphology of the bottom active layer during the procession stepts of the top active layer, SEM images of an ion beam polished cross section were determined. The images of the resulting multilayer stack reveal smooth and homogeneous layers with sharp interfaces.

# Kurzfassung

Nanokomposit-Solarzellen oder anorganische-organische Hybrid-Solarzellen bestehen aus einem organischen Halbleiter, normalerweise ein Polymer, und anorganisch halbleitenden Nanopartikeln. Sie haben das Potential die Vorteile von Polymeren, wie zum Beispiel die Möglichkeit sie mittels Rolle-zu-Rolle Verfahren herzustellen, mit den optischen Eigenschaften von anorganischen, halbleitenden Nanopartikeln zu kombinieren, die aufgrund des Quanten-Confinement-Effekts durch Änderung ihrer Größe und Form variiert werden können.

Der erste Teil dieser Arbeit handelt von der Synthese und Charakterisierung von Metallxanthaten als Ausgangsmaterialien für die Herstellung von Polymer/Metallsulfid Nanokompositen und deren Einsatz in Solarzellen. Der Schwerpunkt wurde auf Bi-, Pb-, Sb-, Ni -, Co- und In-Xanthate gelegt, die durch Temperaturbehandlung in Metallsulfide umgewandelt werden können. Im Fall von Bi-Xanthat konnte sogar eine Kristallstruktur erhalten werden. Wichtige Punkte der Arbeit waren die Untersuchung der Zersetzung der Metallxanthate, welche mit TGA und Hochauflösende-Masspenspektroskopie erfolgte, als auch die Ermittlung der Eigenschaften von den Metallsulfiden und der Polymer/Metallsulfid Nanokompositen. Die Kristallphasen der Metallsulfide wurden mit XRD untersucht, wobei für Bi-, Pb-, Sb- und In-Sulfide nur eine Phase, für Ni- und Co-Sulphide mehrerer Phasen gebildet wurden. Von den $Bi_2S_3$ Nanopartikeln wurden TEM Bilder gemacht, die zeigten, dass sich während des *in situ* Prozesses Nanorods gebildet haben. Die Eignung der neuen Metallxanthate als Ausgangsstoffe für Metallsulfide als Akzeptor Material wurde mittels Photolumineszenz-Quenching und in weiterer Folge mit ihrem Einsatz in Solarzellen überprüft.

Im zweiten Teil der Arbeit wurden Polymer/Nanopartikel Hybrid-Tandem-Solarzellen untersucht. Tandem-Solarzellen bestehen aus zwei Einzelzellen, die aufeinander geschichtet sind. Diese Technologie eröffnet die Möglichkeit der Effizienzsteigerung im Vergleich zu Einzelzellen. Um das zu erreichen wurden unterschiedliche Rekombinationsschichten untersucht. Es konnten Tandem-Solarzellen mit Spannungen, die nahezu das Doppelte der Spannungen der Einzelzellen aufwiesen, realisiert werden. Darüber hinaus, wurden SEM Bilder von einem mit Ionenstrahl poliertem Querschnitt gemacht, um zu überprüfen, ob die Morphologie der unteren Zelle während den Prozessschritten der oberen Zelle stabil geblieben ist. Die Bilder des mehrschichten Aufbaus zeigten glatte und homogene Schichten mit klaren Grenzflächen.

# Acknowledgments

During my time as a PhD student, I had the opportunity to gain vital experience in the field of research, but also at conferences, meetings and in discussions with different people, who give me an insight in their great knowledge. Thus, I want to thank those, who made this thesis possible.

At first, I want to express my gratitude to my supervisor Assoc.Prof. Dipl.-Ing. Dr.techn. Gregor Trimmel for his pleasant permanent support and for giving me the opportunity to present my work at international conferences. In addition, I want to thank Dr. Thomas Rath for sharing his knowledge, and his indefatigability of answering questions with infinite patience. Furthermore, I want to thank all people working at the ICTM (Institute for Chemistry and Technology of Materials), and especially within our working group for the friendly working atmosphere at our institute. Specials thanks go to Elisabeth Ziegler for the friendly atmosphere in the office, Christopher Fradler, Mario Arar and Sebastian Dunst who try to help whenever help is needed and Kathrin Bohnemann for her support synthesising the xanthates. Furthermore, I want to thank Josua Bächle, Maximilian Grandi, Berthold Klatovsky, Andrea Anusic, Elke Huber and Judith Radebner, who carried out small experimental projects.

Many important parts of this thesis could only be realized due to successful collaborations. Therefore, I want to express my gratitude to Birgit Kunert and Prof. Roland Resel for the XRD measurements, Prof. Robert Saf for performing MS measurements, Dr. Wernfried Haas, Dr. Angelika Reichmann and Prof. Ferdinand Hofer for the TEM and SEM pictures and Dr. Petra Kaschnitz for NMR measurements. Furthermore I want to thank Ing. Josefine Hobisch for thermal analysis, Monika Filzwieser for the elementary analyses, Ph.D. Ana Torvisco Gomez for determining the crystal structure, Dr. Bettina Friedel for the AFM images and Birgit Ehmann for logistic support.

Financial support by the Christian Doppler Research Association and the Austrian Federal Ministry of Economy, Family and Youth, FFG, and ISOVOLTAIC AG is gratefully acknowledged.

My deepest gratitude is dedicated to my family and especially to Bastian, who supported and motivated me all over the time.

# Table of Contents

# I General Introduction

Green energy is a highly discussed issue in our society and still becomes more and more important. One reason for this is the steady increase in energy consumption (Fig. 1), caused by an increase in population and technology.[1]

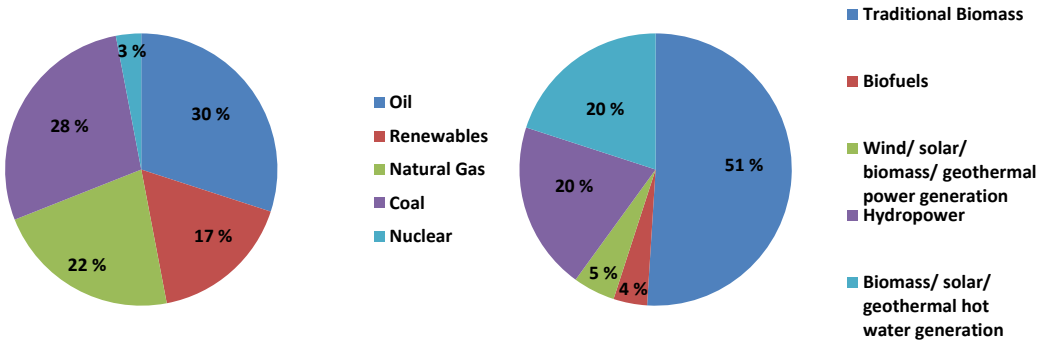


**Fig. 1: World global energy consumption in 2010 (data taken from reference [1]).**

Natural resources of fossil fuels are limited and will run out quickly, but more importantly, the continuing usage of gas and oil leads to further formation of greenhouse gases, which has already reached an alarming level. One promising candidate for green energy supply is photovoltaic.[2] There is 10000 times more solar irradiation available every year to satisfy the annual world energy demand.[3] Especially for sunny areas, solar cells are very considerable, as more power can be generated.

The most common photovoltaic technology, also called first generation, are single junction silicon devices and consist of crystalline or polycrystalline silicon wafers, with power conversion efficiencies around 25 % (measured under the global AM1.5 spectrum 1000 W/m$^2$ at 25°C).[4,5] This technology is based on an indirect band gap absorber material, thus, thick absorber layers are required. In addition, silicon wafers are fragile, which makes the manufacturing process complex and limits potential applications. Furthermore, high purity crystalline silicon wafers are very expensive. Thus, the aim was to reduce the manufacturing costs, via e.g. high efficiency processing sequences and to use cheaper raw materials. Therefore, a lot of research activity has been done on second generation solar cells also called thin film solar cells.[4] These thin film solar cells rely on direct band gap materials, as CIGS (copper indium gallium diselenide, CIS(e) (copper indium diselenide), CdTe cadmium telluride and a-Si (amorphous silicon). This technology has reached the commercialization stage with conversion efficiencies up to 11% in module production.[6] Although thin film solar cells have

lower efficiencies than silicon solar cells, they are cheaper and therefore a considerable alternative to the first generation.

Molecular photovoltaic devices like dye-sensitized solar cells (DSSCs)[7,] and organic solar cells[8] belong to the third generation and have potentially the ability to arise as feasible alternatives to common used solar cells.[9] DSSC consists of 8-12 µm thick mesoporous films of nanocrystalline $TiO_2$ particles (diameters between 8-20 nm), sensitized with a red absorbing dye and a liquid red/ox electrolyte. A power conversion efficiency as high as 11.3%[10] has been reported for this system. Recently, a solid version of dye sensitized solar cells has been developed by substitution of the liquid red/ox electrolyte with a solid inorganic or organic hole transport material. Organic solar cells consist of a polymer as donor material and fullerenes or small molecules as acceptor materials. They have the potential to fulfill the requirements of a negligible environmental footprint and cost efficiency, since they use cheap and plentiful available raw materials and provide the possibility of roll-to-roll processing, leading to a conception, where solar cells can be printed like daily newspapers. Although their power conversion efficiency does not compete with the conventional silicon solar cells until now, a great breakthrough was achieved 2012 with a power conversion efficiency of 10%.[11,12]

Another interesting approach in the field of photovoltaic is the nanocomposite or inorganic/organic hybrid solar cell consisting of an organic semiconductor, which is usually a polymer, and inorganic semiconducting nanoparticles. They offer the potential to combine the properties of polymers like easy processing with the tuneable electrical and optical properties of inorganic semiconducting nanoparticles due to the quantum confinement effect. Thus, these properties can be tuned by varying the size and shape of the nanocrystals.

However, as relatively little research was directed to the field of nanocomposite solar cells, the efficiencies are still lower as the efficiencies of organic solar cells. Nevertheless progress in PCE in the last years and the conceptual advantages make it believable to achieve efficient and stable hybrid solar cells in future.[13] More detailed information about nanocomposite solar cells are given in the chapter *Nanocomposite solar cells*.

# 1 Aims of this thesis

Subject of this work was the preparation and investigation of nanocomposite solar cells, which consists of a polymer and various semiconducting nanoparticles. Furthermore different device architectures were studied. Thus, the thesis deals with two main themes: The synthesis and characterization of metal xanthate precursors and their application in nanocomposite solar cells, as well as the investigation of nanocomposite tandem solar cells. Nanocomposite solar cells using xanthates as precursors for the *in situ* synthesis of metal sulphide nanoparticles as acceptor material were recently investigated. S. A. Haque et al.[14] used this method for the preparation of polymer/CdS solar cells and our group applied it for the fabrication of polymer/CIS[15] solar cells. In the first part of my thesis, I will discuss the synthesis of Bi-, Pb-,Sb-, Co- and Ni-xanthates and their characterization. In addition, the conversion mechanism from the xanthates to their corresponding metal sulphides will be investigated, which occur by temperature treatment. Furthermore, the properties of the metal sulphides, like crystal phase, optical properties and their suitability as acceptor material will be discussed. Additional, nanocomposite solar cells with Bi-, Pb-, Sb- and In sulphides will be fabricated and optimized, to evaluate the potential of these novel precursors. Therefore, various donor polymers, diverse device architectures and different conversion temperatures were investigated.

The second part of my work deals with the investigation of organic and nanocomposite tandem solar cells. Tandem solar cells are two single cells, which are stacked on top of each other. They offer the advantage of improving the power conversion efficiency through doubling the $V_{OC}$ and harvesting a broader part of the solar spectrum. In order to achieve high power conversion efficiencies, the single cells will be optimized and different recombination layers will be explored. For the nanocomposite tandem solar cell an inorganic/organic hybrid solar cell was used as bottom active layer and varying organic solar cells, with PCBM as acceptor material, were used as top active layer. In addition, hybrid-hybrid tandem solar cells were investigated, using two inorganic/organic solar cells as top as well as bottom active layer.

# II Basics

## 1 Nanocomposite solar cells

Organic/inorganic hybrid materials are a highly interesting and versatile class of materials and offer a plethora of applications due to their variety of physical and chemical properties which can be tailored in a wide range by using different material combinations, morphologies and nanostructures. Of particular interest are nanocrystal/polymer hybrid materials, often called nanocomposites, in which inorganic nanocrystals with specific properties e.g. concerning light-emission or light absorption are integrated into a polymer matrix. This allows combining the advantages of easy processing and structural flexibility of polymers, with the optical properties and stability provided by the inorganic material.[16] Semiconducting quantum dots offer the unique possibility of tuning their properties by controlling their size and shape.[17] Organic/inorganic nanocomposites find applications, for example, in photochromic devices,[18] non linear optics,[19] electroluminescent devices,[20] hybrid optical sensors[21] and also in polymer-nanoparticle hybrid solar cells.[22]

Nanocomposite solar cells, consisting of a semiconducting polymer as donor material and semiconducting nanocrystals as acceptor material, combine many of the properties of organic and inorganic materials. They can be fabricated in a more energy efficient way, since high temperature processes are avoided. Furthermore, they can be produced by roll-to-roll processes and benefit from the high absorption coefficients of organic polymers. Based on the quantum size effect tuning of nanocrystal band gap and energy levels is possible by tailoring their size, shape and composition.[23] Moreover, they exhibit a high charge carrier mobility and the electron transport is faster than in polymers, which exhibit higher hole transport properties.[24] Quantum confinement of nanoparticles leads to an enhancement of the absorption coefficient compared to bulk materials. Therefore, in nanocomposite solar cells both compounds contribute to the overall absorption, unlike the typical polymer/fullerene devices where the fullerene adds very little to the photocurrent generation.[25] Thus, in nanocomposite solar cells it is possible to select two compounds with complementary absorption properties for the active layer, which leads to improved charge carrier generation.

Already in 1996 Greenham at al.[26] studied the concept of nanocomposite solar cells by investigating charge separation and transport with CdS or CdSe and poly[2-methoxy-5-(2-ethylhexyloxy)-1,4-phenylenevinylene] (MEH-PPV) as nanocomposite active materials. They

established that the power conversion efficiency has been improved in a nanocomposite approach (heterojunction, chaper 2) compared to a solar cell, consisting only of the pristine MEH-PPV (homojunction, chapter 2). The poor efficiency of this simple architecture is caused by the fact, that this conjugated polymer is a good electron donor but a poor electron acceptor. For a long time P3HT (poly(3-hexylthiophene-2,5-diyl)) was the favoured donor material with efficiencies up to 4%[27] for P3HT/CdS solar cells. Another common polymer/nanocrystal combination is PCPDTBT (Poly[2,1,3-benzothiadiazole-4,7-diyl[4,4-bis(2-ethylhexyl)-4H-cyclopenta[2,1-b:3,4-b']dithiophene-2,6-diyl]]) /CdSe with efficiencies around 3.6%.[28,29]

Up to now research on nanocomposite solar cells grew rapidly, reaching efficiencies around 4.7%, realised with CdSe/polymer[30] and CdTe/polymer[31] hybrid materials.

# 2 Working principle and device architecture of the heterojunction concept

The simplest organic solar cell architecture, also called homojunction, consists of only one material where electron and hole transport occurs, sandwiched between two metal electrodes of different work functions. Charge separation takes place at the interface of the single layer and the electrodes. The rectifying behaviour is caused by the formation of a Schottky-barrier between the p-type organic layer and the metal with the lower work function.[32]

In a heterojunction, charge transport is accomplished by different materials. In polymer based materials, the holes are transported by the donor material and the electrons are transported by the acceptor material. The photoactive layer of organic and nanocomposite solar cells, consists of a donor (conjugated polymer) and an acceptor (organic solar cells: fullerene or small molecules, nanocomposite solar cells: inorganic semiconducting nanoparticles) phase.

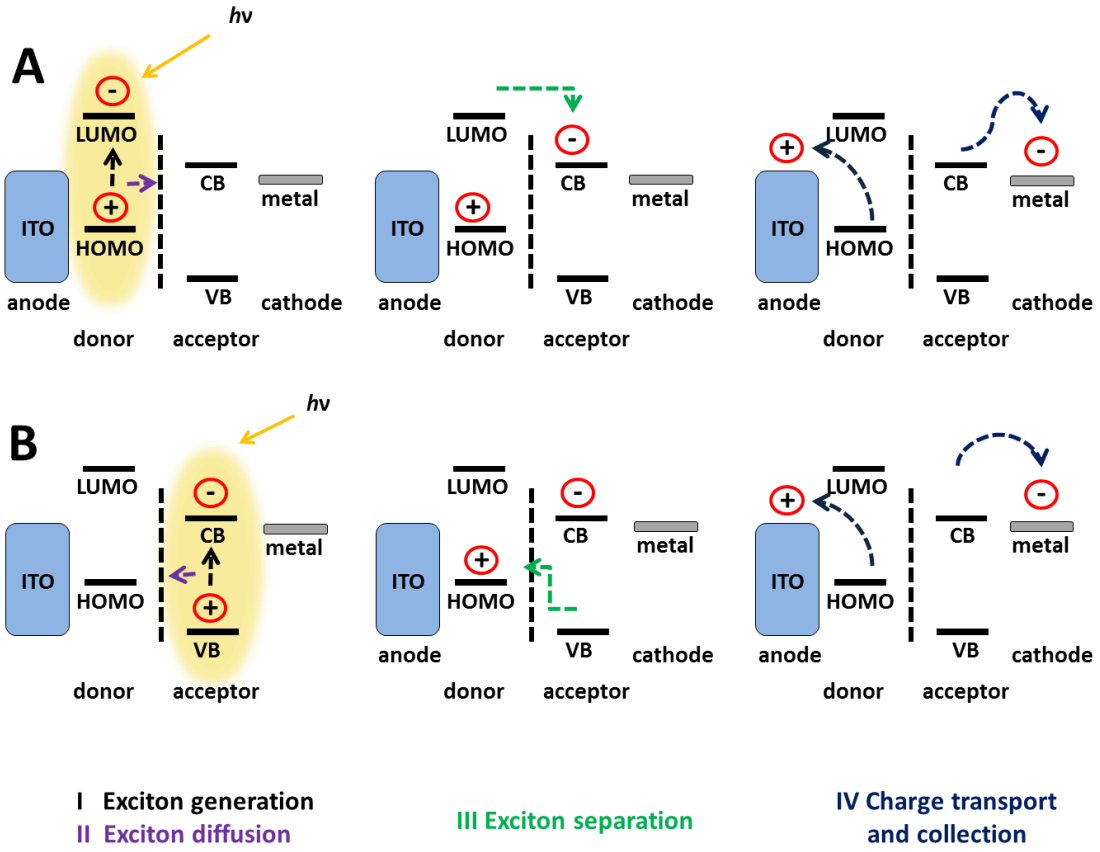


**Fig. 2: Energy levels and the harvesting of energy from a photon in nanocomposite solar cells. A: photo generation in the electron donor, B: photo generation in the electron acceptor.**

The donor is a light harvesting material that absorbs photons with energy higher than the band gap ($E_g$). As mentioned above not only the polymer absorbs the light, but also the inorganic nanoparticles (energy level diagrams are shown in Fig. 2). Neutral excitons are generated, due to the promotion of electrons from the highest occupied molecular orbital (HOMO) to the lowest unoccupied orbital (LUMO). Excitons are bound electron hole pairs and can be dissociated at a suitable junction. Thus, electrons hope to the CB of the inorganic semiconductor material (acceptor), while holes hope to the HOMO of the polymer (donor). For good charge separation, it is important, that the LUMO of the donor material is at least 0.3 eV greater than the LUMO (or conduction band, CB regarding inorganic semiconductors) of the acceptor material. Generally, the HOMO of the donor material should be higher in energy than the HOMO (or valence band, VB, concerning inorganic semiconductors) of the acceptor material.[33] Nevertheless, exciton recombination is possible, associated with the loss of free charge carriers. The average length over which excitons can diffuse without recombination within the donor material is called exciton diffusion length, and depend on the material properties. The exciton diffusion length within P3HT is around 10 nm.[34] After successful

dissociation, the charges diffuse to their corresponding electrodes, due to an internal electric field generated by differences in their Fermi levels.

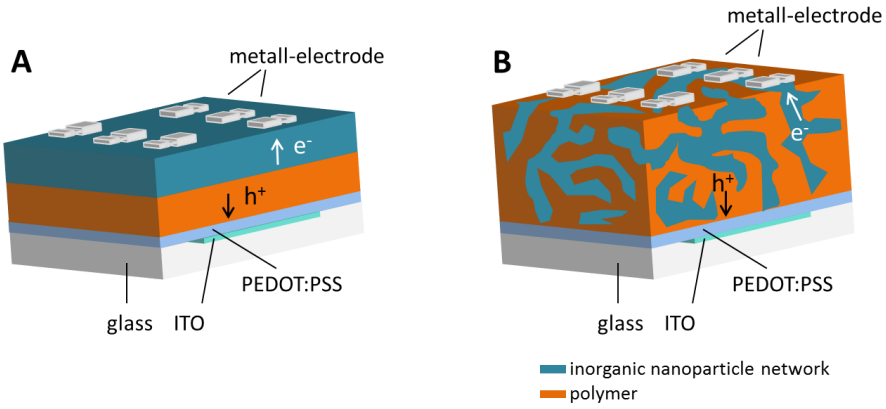


**Fig. 3: Different device architectures: (A) bilayer, (B) bulk-heterojunction.**

Device architecture plays an important rule concerning overall power conversion efficiency.

The most simple heterojunction device architecture is the bilayer device (Fig. 3 A), consisting of separated donor and acceptor layers on top of each other. Thick active layers absorb more light than thin active layers, which should lead to an enhancement in $I_{SC}$, due to more generated charges. Nevertheless, the limiting factor is the maximum exciton diffusion length, thus, more excitons will recombine in thick layers, leading to a drop in $I_{SC}$ and FF. This problem leads to the investigation of bulk heterojunction devices (Fig. 3 B), where donor and acceptor are mixed together, generating an interpenetrating network whose connected nanoparticle segments are separated by a polymer phase. Thus, thicker active layers can be fabricated, with a larger interface for an increase in exciton separation.[34] Nevertheless, not only a large interface is important, but also the creation of efficient conductive pathways through which free electrons and holes may be transported. Thus, the arrangement of donor and acceptor phase, which should be a compromise between generating a large interface without losing persistent pathways for charge transport, is a very important issue for the solar cell performance.[35] In this two architecture types, ITO (indium tin oxide) is commonly used as photoanode, whereas metal electrodes like aluminium are used as photocathode. PEDOT:PSS (poly(3,4-ethylenedioxythiophene) poly(styrenesulfonate)) is mostly applied as hole transport and electron blocking layer.

Recently, the field of inverse architectures emerged. Here, the holes are collected by the metal electrode like Ag or Au, whereas the electrons are collected by the ITO/TiOx electrode. The main advantage is that it is now possible to form the acceptor phases in specific structures, before applying the polymer. Thus defined interpenetrating networks can be built, whereas in

bulk heterojunction solar cells it is very difficult to form defined structures with defined orientation (Fig. 4).

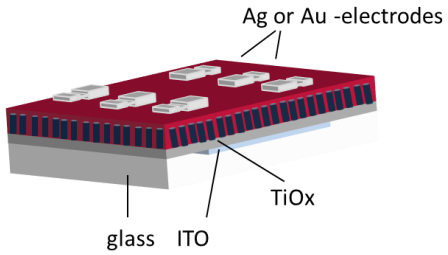


**Fig. 4: Defined structure of the acceptor phase in an inverse architecture.**

# 3 Characteristic solar cell parameters

Current versus voltage characteristics are used for describing the performance of solar cells. Therefore, typically a solar simulator or a source measurement unit with a standard light source is used. The measurements are carried out in the dark and under illumination, by varying the voltage in a controlled manner and measuring the corresponding current. To enable valid comparison of device performance, an international standard for input power is used. This standard is an incident spectrum of AM 1.5G, with an intensity of 1000 W/m$^2$ (100 mW/cm$^2$), at a temperature of 25 °C.[35] The received IV curves have a diode-like shape. Fig. 5 shows a typical IV characteristic.

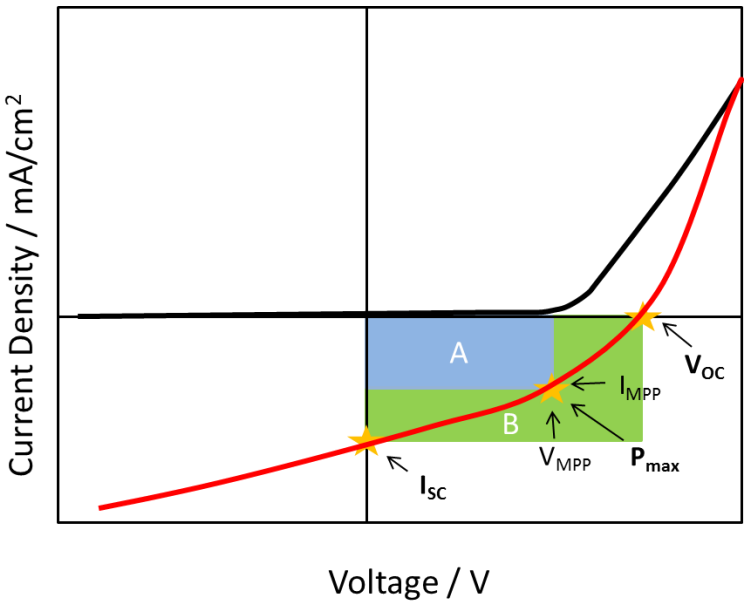


**Fig. 5: IV characteristic of a solar cell including the main data points like $I_{SC}$, $V_{OC}$, $I_{MPP}$, $V_{MPP}$.**

The most important parameters determined from the IV curve are $I_{SC}$ (short circuit current,), which is the current density at zero voltage, $V_{OC}$ (open circuit voltage), which is the voltage at zero current and $P_{max}$ (maximum power output), which is the product of $I_{mpp}$ and $V_{mpp}$. These parameters are used for the calculation of the power conversion efficiency (PCE).

$$FF = \frac{P_{max}}{I_{SC} * V_{OC}} = \frac{I_{mpp} * V_{mpp}}{I_{SC} * V_{OC}} \qquad PCE = \frac{P_{out}}{P_{in}} = \frac{I_{SC} * V_{OC} * FF}{P_{in}}$$

The fill factor (FF) is a measure for the "ideality" of the device, where $I_{mpp}$ and $V_{mpp}$ are the current density and voltage, respectively, at the maximum power point. The PCE is the ratio between the generated electrical power and the incoming power from the light source. Another important parameter is the EQE (external quantum efficiency), which is the ratio of the number of photo-generated electrons collected under short circuit conditions and the number of incident photons.[34] The measurement of the EQE is usually performed under monochromatic light. In organic solar cells it is believed that charge separation and transport occur within five sequent steps. The product of the efficiencies of all steps determines the EQE.

$EQE = \eta_A * \eta_{diff} * \eta_{diss} * \eta_{tr} * \eta_{cc}$

The first step is the absorption of the photon. The photon absorption yield ($\eta_A$) is determined by the optical absorption coefficient of the active layer and its thickness. The next step is the diffusion of the electron in the donor material. The exciton diffusion yield ($\eta_{diff}$) is the probability of the exciton to diffuse without recombination. Thereafter, the exciton is separated at the donor/acceptor interface by the internal electric field. The probability for this separation is given by the exciton dissociation yield ($\eta_{diss}$). The energy provided for this separation should be given by the difference between the LUMOs of the donor and acceptor. In the next step, charge transport to the respective electrodes occurs via hopping processes. This charge carrier transport yield ($\eta_{tr}$) is affected by structural defects and impurity species. These so called traps provide localised energy minima for charge transport and lead therefore to a reduction of the charge mobility. In a last step the charges have to be collected by the electrodes (charge collection yield, $\eta_{cc}$), which is affected by the ability of the charges to be transferred from the active layers to the respective electrodes. Energy levels and interfacial contacts between the active layer and the electrodes can influence this ability crucially.[36]

# 4 Conjugated polymers

Conjugated polymers combine the optoelectronic properties of semiconductors with the mechanical properties of plastics. By functionalizing these polymers with flexible side groups, they become soluble in organic solvents and can be solution processed at room temperature into thin films.[37] These polymers offer the possibility to fabricate plastic LEDs[38,39], photovoltaics[40], transistors[41], and flexible displays.

Most common used polymers in organic and nanocomposite solar cells are p-type polymers. They have extensive conjugation and are used for photogeneration and charge transport. The synthesis of these polymers is often complicated, using multistep methods, thus, they are expensive. Furthermore, it is often difficult to obtain uncommon polymers with the same properties for more than one time, because they differ in molecular weight etc. from synthesis to synthesis. The two major types of polymers are polythiophene and its derivates and poly(p-phenylene vinylene) and its derivates.[22] The most famous representative is P3HT (poly(3-hexylthiophene-2,5-diyl)).

The HOMO and LUMO levels for conjugated polymers are usually determined by cyclic voltammetry (CV) measurements. While the band gap can be determined from the difference between HOMO and LUMO levels determined by CV, it could also be achieved via UV-vis spectroscopy.[34] Unfortunately, band gap values determined with different methods are not always identical.[42,43] It is important to notice, that band gap values for polymers are strongly affected by the local environment. Thus, the values obtained for isolated polymers can be different from those present within a heterojunction.[34]

The most important properties of donor polymers are their HOMO/LUMO levels, band gaps and carrier mobility. To maximize $V_{OC}$ the donor polymer HOMO should be as low as possible and the LUMO levels should be close to the CB of the acceptor. Furthermore these polymers should be able to be arranged in an organized structure with enhanced packing and charge transport. This could be achieved by thermal annealing and solvent additives. The conjugated polymer should properly phase separate from the acceptor, and create a donor phase network with efficient hole transport.[22] The hole mobility should be very high (P3HT has a hole mobility of up to 0.2 $cm^2V^{-1}s^{-1}$).[44]

In the last years low bandgap polymers (<2.0 eV) have been discovered to be suitable for broad spectral light harvesting.[45-48] P3HT with a band gap of 1.9 eV only absorbs photons below a wavelength of 650 nm. At 650 nm just 22.4% of the photons can be harvest, thus, a

decrease of the band gap increases the total amount of photons, which can be absorbed. Nevertheless, it is possible that narrowing of the band gap leads to a decrease in $V_{OC}$, which may lead to no enhancement in power conversion efficiency. One method to obtain polymers with narrow band gaps is to introduce the concept of the donor-acceptor (D-A) approach to conjugated polymer design.[49-55] Therefore, polymers with delocalized π-electron systems that include alternating electron rich (donor) and electron lacking (acceptor) repeat units were synthesised. This combination of high lying HOMO levels from the donor units and the low lying LUMO levels from the acceptor units gives rise to an overall narrow band gap for the polymer.[56] Due to the highly desirable tuneable nature of these D-A polymers there is an on-going extensive research of these materials in the field of light harvesting and light emitting applications.[57-60]

# 5 Acceptor materials

Acceptor materials for nanocomposite solar cells should be n-type semiconductors, due to the fact, that most common used donor polymers are p-type semiconductors. The frequently used acceptor materials in nanocomosite solar cells are metal oxide ($TiO_2$[61], ZnO[62,63]), metal sulfide (CdS, CIS, PbS), metal selenide (CdSe[64], PbSe[65,66]) and metal telluride (CdTe[31]). In order to achieve nanocomposite solar cells with high currents and fill factors, electron and hole mobilities must be optimized and balanced. This balance is necessary to prevent the built up of space charge, which leads to declined charge extraction. The charge carrier mobility can be influenced by increasing the crystallinity of the material or by doping with additional elements in metal-oxide nanostructures.[2] However, important factors, which influence PCE are the nanoparticle structure and the aspect ratio. Different nanoparticle structures are commonly used in nanocomposite solar cells (Fig. 6).[34]

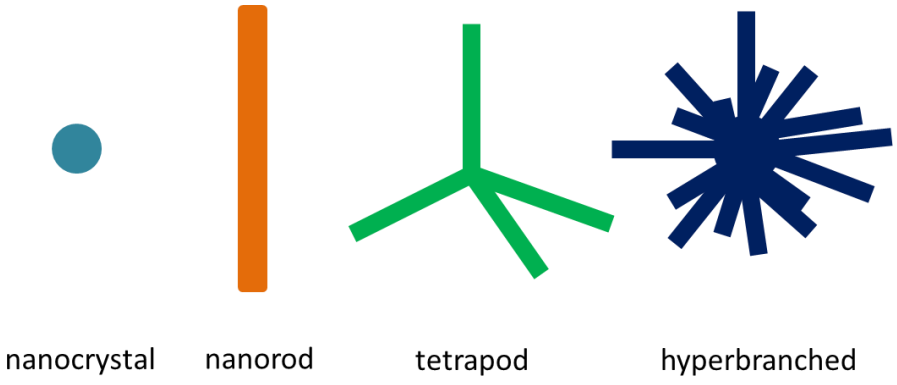


**Fig. 6: Structures of nanoparticles used in nanocomposite solar cells.[34]**

Often additional synthetic steps are needed for the synthesis of nanorod, tetrapod and hyperbranched nanoparticles. Nevertheless, they reduce the number of inefficient electron hopping events between the nanocrystals, which are necessary for transporting the electrons. B. Sun et al.[67] reported CdSe tetrapods incorporated into a poly(phenylene vinylene) derivate, which offers the advantage of nanocrystal 3D shape and vertical phase segregation leading to higher efficiencies. Until now, still many physical mechanisms in nanocomposite solar cells are not fully understood. In order to allow a better understanding of these physical processes, nanostructured devices with defined morphologies and interfaces are necessary. The interface can be designed to efficiently enable charge injection but hinder charge recombination. Furthermore the maximum size of the nanoparticles needed to allow efficient charge transport should be investigated.[2] This knowledge would lead to higher power conversion efficiencies, making nanocomposite solar cells competitive to organic solar cells in future.

# 6 Preparation of the nanocomposite layer

T. Rath et al.[13] divided the different routes for the preparation of the nanocomposite layers in three classes: The classical approach, the infiltration approach and the *in situ* approach (Fig. 7).

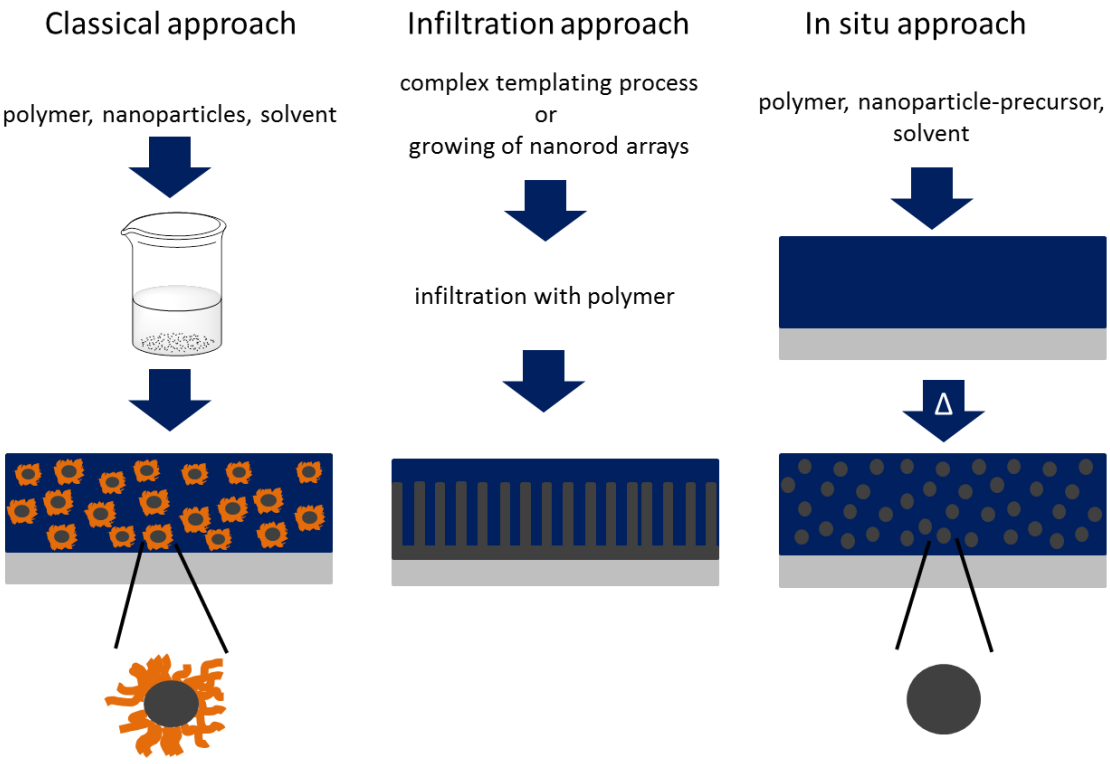


**Fig. 7: Classical, infiltration and *in situ* approach for the nanoparticle synthesis.**

In the classical approach, the inorganic nanoparticles are synthesised in a separated step and afterwards are mixed together with a conjugated polymer for solar cell preparation. These nanoparticles have to be capped with an organic ligand, like long chained amines, bulky phosphines or phosphine oxides, in order to prohibit their aggregation and to control particle growth and shape. Nevertheless, the ligands influence charge dissociation and charge transport, usually by acting as a barrier for both steps. Thus, it is essential to remove or exchange the bulky ligands to smaller ones.[13] Greenham et al.[26] found out that no electron injection from the polymer to the nanoparticle occur through a layer of the TOPO (trioctylphosphine oxide) ligand, which was a most widely used organic ligand in the synthesis of nanoparticles. After removing the TOPO ligand by pyridine treatment, efficient electron injection was observed. The alkyl chain length of the capping ligand also influences the charge transfer efficiency.[68] Y. Zhou et al.[69] showed that the reduction of the capping ligand sphere by acid treatment results in better device performance.

To overcome these limitations, new functional ligands with thermally cleavable chains to partly remove the capping sphere were investigated. Furthermore, another approach is the synthesis of capping ligands, which have conjugated side groups to enhance charge dissociation and charge transport.[70-72] Nevertheless, the synthesis of these new ligands is often complex.

In contrast to this, the nanoparticles are formed directly in the polymer matrix in the *in situ* approach. No capping ligands are needed, thus, the particle to particle distance is typically shorter, which facilitates charge transport. Nevertheless, as the nanoparticle synthesis takes place in presence of the polymer, the formation should occur at moderate temperatures, to avoid harming the structure and the optoelectronic properties of the polymer. As crystal growth is influenced together with the high viscosity of the polymer melts and solutions, the size and shape of the nanostructures cannot be tuned so easily. This may induce a lower crystallinity and higher defect density, which influences the electronic properties of the nanoparticles negatively. Furthermore by-products are generated during an *in situ* approach, leading to problems if they are not completely removed from the material.[13]

In the infiltration approach, nanostructures are synthesised in a first step, followed subsequently by their infiltration with an organic polymer, thus no capping ligands are used. Disadvantages are the often used higher temperature steps and long reaction times, which make this approach not suitable for the favoured roll-to-roll processes. Furthermore, the infiltration of viscous polymers into small pores may be difficult. These more complex processing steps may be a limiting factor in future applications concerning fast and cheap production.[13]

Requirements for an *in situ* approach are high soluble precursors (polymer and precursor should be soluble in the same solvent), which can be converted in the corresponding nanoparticles under moderate conditions, which are compatible with conjugated polymers. The side products, which are formed during the conversion of the precursor, should be easily removable from the material. The advantage of this method is that only one process step is needed, avoiding capper exchange reactions, due the ability of the polymer to react as capper, which prevent extensive particle growth.[13]

A common *in situ* approach for the preparation of TiOx is the usage of titanium-alkoxide, as titanium(IV)isopropoxide[73] or tetrakis(9H-carbazole-9-yl-ethyl-oxy)titanium[74], which are very reactive towards moisture. A similar approach is used for ZnO, where the decomposition of diethylzinc[75] under moisture is used for the preparation of the nanoparticles.

Nevertheless, more relevant for this thesis is the synthesis of polymer/metal sulphide nanocomposites, which can occur in solution, containing the polymer, a metal salt and a sulphur source. Common sulphur sources are elemental sulphur, $H_2S$ and $Na_2S$.[76,77]. The advantages of the synthesis in solution are that the size and shape of the nanoparticels can be tuned quite easily. The size can be controlled by variation of reaction time and temperature. Thus, the absorption can be tuned without changing the material combination by altering the nanoparticle size, due to the quantum confinement effects. The shape of the nanocrystals can be controlled by the used precursor material, solvents and solvent mixtures.[13] An example for these phenomena is given by the research of Watt et al[76], where it was established, that spherical PbS nanoparticles were formed by using elemental sulphur whereas cubic nanostructures were prepared by using $H_2S$ as sulphur source. Additionaly, polymer/metal sulphide nanocomposites can be prepared in the solid state. Therefore, precursors were converted via a mild thermal treatment to their corresponding metal sulphides, directly in the polymer matrix.[13] In first reports metal salts and thiourea were used for the preparation of CdS, ZnS[78] as well as $CuInS_2$[79] nanocrystals. Promising precursors for the *in situ* synthesis of metal sulphides are xanthates, which will be discussed in the next chapter.

## 6.1 Xanthates as precursor material for *in situ* synthesis

Metal xanthates (metal dithiocarbonates) are of great interest due to their wide range of applications. They find usage in petroleum industry either as catalysts or lubricant additive, as biocides and as analytical reagent. Because of their strong complexation with heavy metal ions, xanthates are useful ligands for extraction of heavy metals like Hg, Ag and Cd from soils.[80] Furthermore, transition metal xanthates have been investigated for nonlinear optical

applications.[81] Xanthate complexes show great structural diversity which ranges from monomeric to polymeric supramolecular assemblies. [82] In the last years, there is an on-going interest in the use of metal xanthates for the preparation of metal sulphide nanoparticles and thin films.[82] Xanthate complexes typically decompose by the Chugaev elimination reaction[83] and are suitable precursors for the *in situ* synthesis of metal sulphides in a polymer matrix (Fig. 8).

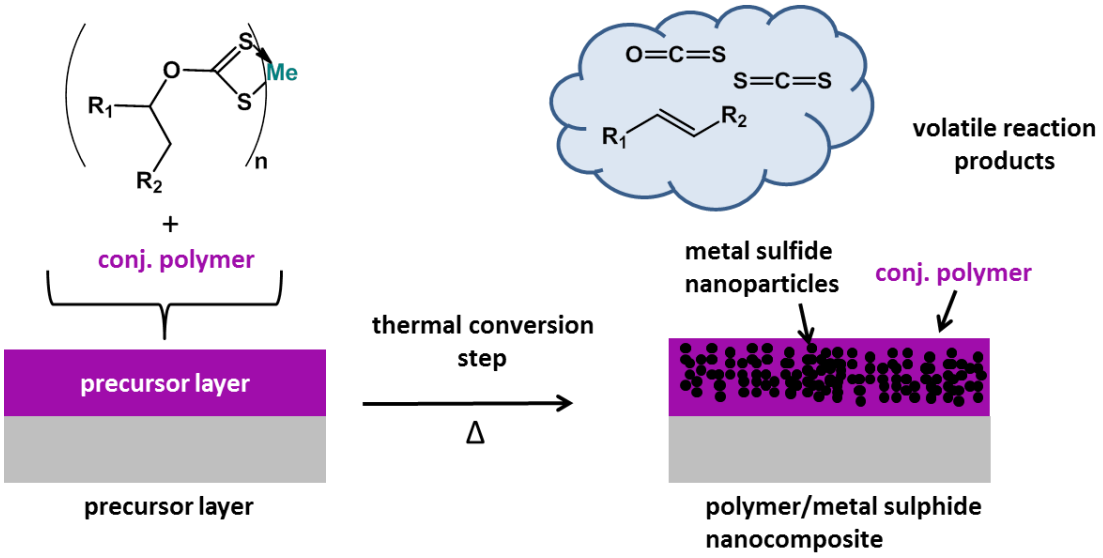


**Fig. 8: Chugaev elimination reaction from metal xanthates directly in a polymer matrix.**

The advantage of this method is that all developing side products are volatile and evaporate during the thermal conversion step. Thus, pure metal sulphide and furthermore heterobimetallic sulphide materials (e.g. $CuInS_2$, $CuBiS_3$ and $CuSbS_2$) can be prepared.

These nanostructured metal sulphides are a very interesting class of materials, due to their possible applications in a variety of devices, such as solar cells, light-emitting diodes, sensors, thermoelectric devices, lithium-ion batteries, fuel cells, and non-volatile memory devices.[84-86] Metal sulphides are often prevalent and cheap, because they usually exist in nature as minerals (pyrite = $FeS_2$).[87] Metal sulphides like CdS, PbS and CIS are common acceptor materials in nanocomposite solar cell applications.

Xanthates as precursor material for CIS as acceptor in nanocomposite solar cells have been extensively investigated by our group leading to efficiencies up to 2.8%.[15] For the preparation of these solar cells, copper and indium O-2,2-dimethylpentan-3-yl xanthates were used as precursors. In addition, reports on nanocomposite solar cells with CdS as acceptor material, which were derived from a xanthate precursor were published by S. Haque et al.[14, 88] In these studies, cadmium ethyl-xanthates with pyridine as co-ligand were used, leading to efficiencies

around 2%. Recently, during the work for this thesis, S.Haque et al[89] published polymer/$Sb_2S_3$ solar cells originating from xanthate precursors with an efficiency of 1.3%.

# 7 Strategies for PCE improvement in bulk heterojunction solar cells

Several parameters have to be optimized in order to achieve solar cells with high power conversion efficiencies, which are presented in this chapter.

## 7.1 Optimization of active layer thickness

As conjugated polymers have a high absorption coefficient (above $10^5$ $cm^{-1}$), several photons can be absorbed already in thin active layers.[90] Although thicker layers can lead to enhanced light absorption, it may be inefficient for charge transport and collection. Charge transport mainly occurs by hopping processes, which differs from the band transport in inorganic semiconductors. When the active layer thickness increases, the built-in electric field is reduced at a given built-in voltage, but a longer hopping path is required to be overcome to extract electrons and holes to their corresponding electrodes. Thus, the charge transport/collection efficiency is reduced. Therefore, the thickness of the active layer has to be optimized for enhanced solar cell performance. The optimal thickness for polymer based solar cells is around 100-300 nm.[22]

## 7.2 Morphology control in the active layer

A large donor/acceptor interlayer is required for efficient exciton dissociation and charge transfer. Furthermore an interpenetrating bicontinuous percolating pathway for effective charge transport to the electrodes is necessary. It is important, that the domain size of the donor polymer, which influences the mobility, is within its exciton diffusion length, to ensure, that any photoexcitation in the active layer is capable to reach the interface for successful dissociation. If electrons and holes are stuck or must pass through each other phase, than the feasibility of bimolecular recombination is increased. Thus, provided phase separation is sufficient to form bicontinuous paths from the interface to the respective electrodes. The nanoscale morphology can be influenced by selection of solvents, additives, solvent mixtures, control of solvent evaporation rate and drying time, control of coating parameters, thermal annealing, acceptor nanocrystal shape and polymer molecular weights.[8,22,91-95]

## 7.3 Engineering of the structure of the nanoparticles

As mentioned above, inorganic nanoparticles can be synthesised in different geometries like spherical nanoparticles, nanorods and tetrapods. Furthermore, their band gap can be tuned by changing their size (the band gap can be increased by decreasing nanoparticle diameter). Due to quantum confinement, their absorption coefficient can be enhanced compared to the corresponding bulk materials.[22] (Detailed information is given in chapter 5.)

## 7.4 Surface modification at the donor/acceptor interface

The interface between the donor polymer and the inorganic acceptor is crucial for solar cell performance. An efficient donor/acceptor interlayer has to support forward electron transfer from donor to acceptor. Furthermore, it has to suppress backward charge recombination between holes in donors and electrons in acceptors.[22] Capping ligands influence the interface between donor and acceptor negatively due to their isolating properties, which are detrimental to charge separation and charge transport.

## 7.5 Tandem solar cells

One approach to enhance power conversion efficiency is the fabrication of tandem solar cells. Therefore two or more subcells with different absorption properties are stacked together, leading to the possibility for an increase in light harvesting. These two subcells can be connected either in series or in parallel by a suitable interlayer, which can in principle lead to a doubled $V_{OC}$ or $I_{SC}$, respectively.[96] A more detailed report on tandem solar cells is given in the following chapter.

# 8 Tandem solar cells

Shockley and Queisser evaluated in 1961 the thermodynamical limitation of the energy conversion efficiency of a single junction solar cell.[97] The two main phenomena, which were considered in their calculations, are the following (Fig. 9 A):[98]

- Photons need higher energy than the band gap of the photoactive material, to be absorbed and to contribute to the photovoltaic conversion.
- Due to the absorption of photons with higher energies than the band gap, hot charge carriers are created, which relax down to the conduction band of the photoactive materials ("thermalization").

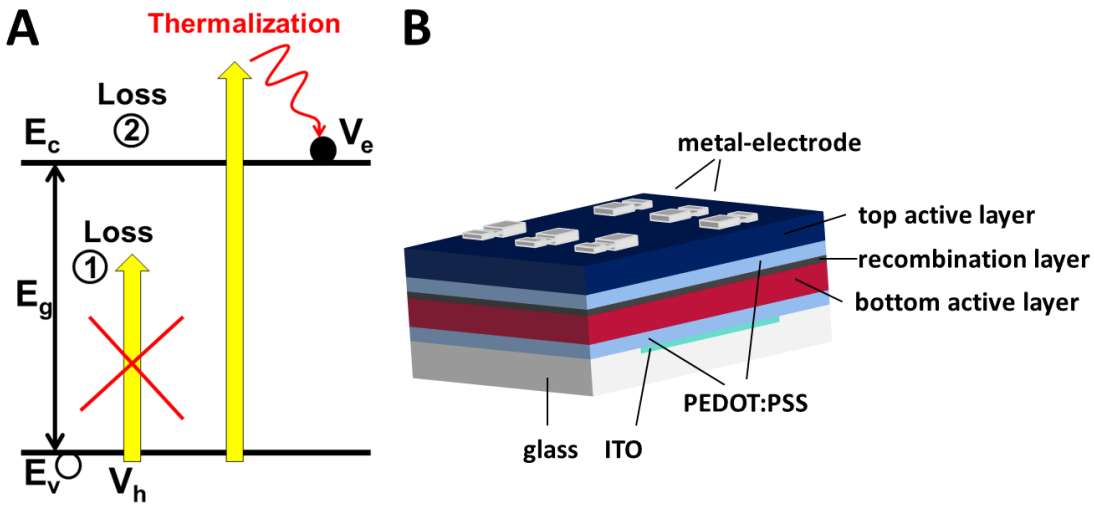


**Fig. 9: A: Description of the absorption and thermalization losses in a single junction solar cell.[98] B: Tandem solar cell architecture.**

One way to circumvent these two effects is the fabrication of tandem architectures. Tandem solar cells consist of two sub cells, stacked on top of each other (Fig. 9 B). De Vos[99] reported that theoretical efficiencies far beyond the Schockley-Queisser limitation are possible using tandem architectures. The maximum efficiency of a single cell under non-concentrated sunlight is calculated to be 30%, and can be extended to 42% using a tandem solar cell consisting of two sub cells, which have a band gap of 1.9 and 1.0 eV. This maximum efficiency can be further extended to 49% for a triplet junction, consisting of 3 sub cells, with a band gap of 2.3, 1.4 and 0.8 eV. This model enables the calculation of the ideal efficiency of a stack with an infinite number of solar cells, which is 68%.[98,99] Concerning organic solar cells and nanocomposite solar cells the tandem architectures provides the possibility to overcome two additional issues. Quite poor charge carrier mobility and lifetime limit the distance over which

the carriers can be transported. Thus, this makes it impossible to realize thick active layers that would absorb a maximum of light. The absorption spectrum of polymers is not made of a continuum like it is in inorganic semiconductors. Thus, by combination of materials with different absorption properties, it is possible to cover more efficiently the emission spectrum of the sun (Fig. 10).

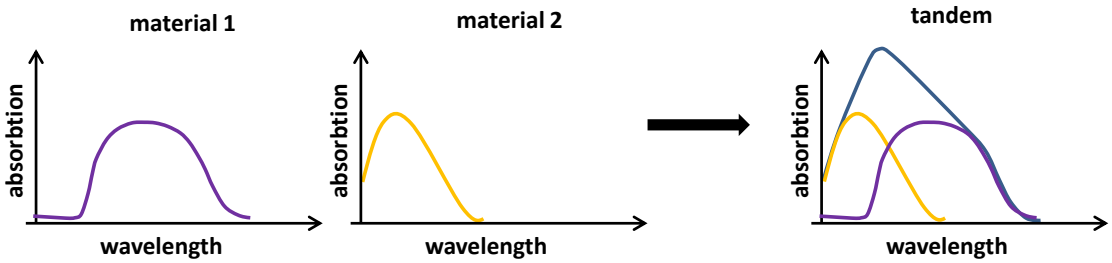


**Fig. 10: Schematic representation of two different materials with complementary absorption spectra.**

The light which is not absorbed in the bottom solar cell can be absorbed in the top solar cell. The bottom solar cell is the first active layer prepared, which is fabricated directly onto the ITO/PEDOT:PSS electrode. Thus, during fabrication it is situated below the second active layer also called top solar cell. Nevertheless, the light passes during illumination at first the bottom cell before it reaches the top cell. This nomination may be confusing, due to the fact, that during illumination by the sun the light is coming from above and the solar cell has to be turned around. Hence, the bottom solar cell is situated on top of the top solar cell during illumination by the sun.

In addition to enhanced light harvesting, thermalization losses are reduced, because of the different band gaps of the materials. Thus, low energy photons are converted to low energy excitons in a low band gap polymer.[96] The two sub cells can be connected in series, or in parallel depending of the recombination layers and the way the recombination layer and the two electrodes are connected. Mostly the connection in series is used for the preparation of tandem solar cells. Excitons are formed in all sub cells during light absorption. After exciton dissociation at the donor/acceptor interface, electrons in one sub cell and holes from the other sub cell diffuse to the interlayer, also called recombination layer, to recombine while the remaining free carriers are collected at the outer electrodes (Fig. 11).[96]

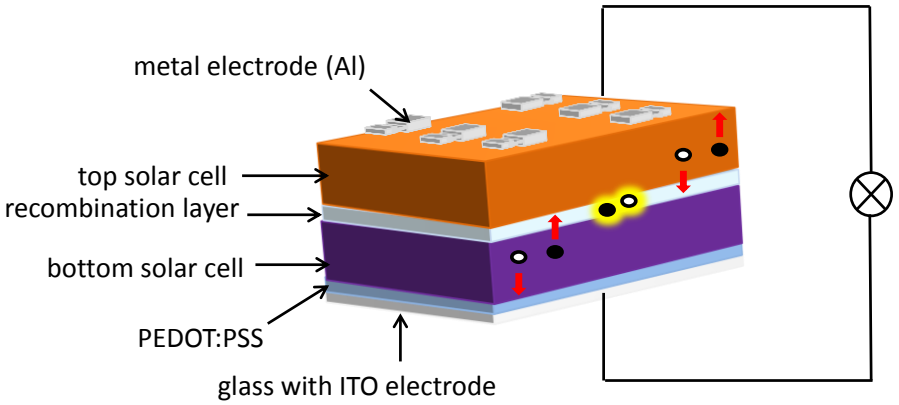


**Fig. 11: Illustration of the recombination mechanism, required in a tandem solar cell.**

Thus, the recombination layer should align the quasi-Fermi level of the acceptor of the bottom solar cell with the quasi-Fermi level of the donor of the top solar cell.

When the two sub cells are connected in series, the open circuit voltage of the tandem device is equal to the sum of the open circuit voltages of each sub cell, according to Kirchhoff's law.[98] The current is limited by the device with the smallest current, when the FF is the same for both cells.[100] When the sub cells are connected in parallel, the $I_{SC}$ is the sum of the $I_{SC}$ of all sub cells, whereas the $V_{OC}$ is the minimum of individual sub cells.[96] Thus, to achieve tandem cells with high power conversion efficiencies, optimized single solar cells are required.

In a tandem architecture, which is connected in series, polymer semiconductors with different band gaps are used for the preparation. The wide band gap polymer is placed in the bottom cell, whereas the narrow band gap polymer is used in the top cell. Therefore, the bottom cell absorb high energy photons and led the low energy photons pass through, thus they can be absorbed by the low band gap material in the top cell.[96]

Organic tandem solar cells, which are connected in parallel, are not as common as tandem devices, which are connected in series. Nevertheless Zhang et al.[101] reported a tandem device, where a PCBM layer was used to form a bilayer heterojunction subcell with the underlying CuPc and furthermore a bulk-heterojunction subcell blended with P3HT. The $I_{SC}$ and the power conversion efficiency could be enhanced significantly, and the values were close to the sum of those from the individual subcells.[96]

# III Results and Discussion

# 1 Metal xanthates as precursos for metal sulphides in solar cell applications

## 1.1 Synthesis of metal xanthates

The synthesis of the metal xanthates requires only two synthetic steps (Fig. 12).[102-105] The synthesis route is mainly the same, there are only some differences depending on the solvents, bases and metal salts used. The first step involves the synthesis of an alkali-xanthate, which will later serve as an ion source for further xanthate preparation. Therefore an aqueous solution of alkali-hydroxide (sodium or potassium) followed by a solution of carbondisulphide is added drop by drop to the respective alcohol. An alternative method investigated by A. Gonzáles-Roura et al[106] describes the alkali-xanthate synthesis using alkali-alcoholate instead of alkali-hydroxide. For the synthesis of the desired metal xanthate complex the alkali-xanthate is added drop by drop to a solution of the corresponding metal salt.

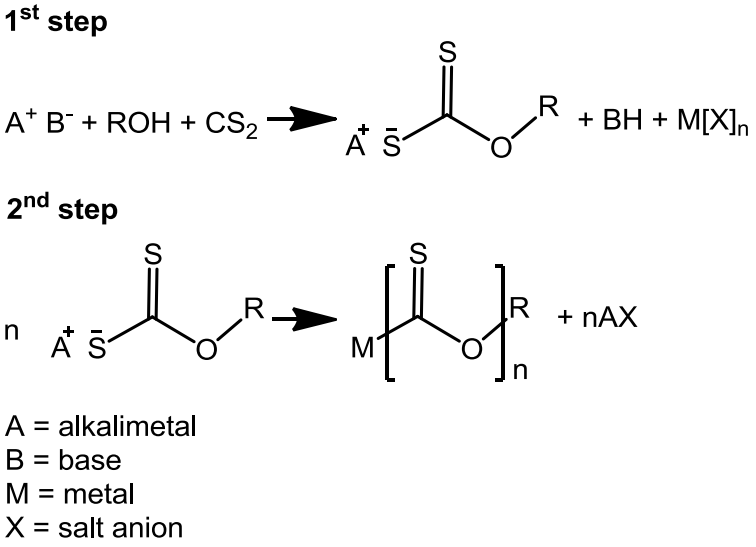


**Fig. 12: General route for metal xanthate synthesis.**

Up to now several studies of xanthates with different side chains have been published, the most common are methyl, ethyl, isopropyl and isobutyl side chains.[82,102,107] For the application as a precursor for metal sulphides in nanocomposite solar cells, high solubility in apolar solvents is required, due to the fact, that conjugated polymers are usually only soluble in these solvents. Xanthates with side chains mentioned above often do not fulfill this requirement.

Thus, they are not suitable to obtain sufficiently concentrated precursor solutions containing the photoactive polymer and the metal xanthates for the *in situ* preparation of polymer/metal sulphide nanocomposite layers. Recently Achim Fischereder[108] has investigated copper and indium xanthates with different side chains to optimize their solubility in organic solvents. Xanthates with 2,2-dimethylpentan-3-yl-group and the 3,3-dimethylbutan-2-yl-group side chains, are soluble in many common organic solvents, like chloroform, toluene and chlorobenzene and therefor suitable for solar cell fabrication (Fig. 13).

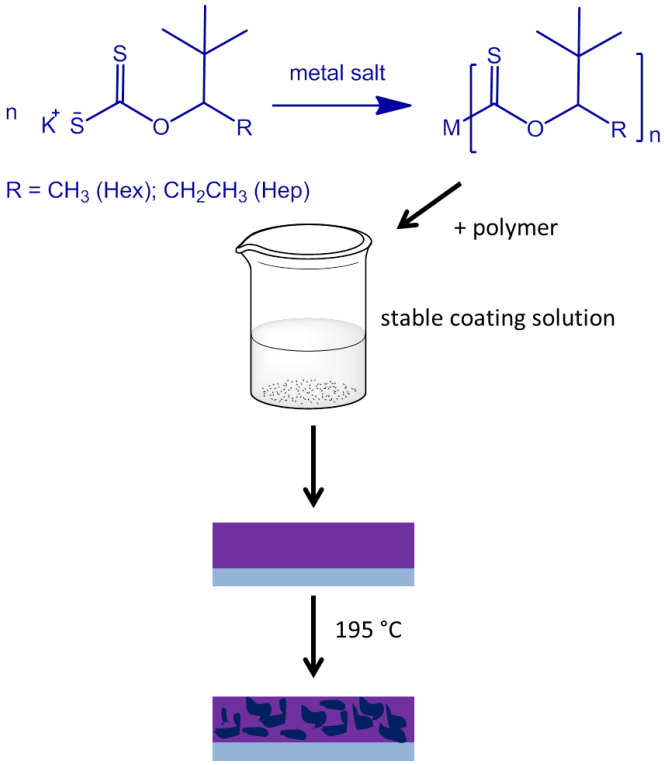


**Fig. 13: Fabrication of nanocomposite active layers with Hex, and Hep-xanthate precursors.**

To expand his work, further metals were used for the fabrication of xanthates featuring a 2,2-dimethylpentan-3-yl-group (Hep-xanthate) or a 3,3-dimethylbutan-2-yl-group (Hex-xanthate). The main focus of the presented investigation on xanthates was the suitability of the corresponding metal sulphides as an active material in solar cells. Whereas $Bi_2S_3$ (band gap = 1.3 – 1.7 eV)[109,110], $Sb_2S_3$ (band gap = 1.7 eV)[89,111] and PbS (band gap = 0.9 eV)[112,113] are well known as active materials in the solar cell community, nickel and cobalt sulphides have been applied in dye sensitised solar cells as electrode material[114,115], but may be interesting as compound of the active layers as well, due to their band gap (CoS band gap = 1.1 eV[116], NiS band gap = 0.8 eV[117]). All xanthates were synthesised from their metal salts and the respective potassium xanthates, resulting in pure products after workup and recrystallization. For bismuth and lead ethyl, hexyl and heptyl xanthates were prepared, in order to investigate the

differences in thermal conversion to the metal sulphides. In contrast to this, for antimony, cobalt and nickel only heptyl xanthates were synthesised.

A general overview of the synthesised metal-xanthates is shown in Table 1.

**Table 1: General view of the synthesised metal-xanthates.**

| Abbreviation | Chemical name | Structure | Colour | Yield / % |
|---|---|---|---|---|
| **Bi-Et** | Bismuth(III) ethyl dithiocarbonate | 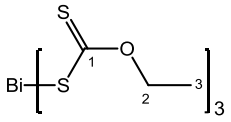 | orange crystals | 42 |
| **Bi-Hex** | Bismuth (III) O-3,3-dimethylbutan-2-yl dithiocarbonate | 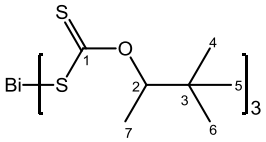 | orange crystals | 83 |
| **Bi-Hep** | Bismuth(III) O-2,2-dimethylpentan-3-yl dithiocarbonate | 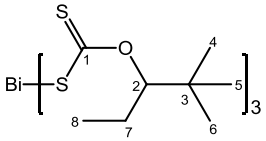 | orange crystals | 81 |
| **Pb-Et** | Lead(II) ethyl dithiocarbonate | 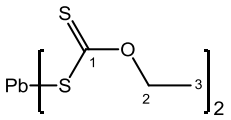 | white crystal needels | 93 |
| **Pb-Hex** | Lead(II) O-3,3-dimethylbutan-2-yl dithiocarbonate | 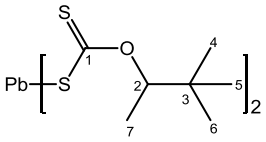 | white crystal needels | 61 |
| **Pb-Hep** | Lead(II) O-2,2-dimethylpentan-3-yl dithiocarbonate | 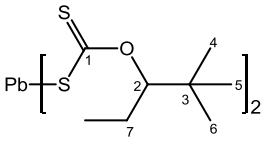 | white crystal needels | 26 |
| **Sb-Hep** | Antimony(III) O-2,2-dimethylpentan-3-yl dithiocarbonate | 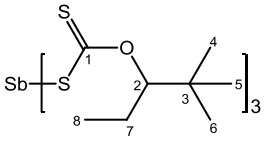 | dark orange powder | 48 |
| **Co-Hep** | Cobalt(II) O-2,2-dimethylpentan-3-yl dithiocarbonate | 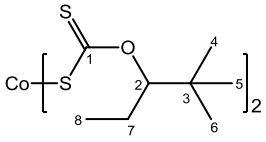 | dark green powder | 89 |
| **Ni-Hep** | Nickel(II) O-2,2-dimethylpentan-3-yl dithiocarbonate | 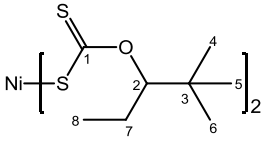 | green crystal needels | 62 |

Detailed information about the synthesis is given in the experimental part. Elementary analyses were performed to investigate the purity of the xanthates. These analyses showed that the calculated amounts of the different atoms correlate well with the expected ones. Furthermore Fourier transformation spectroscopy (FTIR), Nuclear magnetic resonance spectroscopy (NMR) and, in the case of Bi-Hex X-ray diffraction measurements were performed to achieve detailed information about the synthesised complexes.

### 1.1.1 Fourier-transformation-infrared-spectroscopy (FTIR)

In Fig. 14 the FTIR spectra of all synthesised xanthates are shown. The most intense bands were observed at 1180-1270, 1070-1080 and 1003-1050 $cm^{-1}$ and can be related to COC, CCC and $CS_2$ out-of-phase stretching vibrations. The assignment of the FTIR results is based on literature data[118-121] and is summarized in Table 2.

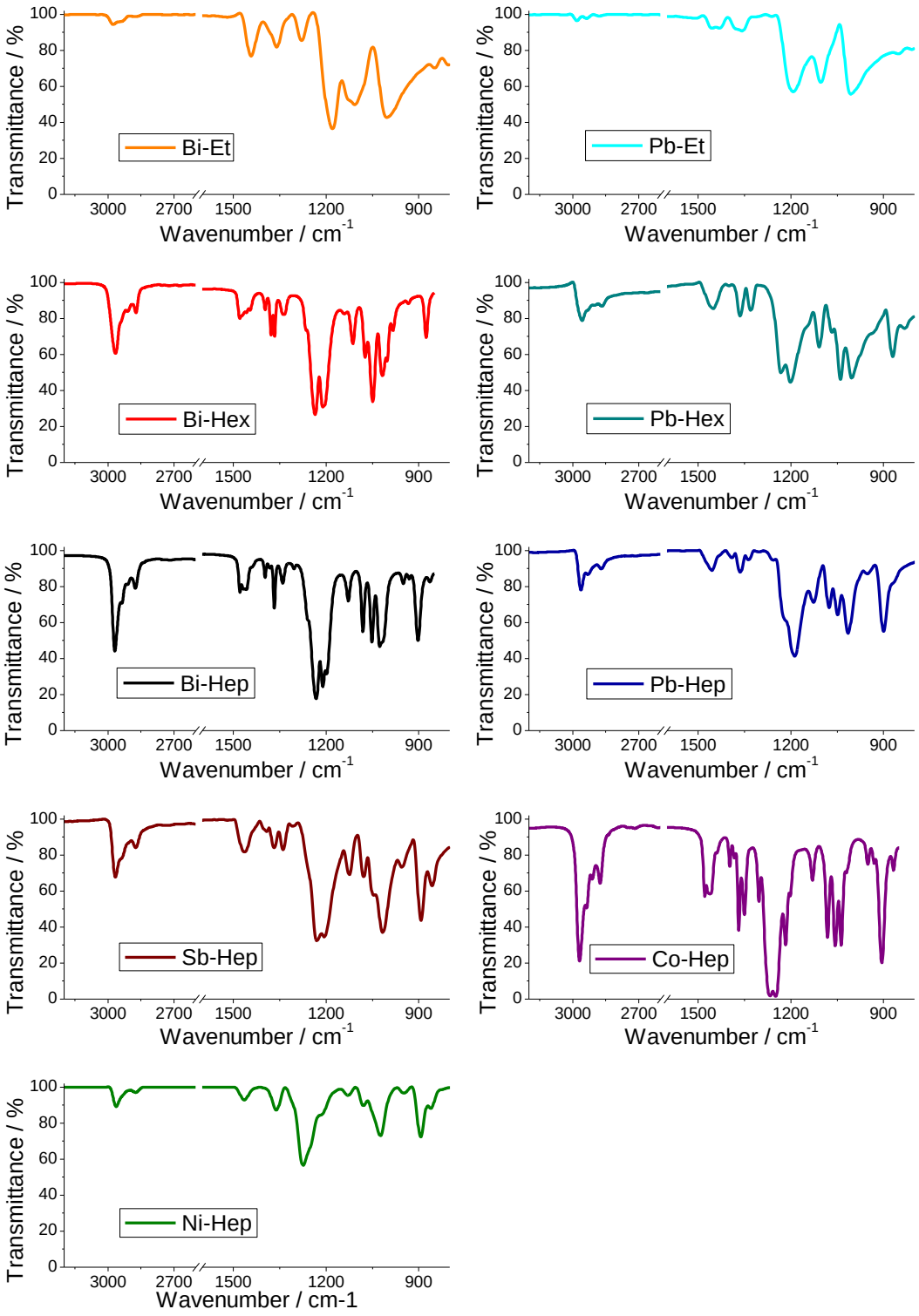


**Fig. 14: FTIR-spectra of all synthesised metal xanthates.**

The bands in the IR spectra of the metal xanthates describing the $CH_3$ stretching vibrations are all between 2870 and 2980 $cm^{-1}$. The respective signals for the $CH_3$ deformations are observed between 1330 and 1480 $cm^{-1}$. The $CH_3$ out-of-phase rocking band at around 890 $cm^{-1}$, is not

visible in the FTIR spectra of the ethyl xanthates, whereas the bands are very intense in the FTIR spectra of the hexyl and heptyl xanthates (Fig. 14).

**Table 2: Infrared frequencies and their assignments of all synthesised metal xanthates.**

| Infrared frequency / $cm^{-1}$ | | | | | | | | | Assignment |
|---|---|---|---|---|---|---|---|---|---|
| | Bi | | | Pb | | Sb | Ni | Co | |
| Et | Hex | Hep | Et | Hex | Hep | Hep | Hep | Hep | |
| 2977 | 2965 | 2969 | 2981 | 2957 | 2962 | 2966 | 2963 | 2969 | $CH_3$ out-of-phase stretching |
| | 2873 | 2875 | | 2867 | 2870 | 2874 | 2874 | 2875 | $CH_3$ in-phase stretching |
| 1443 | 1479 | 1478, 1467 | 1455, 1431 | 1451 | 1456 | 1465 | 1465 | 1478, 1462 | $CH_3$ out of phase deformation, $CH_2$ deformation |
| 1359 | 1397, 1378, 1366, 1339 | 1397, 1367, 1340 | 1358 | 1365, 1329 | 1389, 1363, 1337 | 1369, 1339 | 1360 | 1368, 1350 | $CH_3$ in phase deformation |
| 1179 | 1235, 1211 | 1232, 1211, 1198 | 1193 | 1231, 1202 | 1225, 1187 | 1230, 1206 | 1274 | 1266, 1249 | COC out-of phase stretching |
| 1107 | 1113 | 1128 | 1102 | 1108 | 1128 | 1125 | 1129 | 1130 | $CH_3$ rocking, (S)CO stretching |
| | 1074 | 1081 | | 1070 | 1076 | 1078 | 1080 | 1081 | CCC out-of-phase stretching |
| 1003 | 1049, 1018 | 1052, 1026 | 1006 | 1040, 1003 | 1048 1014 | 1046 1017 | 1025 | 1057, 1037 | $CS_2$ out of phase stretching |
| | 876 | 902 | | 870 | 901 | 893 | 894 | 905 | $CH_3$ out-of-phase rocking perpendicular to OC(H) |

Three different resonance structures can be assigned to xanthate ions (Fig. 15).

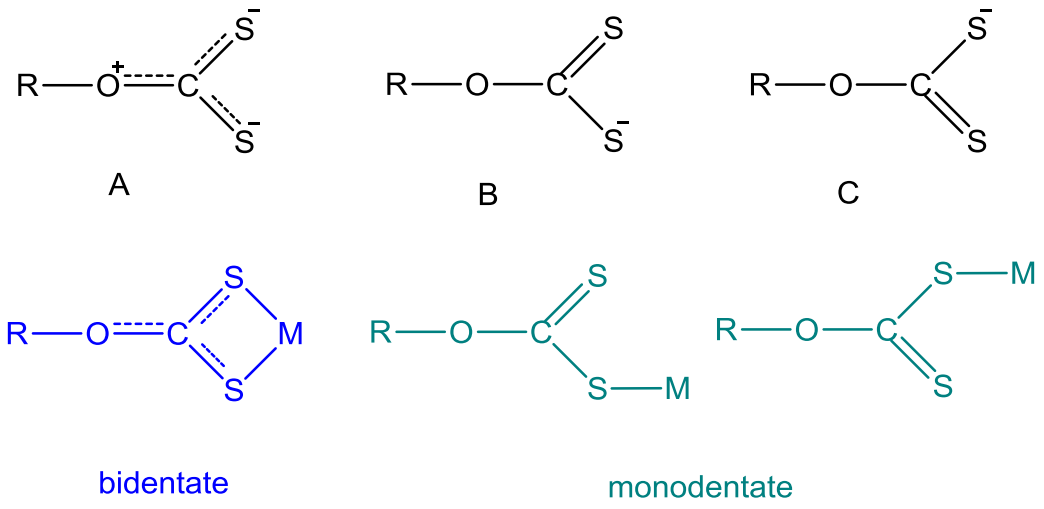


**Fig. 15: The three different resonance structures assigned to xanthate ions.**

The resonance forms B and C are related to a monodentate coordination of the xanthate to the metal. Both forms feature an enhanced π-bond character between the carbon atom and the non-coordinated sulphur atom. The zwitterionic structure A is present in bidentate ligated xanthate complexes. The σ-bond acquires a partial π-bond character whereas the π-bond character of the C-S bond is lowered. Notably, metal xanthates can also be present in oligomeric or polymeric structures. In such compounds one sulphur atom of the $CS_2$ moiety acts as a linker between two metal centers.

Shankaranarayana et al.[121] assigned the absorption band at 1268 $cm^{-1}$ to the C-S frequency and the band at 1025 $cm^{-1}$ to the C-O-C vibration. More recent studies suggest the opposite assignment of the two bands. Vreugdenhil et al. [122] denoted that in some cases the M-S bond strength can be directly related to the C-O vibration frequency. Hunt et al.[119] stated that S-C-S angle influences the position of the C-O-C absorption band. Larger S-C-S angles result in a higher π-character of the C=S bond decreasing the C-O-C vibration in energy.

Mass effects and different electronegativities of the ligated metal atoms as well as the coordination number further influence the coordination mode and the related stretching vibrations of the xanthate moiety.[121,123] Higher coordination numbers lead to more C-S and C-O-C vibtrations, which can be highly coupled depending on geometry and symmetry. This results in more absorption bands overlaying each other and thus yielding broad signals with shoulders.

Notably, a clear assignment of IR absorption bands remains a difficult task without X-ray crystallographic or quantum chemical data. The absorption bands in the IR spectra of the

synthesized metal xanthates were hence assigned according to more recent literature procedures.[118]

For the synthesised Bi and Pb compounds the C-O-C stretching vibration increases with the size of the xanthate side chain. The C-O-C absorption bands of both transition metal xanthates are close to each other at around 1260-1270 $cm^{-1}$. The corresponding signal for the heptyl xanthates of the three main group metals is shifted to lower frequencies at around 1230 $cm^{-1}$. Notably, the C-O-C absorption band of all synthesized metal xanthates shows 80 to 170 $cm^{-1}$ higher frequencies than the corresponding sodium or potassium salts.

### 1.1.2 Nuclear magnetic resonance spectroscopy (NMR)

The $^{1}H$ NMR and $^{13}C$ NMR spectra revealed the expected signals for the different H atoms according to literature data.[124] All measured xanthates exhibited the typical high resonance shift of the C1 carbon atoms at approximately 225 ppm and of the C2 carbon atoms at approximately 95 ppm (at 71 ppm in the case of Bi-Et) (Fig. 16) in the $^{13}C$ NMR spectra and of the proton at the C1 carbon atom in the $^{1}H$ NMR spectra. The shifts of the resonances are shown in Table 3.

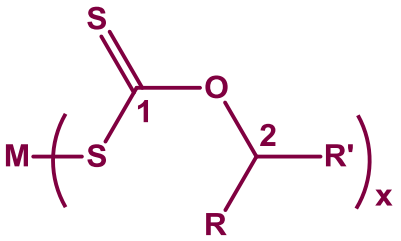


R' = H (Et-xanthate)
R' = $C(CH_3)_3$ (Hex- & Hep-xanthate)
R = $CH_3$ (Et- & Hex-xanthate)
R = $CH_2CH_3$ (Hep-xanthate)

**Fig. 16: Chemical structure of the xanthate for NMR analysis.**

**Table 3: Resonance shifts of the synthesised xanthates, expect of Pb-Et and Pb-Hex, which were not soluble in chloroform. Data for K-Hex and K-Hep were taken from A. Schenk.[125]**

| Xanthate | $HC_2$ in ($^{1}H$-NMR) | $C_1$ ($^{13}C$-NMR) | $C_2$ in ($^{13}C$-NMR) |
|---|---|---|---|
| Bi-Et | 4.72 | 226.0 | 71.4 |
| Bi-Hex | 5.43 | 225.5 | 91.1 |
| Bi-Hep | 5.50 | 227.1 | 96.4 |
| Pb-Hep | 5.47 | 229.7 | 94.2 |
| Sb-Hep | 5.37 | 224.3 | 96.9 |
| Co-Hep | 5.12 | 224.9 | 91.9 |
| Ni-Hep | 5.00 | 229.1 | 93.8 |
| K-Hex[125] | 5.40 | 233.7 | 84.4 |
| K-Hep[125] | 5.62 | 235.4 | 88.7 |

In the $^{1}H$ NMR spectra the resonances of Bi-Hex, Bi-Hep, Pb-Hep, Sb-Hep, K-Hex and K-Hep showed similar shifts, whereas the resonances of Co-Hep and Ni-Hep are shifted upfield. In the $^{13}C$ NMR spectra, the resonances of the C1 atoms are shifted generally upfield, whereas the resonances of the C2 atoms are shifted downfield compared to the potassium xanthates.

### 1.1.3 Crystal structure

In the case of Bismuth(III) hexyl xanthate, single crystals suitable for X-ray diffraction analysis were obtained (Fig. 17; Table 4).

**Table 4: Crystallographic data for Bi-Hex.**

| | |
|---|---|
| **Empirical formula** | $C_{43}H_{78}Bi_2Cl_4O_6S_{12}$ |
| **Formula weight** | 1635.53 |
| **Crystal system** | Monoclinic |
| **Space group** | C2/c |
| **Volume** | 6364.7(4) $Å^3$ |
| **Z** | 4 |
| **Density (calculated)** | 1.707 $Mg/m^3$ |

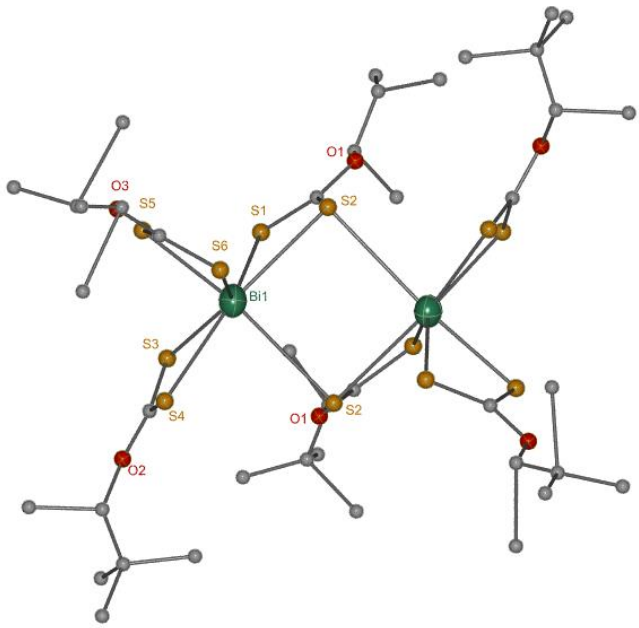


**Fig. 17: Crystal structure of the Bi-Hex (image taken by A. Torvisco Gomez).**

The Bi-Hex compound crystallizes in the monoclinic space group C2/c. The crystal structure contains residual amounts of chloroform used as a solvent for crystallisation. The Bi central atom is surrounded by six sulphur atoms derived from the three asymmetrically bound

xanthate ligands. An additional interaction with a bridging sulphur atom from the neighbouring Bi(xanthate)$_3$ unit results in the formation of a dimer complex with a Bi-S interatomic distance of 3.205(2) Å which is significantly longer than the direct chelating Bi-S bonds (see also table 1). Thus, the environment of the bismuth atom is seven coordinated, and a four membered ring is formed by the bismuth metal and the bridging xanthate ligand, with all angles close to 90 °. Similar dimeric structures with a bridging sulphur bond have been found for Bi($S_2COCH_3$)$_3$ [126] as well as for the dithiocarbonate compound Bi[$S_2CN(C_2H_5)_2$]$_3$[127]. In contrast to our results, a polymeric structure caused by a similar bridging Bi-S-interaction has been found in the tris(O-isopropylxanthato)-Bismuth(III) presented by B.F. Hoskins et al. [128]

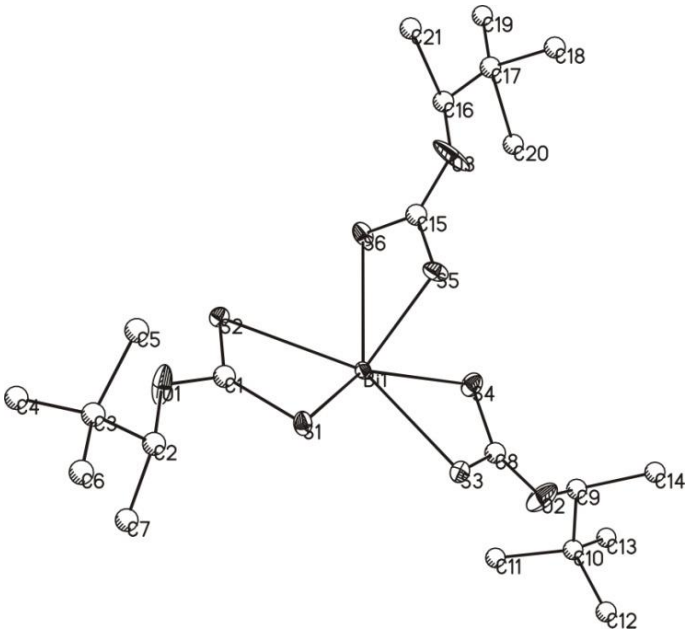


**Fig. 18: Numbering of the atoms in the crystal structure.**

**Table 5: Selected interatomic distances (Å) and angles (°) for Bi-Hex.**

| | | | |
|---|---|---|---|
| Bi(1)-S(1) | 2.7782(15) | Bi(1)-S(2) | 2.9772(14) |
| Bi(1)-S(3) | 2.7134(15) | Bi(1)-S(4) | 2.8350(16) |
| Bi(1)-S(5) | 2.6032(15) | Bi(1)-S(6) | 2.9614(16) |
| Bi(1)-S(2a) | 3.205(2) | S(1)-C(1) | 1.692(6) |
| S(2)-C(1) | 1.709(6) | C(1)-O(1) | 1.308(7) |
| O(1)-C(2) | 1.503(9) | S(3)-C(8) | 1.702(7) |
| S(1)-C(1)-S(2) | 123.2(4) | S(1)-Bi(1)-S(2) | 62.51(4) |
| S(3)-C(8)-S(4) | 122.7(4) | S(3)-Bi(1)-S(4) | 64.79(5) |
| S(5)-C(15)-S(6) | 124.0(4) | S(5)-Bi(1)-S(6) | 64.65(4) |
| S(2)-Bi(1)-S(2a) | 90.53(2) | Bi(1)-S(2)-Bi(1a) | 89.22(2) |

The Bi-S distances of the Bi-Hex vary between 2.6032(15)-2.9772(14) Å (table 3). All measured interatomic distances correlate very well with the distances found in other Bi-xanthates. Interestingly, there are two groups of Bi-S distances; one of them exhibits short M-S bonds, the other one long M-S ones, due to the intermediate mode of coordination of the xanthate ligand.[126,128] The C-O bonds of the $S_2CO$-group (e.g. C(1)-O(1)) show interatomic distances of approx. 1.31 Å typical of carbonate type bonding, whereas the C-O bonds to the alkyl moiety exhibit significantly larger values of 1.50 Å (e.g. O(1)-C(2)).

## 1.2 Formation of the metal sulphides

In this chapter the decomposition behaviour of the synthesized metal xanthates and the formation of the corresponding metal sulphides is investigated.

### 1.2.1 Thermal gravimetric analysis

For the thermal gravimetric analysis (Fig. 19), the samples were analysed as synthesised, without any further sample preparation.

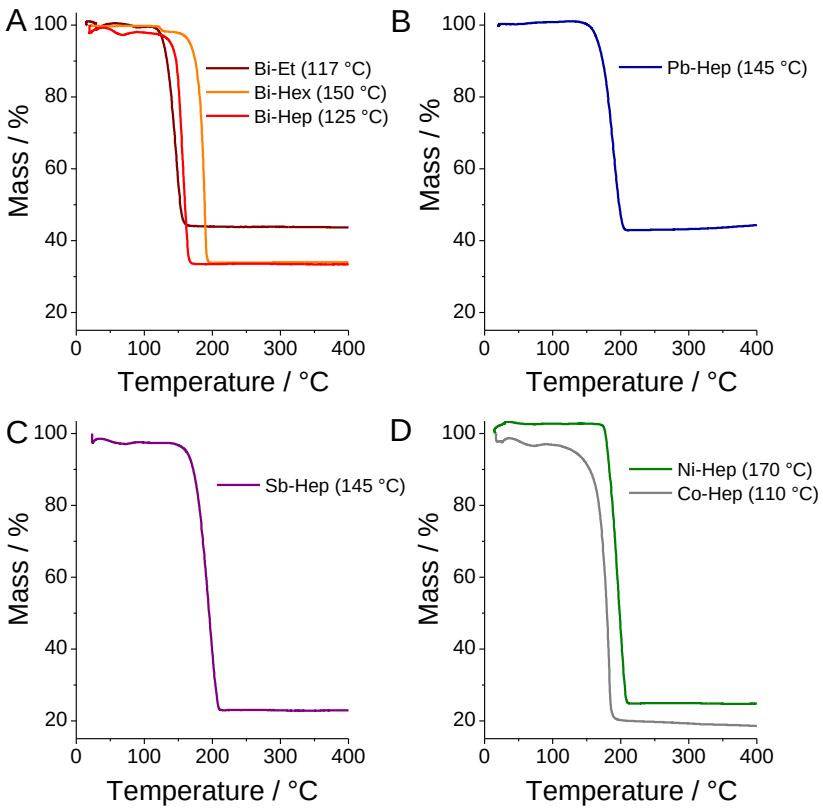


**Fig. 19: Thermal gravimetric analysis for A: Bi-xanthates, B: Pb-Hep, C: Sb-Hep and D: Co-and Ni-Hep.**

In general, decomposition starts between 110 and 170 °C followed by a rapid weiht loss. After this weight loss, a long plateau is evidence for metal sulphide formation. Fig. 19 A shows the thermal gravimetric analysis for the Bi-xanthates. Bi-Et decomposes at 117 °C, which is the lowest decomposition temperature of the three Bi-xanthates. Interestingly, Bi-Hex decomposes at a higher temperature than Bi-Hep. Pb-Hep (Fig. 19 B) and Sb-Hep (Fig. 19 C) show a conversion temperature of around 145 °C. Fig. 19 D shows the thermal gravimetric analysis for Co and Ni-xanthates. Co-Hep decomposes at a comparatively low temperature of around 110 °C, whereas Ni-Hep reveals a conversion temperature of 170 °C. In general, decomposition starts between 110 °C and 170 °C, depending on the xanthate moiety and the metal atom, followed by a rapid loss in weight. The decomposition is finished between 165 °C and 210 °C. Table 6 summarizes all thermo gravimetric data.

**Table 6: TGA results of the synthesised xanthates.**

| Xanthate | Decomposition Onset / °C | Decomposition End Point/ °C | Mass Loss / % (practically) | Mass Loss / % (theoretically) |
|---|---|---|---|---|
| Bi-Et | 117 | 165 | 60 | 55 |
| Bi-Hex | 150 | 195 | 67 | 65 |
| Bi-Hep | 125 | 172 | 68 | 67 |
| Pb-Hep | 140 | 206 | 58 | 58 |
| Sb-Hep | 140 | 210 | 77 | 76 |
| Ni-Hep | 170 | 210 | 81 | 79 |
| Co-Hep | 110 | 190 | 81 | 79 |

The practical mass loss of all xanthates is in good accordance with the theoretical one. The slightly higher practical mass loss of Bi-Et can be related to solvent residues in the samples. Concerning their application in nanocrystal-polymer solar cells the conversion of the precursor xanthates has to be at a moderate temperature, because the formation takes place in the presence of the conjugated polymers. High temperatures could harm the structure and the optoelectronic properties of these polymers leading to poorer power conversion efficiencies in solar cells. Hence one important result was that the thermal gravimetric analysis shows complete conversion at ≤210 °C for all presented metal-xanthate complexes.

### 1.2.2 High resolution mass spectrometry

The thermal decomposition of the Bi-Hex, Bi-Hep and Pb-Hep was investigated additionally by high resolution mass spectrometry (HRMS; the MS of Bi-xanthates is shown in Fig. 20; the MS of Pb-xanthate in Fig. 21). For this analysis the samples were heated from room temperature to 350 °C with different heating rates for Bi-and Pb-xanthates (Bi-Hex & Bi-Hep: in 2 min to

40 °C, than 10 °C/min under high vacuum; Pb-Hep: in 2 min to 40 °C, than 10 °C/min until achieving 160 °C, 2 min holding 160 °C, than with 10 °C/min to 180 °C, afterwards fast heating to 350 °C).

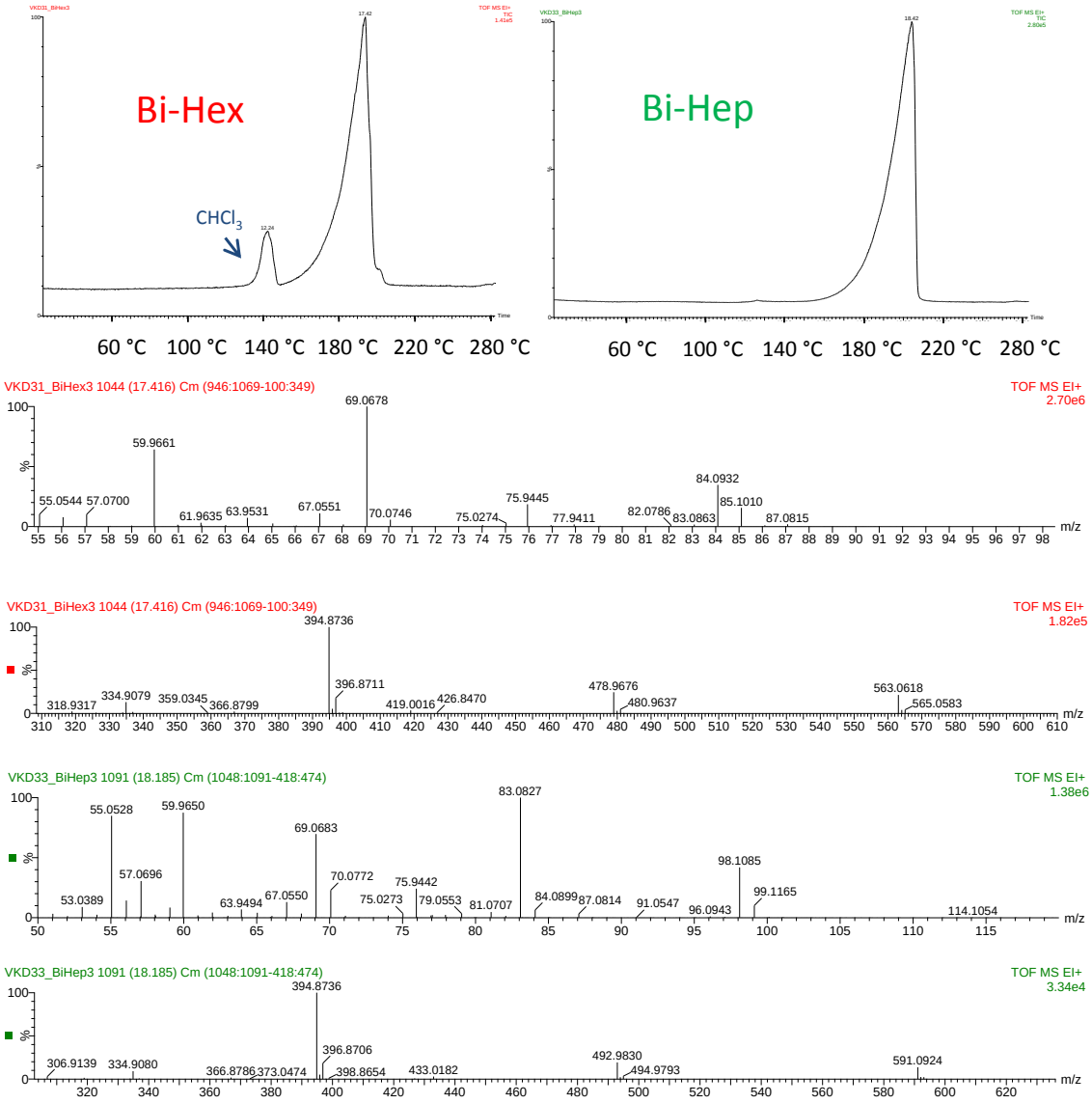


**Fig. 20: MS-spectra for Bi-Hex and Bi-Hep (MS measurements were done by R. Saf).**

The analysed xanthates do not only decompose, but also partly evaporate, due to the high vacuum used during MS measurements. This issue should be considered, if a vacuum process is applied for the fabrication of polymer/metal sulphide nanocomposite layers. The decomposition and simultaneous evaporation of both Bi-xanthates started at approx. 150 °C. The main products were typical fragments of the Chugaev rearrangement like carbonyl sulphide at m/z = 60, carbon disulphide at m/z = 75.9, 2,2-dimethylbutane at m/z = 84.1 for Bi-Hex, as well as 2,2-dimethylpentane at m/z = 98.1 for Bi-Hep. In addition different small fragments of the alkyl group, but no molecular ion peak were obtained.

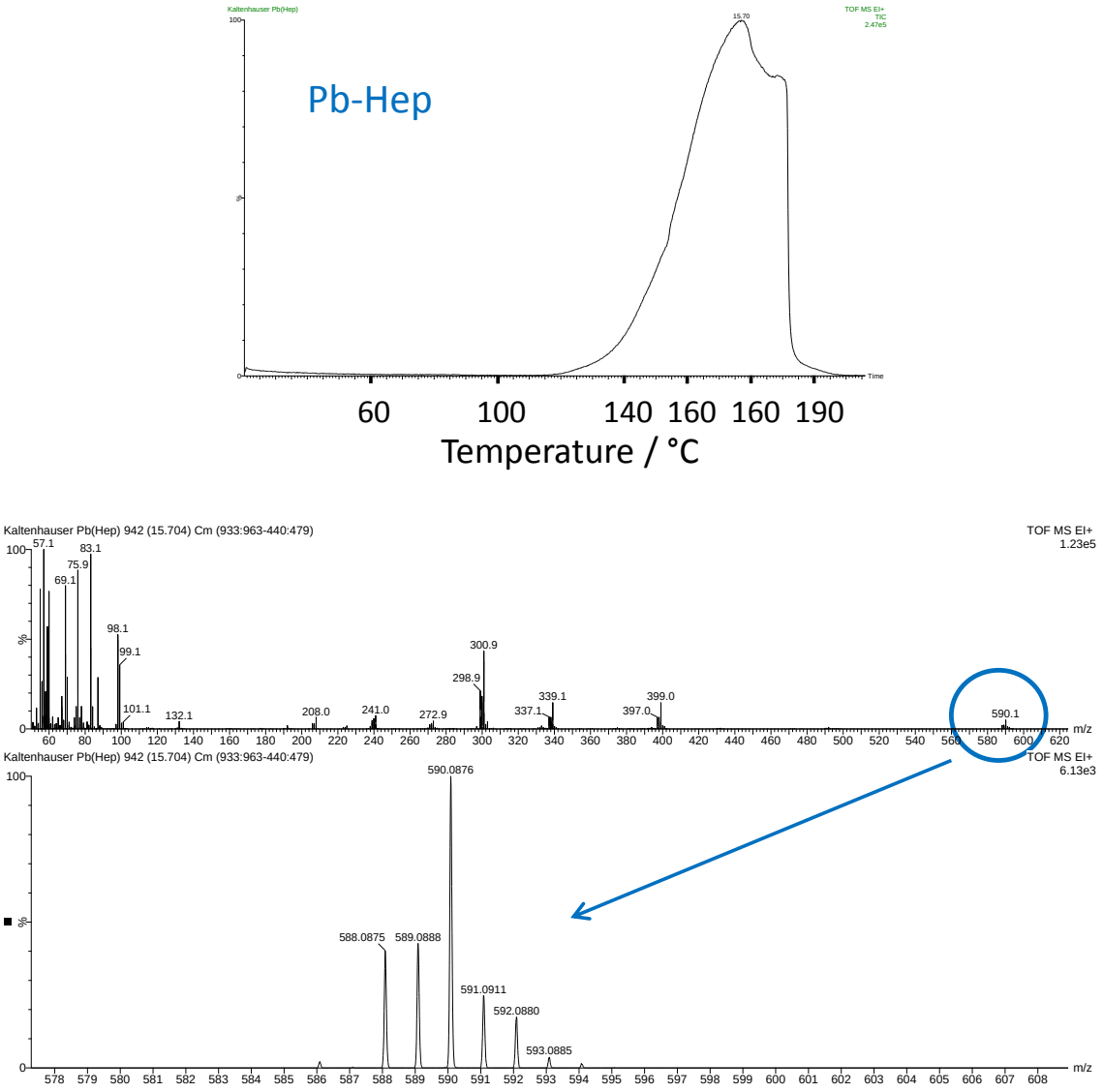


**Fig. 21: MS spectra for Pb-Hep (MS measurements were done by R. Saf).**

The decomposition and simultaneous evaporation of Pb-Hep started at approx. 115 °C. The typical fragmentations relating to the decomposition products of the Chugaev rearrangement are also presented in the mass spectra of Pb-Hep. Moreover, in contrast to Bi-xanthates, the molecular ion peak with a m/z ratio of 590.1 and the characteristic isotope pattern could be determined.

## 1.1. X-ray powder diffraction (XRD)

To investigate which crystal phase of the metal sulphides has been formed, XRD measurements were performed. For the sample preparation for the XRD analysis the Hep-xanthates (except for Bi, where the Bi-Hex was used) were dissolved in chloroform, drop-coated on glass substrates and converted into the corresponding metal sulphides via a standard temperature program (in 11 °C/min to 195 °C, holding the temperature for 15 min) in a tube furnace in $N_2$ atmosphere (Ni-Hep and Co-Hep) or on a programmable heating plate in a glove box system (Bi-, Pb- and Sb-xanthates).

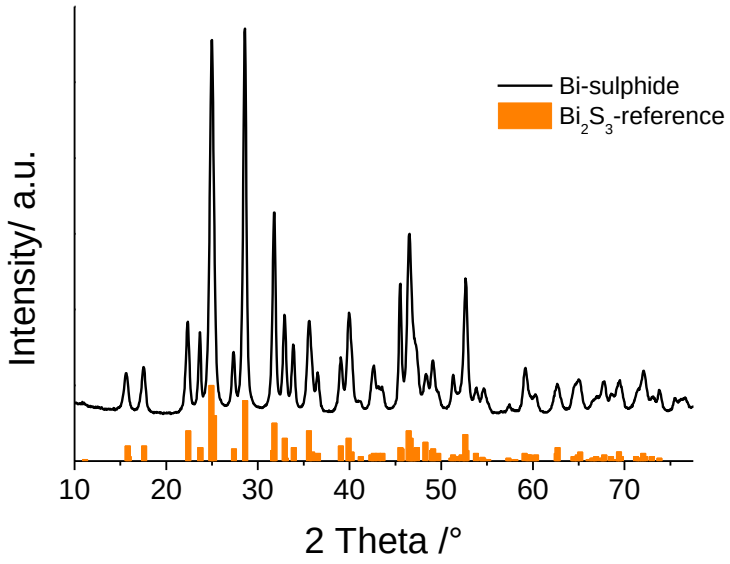


**Fig. 22: XRD pattern of the $Bi_2S_3$ nanoparticles (reference data: PDF 17-320).**

Fig. 22 shows the XRD pattern of the converted bismuth-sulphide. The numerous diffraction peaks (main peaks: 25° (1 3 0), 28.5° (2 1 1), 31.8° (2 2 1), 46.6° (5 0 1) and 52.7° (3 1 2)) of $Bi_2S_3$ correlate very well with the reference diffractions (Powder Diffraction File (PDF) 17-320) and no impurities or secondary phases were found. In the solid-state reaction induced by the decomposition of the Bi-xanthate a pure orthorhombic $Bi_2S_3$ phase (a = 1.114 nm, b = 1.130 nm and c = 0.3981 nm) is formed and the shape of the diffraction peaks reveals that the nanoparticles are well-crystallized. The size of the nanoparticles was estimated by Scherrer formula and revealed a size in the order of 25-29 nm estimated from the (2 1 1) (27 nm), (2 2 0) (29 nm) and (1 2 0) (25 nm) reflections.

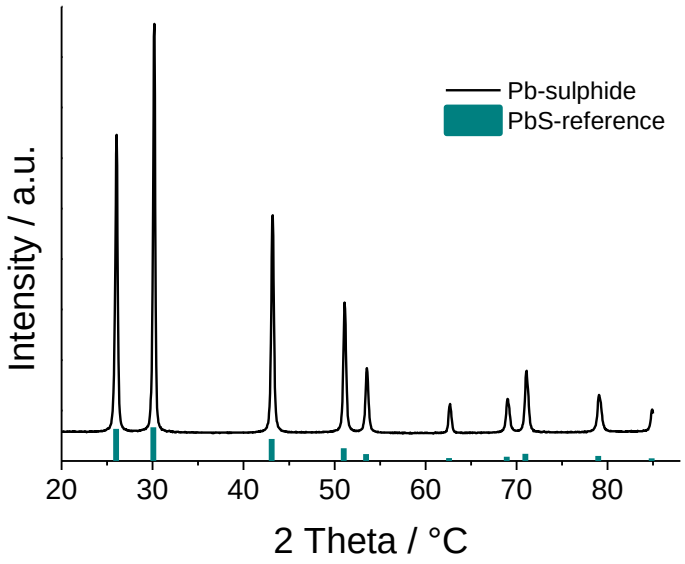


**Fig. 23: XRD pattern of the PbS nanoparticles (reference data: PDF 77-244).**

The XRD pattern of PbS (Fig. 23) reveals a nanoparticle size of around 45-59 nm according to Scherrer formula estimated from (2 0 0) (59 nm), (1 1 1) (49 nm) and (2 2 0) (45 nm) reflections. The diffraction peaks (main peaks: 26,05° (1 1 1), 30,2° (2 0 0), 43,2° (2 2 0) and 51,1° (3 1 1)) fit well with the reference diffractions (Powder Diffraction File 77-244) and a cubic face centred (a = 0.5934 nm) phase is formed.

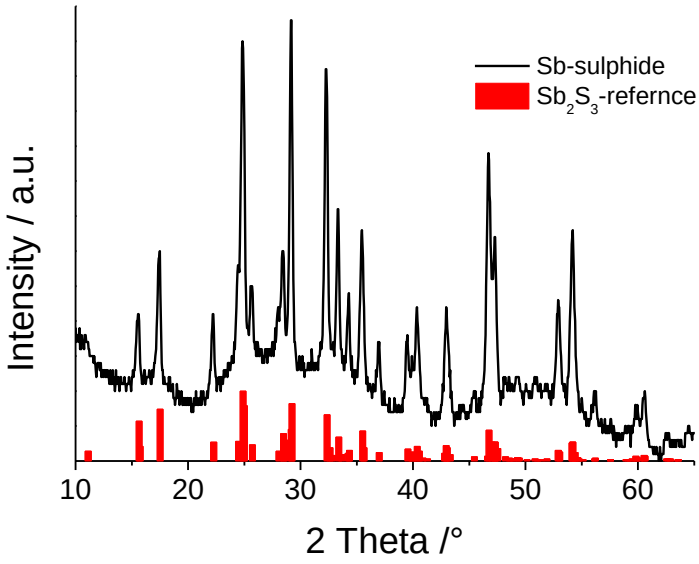


**Fig. 24: XRD pattern of the $Sb_2S_3$ (reference data: PDF 42-1393).**

$Sb_2S_3$ (Fig. 24) occurs in an orthorhombic phase (a = 1.123 nm, b = 1.131 nm, c = 0.3841 nm; Powder Diffraction File 42-1393) as well as $Bi_2S_3$. The numerous diffraction peaks (main peaks:

24.9° (1 3 0), 29.2° (2 1 1), 32.3° (2 2 1) and 46.7° (5 0 1)) correlates well with the reference diffraction, but in contrast to $Bi_2S_3$ and PbS, $Sb_2S_3$ nanoparticles seem to be not as well crystallized with a crystal size in the order of 38-50 nm according to Sherrer formula estimated from (1 2 0) (38 nm), (2 2 0) (50 nm) and (2 2 1) (48 nm) reflections.

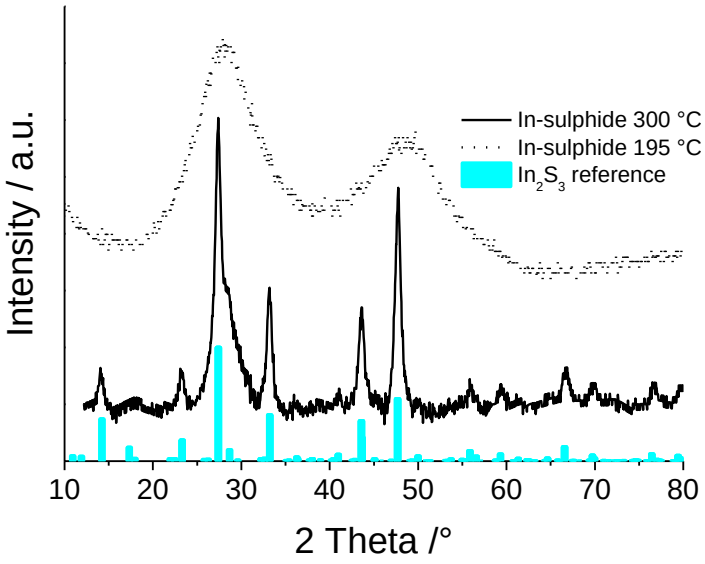


**Fig. 25: XRD pattern of the $In_2S_3$ (reference data: PDF 73-1366).**

The conversion at 195 °C of In-Hep (Fig. 25) did not clearly prove the formation of indium-sulphide, the broad peaks indicate a nanocrystalline behaviour. Therefore, a new sample was prepared, using a conversion temperature of 300 °C instead of 195 °C, to increase the nanoparticle size and crystallinity. Due to the high temperature required, the conversion of the xanthate was performed in a tube furnace in $N_2$ atmosphere instead of the thermal heating plate (in 18°C/min to 300 °C, holding this temperature for 15 min). The XRD pattern of $In_2S_3$ at 300 °C present smaller peak width than the sample prepared at 195 °C and reveals the formation of a tetragonal $In_2S_3$ phase (a = 0.7623 nm and c = 3.2360 nm; Powder Diffraction File 73-1366). The sample exhibits broad peaks at approximately 27.4° (1 0 9/2 1 3), 33.2° (0 0 12/ 2 2 0), 43.6° (3 1 8) and 47.8° (2 2 12/ 4 0 0). The $In_2S_3$ nanoparticles converted at 300 °C have a size of around 16 nm according to Sherrer equation estimated from (2 2 12/ 4 0 0) (16 nm), (0 0 12/ 2 2 0) (17 nm) and (1 1 6/ 2 0 0) (15 nm) reflections.

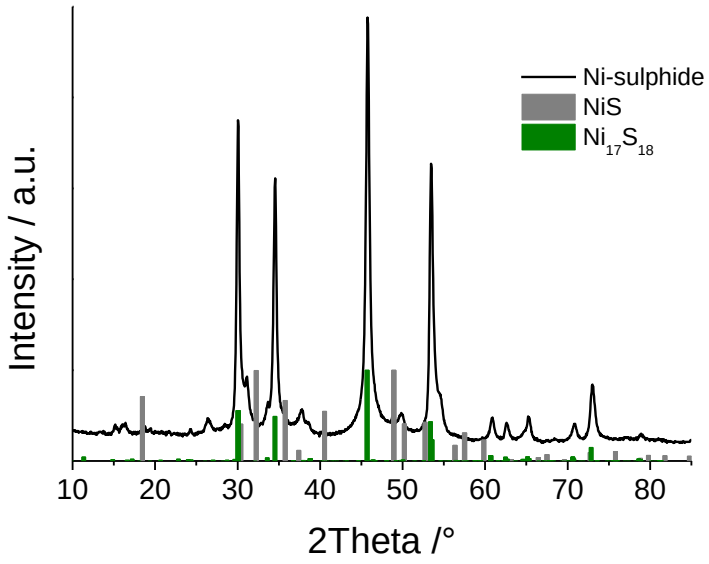


**Fig. 26: XRD pattern of the Ni-sulphide (reference data: PDF 37164 for $Ni_{17}S_{18}$ and PDF 86-2280 for NiS).**

In Fig. 26 the XRD pattern of nickel-sulphide is shown indicating that mainly a sulphur reach nickel sulphide phase is formed. The main diffraction peaks are in good correspondance with hexagonal (a = 1.029, c = 1.5993; Powder Diffraction File 37164) $Ni_{17}S_{18}$. The sample exhibits main peaks at approximately 30.1° (2 0 4/ 3 0 0), 34.6° (3 0 3), 45.8° (3 0 6) and 53.5° (3 3 0). Furthermore, a secondary phase is formed, with peaks e.g. at 31.2° (1 0 1), 37.8° (2 2 0) and 49.9° (4 1 0), which is most likely rhombohedral NiS (a = 0.9607 nm, c = 0.3143 nm; PDF 86-2280). The size of the sulphur rich nickel sulphide nanoparticles is around 23 nm estimated from (2 0 4) (22 nm), (3 0 3) (23 nm) and (3 0 6) (23 nm) reflections by Sherrer formula.

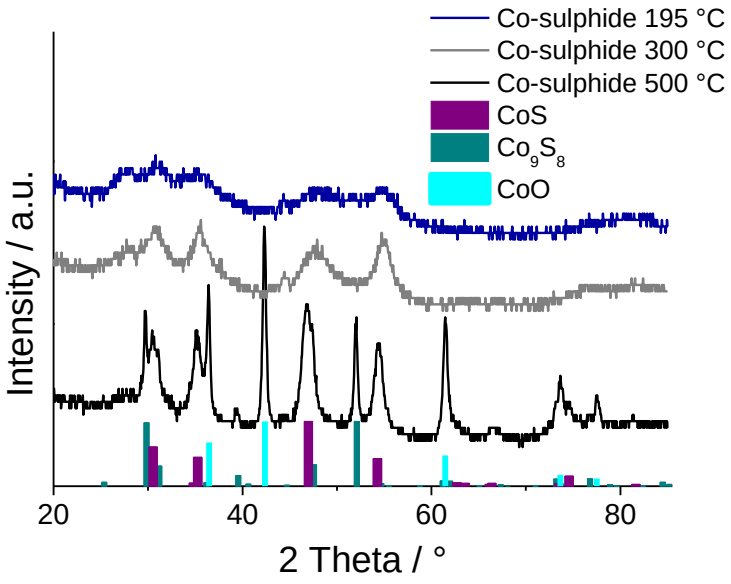


**Fig. 27: XRD pattern of Co-sulphide (reference data: PDF 75-0605 (hexagonal CoS), PDF 86-2273 (cubic $Co_9S_8$) and PDF 71-1178 (CoO)).**

Conversion at 195 °C of Co-Hep did not prove the formation of cobalt-sulphide (Fig. 27). As estimated before for $In_2S_3$ the broad peaks indicate nanocrystalline behaviour. Therefore, another sample was prepared; using a conversion temperature of 300 °C (tube furnace in $N_2$-atmosphere: in 18 °C/min to 300 °C, holding this temperature for 15 min) instead of 195 °C. Although the peak width became a little bit smaller, it was not possible to assign all peaks to a defined cobalt-sulphide. Further temperature increase was required to estimate, which crystal phase-formation is preferred. Therefore a sample using a conversion temperature of 500 °C was prepared (tube furnace: in 31 °C/min to 500 °C, holding this temperature for 15 min). The diffraction pattern indicates that beneath hexagonal CoS (PDF 75-0605; a = 0.3377 and c = 0.515) two other phases have been formed at 500 °C, a cubic sulphur poor cobalt-sulphide ($Co_9S_8$; PDF 86-2273; a = 0.9923) and cubic face centered CoO (a = 0.4263; PDF 71-1178). Broad peaks, which can be assigned to CoS occur at 35.1° (1 0 1), 46.8 ° (1 0 2) and 54.5° (1 1 0). Peaks that can be related to $Co_9S_8$ can be seen at 29.7° (3 1 1), 39.5° (3 3 1) and 52.1° (4 4 0). Broad peaks which can be assigned to CoO are observed at 36.4° (1 1 1), 42.3° (2 0 0) and 61.5° (2 2 0). Peaks that can be assigned to CoO do not occur in the samples fabricated at lower temperatures. Thus, it seems that CoO is formed favourable at higher temperatures due to leftover oxygen in the tube furnace. Nanoparticle size could only be estimated for CoO by Sherrer formula with a crystallite size of 19 nm (2 0 0). It was not possible to achieve reliable results for the other materials due to the overlap of different peaks.

### 1.2.3 Band gap determination

For the determination of optical absorption coefficients and band gaps the xanthates were dissolved in chlorobenzene and doctor bladed on glass substrates, followed by a thermal conversion step at 195 °C (200 °C for $Bi_2S_3$). The optical band gap (Eg) was determined by plotting the straight line of $(\alpha h\nu)^2$ against hν; the thicknesses of the metal sulphide layers were determined with a surface profiler.

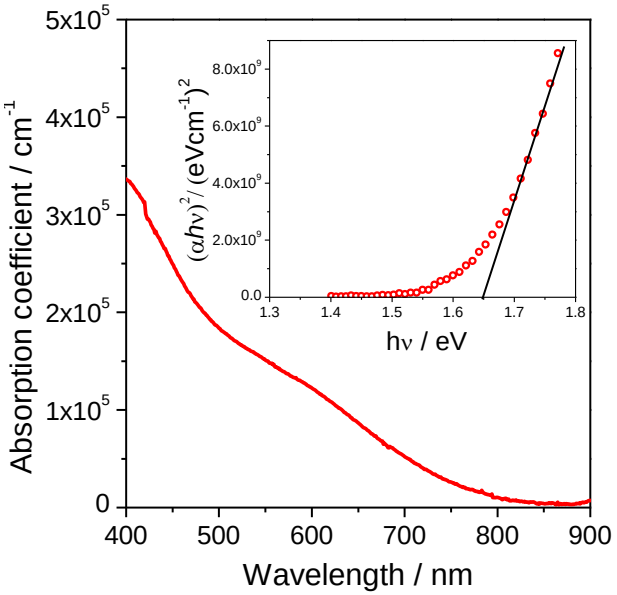


**Fig. 28: Absorption coefficient and band gap of $Bi_2S_3$.**

Fig. 28 shows optical absorption measurements of a 30 nm thick $Bi_2S_3$ film formed at 200 °C exhibiting absorption coefficients larger than $1*10^5$ $cm^{-1}$ and an optical band gap of 1.62 eV, which is near to the optimum for photovoltaic conversion but higher compared to the most cited direct band gap of 1.3 eV[129] of the bulk crystals. Nevertheless, Eg values of 1.67 eV[9] for $Bi_2S_3$ nanocrystalls have also been reported in literature, interestingly amongst others for $Bi_2S_3$ nanorods obtained from xanthate decomposition.[102] These differences in the optical band gap may be explained by quantum size effects in the optical spectrum.[130] Furthermore, pnictide chalcogenites, especially $Bi_2S_3$, are known to show extremely wide changes in the band energy and conductivity with changes in stoichiometry.[131,132]

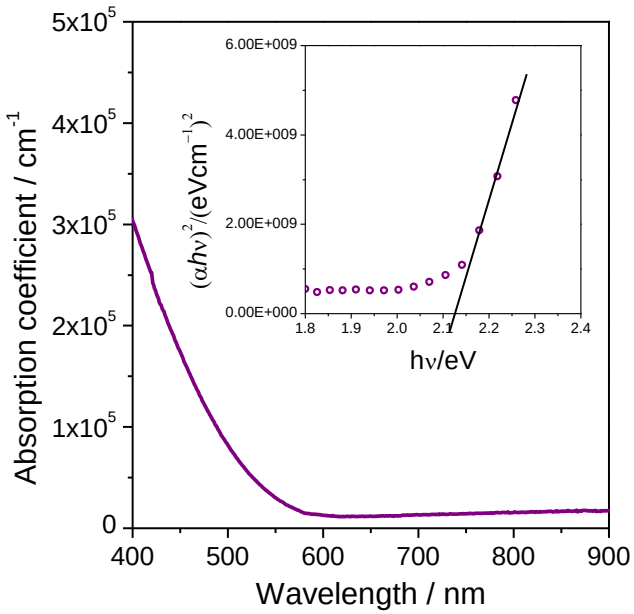


**Fig. 29: Absorption coefficient and band gap of $Sb_2S_3$.**

Fig. 29 exhibits optical absorption measurements of a 60 nm thick $Sb_2S_3$ film formed at 195 °C exhibiting absorption coefficients larger than $1*10^5$ $cm^{-1}$ and an optical band gap of 2.1 eV. In literature, optical band gaps between 1.7 eV and 2.2 eV for nanoparticles[111,133,134] and bulk energy gaps between 2.2 eV and 3.8 eV[135] have been reported.

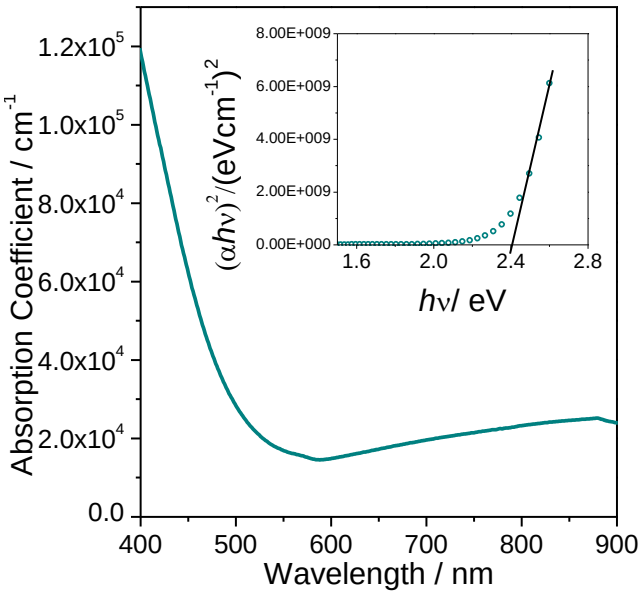


**Fig. 30: Absorption coefficient and band gap of $In_2S_3$.**

Fig. 30 shows optical absorption measurements of a 107 nm thick $In_2S_3$ film formed at 195 °C, which exhibits absorption coefficients larger than $1*10^5$ $cm^{-1}$ and an optical band gap of 2.4 eV. In literature, optical band gaps between 2-3 eV[136] have been reported. The onset of the absorption is at a wavelength of 588 nm, absorption at higher wavelength is contributed to scattering and interference effects.

The optical band gap of lead sulphide could not be determined, due to its high roughness; thus, no trustable layer thicknesses could be measured, which is a requirement for the calculation of the absorption coefficient.

To summarize the results, novel highly soluble metal xanthates are presented. The decomposition in the corresponding metal sulphides was investigated, and was found to be completed at <210 °C. Furthermore the crystal phases of the metal sulphides were determined. Due to the fact, that no defined phases could be revealed in XRD measurements for nickel-and cobalt-sulphides only the use of Bi-, Pb-, Sb- and In-xanthates are investigated for the fabrication of nanocomposite solar cells in the following chapter.

## 1.3 Nanocomposite layers & solar cells

### 1.3.1 General solar cell preparation

For bulk heterojunction devices, ITO coated glass substrates were cleaned with deionized water and isopropanol. PEDOT:PSS was used as a hole transport layer and was applied on ITO substrates priviously treated with oxygen plasma. The PEDOT:PSS substrates were dried on a heating plate at 150 °C for 10 minutes under inert conditions. For the fabrication of the active layer a blend of the respective polymer and xanthate with different donor to acceptor ratios was dissolved in chlorobenzene. The solutions were applied onto the PEDOT:PSS layer using different adjustments of doctor blading to modify the thickness of the active layer. The thermal conversion was performed on a programmable heating plate in a glove box system or in a tube furnace under vacuum or $N_2$-flow. Therefore, the device was heated to 195 °C using a heating rate of 11 °C/min and holding the temperature for 15 minutes. Finally 2 nm silver followed by aluminium electrodes were evaporated onto the active layer to complete the solar cell device.For the inverse device structure, TiOx was used instead of PEDOT:PSS and the device was finished by the evaporation of Au instead of AgAl. In the case of inverse bilayer devices, a blend of xanthate in chlorobenzene was applied on the TiOx layer, followed by the thermal conversion step described above. Thereafter, a polymer in chlorobenzene solution was applied on the metal sulphide layer and was dried on a heating plate at 100 °C for 15 min.

### 1.3.2 $Bi_2S_3$ solar cells

*Parts of this chapter are under submission in: V. Kaltenhauser, T. Rath, W. Haas, A. Trovisco Gomez, S. K. Müller, B. Friedel, B. Kunert, R. Saf, F. Hofer, G. Trimmel "Bismuth sulphide/polymer nanocomposites from a highly soluble bismuth xanthate precursor".*

$Bi_2S_3$ nanocrystalls are suitable as acceptor material in nanocomposite solar cells, due to the low band gap between 1.3 eV-1.7 eV[137], that matches well with the solar light spectrum. Furthermore it exhibits a high optical absorption coefficient in the order of $10^5$ $cm^{-1}$ [138] and it consists only of nontoxic elements in contrast to other common acceptor materials in solar cells, such as CdS, CdSe and PbS, PbSe. There are already some publications about $Bi_2S_3$ as acceptor material in nanocomposite solar cells in the literature[110,139], but the efficiencies are still very low. This chapter investigates the *in situ* in a polymer matrix prepared $Bi_2S_3$ nanocrystals and their application in solar cells.

#### *1.3.2.1 Characterization of the nanocomposite layers*

For the optical characterisation of the hybrid nanocomposite formation we used poly(methyl methacrylate) (PMMA) (polymer to inorganic ratio of 1:5 (w:w)) as matrix material because of its transparency in the near UV and visible wavelength range.

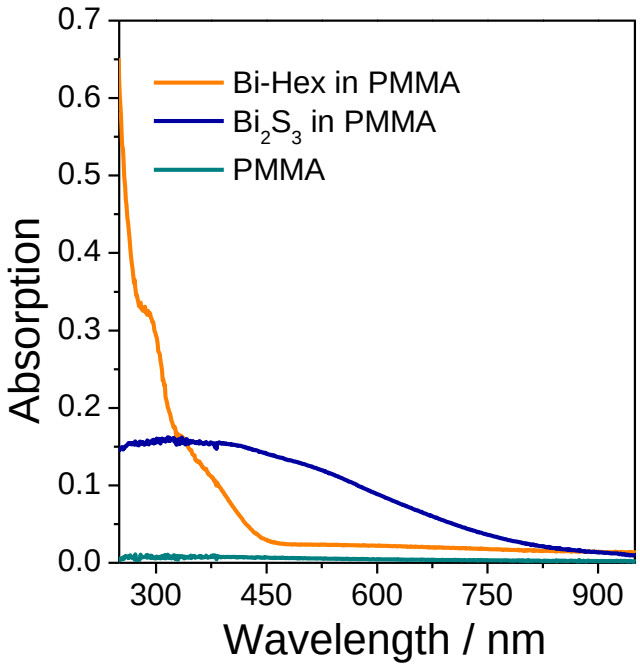


**Fig. 31: UV-Vis spectra of Bi-Hex before (Bi-Hex/PMMA) and after heating to 195 °C ($Bi_2S_3$/PMMA) in PMMA matrix.**

In Fig. 31 the UV-Vis spectra of Bi-Hex before (Bi-Hex/PMMA) and after heating to 195°C ($Bi_2S_3$/PMMA) in PMMA matrix are depicted, which clearly illustrates the differences in optical properties of the material before and after thermal conversion. In the Bi-Hex sample, an intensive absorption in the UV-range between 250 and 450 nm is observed. This distinct UV absorption vanishes after thermal treatment and a typical absorption profile of $Bi_2S_3$ nanoparticles with an absorption onset between 800 and 900 nm is visible in the spectrum. PMMA, which was used as a matrix polymer for the nanocomposite formation, does not exhibit significant absorption in this wavelength range. The absorption of $Bi_2S_3$ in PMMA is similar to the absorption of the pure $Bi_2S_3$ film (Fig. 28).

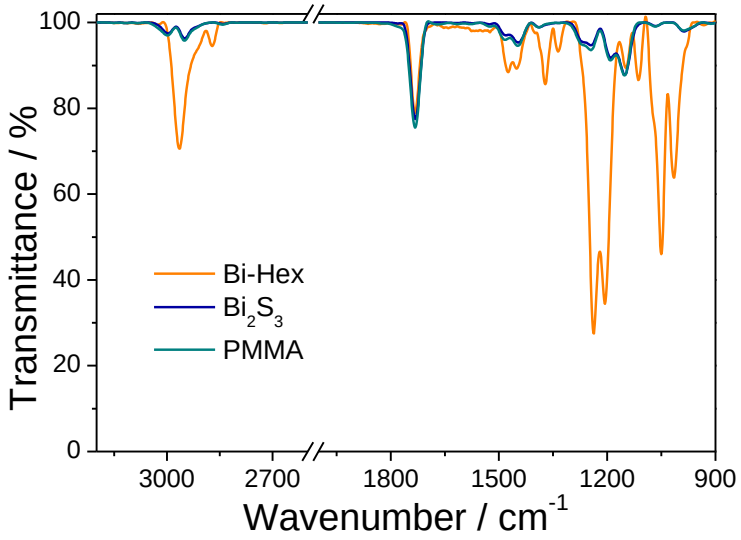


**Fig. 32: IR-spectra from a Bi-Hex sample embedded in PMMA before and after annealing at 195 °C.**

To confirm the decomposition of the metal xanthate in a matrix polymer, IR-spectra were recorded from a Bi-Hex sample embedded in a PMMA matrix before and after annealing at 195°C (Fig. 32). This is a temperature which is high enough for complete decomposition of the bismuth xanthate for 30 min according to thermogravimetric analysis. In the Bi-Hex/PMMA the typical vibrations of xanthates are detected. The most intense peaks at 1238 and 1203 $cm^{-1}$ can be attributed to the asymmetric C-O-C stretching vibrations, the bands at 1047 and 1017 $cm^{-1}$ to the C-S stretching vibrations.[118] After the annealing step, all vibrational bands of the Bi-Hex fully vanish and the spectrum of $Bi_2S_3$/PMMA resembles the pure PMMA spectrum with its most prominent peak at 1732 $cm^{-1}$ attributable to the carbonyl stretching vibration.

For the investigation of polymer/$Bi_2S_3$ nanocomposite layers suitable for solar cell fabrication, we investigated nanocomposite films with different polymer to inorganic ratios. For this

purpose we chose polymers, which are commonly used in solar cell architectures as P3HT, PSiF-DBT and PTB7 (chemical structures are shown in Fig. 33).

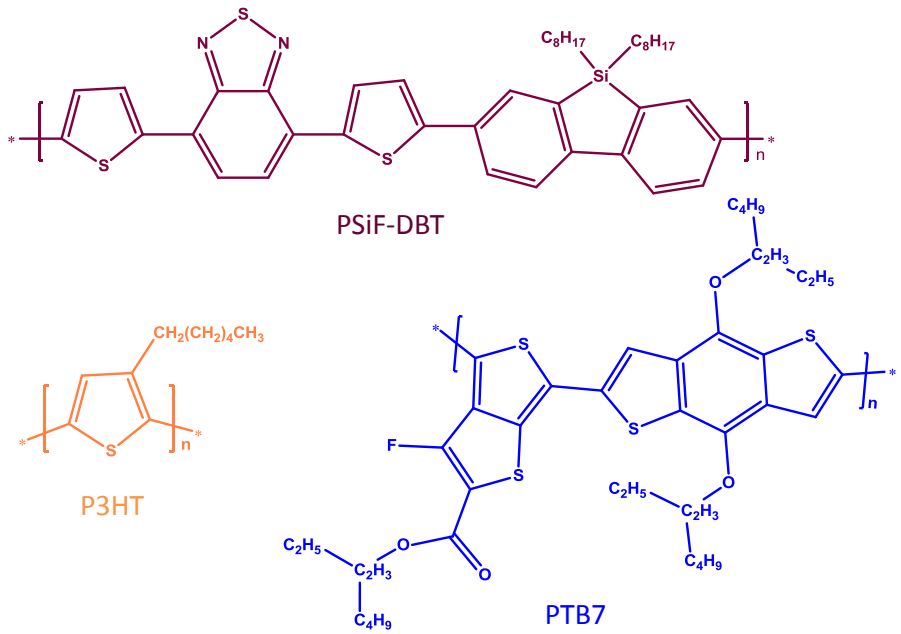


**Fig. 33: Chemical structures of the used polymers.**

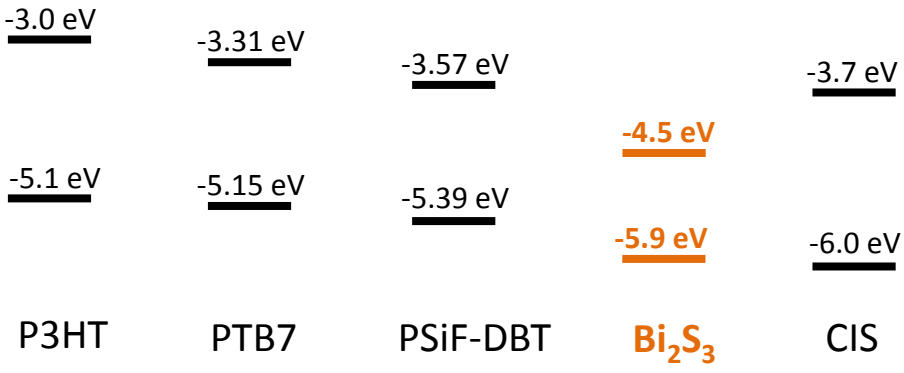


**Fig. 34: Band alignment of $Bi_2S_3$ in comparison to our commonly used CIS nanoparticles with different polymers. The energy positions of the semiconductor band edge are taken from literature (P3HT[140], PTB7[141], PSiF-DBT[142], $Bi_2S_3$[129], CIS[143]).**

From the energy alignment (Fig. 34) it can be seen, that all considered polymers should be suitable as hole conduction layers in combination with $Bi_2S_3$. Thus, efficient heterojunction between $Bi_2S_3$ and polymers should be formed, allowing exciton dissociation due to the sufficiently large offset between HOMO and LUMO levels of the polymer and the $Bi_2S_3$ phase.

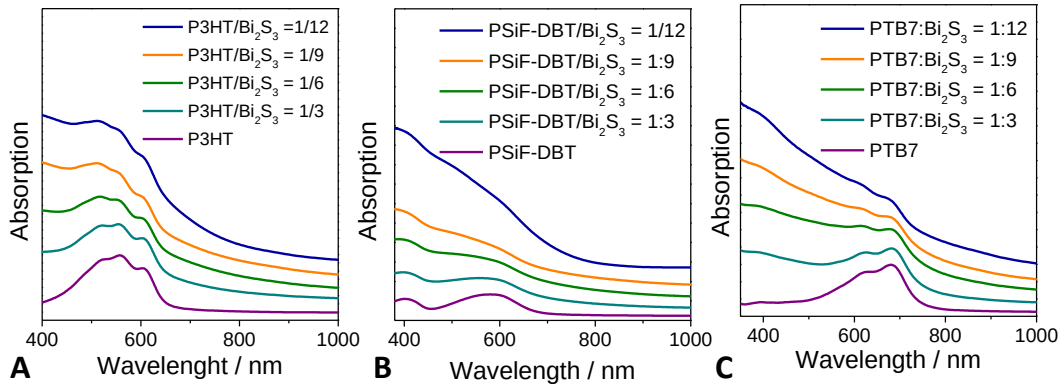


**Fig. 35: Absorption spectra of polymer/$Bi_2S_3$ nanocomposite layer with varying polymer to inorganic ratios (the spectra are shifted vertically for better visibility).**

UV-Vis analyses of nanocomposite layers with different polymer to inorganic ratios (their spectra are shifted vertically for better visibility; Fig. 35) show a polymer maximum at a wavelength of 556 nm for P3HT (580 nm for PSiF-DBT and 679 nm for PTB7). The absorption spectra of the measured polymers correlate very well with the absorption spectra of these polymers given in literature.[15,144,145] In all nanocomposite layers a light blue shift of the maximum can be observed with increasing inorganic content. This is caused by the proportional decrease of the polymer content within the active layer. The onset of the absorption of the $Bi_2S_3$ nanoparticles is between 800 and 900 nm, as it was before exhibited for $Bi_2S_3$ in a PMMA matrix.

To investigate the optical properties of the prepared P3HT/$Bi_2S_3$ nanocomposites in more detail, we performed photoluminescence (PL) quenching measurements on P3HT/$Bi_2S_3$ nanocomposites with different contents of the inorganic component. The photoluminescence is found to be strongly quenched in composites, where charge separation can occur, because the singlet exciton is no longer able to decay radioactively to the ground state.[26]

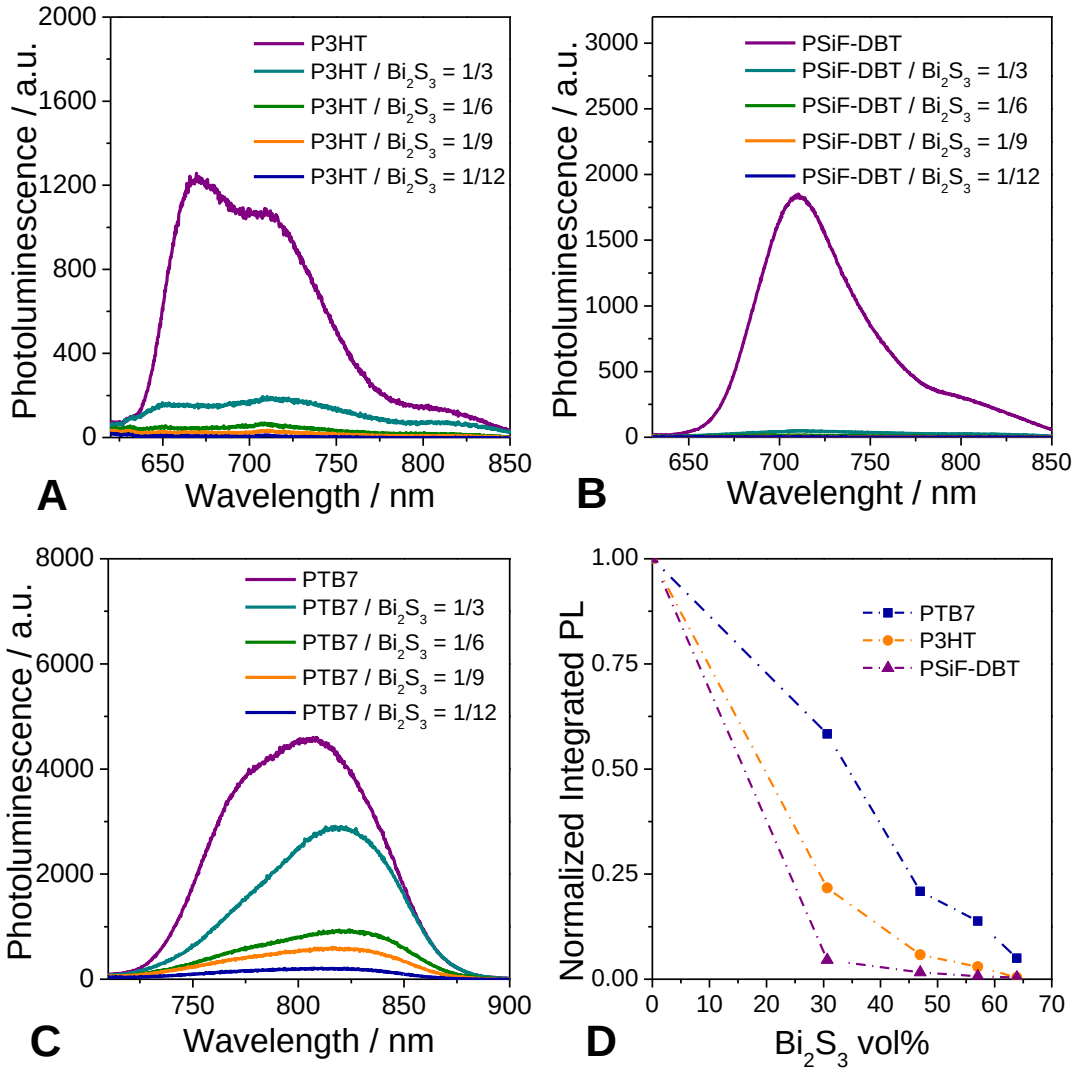


**Fig. 36: Photoluminescence quenching measurements of polymer/$Bi_2S_3$ films. Excitation occurred at the wavelength of the absorption maximum of the pristine polymer (560 nm for P3HT; 580 nm for PSiF-DBT; 680 nm for PTB7).**

The photoluminescence is found to be strongly quenched when $Bi_2S_3$ is present in the composites. The detailed results of the PL-quenching study of the polymer/$Bi_2S_3$ nanocomposites are summarized in Fig. 36, which shows the PL spectra of P3HT, PSiF-DBT and PTB7 / $Bi_2S_3$ nanocomposite active layers with different polymer:$Bi_2S_3$ weight ratios in comparison to pure polymers. To obtain reliable results, we increased the thickness of the layers with increasing $Bi_2S_3$ content to ensure that the polymer content was equal in each sample. Optical excitation of a pristine polymer film at 560 nm for P3HT (absorption maxiumum; 580 nm for PSiF-DBT and 680 nm for PTB7) resulted in the appearance of an emission band at 670 nm for P3HT (710 nm for PSiF-DBT and 810 nm for PTB7). This emission is quenched with increasing amount of the $Bi_2S_3$ nanocrystals in all polymer films, a comparison of the quenching behaviour of the three different polymer/$Bi_2S_3$ compounds is shown in Fig.

36 D. In the case of P3HT, which has mostly been applied as a polymer in nanocrystal-polymer solar cells so far, the PL emission was quenched to only 22% of the initial emission intensity at a P3HT:$Bi_2S_3$ weight ratio of 1:3 and is further reduced to 6% (P3HT:$Bi_2S_3$ = 1:6) and 3% (P3HT:$Bi_2S_3$ = 1:9) of the original level. PSiF-DBT is quenched even more efficiently than P3HT (2% for PSiF-DBT:$Bi_2S_3$ = 1:3), which leads to the assumption that nanocrystal-polymer hybrid solar cells with PSiF-DBT instead of P3HT could result in higher power conversion efficiencies. In contrast to this, PTB7 (Fig. 36 C) was quenched poorly with $Bi_2S_3$, resulting in a PL emission of 58% of the initial emission intensity at a PTB7:$Bi_2S_3$ weight ratio of 1:3, which could only be reduced to 5% at a PTB7 to $Bi_2S_3$ weight ratio of 1:12. Due to these results, P3HT and PSiF-DBT were investigated as donor material in $Bi_2S_3$ nanocomposite solar cells.

The morphology of the prepared $Bi_2S_3$/polymer nanocomposite layers was characterised by transmission electron microscopy (TEM). Therefore, P3HT was chosen as matrix polymer, due to its promising photoluminescence results.

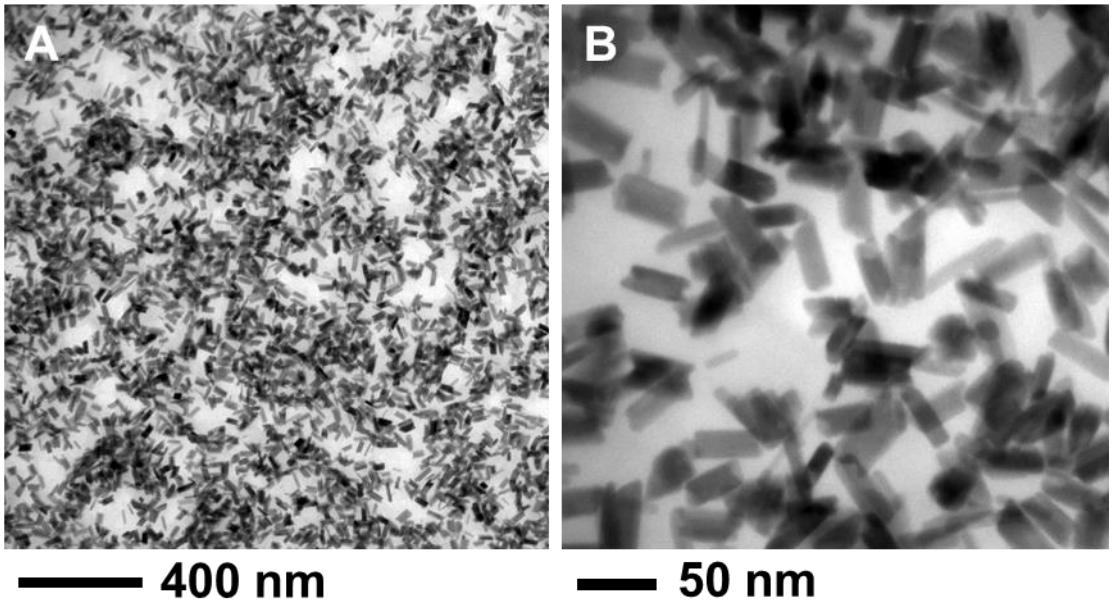


**Fig. 37: TEM images of $Bi_2S_3$ nanorods in a P3HT matrix at different magnifications (TEM pictures were determined by W. Haas).**

TEM images of the same sample at different magnifications are shown in Fig. 37, which depictes that nanorods are formed in the conjugated polymer matrix. The $Bi_2S_3$ nanorods reveal regular shapes with a diameter of 7-22 nm and a length of 40-70 nm.

The formation of nanorods in the matrix of a conjugated polymer via a ligand free *in situ* process in the solid state is a highly interesting result, as it was not possible before to realize nanorod structures via ligand free *in situ* processes.[9,15] In particular, nanorods are very

desirable for the application of the nanocomposites as absorber layers in hybrid solar cells, because they inherently facilitate charge transport through the layer, while retaining a high polymer/nanoparticle interfacial area. As early as 2002, Alivisatos et al.[64] reported an improvement in power conversion efficiency of P3HT/CdSe hybrid solar cells by using nanorods instead of spherical nanoparticles in the absorber layers and current record power conversion efficiencies of hybrid solar cells of 4.7% are also reached using CdSe nanorods in combination with the low band gap polymer PCPDTBT.[30]

The reason for the formation of $Bi_2S_3$ nanorods in this solid state reaction is most presumably the predominant growth of the orthorhombic $Bi_2S_3$ nanocrystals along the [001] direction.[137,146] Therefore, the elongated $Bi_2S_3$-nanostructure is quite common and there exist several publications reporting on $Bi_2S_3$ nanorods or nanowires produced by different synthetic approaches.[110,138,147-149] The aspect ratio of $Bi_2S_3$ nanorods presented in literature is different compared to $Bi_2S_3$ nanorods obtained by the xanthate route. Mostly, the nanorods exhibited a length of 100 nm and diameters around 10-30 nm[110,147,148] , but 10 nm by 18 nm are also reported[138], which indicates that the structure of nanomaterials strongly depends of the synthesis route and conditions.

The fact that nanorods are formed may provide the opportunity to increase the film thickness of absorber layers in hybrid solar cells. Thicknesses in hybrid solar cells are often only between 50 and 100 nm and seems to be limited by charge transport. This limitation can be overcome by elongated structures of the nanoparticle phase, enabling the usage of thicker absorber layers and thereby also the absorption of a higher amount of photons.

#### *1.3.2.2 Solar cell fabrication*

In our first series we studied P3HT/$Bi_2S_3$ bulk heterojunction solar cells with different polymer/inorganic ratios (1:5, 1:9). Although Bi-Hep starts to decompose at 140 °C according thermal gravimetric measurements, we chose 195 °C as conversion temperature, in order to ensure a total conversion of the precursor material and to encourage the evaporation of the side products. Furthermore, 195 °C was found to be the actual optimal conversion temperature for our CIS nanoparticles, which seems to be a quite good starting point for our research activity. The formation was carried out at a temperature of 200 °C (22 min, 24 °C/min) under vacuum and furthermore under a nitrogen flow in a tube furnace, because the active layer was turbid and we wanted to investigate, if this turbidity was caused by the vacuum process. As we found out this was not the case. All solar cells failed; zero $V_{OC}$ and no diode behaviour were obtained, which lead to the assumption that a physical short circuit

occurred. In order to exclude this failure, inverse bilayer devices at different conversion temperatures (130 °C, 6.7 °C/min; 150 °C, 8 °C/min; 195 °C, 11°C/min) were fabricated in a second series, using Bi-Hex instead of Bi-Hep, leading to smooth clear layers. 130 °C and 150 °C were chosen, although they are beneath the decomposition temperature revealed with thermogravimetric analysis measurements. The most surprisingly result was that the only device showing a photovoltaic effect was obtained at 130 °C ($V_{OC}$ = 0.46 V, $I_{SC}$ = 0.2 mA/cm$^2$, FF = 26%, Eff = 0.026%; Fig. 38) while all other devices showed the same behaviour as in the first series (no $V_{OC}$, no diode behaviour).

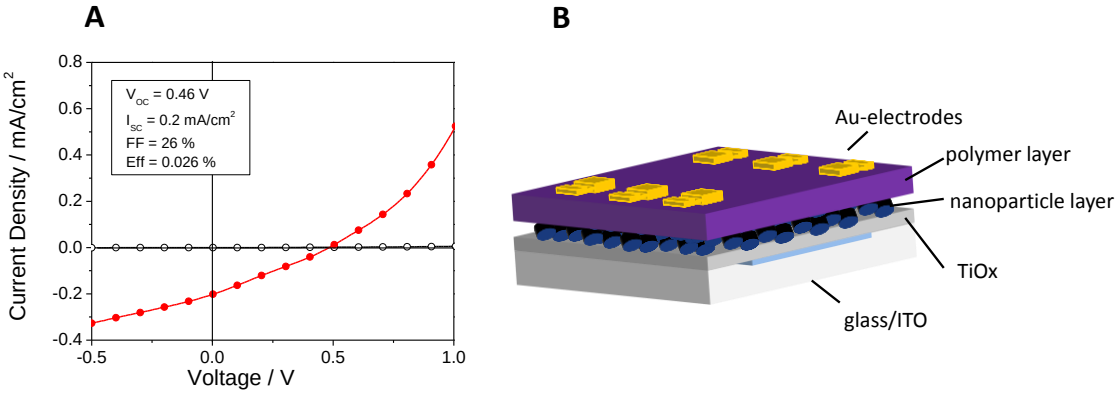


**Fig. 38: A: IV characteristic of an inverse bilayer device fabricated at 130 °C (filled symbols denote measurements under AM1.5 illumination, empty symbols without illumination) B: inverse device architecture.**

To find out, if $Bi_2S_3$ is even generated at this temperature, XRD, TEM and an isotherm thermogravimetric analysis were performed. Fig. 39 compares the TEM pictures of the $Bi_2S_3$ nanorods after conversion at 130 °C and 195 °C.

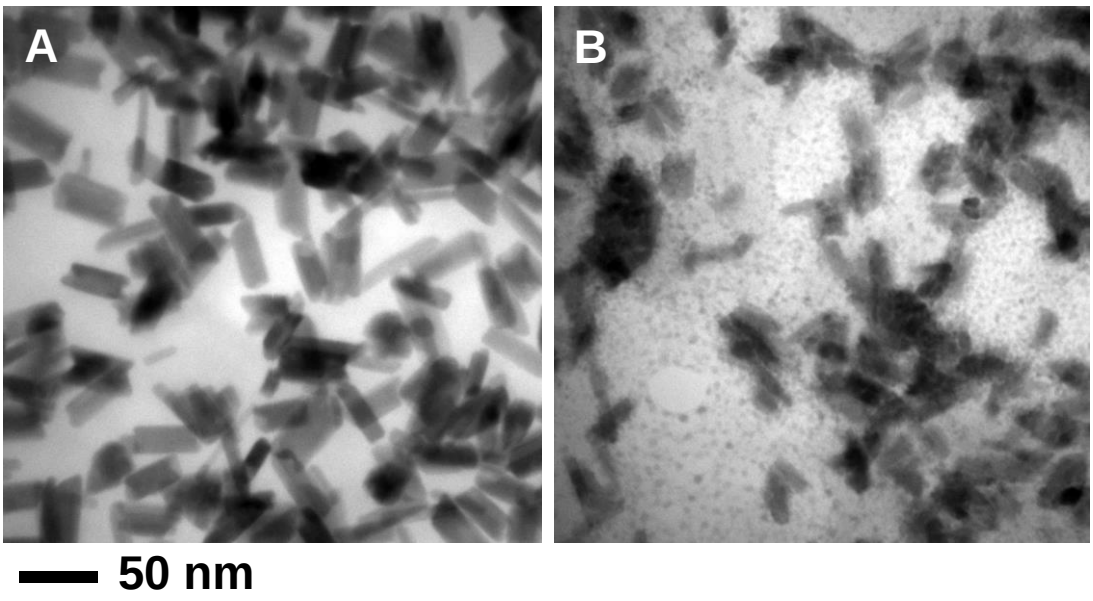


**Fig. 39: TEM pictures of $Bi_2S_3$ nanorods converted at 195 °C (A) and 130 °C (B). (TEM pictures were taken from W. Haas)**

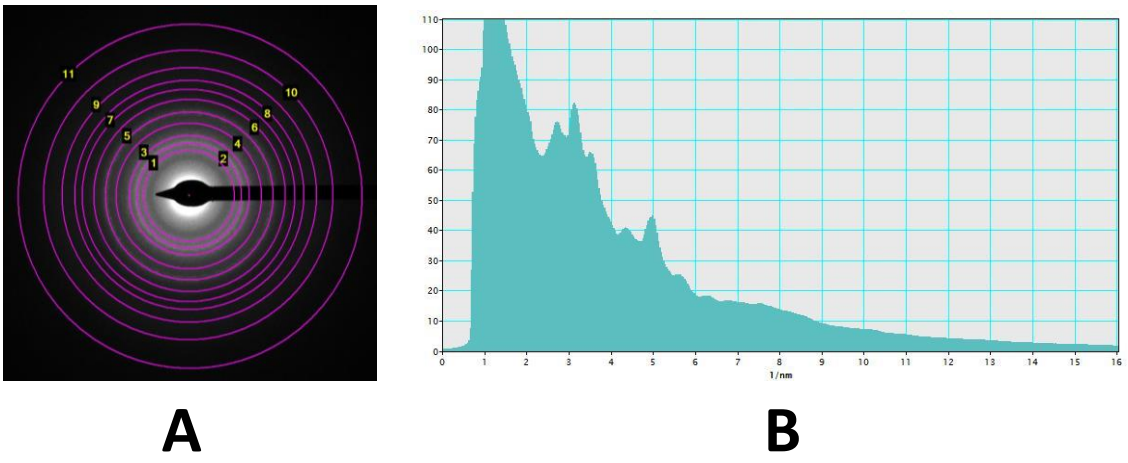


**Fig. 40: (A) Selected area electron diffraction of the P3HT/$Bi_2S_3$ nanocomposite layer with a weight ratio of 1:5 prepared at 130 °C and (B) radial intensity profile (SAED images were taken by W. Haas).**

**Table 7: Radii of the diffraction rings gained from SAED.**

| Ring | Radius 1/nm | 1/Radius |
|---|---|---|
| 1 | 2.711 | 0.369 |
| 2 | 3.103 | 0.322 |
| 3 | 3.555 | 0.281 |
| 4 | 4.325 | 0.231 |
| 5 | 4.970 | 0.201 |
| 6 | 5.684 | 0.176 |
| 7 | 6.299 | 0.159 |
| 8 | 6.793 | 0.147 |
| 9 | 7.533 | 0.133 |
| 10 | 8.568 | 0.117 |
| 11 | 10.192 | 0.098 |

The $Bi_2S_3$ nanorods converted at 130 °C are smaller (5-7 nm diameter, 20-40 nm length) and less uniform than $Bi_2S_3$ nanorods converted at 195 °C (7-22 nm diameter, 40-70 nm length). Furthermore, plenty of smaller point shaped particles appear in the 130 °C sample, which have a size of 2-4 nm. With TEM it is not possible to classify if there is some unconverted xanthate precursor left in the 130 °C sample, as the high energetic ion beam used in TEM measurements would lead to xanthate decomposition. Furthermore, an electron diffraction (SAED) image from a representative area of the nanocomposite is shown in Fig. 40, which depicts the typical diffraction rings of nanocrystals. The maxima of the SAED radial intensity profile are in good accordance with the orthorhombic $Bi_2S_3$ structure (ICSD-84279).

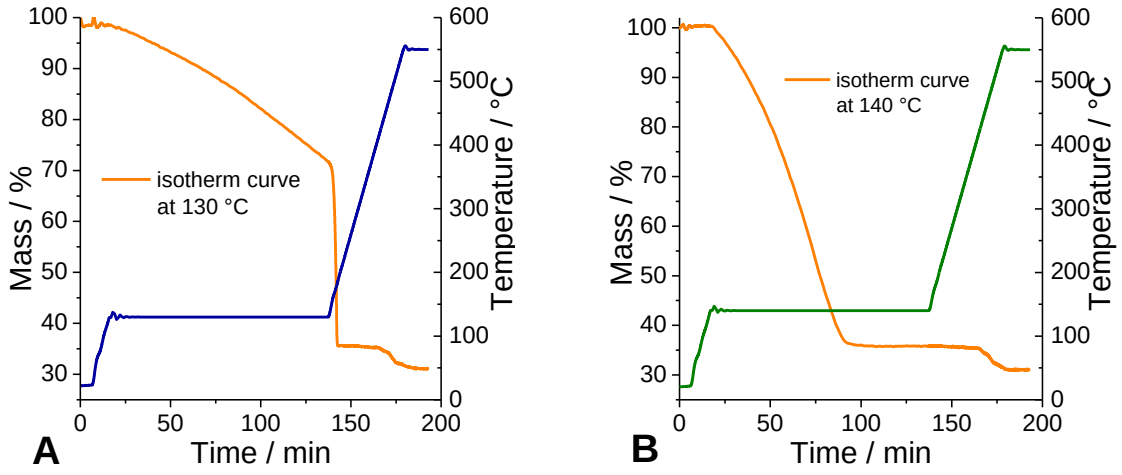


**Fig. 41: Isotherm gravimetric analysis, A: decomposition of Bi-Hex at 130 °C, B: decomposition of Bi-Hex at 140 °C.**

Fig. 41 presents the isothermal gravimetric analysis of Bi-Hex. In order to achieve comparable results to the Bi-Hex decomposition in the nanocomposite solar cells, a temperature method adopted from the solar cell fabrication was used: heating in 15 min to 130 °C and 140 °C respectively and holding this temperature for 2 h. Fig. 41 A exhibits, that the decomposition was not completed within this time at 130 °C, but Fig. 41 B shows, that at 140 °C the conversion was finished after 90 min. Nevertheless, this implies that the Bi-Hex has not been fully converted in our solar cells fabricated at 130 °C in 15 min.

Finally, a XRD measurement of a Bi-Hex sample after decomposition at 130°C was performed, in order to ensure if $Bi_2S_3$ has already been formed in the composite(Fig. 42).

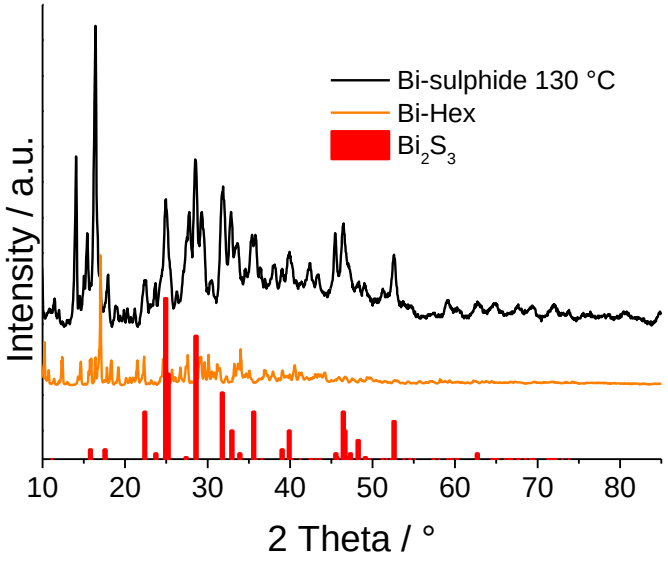


**Fig. 42: XRD-pattern of bismuth-sulphide prepared at 130 °C.**

The main peaks of $Bi_2S_3$ (PDF: 17-320) are observed in the XRD-pattern of the bismuth-sulphide prepared at 130 °C (24.9° (1 3 0), 28.5° (2 1 1), 31.8° (2 2 1), 46.5° (5 0 1) and 52.6° (3 1 2)). Thus, $Bi_2S_3$ has already been formed at 130 °C, but other phases also appear in the XRD pattern. There is some leftover xanthate at a reflection of e.g. 16.4° and 18.8°. Furthermore, another unknown phase with reflection at e.g. 14.1° emerged, which is not assignable. In contrast to our solar cells with a maximum thickness 200 nm, the layer of Bi-Hex for XRD measurements is a few µm thick, so the XRD results cannot reflect perfectly the conditions in the solar cell. In conclusion it can be stated that some $Bi_2S_3$ has already been built at 130 °C, but the phase is not pure, so solar cells fabricated at 130 °C will probably never exhibit high efficiencies due to the impurities of the acceptor phase. Thus, further attempts were made, to achieve solar cells showing a photovoltaic effect at a conversion temperature of 195 °C.

In a third series the nanocomposite solar cell approach of the first series (195 °C) was extended, with the introduction of two additional interlayers (a polymer interlayer and TiOx), to prevent the shortening of the device. Furthermore, a programmable heating plate in the glove box system was used for the xanthate decomposition instead of a tube furnace. Different polymer/inorganic ratios (1:0, 1:3, 1:6, 1:12) were investigated and PSiF-DBT was used as donor polymer, because of the promising photoluminescence quenching results. The solar cell architecture was ITO/PEDOT:PSS/PSiF-DBT/PSiF-DBT:$Bi_2S_3$/$TiO_x$/Al; the IV characteristic is shown in Fig. 43.

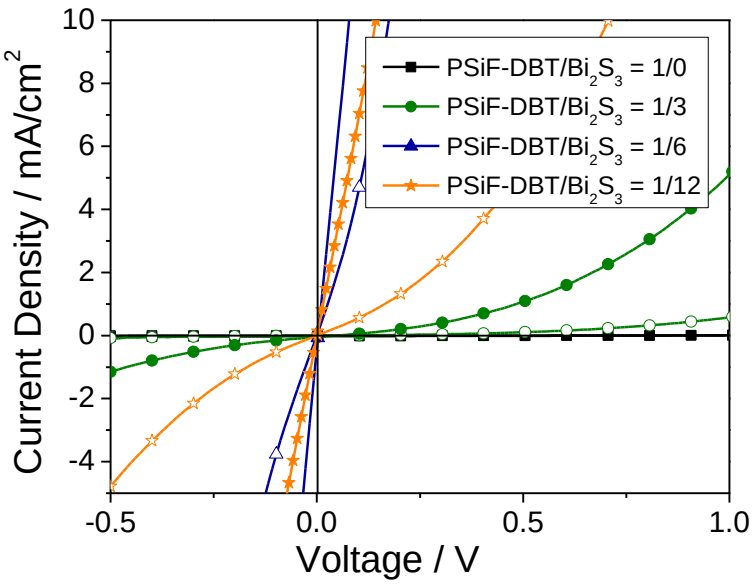


**Fig. 43: IV characteristic of PSiF-DBT/$Bi_2S_3$ nanocomposite solar cells with different organic to inorganic ratios (filled symbols denote measurements under AM1.5 illumination, empty symbols without illumination).**

The device with a diode characteristic was the PSiF-DBT/TiOx bilayer solar cell without any $Bi_2S_3$ nanocomposite inside. With increasing $Bi_2S_3$ content the $V_{OC}$ decreases while the $I_{SC}$ increases which leads to a loss in diode behaviour of the IV characteristic. To investigate if the short circuit occurs due to high surface roughness, AFM pictures of solar cells were accomplished as shown in Fig. 44.

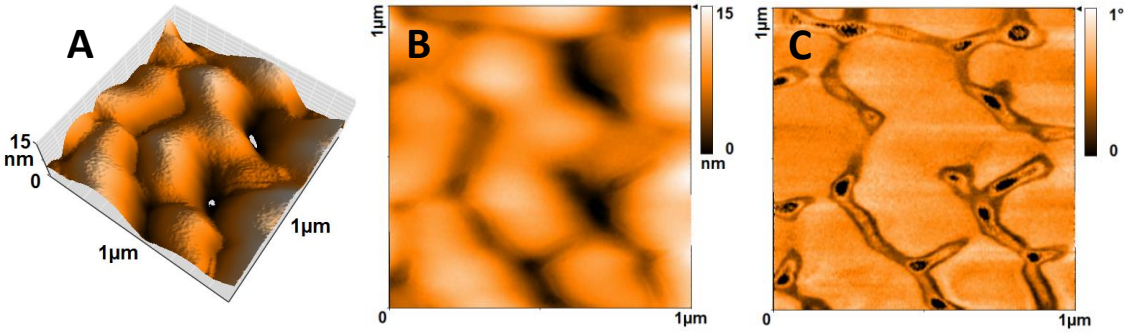


**Fig. 44: AFM-pictures of solar cells with a polymer : inorganic ratio of 1:5 (A, B: topography; C: phase contrast; AFM pictures were determined from B. Friedel).**

The images of the nanocomposites reveal that the polymer forms a few 100 nm large domains, which can be clearly seen in the topographic as well as in the phase contrast image. Nevertheless, we could not find any explanation for the shortening in the AFM images, because the layers were very smooth.

Fig. 45 shows the IV characteristic of PSiF-DBT:$Bi_2S_3$ (polymer : inorganic ratio = 1:5) nanocomposite solar cells without any different interlayers. The IV characteristic was first measured directly after fabrication, and furthermore after 24 h and 48 h storage under ambient conditions. It was found, that the aging process under ambient conditions leads to an increase in $V_{OC}$ (characteristic parameters are shown in Table 8), but under inert condition no change in solar cell performance could be observed. Furthermore the influence of light storage was investigated (under ambient and under inert conditions), but no significant changes could be found.

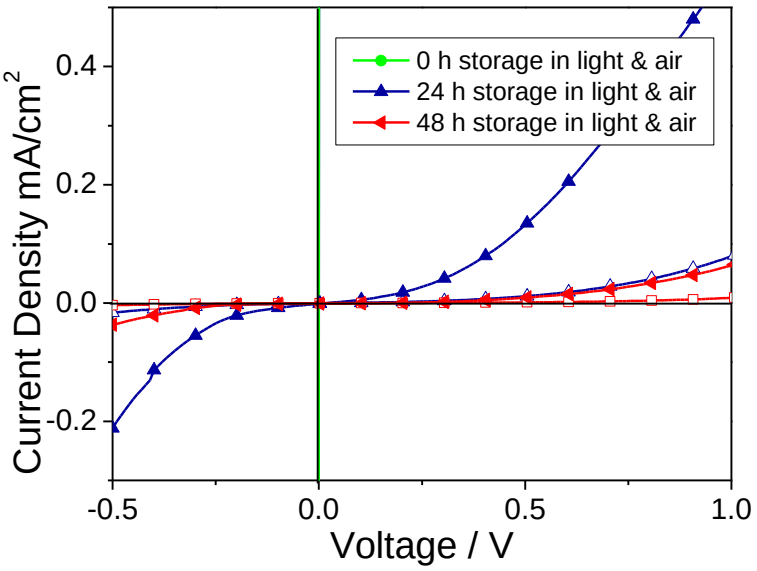


**Fig. 45: IV characteristics of a bulk-heterojunction PSiF-DBT:$Bi_2S_3$ solar cell, directly after fabrication in the glove box, after 24 h exposed to air and light, and after 48 h air and light exposition (filled symbols denote measurements under AM1.5 illumination, empty symbols without illumination).**

**Table 8: Characteristic parameters of a bulk heterojunction PSiF-DBT:$Bi_2S_3$ solar cell, directly after fabrication in the glove box, after 24 h exposed to air and light, and after 48 h air and light exposition.**

| | $V_{OC}$ / V | $I_{SC}$ / mA/cm² | FF / % | Eff / % |
|---|---|---|---|---|
| **0 h light & air** | 0.003 | 4.61 | 100 | 0 |
| **24 h light & air** | 0.023 | 1.3E-3 | 27 | 8E-6 |
| **48 h light & air** | 0.173 | 1.27E-3 | 32 | 7E-5 |

Based on these results, an active layer without metal electrodes was stored under ambient conditions for one week. Thereafter, the solar cell fabrication was finished by evaporation of AgAl electrodes, but no diode behaviour could be determined. This leads to the assumption that the aging of the electrodes leads to diode behaviour, which may be caused by the formation of an isolating metal oxide interlayer, due to electrode degradation.

All experiments were also carried out with P3HT as donor polymer, leading to similar results.

### 1.3.3 Polymer/PbS solar cells

PbS nanocrystals are very interesting for solar cell fabrication, due to their absorption properties which lead to better light harvesting in the near- and mid-infrared.[112,150] It is a IV-VI semiconductor, which can be n- or p-type depending on stoichiometry,[151] with a bulk energy gap of 0.41 eV and large exciton Bohr radii (18 nm). Therefore, the band gap of the nanoparticles can be tuned over the entire NIR spectral range.[152] There are already some

publications about polymer/PbS solar cells in literature. Most of these devices show low power conversion efficiencies, due to inefficient carrier generation (energy alignment shown in Fig. 46).[112,153,154]

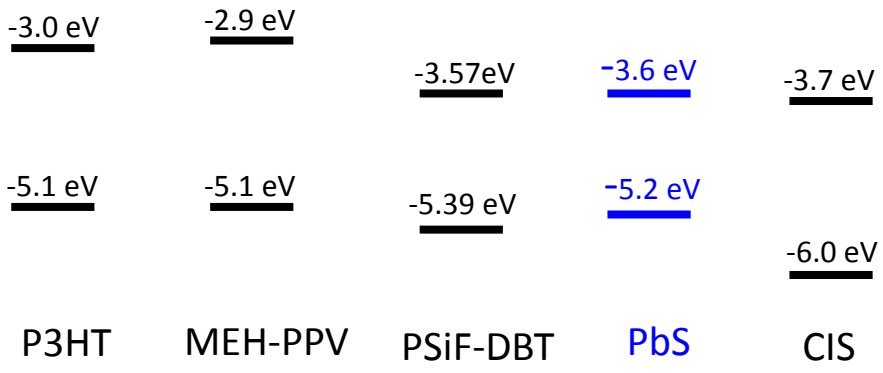


**Fig. 46: Energy band diagramm of common polymers and PbS nanoparticles in comparison with CIS. The energy positions of the semiconductor band edge are taken from literature (P3HT[140], MEH-PPV[155], PSiF-DBT[142], PbS[140], CIS[143]). The energy values for PbS are for particles with a diameter of 2.7 nm.**

By means of energy alignment (Fig. 46) it is observed, that there is only a small energy difference between the valence band of PbS and the highest occupied molecular orbitals (HOMO) of the polymers. In P3HT/PbS systems an additional electron acceptor (e.g. $TiO_2$) can lead to exciton dissociation improvement.[140] P. N. Prasad et al.[112] reported in 2011 a polymer/PbS solar cell, that exhibits a power conversion efficiency of 3.7% by introducing a new low-band gap polymer PDTPBT (poly(2,6-( N -(1-octylnonyl)dithieno[3,2-b :20,30- d ]pyrrole)- alt -4,7-(2,1,3-benzothiadiazole))) with a HOMO level of 4.61 eV.

In this chapter PbS nanoparticles prepared *in situ* in a polymer matrix and their application in solar cells were investigated.

### *1.3.3.1 Characterization*

For the optical characterisation of the nanocomposite formation, PMMA was used again as a matrix polymer.

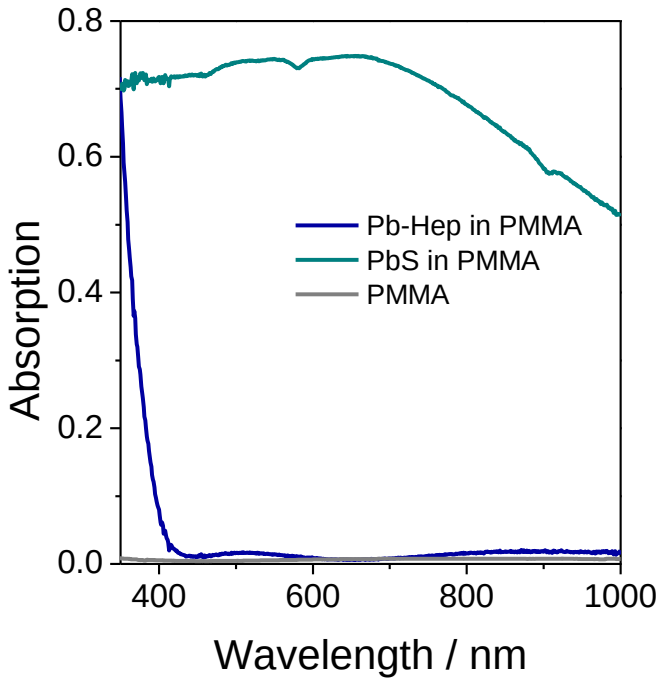


**Fig. 47: UV-vis spectra of Pb-Hep before (Pb-Hep/PMMA) and after heating to 195 °C (PbS/PMMA) in PMMA matrix.**

The UV-vis spectra of Pb-Hep before (Pb-Hep/PMMA) and after heating to 195 °C (PbS/PMMA) in a PMMA matrix (Fig. 47), illustrate the difference in optical properties of the material before and after thermal conversion. In the Pb-Hep sample, and intense absorption in the range of 300 and 430 nm is observed, which can be contributed to the xanthate and vanishes after thermal treatment. Now the absorption profile of PbS is visible in the spectrum, which exhibite a strong absorption in the hole measured wavelength range. The absorption onset is not visible in the spectrum. The absorption at wavelength higher than 1000 nm may occure due to the bulk properties (bulk energy gap is 0.41 eV[152]) of the large nanoparticles (according to XRD measurements around 50 nm).

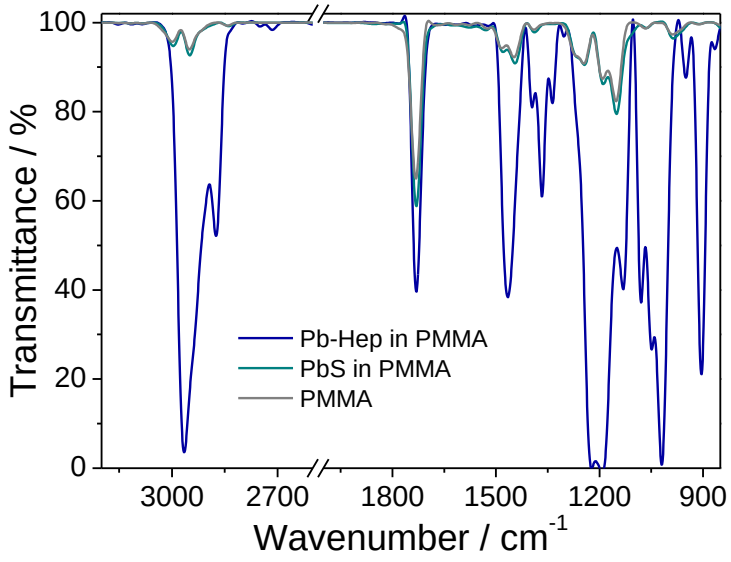


**Fig. 48: IR-spectra from Pb-Hep sample embedded in PMMA before and after annealing at 195 °C.**

The conversion of the Pb-xanthate in a matrix polymer was confirmed by IR-measurements (Fig. 48) from Pb-Hep embedded in a PMMA matrix before and after annealing to 195 °C which is the same temperature where XRD measurements revealed complete conversion. The most intense peaks at 1224 and 1190 $cm^{-1}$ can be attributed to the asymmetric C-O-C stretching vibrations, the bands at 1050 and 1019 $cm^{-1}$ to the C-S stretching vibrations.[118] After the annealing step, all vibrational bands of the Pb-Hep fully vanish and the spectrum of PbS/PMMA resembles the pure PMMA spectrum with its most prominent peak at 1732 $cm^{-1}$ attributable to the carbonyl stretching vibration.

For the investigation of PbS/polymer nanocomposite layers as suitable active layers in solar cells, common conjugated donor polymers as P3HT and PSiF-DBT were used instead of PMMA.

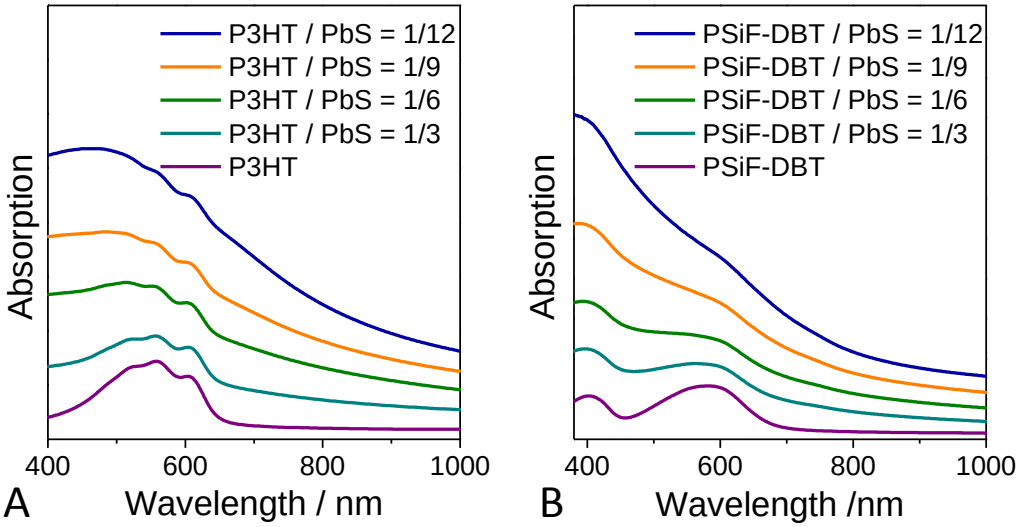


**Fig. 49: Absorption spectra of polymer/PbS nanocomposite layers with varying polymer to inorganic ratios (the spectra are shifted vertically for better visibility).**

UV-Vis analysis of nanocomposite layers with different polymer (P3HT and PSiF-DBT) to inorganic ratios (the spectra are shifted vertically for better visibility) (Fig. 49) show a polymer maximum at a wavelength of 556 nm for P3HT and at 580 nm for PSiF-DBT. In all nanocomposite layers a light blue shift of the maximum can be observed with increasing inorganic content, similar to $Bi_2S_3$/polymer nanocomposites. This is caused by the proportional decrease of the polymer content within the active layer. Interestingly, the UV-vis spectra of PbS embedded in a conjugated polymer matrix is different to the absorption spectrum of PbS embedded in the PMMA matrix (Fig. 47). This phenomenon may be caused by size differences of the nanoparticles formed in the respective polymers. In PMMA larger nanoparticles may have been formed, leading to a broad intense absorption in the wavelength range of 400-1000 nm. This broad absorption is also obtained for PbS, formed in the conjugated polymer matrix, but it reveals less intensity.

To investigate charge transfer in this nanoparticle/polymer active layers and their suitability as active layers, photoluminescence quenching measurements with P3HT and PSiF-DBT were performed. The photoluminescence is found to be strongly quenched when PbS is present in composites (Fig. 50).

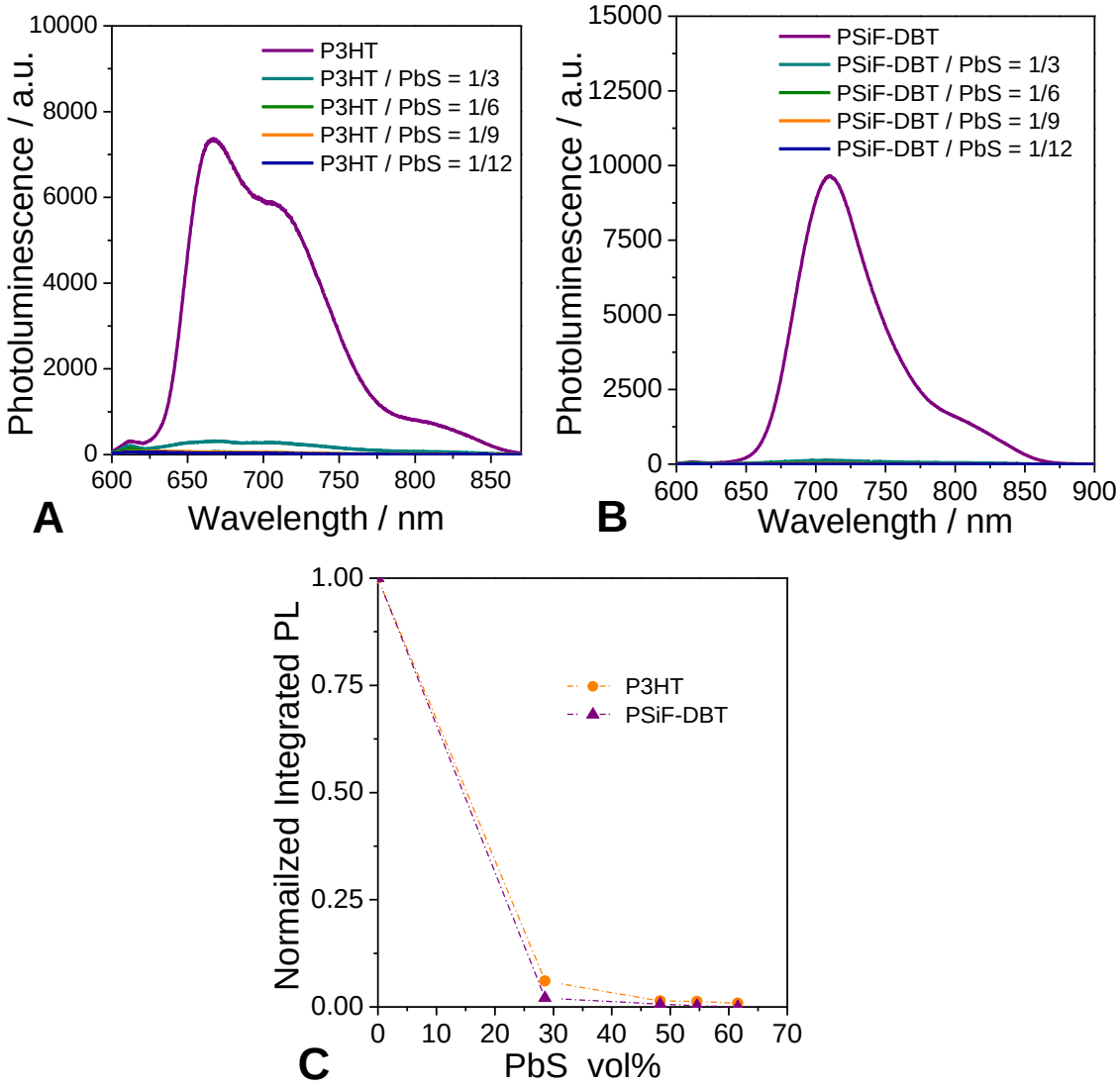


**Fig. 50: Photoluminescence quenching results of polymer/PbS nanocomposites. The emission of the pristine polymers is already nearly complete quenched after introduction of only 30 vol% PbS nanocrystals to the polymer films.**

The detailed results of the PL-quenching study show the PL spectra of pure polymer and polymer/PbS nanocomposite layers with different polymer : PbS weight ratios of 1:3, 1:6, 1:9 and 1:12. The optical excitation of the films was performed following the procedure described for the polymer/$Bi_2S_3$ quenching experiments. Optical excitation of the pristine P3HT film at 560 nm resulted in the appearance of an emission band at 667 nm (for PSiF-DBT optical excitation at 580 nm, emission band at 710 nm). The emission of the pristine polymers is already quenched nearly completely after introduction of only 30 vol% PbS nanocrystals to the polymer films. As discovered before for $Bi_2S_3$, PSiF-DBT is quenched even more efficiently than P3HT (2% for PSiF-DBT : PbS = 1:3 compared to 6% for P3HT:PbS = 1:3).

### *1.3.3.2 Solar cell fabrication*

To investigate the suitability of Pb-Hep as precursor material, commercial available polymers like MEH-PPV, P3HT and PSiF-DBT were applied as donor materials. To achieve high power conversion efficiencies, other not commercial available polymers with a higher value of valence band-edge have to be considered.

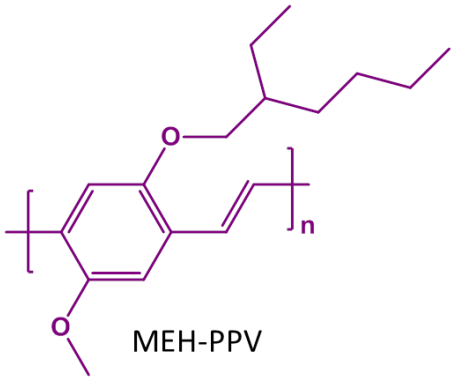


**Fig. 51: Structure of MEH-PPV, a common polymer for polymer/PbS solar cells.**

In a first attempt bulk-heterojunction solar cells with different polymer to inorganic ratios were fabricated, using the standard conversion temperature program (in 11 °C/min to 195 °C, holding this temperature for 15 min). Nevertheless, the active layers were turbid and exhibited a relatively high roughness compared to standard CIS device (PSiF-DBT : CIS Ra around 2 nm; MEH-PPV:PbS Ra around 10 nm). Furthermore they did not obtain any open circuit voltage, leading to the assumption that a physical short circuit occurred. To reduce the feasibility of a short circuit, inverse bilayer devices were fabricated. The device architecture was glass/ITO/TiOx/PbS/P3HT/Au; instead of P3HT also MEH-PPV was used. The thicknesses of the active layers were determined with surface profiler and are around 80 nm for the P3HT/PbS inverse bilayer devices and around 110 nm for MEH-PPV inverse bilayer devices. The thickness of the pure PbS could not be determined, due to its very high surface roughness. The P3HT/PbS inverse bilayer device exhibited a lower power conversion efficiency ($V_{OC}$ = 113 mV, $I_{SC}$ = 0.25 mA/cm$^2$, FF = 31%, Eff = 0.009%) than the device with MEH-PPV ($V_{OC}$ = 394 mV, $I_{SC}$ = 0.13 mA/cm$^2$, FF = 37%, Eff = 0.02%). Due to the limited exciton diffusion length, the thickness of the active layer influences the characteristic device parameters crucially. Thus, inverse bulk-heterojunction solar cells, with and without additional polymer interlayers were investigated. The device architecture was glass/ITO/TiOx/MEH-PPV:PbS/MEH-PPV/Au and glass/ITO/TiOx/MEH-PPV:PbS/Au respectively. The thicknesses of the active layers were determined with a surface profiler, and varied between 70 and 110 nm for the devices without additional interlayers. The additional polymer interlayers varied between 30-40 nm, except for

the device with a polymer to inorganic ratio of 1:12, where the thickness of the polymer interlayer was doubled (80 nm). The layer thickness has a great impact on the characteristic solar cell parameters. According to Lambert-Beer it is possible to absorb more light with increasing layer thickness. Furthermore, the series resistance increases with increasing layer thickness, leading to a decrease in the efficiency.

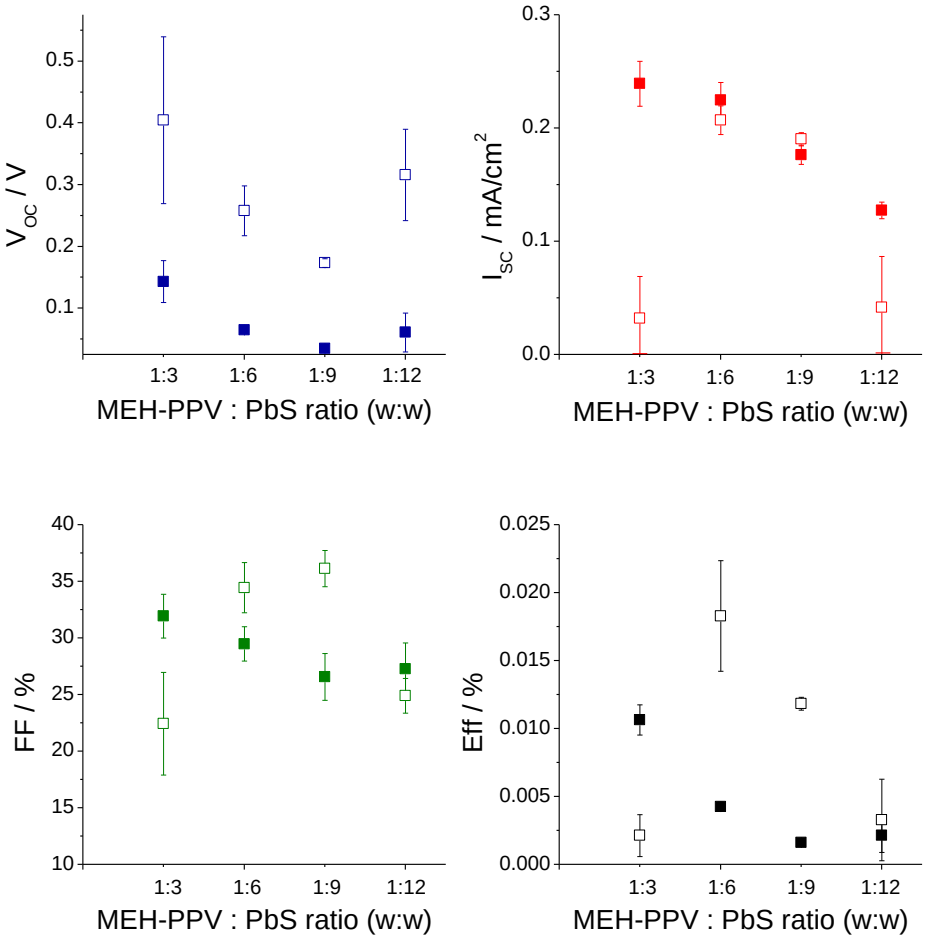


**Fig. 52: Influence of the MEH-PPV/PbS weight ratio and additional polymer interlayer on the parameters $I_{SC}$, $V_{OC}$, FF and efficiency of MEH-PPV/PbS hybrid solar cells annealed at 195 °C (filled symbols denote solar cells without additional interlayer, empty symbols denote solar cells with an additional polymer interlayer; mean values of 5 best devices).**

The influence of the polymer to inorganic ratio and of the additional interlayer is shown in Fig. 52. The $V_{OC}$ decreases with increasing PbS content until a polymer to inorganic ratio of 1:12, where a slight increase is obtained, which can be explained by the increase in layer thickness (around 70 nm for devices with a ratio of 1:3-1:9; around 110 nm for devices with a ratio of 1:12). The devices with an additional polymer interlayer exhibit higher $V_{OC}$ values than the

devices without additional interlayers, which can be explained by the increasing thickness of the active layer (with additional polymer interlayer increasing active layer thickness of + 40 nm). The device with a ratio of 1:12 and an additional polymer interlayer reveals a significantly higher $V_{OC}$ than the devices with ratios of 1:6 and 1:9. This can be explained by the obviously higher polymer interlayer thickness of 80 nm in contrast to 40 nm measured for the other devices. The $I_{SC}$ decreases with increasing PbS content. The device with a ratio of 1:3 with an additional polymer interlayer reveals nearly the same $I_{SC}$ than the device with a ratio of 1:12, which is very low. The fill factors of all devices reveal values of 20 to 35% only the devices with a ratio of 1:6 and 1:9 exhibit fill factors which are slightly higher. This leads to a clear maximum of power conversion efficiency at a weight ratio of 1:6 with an additional polymer interlayer.

In Fig. 53 the difference of the IV characteristics of an inverse bilayer device and an inverse bulk heterojunction device is shown; the characteristic device parameters are listed in Table 9. As expected, the inverse bilayer device exhibited a higher open circuit voltage but a lower short circuit current. Due to the fabrication of a bulk heterojunction, interpenetrating networks of donor and acceptor materials were built, and lead to a greater interface between donor and acceptor materials. This is important due to the limited diffusion length of excitons (10 nm) and the risk of exciton recombination before reaching the interface, where exciton dissociation occurs.

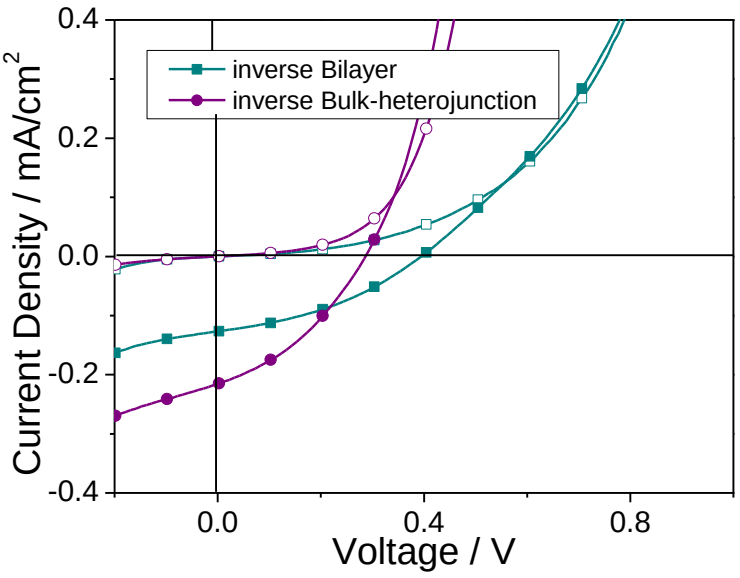


**Fig. 53: Comparison of the IV characteristics of inverse bilayer devices and inverse bulk heterojunction devices with additional polymer interlayer (filled symbols denote measurements under AM1.5 illumination, empty symbols without illumination).**

**Table 9: Characteristic parameters of inverse bilayer devices and inverse bulk-heterojunction devices with adittional polymer interlayer.**

| | $V_{OC}$ / V | $I_{SC}$ / mA/cm$^2$ | FF | Eff. / % |
|---|---|---|---|---|
| Inverse bilayer | 0.39 | 0.13 | 0.37 | 0.019 |
| Inverse bulk heterojunction | 0.28 | 0.22 | 0.37 | 0.022 |

Based on these results, solar cells with P3HT as a donor polymer were fabricated. The best performing solar cell was a device with a P3HT:PbS ratio of 1:3 with additional polymer interlayer, exhibiting a power conversion efficiency of 0.043% (IV characteristic is shown in Fig. 54; thickness of the active layer was 80-90 nm).

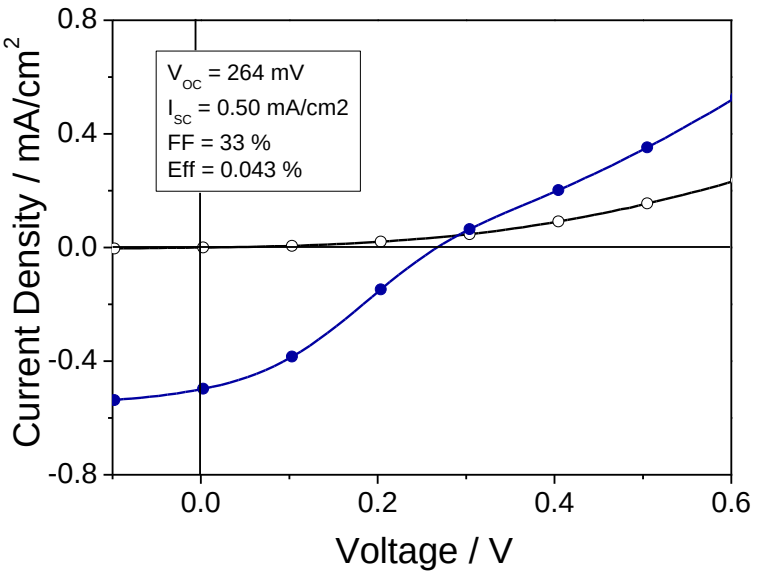


**Fig. 54: : IV curves of a typical P3HT / PbS hybrid solar cell with a P3HT:PbS weight ratio of 1:3 with an additional P3HT interlayer prepared at 195 °C showing an efficiency of 0.043% (filled symbols denote measurements under AM1.5 illumination, empty symbols without illumination).**

In conclusion we fabricated polymer/PbS nanocomposite solar cells with power conversion efficiencies up to 0.04%, which is similar to the results achieved by S. Günes et[156] al in 2007 with a P3HT/PbS nanocomposite. The use of new low band gap polymers and further device optimization is necessary including the decreased surface roughness in order to achieve nanocomposite solar cells, based on a Pb-Hep precursor, with higher power conversion efficiency.

### 1.3.4 Polymer/$Sb_2S_3$ solar cells

Crystalline antimony sulphide (stibnite) is a very promising semiconductor material for photovoltaic cells because of its high absorption coefficient ($1.8*10^5$ $cm^{-1}$ at 450 nm) and its optimum band gap (Eg = 1.7 eV for nanoparticles; also values up to 3.8 eV for bulk $Sb_2S_3$ have been reported).[111,133,135]

There are already some publications about the usage of $Sb_2S_3$ in solar cells, but predominantly $Sb_2S_3$ was used as a sensitizer onto mesoporous-TiOx in solid-state nanocrystal sensitized solar cells.[111,157-159] Furthermore, in parallel to my thesis, S. A. Haque et al.[89] recently investigated P3HT/$Sb_2S_3$ nanocomposite solar cells with a power conversion efficiency of 1.3% . They applied antimony triethyl dithiocarbonate (antimony ethyl xanthate) as precursor material in an inverse architecture with a CdS buffer layer.

In this chapter Sb-Hep was applied as precursor for $Sb_2S_3$ in nanocomposite layers, and the application of these layers in solar cells was investigated.

#### *1.3.4.1 Characterization*

For the optical characterisation of the nanocomposite formation, PMMA was applied as a matrix polymer again.

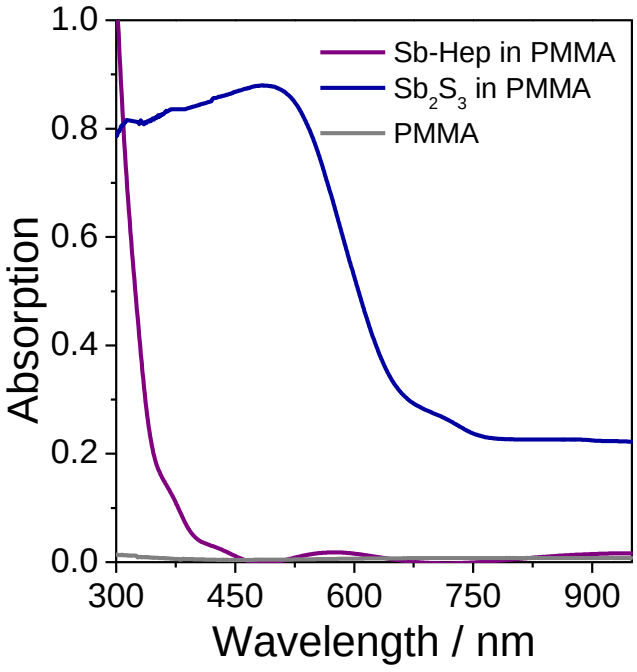


**Fig. 55: UV-vis spectra of Sb-Hep before (Sb-Hep/PMMA) and after heating to 195 °C ($Sb_2S_3$/PMMA) in PMMA matrix.**

The absorption differences before and after thermal conversion are shown in Fig. 55. Regarding Sb-Hep, an intense absorption in the UV-range between 300 and 450 nm is determined, whereas this UV absorption completely vanished after thermal treatment in the $Sb_2S_3$ sample. A typical absorption profile of $Sb_2S_3$ nanoparticles with an absorption onset around 770 nm was observed. Absorption at higher wavelength is contributed to scattering effects.

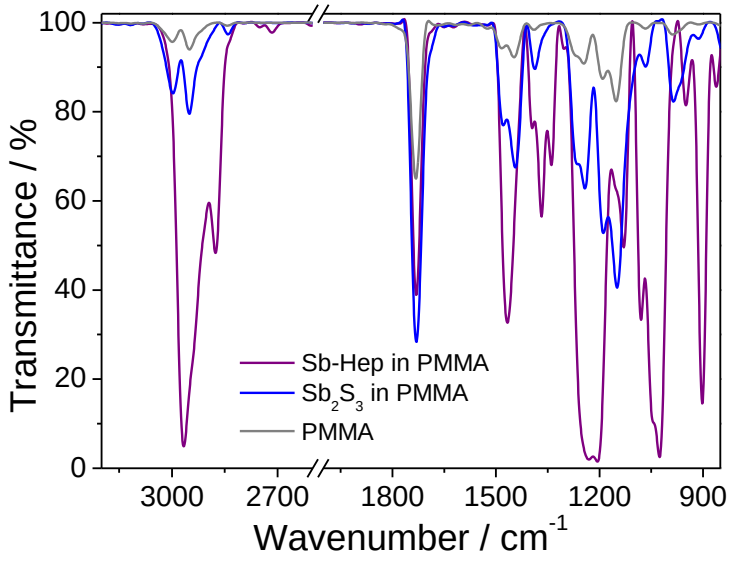


**Fig. 56: IR spectra of Sb-Hep in PMMA before and after temperature treatment.**

The IR-spectra (Fig. 56) after thermal conversion of Sb-Hep embedded in a PMMA matrix at 195 °C reveals that all IR-vibrations stemming from the xanthate moiety are fully vanished. In the spectrum of Sb-Hep/PMMA the typical vibrations of xanthates are detected. The most intense peaks at 1231 and 1206 $cm^{-1}$ can be attributed to the asymmetric C-O-C stretching vibrations, the bands at 1047 and 1026 $cm^{-1}$ to the C-S stretching vibrations.[118] After the annealing step, all vibrational bands of the Sb-Hep fully vanish and the spectrum of $Sb_2S_3$/PMMA resembles the pure PMMA spectrum with its most prominent peak at 1730 $cm^{-1}$ attributable to the carbonyl stretching vibration, similar to the previously discussed Bi- and Pb-samples. Thus, the decomposition of the metal xanthate in a polymer matrix is confirmed.

To investigate nanocomposite layers suitable as active layers in solar cells, hybrid layers with P3HT and PSiF-DBT as donor materials were fabricated (energy alignment is shown in Fig. 57).

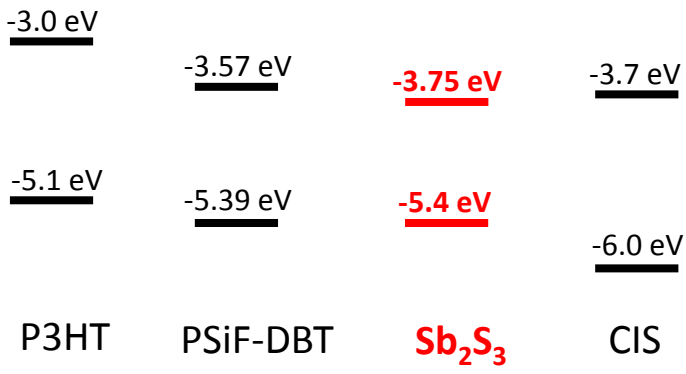


**Fig. 57: Energy alignment of $Sb_2S_3$ and common polymers. The energy positions of the semiconductor band edge are taken from literature (P3HT[140], PSiF-DBT[142], $Sb_2S_3$[160], CIS[143]).**

Both considered polymers are suitable as hole conduction layers in combination with $Sb_2S_3$ according to the energy alignment. Thus, efficient heterojunction between $Sb_2S_3$ and polymers should be formed, allowing exciton dissociation due to the sufficiently large offset between HOMO and LUMO levels of the polymer and the $Sb_2S_3$ phase.

UV-vis analysis of nanocomposite layers with varying polymer to $Sb_2S_3$ ratio is shown in Fig. 58.

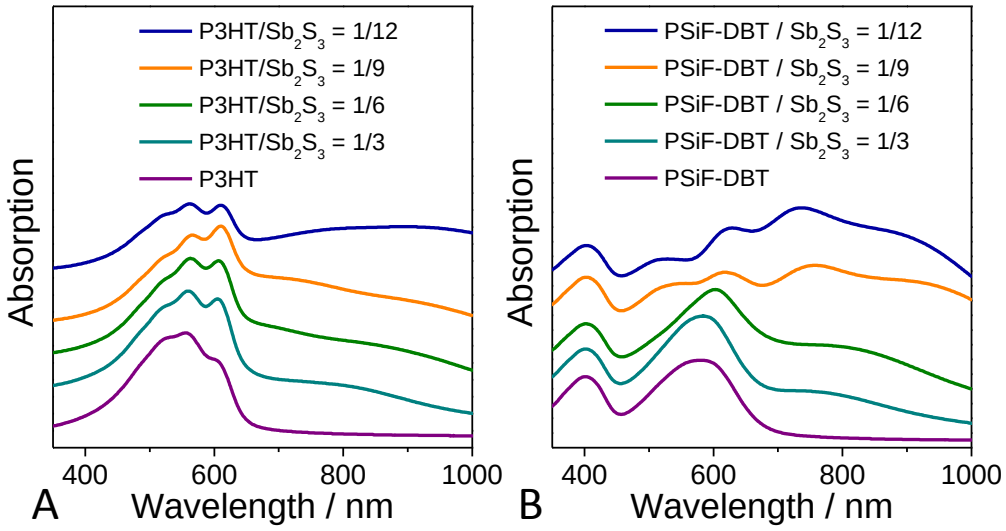


**Fig. 58: Absorption spectra of polymer/$Sb_2S_3$ nanocomposite layer with varying polymer to inorganic ratios (the spectra are shifted vertically for better visibility).**

As observed before for $Bi_2S_3$ as well as for PbS nanocomposites, a polymer maximum at a wavelength of 556 nm for P3HT and 580 nm for PSiF-DBT is shown. In contrast to $Bi_2S_3$ and PbS nanocomposite layers instead of a light blue shift a light red shift could be obtained with increasing inorganic content. This may be caused by an increase in crystallinity of P3HT with increasing $Sb_2S_3$ content.[144] Absorption at higher wavelength than 800 nm is contributed to

scattering effects. Interestingly, especially the absorption spectra of PSiF-DBT/$In_2S_3$ (Fig. 58 B) with higher inorganic content, showing additionally some fine oscillations, look completely different than the spectra with low inorganic content. It is very unlikely that this difference in absorption is caused by the optical properties of $Sb_2S_3$, but may be caused by Mie scattering on spherical particles. According to Mie theory, dielectric spheres with a radius comparable to the wavelength of the light are efficient scatterers.[161]

To investigate the suitability of the $Sb_2S_3$ nanocomposites as active layers in solar cells, photoluminescence quenching measurements were performed (Fig. 59).

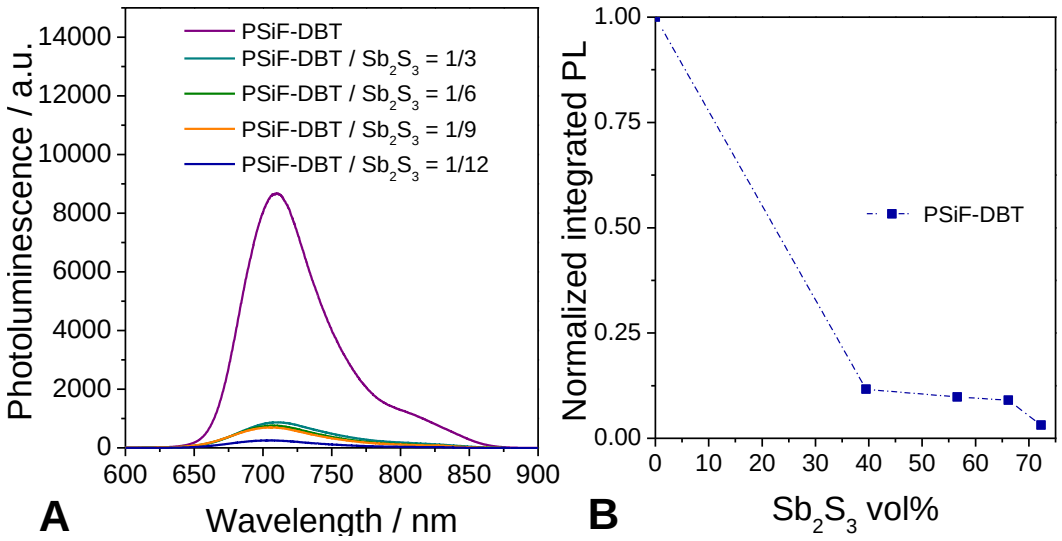


**Fig. 59: Photoluminescence quenching results of polymer/$Sb_2S_3$ nanocomposites. The emission of the pristine polymers is already nearly complete quenched after introduction of only 30 vol% PbS nanocrystals to the polymer films.**

In the case of polymer/$Sb_2S_3$ nanocomposites, PSiF-DBT was used for fluorescence quenching measurements. The PL emission of PSiF-DBT was quenched to only 12% of the initial emission intensity at a PSiF-DBT:$Sb_2S_3$ weight ratio of 1:3 and is reduced still further to 10% (PSiF-DBT:$Sb_2S_3$ = 1:6) and 3% (PSiF-DBT:$Sb_2S_3$ = 1:12) of the original level. So, PSiF-DBT is suitable for polymer/$Sb_2S_3$ nanocomposite solar cells. Unfortunately, Sb-Hep is not stable for more than one week. Freshly prepared Sb-Hep is well soluble in apolar solvents, but after a maximum of one week, the complex is only poorly soluble anymore. Thus, no further photoluminescence quenching with e.g. P3HT was investigated. Nevertheless, for solar cell fabrication P3HT was used as donor polymer, due to the promising high efficiency achieved by S. A. Haque et al.[89]

### *1.3.4.2 Solar cell fabrication*

Due to the poor solubility of the Sb-Hep caused by its poor stability, the fabrication of bulk-heterojunction devices with different polymer to inorganic ratios is not reproducible due to the varying amounts of dissolved $Sb_2S_3$. Nevertheless, P3HT/$Sb_2S_3$ nanocomposite solar cells with different polymer to inorganic ratios (1:5, 1:8, 1:11, 1:15) were fabricated. Before the coating of the active layer, the P3HT/Sb-Hep/chlorobenzene blend was filtered to remove all insoluble parts of Sb-Hep.

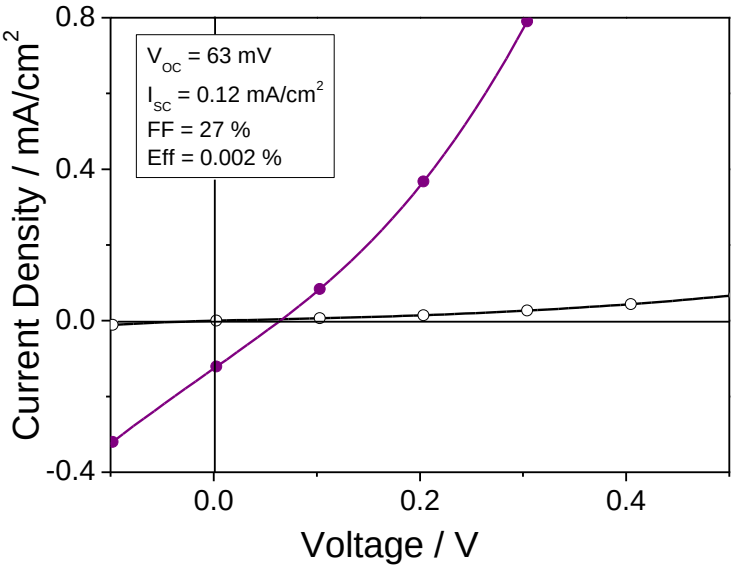


**Fig. 60: IV characteristic of a P3HT/$Sb_2S_3$ bulk heterojunction solar cell (filled symbols denote measurements under AM1.5 illumination, empty symbols without illumination).**

All devices exhibited very poor efficiencies. The device with the highest power conversion efficiency (0.002%) was achieved with a calculated polymer to inorganic ratio of 1:11 (Fig. 60). Layer thicknesses were measured with a surface profiler and exhibited layer thicknesses from 85-130 nm. The thickness and roughness of the active layer increased with increasing amount of $Sb_2S_3$ (roughness of the substrate with a polymer : inorganic ratio of 1:5 = 4 nm; roughness of the substrate with a polymer : inorganic ratio of 1:11 = 17 nm). In a second attempt inverse bilayer devices with the following device architecture: ITO/glass/TiOx/$Sb_2S_3$/P3HT/Au were fabricated. This device architecture is similar to the architecture of a solid state dye sensitized solar cell presented by J. A. Chang et al.[111] (Fig. 61) that achieved a power conversion efficiency of 5%. The only significant difference is the TiOx layer employed. Whereas in the dye sensitized solar cell a mesoprous-$TiO_2$ is applied, we used the same imporous TiOx layer as in the $Bi_2S_3$ and PbS inverse solar cell approaches.

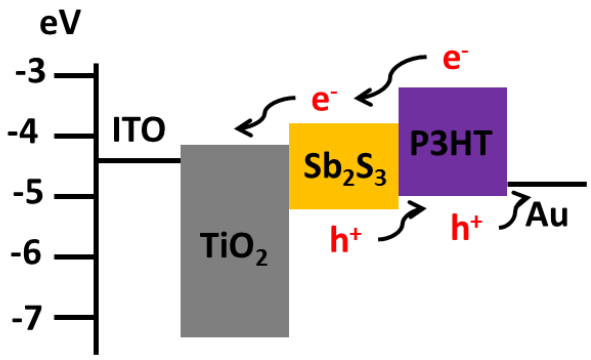


**Fig. 61: Energy structure diagram and schematic configuration of the device presented by J. A. Chang et al.[111]**

To vary the $Sb_2S_3$ thickness, different coating speeds (7.5 mm/s, 10 mm/s, 15 mm/s, 20 mm/s) for the Sb-Hep precursor layer were investigated (Fig. 62).

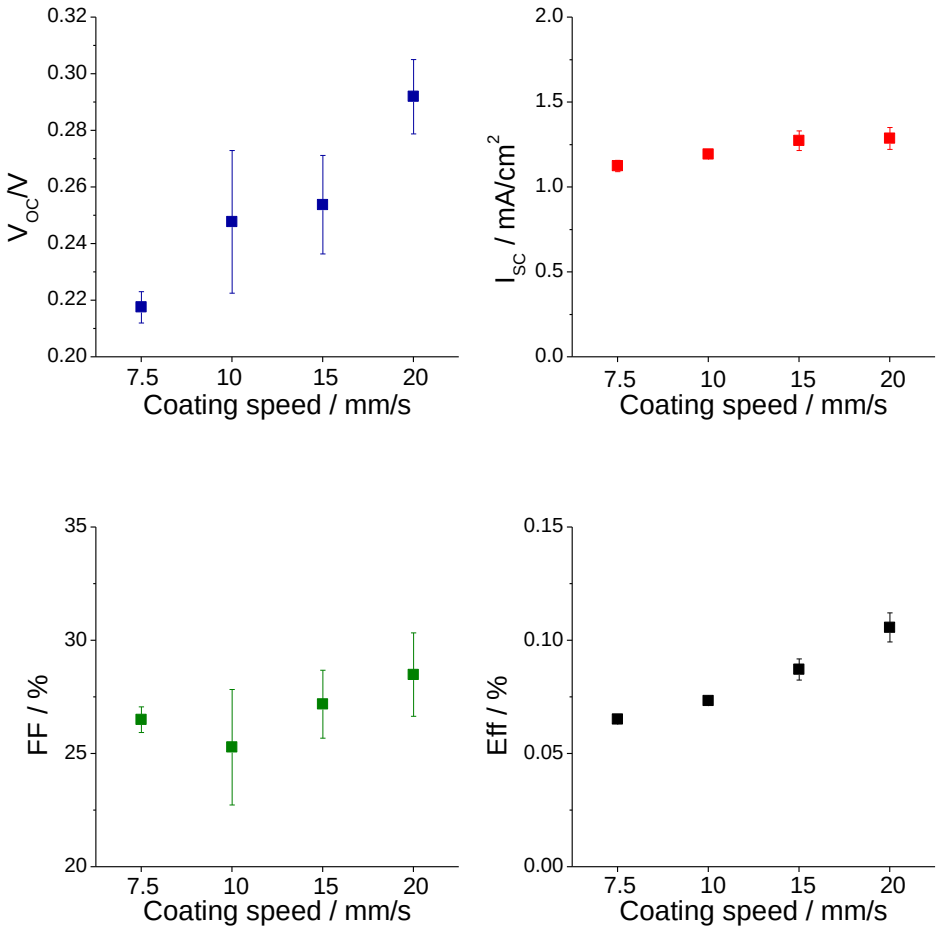


**Fig. 62: Comparison of the characteristic parameters of inverse polymer/$Sb_2S_3$ bilayer solar cells fabricated with different coating speeds for the $Sb_2S_3$ layer.**

Layer thickness increases with increasing coating speed. Unfortunately it was not possible to investigate the layer thicknesses with a surface profiler, due to the high roughness of the samples, which lead to unreliable results (layer thicknesses between 200 and 100 nm with a roughness of 100 nm). Nevertheless, $V_{OC}$, $I_{SC}$ and fill factor increase with increasing coating speed, leading to a maximum of power conversion efficiency of 0.11% with a coating speed of 20 mm/s (Fig. 63).

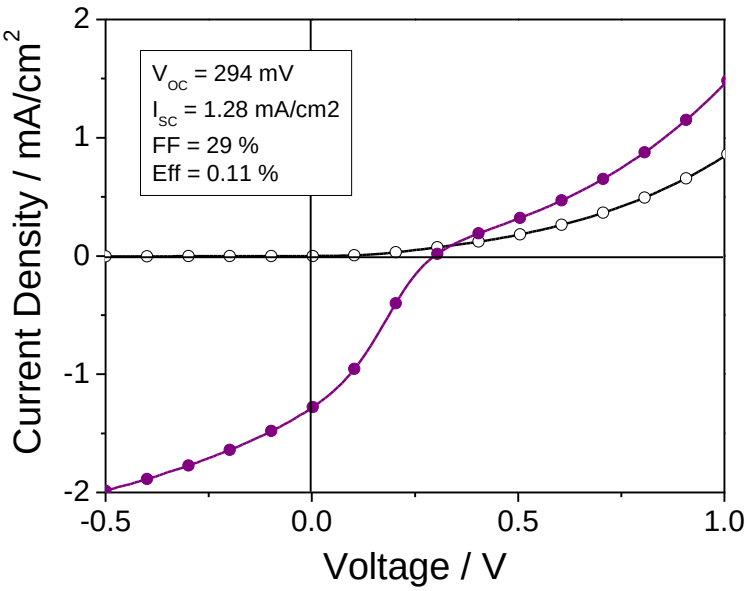


**Fig. 63: IV characteristic of the best performing inverse bilayer P3HT/$Sb_2S_3$ device with a coating speed of 20 mm/s (filled symbols denote measurements under AM1.5 illumination, empty symbols without illumination).**

In this chapter we demonstrated the suitability of Sb-Hep for solar cell fabrication. Although Sb-Hep exhibits poor stability resulting in poor solubility, inverse bilayer solar cells with a power conversion efficiency of up to 0.1% could be obtained.

### 1.3.5 Polymer/$In_2S_3$ solar cells

$In_2S_3$ belongs to III-VI materials. It is a direct semiconductor with a large band gap that can be varied between 2-3 eV.[136] $In_2S_3$ appears to be a suitable material for solar cell applications due to its stability[162] and photoconductor behaviour[163]. Up to now $In_2S_3$ is mainly considered as buffer layer material to replace toxic CdS buffer layers in CIGS thin film solar cell devices.[164] In 2011 H. Jia et al[165] reported $In_2S_3$/P3HT hybrid solar cells with a quite low power conversion efficiency of 0.04%.

In this chapter In-Hep was investigated as a precursor material for hybrid nanocomposite layers and their potential application in solar cells.

### *1.3.5.1 Characterisation*

For the optical characterisation of the hybrid nanocomposite formation PMMA was used as a matrix polymer.

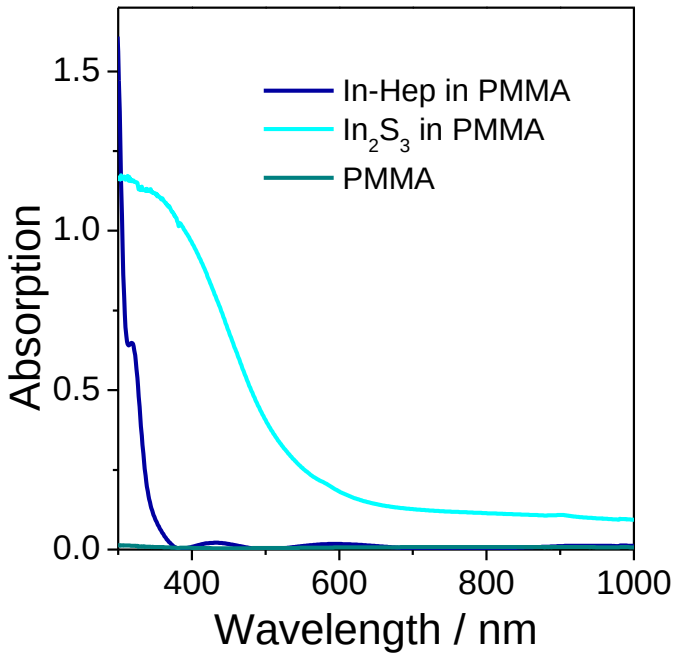


**Fig. 64: UV-vis spectra of In-Hep before (In-Hep/PMMA) and after heating to 195 °C ($In_2S_3$/PMMA) in PMMA matrix.**

The UV-vis spectra (Fig. 64) of In-Hep before (In-Hep/PMMA) and after thermal treatment ($In_2S_3$/PMMA) in a PMMA matrix illustrate the differences in the optical properties of the materials. An intense absorption in the UV-range between 300 and 400 nm is observed for the In-Hep sample. This absorption vanishes after heating to 195 °C and the absorption profile of $In_2S_3$ nanoparticles with an absorption onset at around 700 nm is visible in the spectrum. Absorption at higher wavelength is contributed to scattering effects.

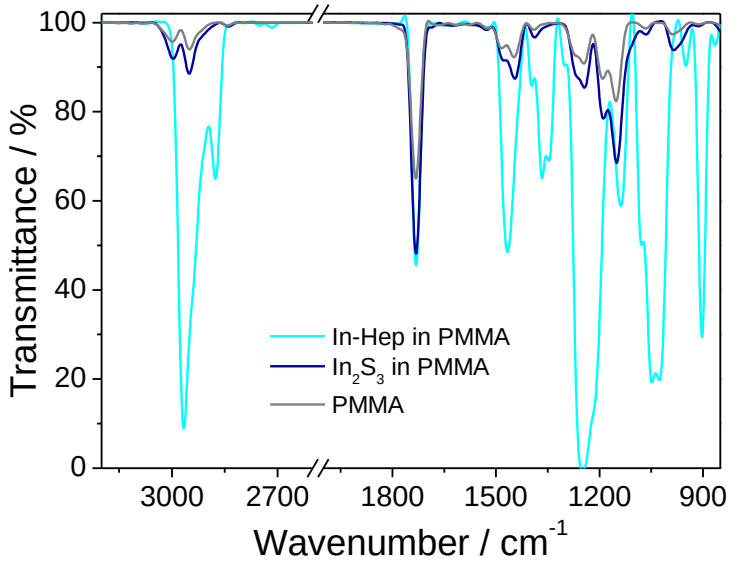


**Fig. 65: IR-spectra from In-Hep sample embedded in PMMA before and after annealing to 195 °C.**

To prove the conversion of the metal xanthate in a matrix polymer, IR-spectra (Fig. 65) were recorded from an In-Hep sample embedded in a PMMA matrix before and after annealing to 195 °C. In the In-Hep/PMMA the typical vibrations of xanthates are detected. The most intense peaks at 1248 and 1215 $cm^{-1}$ can be attributed to the asymmetric C-O-C stretching vibrations, the bands at 1047 and 1026 $cm^{-1}$ to the C-S stretching vibrations.[118] After the annealing step, all vibrational bands of the In-Hep fully vanish and the spectrum of $In_2S_3$/PMMA resembles the pure PMMA spectrum with its most prominent peak at 1732 $cm^{-1}$ attributable to the carbonyl stretching vibration.

For the investigation of $In_2S_3$ hybrid layers suitable for the application in solar cells, nanocomposite films with P3HT and PSiF-DBT were investigated.

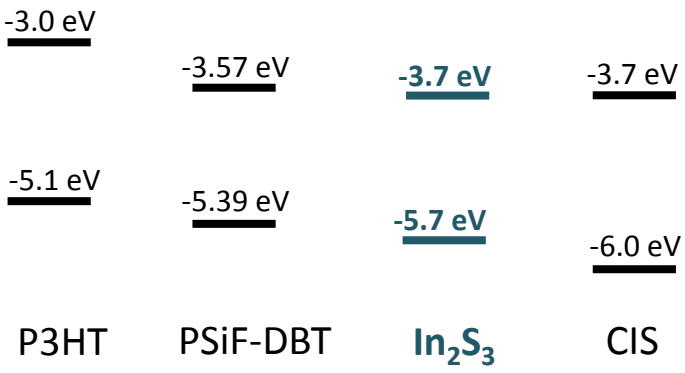


**Fig. 66: Energy levels of donor polymers and $In_2S_3$ nanoparticles. The energy positions of the semiconductor band edge are taken from literature (P3HT[140], PSiF-DBT[142], $In_2S_3$[165], CIS[143]).**

The energy levels (Fig. 66) of $In_2S_3$ and both polymers are well matched for the fabrication of nanocomposite solar cells. The conduction band of the $In_2S_3$ nanoparticles is more negative than the lowest unoccupied molecular orbital (LUMO) level of the polymers. The HOMO level of the polymers is less negative than the valence band of $In_2S_3$ nanoparticles. Thus, efficient exciton dissociation should be possible.

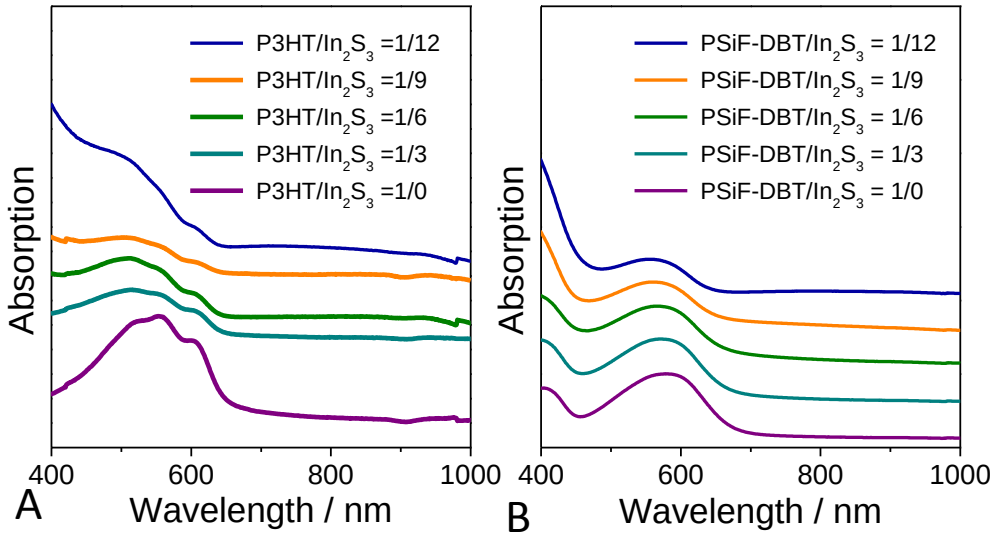


**Fig. 67: Absorption spectra of polymer/$In_2S_3$ nanocomposite layer with varying polymer to inorganic ratios (the spectra are shifted vertically for better visibility).**

UV-vis analysis of nanocomposite layers with different polymer to inorganic ratios (Fig. 67; the spectra are shifted vertically for better visibility) reveal a polymer maximum at a wavelength of 554 nm for P3HT and 580 nm for PSiF-DBT. In all hybrid films a light blue shift of the maximum could be observed, which can be related to the increasing inorganic content.

To confirm the suitability of the $In_2S_3$ nanocomposites in solar cell applications and to investigate charge transfer, photoluminescence measurements were performed. The PL is found to be strongly quenched when $In_2S_3$ is present in the composite.

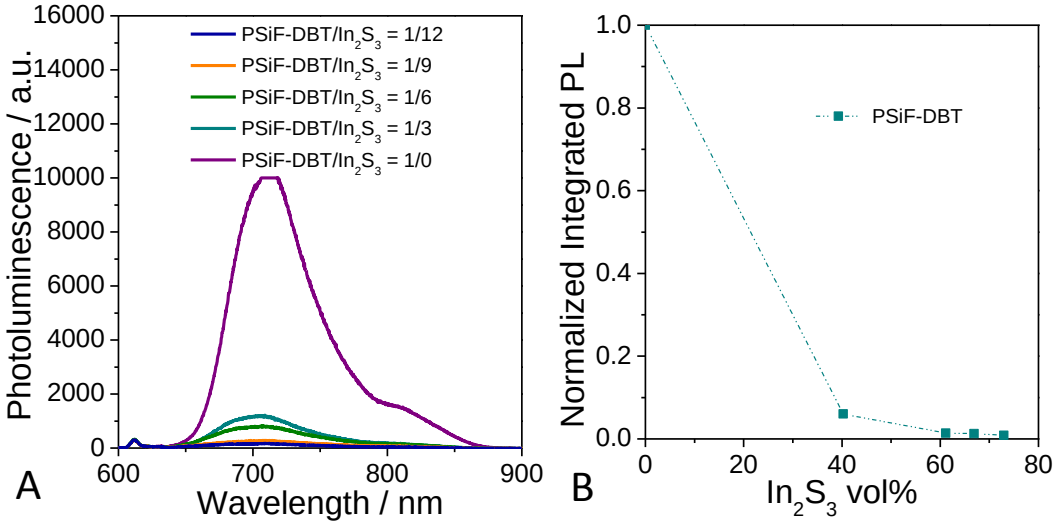


**Fig. 68: Photoluminescence quenching results of PSiF-DBT/$In_2S_3$ nanocomposites. The emission of the pristine polymers is already nearly complete quenched after introduction of only 40 vol% $In_2S_3$ nanocrystals to the polymer films.**

In Fig. 68 the PL spectra of pure PSiF-DBT and PSiF-DBT/$In_2S_3$ nanocomposite layers with different weight ratios of 1:3, 1:6, 1:9 and 1:12 are shown. Optical excitation of the pristine PSiF-DBT film at 580 nm resulted in the appearance of an emission band at 710 nm. The emission of the pristine polymers is already quenched nearly complete (12% of the initial emission intensity) after introduction of only 40 vol% $In_2S_3$ nanocrystals (ratio of 1:3 (w:w))to the polymer films. The PL was further reduced to 9% (PSiF-DBT : $In_2S_3$ = 1:6) and 3% (PSiF-DBT : $In_2S_3$ = 1:9) and finally to 2% (PSiF-DBT : $In_2S_3$ = 1:12)of the original level. Due to the promising results obtained from the photolumisecencequenching measurements, PSiF-DBT was used as donor polymer in polymer/$In_2S_3$ solar cells.

### *1.3.5.2 Solar Cell fabrication*

Nanocomposite solar cells with different polymer to inorganic ratios (1:3 to 1:12) were fabricated at different conversion temperatures (in 9.5 °C/min to 175 °C, in 10 °C to 185 °C, in 11 °C to 195 °C and in 12 °C to 205 °C, holding the temperatures for 15 min) using PSiF-DBT as donor material. The nanocomposite layers of all prepared solar cells have thicknesses between 60 and 90 nm, which was measured using a surface profiler and they are very smooth exhibiting a roughness $r_a$ of only 1-3 nm. Conversion efficiency maxima were

achieved for different polymer to inorganic ratios at different temperatures. For a conversion temperature of 175 °C and 205 °C, the ratio of 1:3 exhibited the highest power conversion efficiency, whereas for a temperature of 185 °C a ratio of 1:6 and for 195 °C a ratio of 1:4 showed the highest efficiencies. The best solar cells with associated conversion temperature are shown in Fig. 69.

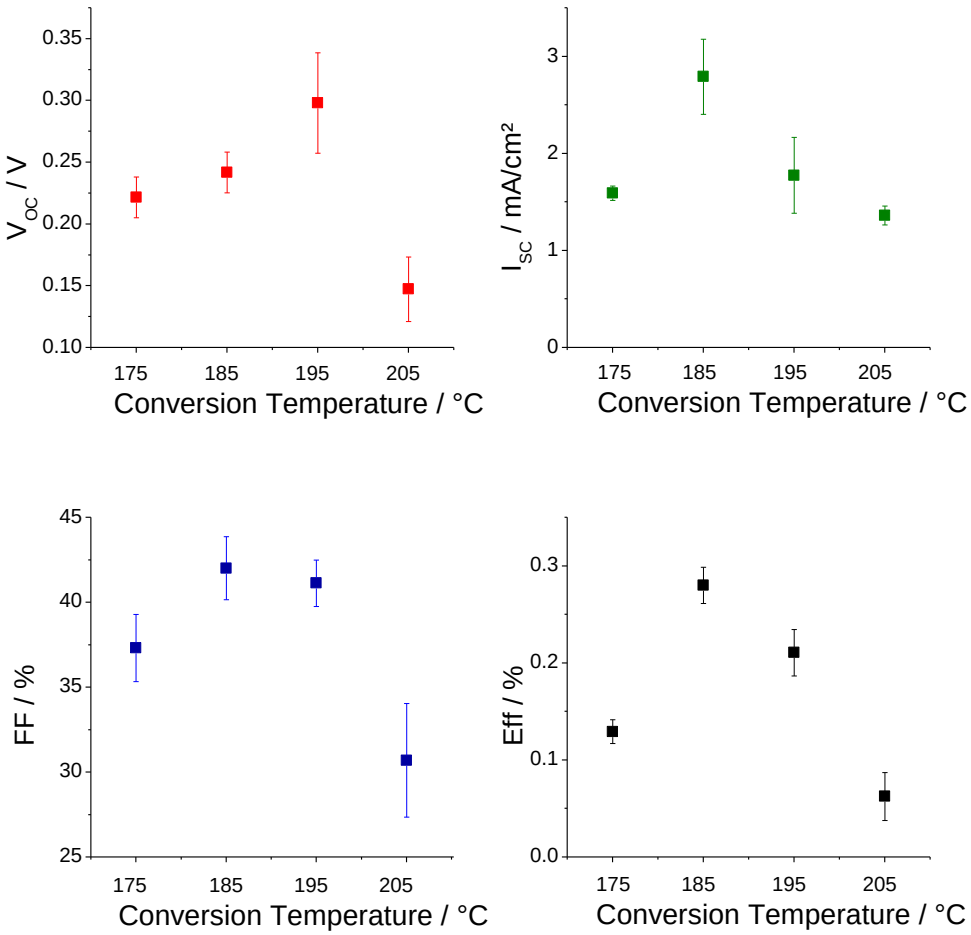


**Fig. 69: Comparison of the parameters $I_{SC}$, $V_{OC}$, FF and efficiency of the best PSiF-DBT/$In_2S_3$ hybrid solar solar cells fabricated at different conversion temperatures (mean values of the best 5 solar cells).**

The $I_{SC}$ shows maximum values (3.2 mA/cm²) at a conversion temperature of 185 °C. The highest values for the $V_{OC}$ (254 mV) are observed at a conversion temperature of 195 °C. The fill factors are between 30 and 45% for all weight ratios, the highest fill factors could be achieved with conversion temperatures of 185 °C and 195 °C. This leads to a clear maximum of the solar cell efficiencies at a conversion temperature of 185 °C. At this temperature efficiencies of around 0.3% are reached while at conversion temperatures of 175 °C and 205 °C

efficiencies of around 0.1% are observed. The thicknesses of the active layers were determined with surface profiler and are between 40 and 60 nm.

In Fig. 70 the different polymer to inorganic ratios at a conversion temperature of 185 °C are shown. Devices with higher polymer to inorganic ratios than 1:6 exhibited no $V_{OC}$, thus they are not shown in the figure.

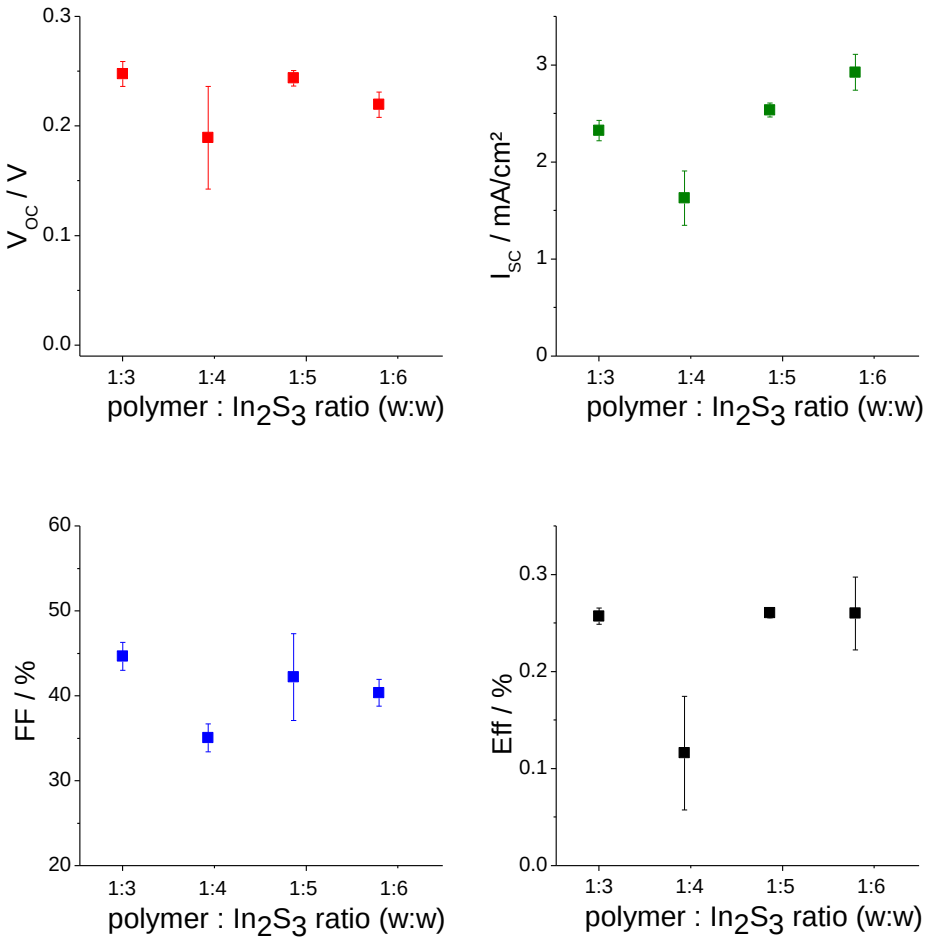


**Fig. 70: Polymer to $In_2S_3$ ratios at a conversion temperature of 185 °C (mean values of the best 5 solar cells).**

The $I_{SC}$ shows maximum values (3.2 mA/cm²) at a PSiF-DBT : $In_2S_3$ weight ratio of 1:6. All devices exhibited $V_{OC}$ values around 0.25 V, except the device with a ratio of 1:4, which revealed only around 0.18 V. The fill factors are between 30 and 45% for all weight ratios, the lowest fill factor was achieved for the device with a ratio of 1:4. All nanocomposite solar cells exhibited efficiencies around 0.26% except for the device with a ratio of 1:4. The thicknesses of the active layers were determined with surface profiler and are around 50-80 nm.The highest

efficiency with a value of 0.31% could be achieved at a polymer to inorganic ratio of 1:6 (IV characteristic is shown in Fig. 71).

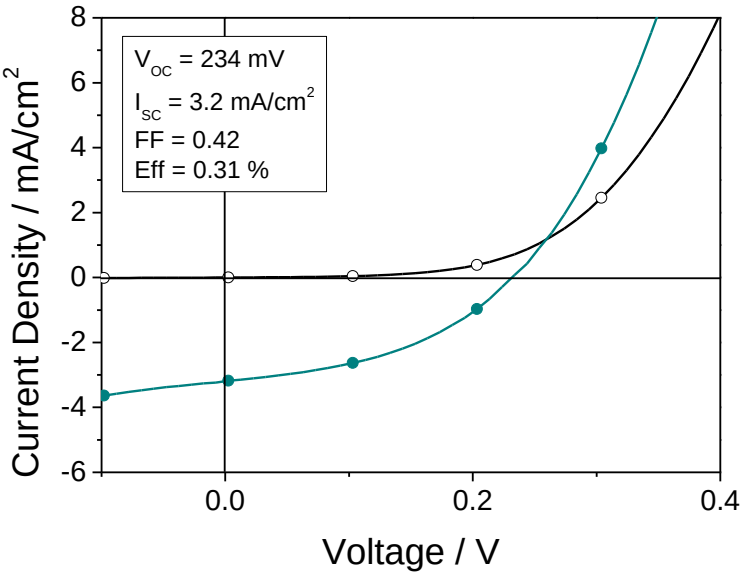


**Fig. 71: IV characteristic of PSiF-DBT : $In_2S_3$ nanocomposite solar cell with a ratio of 1:6 (w:w), fabricated at 185 °C (filled symbols denote measurements under AM1.5 illumination, empty symbols without illumination).**

In conclusion we fabricated PSiF-DBT/$In_2S_3$ nanocomposite solar cells with power conversion efficiencies up to 0.3%, which is much higher as the results (0.04%) achieved by H. Jia et al in 2011[165] (P3HT/$In_2S_3$). Thus, In-Hep is a promising precursor for $In_2S_3$ nanocomposite solar cells.

## 1.4 Conclusion

Bi-and Pb- Et, Hex and Hep xanthates and Sb-, Co-, Ni-Hep xanthates were synthesised with high purity according to NMR, FT-IR and elementary analysis. In addition, a crystal structure for Bi-Hex was obtained revealing a dimeric structure. Furthermore, the thermal conversion of all synthesised xanthates and In-Hep, which was obtained from Aglycon, was investigated by thermal gravimetric analysis and high resolution mass spectroscopy. These measurements showed that all xanthates decompose at moderate temperatures <210 °C. To investigate which crystal phase is formed, XRD measurements were performed, showing that $Bi_2S_3$, PbS, $Sb_2S_3$ and $In_2S_3$ were generated. In contrast to this, in the case of Ni- and Co-sulphides more than one phase was formed, thus, they were not further investigated.

In combination with the high solubility in non-polar organic solvents caused by the branched alkyl side chains, this synthetic route for metal sulphides is of particular interest for the preparation of metal sulphide/polymer nanocomposites. By mixing the xanthates with PMMA as well as with a conjugated polymer in a solvent, coating of precursor layers and heating them

to 200°C in inert atmosphere, metal sulphide nanocrystals are formed within the polymer matrix. This ligand-free solid state *in situ* reaction path is very interesting for the fabrication of nanocomposite solar cells.

In the case of $Bi_2S_3$ nanorods were obtained, which may be of special interest for this application as nanorods facilitate charge transport and also provide a high interfacial area towards the conjugated polymer. Studying $Bi_2S_3$/polymer nanocomposites concerning their applicability in nanocomposite solar cells, it was not possible to realise working solar cells using the *in situ* prepared $Bi_2S_3$/polymer hybrid layers, even though we observed that the fluorescence of the conjugated polymer is efficiently quenched by the $Bi_2S_3$ nanorods, which points to an efficient charge transfer at the hybrid interface.

Furthermore, PbS, $Sb_2S_3$ and $In_2S_3$ /polymer nanocomposite solar cells were prepared. Also the fluorescence of the conjugated polymer is efficiently quenched by these metal sulphides, only low efficiencies could be obtained. Regarding PbS/polymer solar cells, further optimization is necessary including decreasing the surface roughness in order to achieve nanocomposite solar cells with higher power conversion efficiency. Sb-Hep seems to be not stable and was therefore only poorly soluble in apolar solvents after one week after synthesis. Therefore, to achieve higher efficiencies, Sb-xanthates with different side chains should be investigated. The most promising results were achieved with $In_2S_3$ as acceptor material in nanocomposite solar cells with an efficiency of 0.3%.

# 2 Tandem solar cells

## 2.1 Exploring polymer/nanoparticle hybrid solar cells in tandem architecture

*This chapter was first published in V. Kaltenhauser, T. Rath, M. Edler, A. Reichmann, G. Trimme, RSC Adv., DOI:10.1039/C3RA43842B.*

*Reproduced by permission of The Royal Society of Chemistry*

### 2.1.1 Introduction

In the field of organic photovoltaics the concept of tandem solar cells is extensively researched.[96,98,100,166,167] Tandem solar cells already exceed the efficiencies of solar cells with one absorbing layer in the case of polymer/fullerene and small molecule solar cells.[168,169] The reasons for that are that challenges of many organic materials like narrow absorption bands or the limited active layer thickness and thus limited absorption due to low hole mobility can be overcome by a tandem configuration. By stacking solar cells with complementary absorbing materials the absorption range is extended in the best case from the UV-part up to the IR-region, and, in addition to that, the subcells can have thinner absorber layers compared to a single cell to harvest the same amount of photons or even more, which largely reduces the problems associated with low carrier mobilities.

For hybrid solar cells having absorber layers consisting of conjugated polymers and inorganic semiconducting nanoparticles,[33,35,36,170,171] the tandem concept is entirely not explored up to now, even though this concept bears the chance to significantly improve the efficiencies of hybrid solar cells. Similar to classical organic solar cells, low charge carrier mobilities are often observed. The absorption range in single hybrid solar cells can be already extended by choosing proper inorganic semiconductors, e.g. NIR-absorbing PbS nanoparticles.[112] Therefore, the tandem architecture gives the auspicious possibility to tune the absorption properties of the solar cells using four materials with complementary absorption profiles in order to harvest as much sunlight as possible.

Up to now, a large variety of hybrid materials consisting of conjugated polymers and inorganic semiconducting nanoparticles with different absorption properties (e.g. ZnO,[172] CdS,[27,88] CdSe,[173,174] PbS,[112] $CuInS_2$[15,79]) were used for the preparation of hybrid solar cells. The maximum power conversion efficiencies of hybrid solar cells are today around 4% realised with CdS/polymer[27], CdSe/polymer[28,29], PbS/polymer[112] hybrid materials. Because of the above

mentioned challenges of limited hole mobility and the advantage of an extended absorption range, the tandem concept should contribute to a significant increase of the power conversion efficiencies (PCEs) of hybrid solar cells in the future.

In this work, we explore the application of polymer/nanoparticle hybrid solar cells in tandem architecture. First, nanoparticle/polymer-$PC_{61}BM$ ([6,6]-phenyl $C_{61}$ butyric acid methyl ester)/polymer tandem solar cells (hybrid-organic tandem solar cells) were realised using a hybrid poly[(2,7-silafluorene)-alt-(4,7-di-2-thienyl-2,1,3-benzothiadiazole (PSiF-DBT)/copper indium sulphide (CIS) bottom cell and a poly({4,8-bis[(2-ethylhexyl)oxy]benzo[1,2-b:4,5-b']dithiophene-2,6-diyl}{3-fluoro-2-[(2-ethylhexyl)carbonyl]thieno [3,4-b]thiophenediyl}) (PTB7)/$PC_{61}BM$ top cell. Secondly, polymer/nanoparticle-polymer/nanoparticle (hybrid-hybrid) tandem solar cells were fabricated consisting of two PSiF-DBT/CIS hybrid solar cells. The hybrid PSiF-DBT/CIS solar cells are prepared via the xanthate route, which was recently introduced for the preparation of polymer/CdS[14] and polymer/CIS[15] hybrid solar cells. Following this route, the nanoparticles are formed *in situ* in the matrix of the conjugated polymer by conversion of the metal xanthate precursors to metal sulphide nanoparticles during a mild thermal annealing step. The advantage of this *in situ* route is that no capping agents, which would hinder charge separation and transport in the active layer,[9,175] are necessary for the stabilisation of the nanoparticles. The growth of the metal sulphide nanoparticles is thereby controlled by the polymer matrix. Alternatively to conjugated polymers, solution-processable small molecules can fulfil this task.[176] In addition, the active layer can be prepared without tedious nanoparticle synthesis and ligand exchange processes by a facile, short and mild thermal annealing step. The organic moieties of the metal xanthate precursors have been additionally tailored to guarantee high solubility in organic solvents and to form the metal sulphides at low temperatures.

### 2.1.2 Results and discussion

Up to now there are no reports about polymer/nanoparticle hybrid solar cells in tandem architectures. Therefore, it is necessary to investigate if series connection via recombination layers known from organic tandem solar cells is possible and if the hybrid absorber layers are inert to further processing steps during the preparation of the tandem solar cells. This is especially challenging for double hybrid tandem solar cells prepared via the *in situ* route, where thermal annealing is required for the preparation of both absorber layers, and thus, the bottom cell experiences more thermal stress. To separate this issue from finding a suitable recombination layer, we combined in a first step an *in situ* prepared hybrid PSiF-DBT/CIS bottom cell with a polymer/PCBM top cell, which does not need a thermal treatment during

preparation, in the tandem architecture. Fig. 1A shows the device geometry of the prepared hybrid organic tandem solar cell. We chose PTB7/$PC_{61}BM$ as material for the organic solar cell because the absorption profile of this material combination complements the absorption of the PSiF-DBT/CIS hybrid material quite well in order to harvest an increased amount of light (for the chemical structures of the polymers see Fig. 72 B).

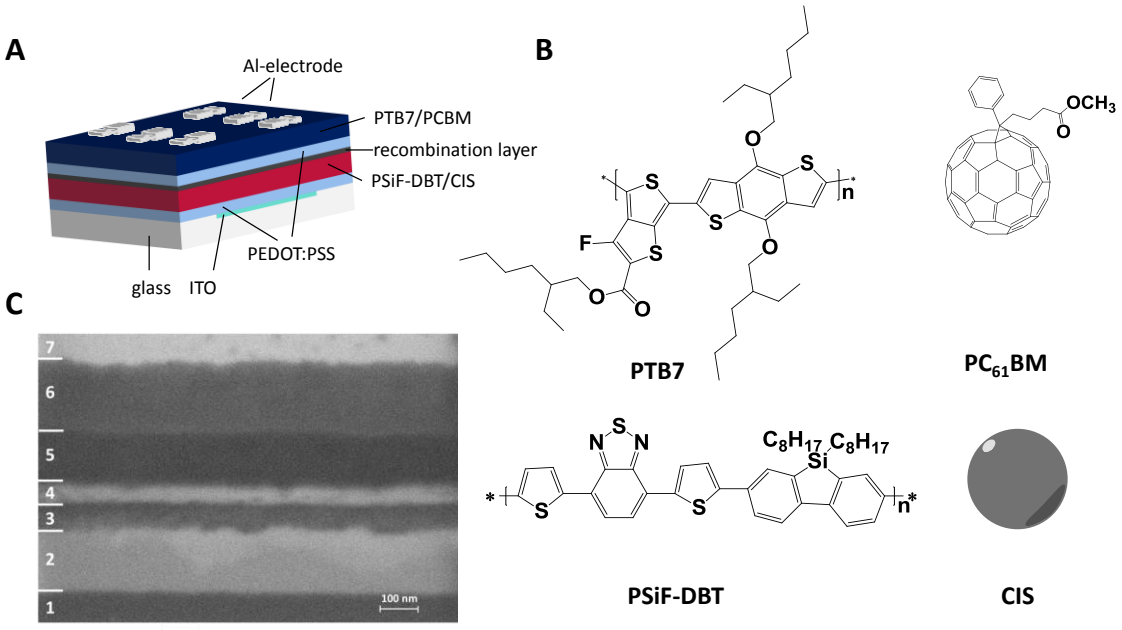


**Fig. 72 A: Device architecture of the hybrid-organic tandem solar cell; B: corresponding chemical structures of the absorber layers; C: SEM image of an ion milled cross section: 1: glass, 2: ITO, 3: PEDOT:PSS, 4: PSiF-DBT/CIS, 5: PEDOT:PSS & PTB7/PCBM, 6: Al electrode, 7: protection layer.**

The PSiF-DBT/CIS bottom cells as well as corresponding reference cells were prepared via a *in situ* preparation route.[15] Thus, a common solution of Cu and In xanthates with the conjugated polymer is coated directly on the PEDOT:PSS layer already deposited onto ITO-glass substrates. The metal xanthates are subsequently converted to copper indium sulphide nanoparticles directly within the polymer matrix at a temperature of 195 °C. On top of this layer, either the recombination layer was deposited for the tandem cells (vide infra) or an Ag (2nm)/Al (180 nm) back electrode[177] was vapour deposited for the reference cells. The PTB7/$PC_{61}BM$ top cell as well as reference cells were knife coated from chlorobenzene solutions containing 1,8-diiodooctane (3 vol%) following a modified literature protocol. 168 The solar cell fabrication was completed by deposition of Al back electrodes.

Before focusing on the tandem cells, the optical properties of both materials combinations as well as the solar cell parameters of the corresponding single cells are discussed. The absorption spectra of PSiF-DBT and PTB7 (Fig. 73 A) complement each other and make these two polymers suitable for the use in tandem devices. The absorption spectrum of PSiF-DBT

exhibits two maxima; the first is located at 400 nm and the second at 570 nm whereas the absorption maximum of PTB7 appears at 670 nm.

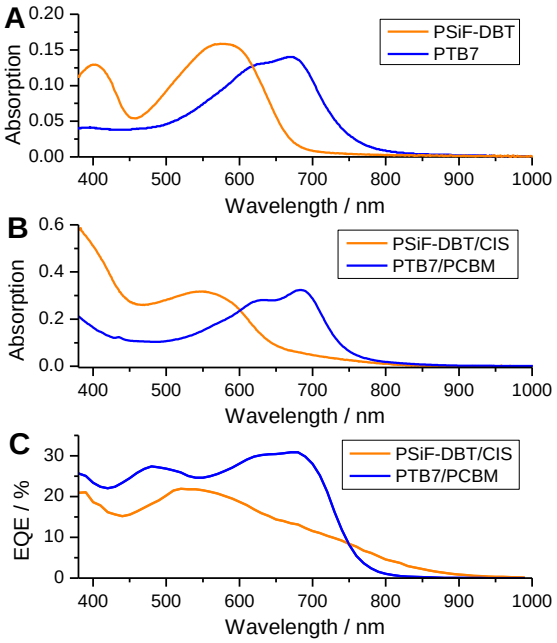


**Fig. 73: Absorption spectra of PSiF-DBT and PTB7 (A), absorption spectra of the two absorber layers (PSiF-DBT/CIS and PTB7/PCBM) (B) and EQE spectra of the corresponding solar cells (C).**

A comparison of the absorption spectra of the pure polymers (Fig. 73 A) with the absorption spectra of the bulk-heterojunction layers (Fig. 73 B) evidences that in the case of the PSiF-DBT/CIS hybrid layer the nanoparticle phase contributes to the absorption especially between 700 nm and 850 nm. The spectrum of the PTB7/$PC_{61}BM$ layer is dominated by the absorption features of the polymer. The EQE spectra of the corresponding PSiF-DBT/CIS as well as the PTB7/PCBM single solar cells are depicted in Fig. 73 C. In the EQE spectrum of the PSiF-DBT/CIS solar cell, the maximum in photocurrent generation is blue-shifted compared to the maximum of the PSiF-DBT/CIS absorption spectrum. This is most presumably caused by the fact that the contribution to current generation of the amorphous part of the polymer is more dominant compared to semicrystalline parts.[178] Furthermore, the EQE of the PSiF-DBT/CIS absorber layers evidences that the copper indium sulphide nanoparticles significantly contribute to the current generation. The EQE spectrum of the PTB7/PCBM solar cell shows also a charge separation over a broad wavelength range (approx. 750 - 400 nm) and is consistent with previous literature reports.[141] Fig. 74 shows the current density-voltage (IV) characteristics of the two single cells and the corresponding tandem cell under AM1.5 simulated illumination with an intensity of 100 mW/$cm^2$.

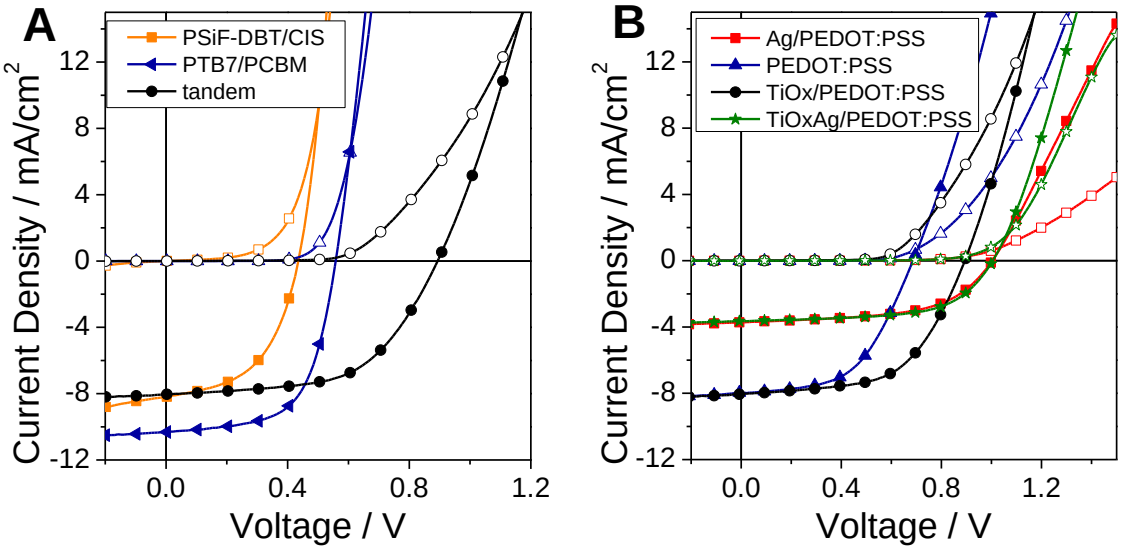


**Fig. 74: A: IV characteristics of the single cells in comparison to the optimised hybrid-organic tandem cell in the dark and under 100 mW/cm$^2$ illumination; B: IV curves of hybrid-organic tandem cells with different interlayers in the dark and under 100 mW/cm$^2$ illumination.**

**Table 10: Characteristic parameters of PSiF-DBT/CIS and PTB7/$PC_{61}$BM solar cells, hybrid-organic (PSiF-DBT/CIS / PTB7/$PC_{61}$BM) tandem solar cells and hybrid-hybrid (PSiF-DBT/CIS / PSiF-DBT/CIS) tandem solar cells using different recombination layers.**

| | | | $V_{OC}$ / V | $I_{SC}$ / mA/cm$^2$ | FF | Eff. / % |
|---|---|---|---|---|---|---|
| Single | | PSiF-DBT/CIS | 0.44 | 8.19 | 0.51 | 1.8 |
| | | PTB7/$PC_{61}$BM | 0.56 | 10.4 | 0.61 | 3.5 |
| Tandem | Hybrid-organic | Ag/PEDOT:PSS | 1.01 | 3.72 | 0.56 | 2.1 |
| | | PEDOT:PSS | 0.69 | 7.99 | 0.53 | 2.9 |
| | | $TiO_x$/PEDOT:PSS | 0.90 | 8.04 | 0.57 | 4.1 |
| | | $TiO_x$/Ag/PEDOT:PSS | 1.01 | 3.72 | 0.56 | 2.1 |
| | Hybrid-hybrid | Ag/PEDOT:PSS | 0.72 | 4.19 | 0.42 | 1.3 |
| | | PEDOT:PSS | 0.38 | 1.68 | 0.18 | 0.1 |
| | | $TiO_x$/PEDOT:PSS | 0.46 | 4.60 | 0.32 | 0.7 |

The hybrid solar cell (PSiF-DBT/CIS) exhibited an open circuit voltage ($V_{OC}$) of 0.44 V, a short circuit current density ($I_{SC}$) of 8.19 mA/cm$^2$, a fill factor (FF) of 0.51 and a PCE of 1.81%. The organic single cell (PTB7/$PC_{61}$BM) exhibited a $V_{OC}$ of 0.56 V, a $J_{SC}$ of 10.4 mA/cm$^2$, a FF of 0.61 and a PCE of 3.51%. The obtained efficiency for the PTB7/$PC_{61}$BM solar cells is lower in contrast to recently reported PCE values for PTB7 fullerene solar cells (7.4% and 9.2%).[22,168] In this case, $PC_{71}$BM which usually gives higher efficiencies as well as additional interlayers (polymeric polyelectrolyte interlayers) were used. However, the incorporation of such interlayers increased mainly the $I_{SC}$ values, which is in view of our experiments not necessary.

The $I_{SC}$ of tandem devices is limited by the lowest value of the involved subcells. The $I_{SC}$ of the PTB7/$PC_{61}BM$ solar cell is without interlayers already higher than the $I_{SC}$ of the PSiF-DBT/CIS hybrid solar cell. To connect the two single cells in series we investigated different interlayer combinations. These interlayers have to be sufficient conductive and transparent and have to provide high charge carrier mobility, so that no charge trapping occurs. Moreover, the interlayer has to efficiently collect electrons from one subcell and holes from the other and should provide an efficient recombination zone without any potential loss.[100] Ultrathin metal films of silver[179] and gold,[180] vacuum deposited metal oxides like indium tin oxide (ITO),[181] molybdenum oxide ($MoO_3$))[182-184] or solution processed metal oxides such as $TiO_x$[48] and ZnO[185] are described in the literature. Mostly, these metal oxides are used in combination with PEDOT:PSS. We investigated Ag/PEDOT:PSS (poly(3,4-ethylenedioxylenethiophene)-polystyrene sulphonic acid), $TiO_x$/PEDOT:PSS and a single PEDOT:PSS layer. Whereas the Ag layer was directly evaporated in the glovebox, the $TiO_x$ layer was prepared by evaporation of 4 nm of metallic Ti in the glovebox which is subsequently converted to $TiO_x$ by exposure to air. Ti has a very high affinity to oxygen and forms within µs an oxide layer with a thickness of 2-5 nm.[186,187] Fig. 74 B shows the IV characteristics of hybrid-organic tandem cells with different recombination layers and Table 10 summarises the characteristic parameters of the prepared tandem devices. As can be seen from the characteristic parameters and the IV curves in Fig. 74 B, the interlayer plays an important role in the device performance of the tandem cell. The device with Ag/PEDOT:PSS interlayer exhibited the highest $V_{OC}$ with a value of 1 V which is exactly the sum of the values of both single cells. Whereas the fill factor has a value of 56% and is still high, the $I_{SC}$ drastically drops to only half of the value of the PSiF-DBT/CIS hybrid cells. Thus, the overall efficiency only yields a value of 2.1%, which is lower than the efficiency of the single PTB7/ PCBM solar cell. This loss in $I_{SC}$ with Ag recombination layers has already been reported for organic tandem solar cells and could be caused by the reduced transmittance of the Ag interlayer in the wavelength range of 400-800 nm.[188] The hybrid-organic tandem solar cell with a single PEDOT:PSS interlayer showed a $V_{OC}$ of about 0.69 V, which was higher than the $V_{OC}$ of the single cells, but far away from the theoretical possible value, the sum of both $V_{OC}$s. The $I_{SC}$ of the tandem device reaches almost the $I_{SC}$ of the hybrid single solar cells, and was doubled compared to the tandem cell with the Ag/PEDOT:PSS layer. The best performance could be realised with a tandem device comprising a $TiO_x$/PEDOT:PSS recombination layer. The $V_{OC}$ with 0.90 V was slightly lower than the sum of the $V_{OC}$s of the single cells (PSiF-DBT/CIS: 0.44 V and PTB7/PCBM: 0.56 V) but the $I_{SC}$ (8.04 mA/$cm^2$) also catches up with the value of the PSiF-DBT/CIS hybrid cells leading to a power conversion efficiency of 4.1%.

To complete the series, we have also investigated a combined Ag/$TiO_x$/PEDOT:PSS interlayer. However, the tandem solar cells show the same solar cell characteristics as those prepared with the Ag/PEDOT:PSS interlayer, high $V_{OC}$s but only half of the theoretical $I_{SC}$ values (see Fig. 74).

Fig. 72 B shows a SEM image of an ion milled cross section of the hybrid-organic tandem cell which showed the best performance (4.1%) in this series. The tandem structure (1: glass; 2: ITO; 3: PEDOT:PSS; 4: PSiF-DBT/CIS; 5: PEDOT:PSS & PTB7/PCBM; 6: Al; 7: protection layer) is precisely visible in the micrograph, the layers are smooth and the PSiF-DBT/CIS layer with a thickness of 80 nm is clearly identifiable. However, it is not possible to distinguish between the different organic materials (PTB7/PCBM and PEDOT:PSS), so the second PEDOT:PSS layer and the subsequent PTB7/$PC_{61}$BM layer appear as one single layer with a thickness of 140 nm. As expected, the $TiO_x$ layer is not visible at all because of its thickness of only 4 nm. Also due to the limited resolution of SEM, the phase separation as well as single nanoparticles are not identifiable. However, TEM images from equally prepared PSiF-DBT/CIS absorber layers presented in a previous publication,[15] show that copper indium sulphide nanoparticles of approx. 5 nm are formed in the polymer matrix and no larger agglomerates are present in the layer. Additionally to SEM characterisation, we used a surface profiler to determine the accurate layer thicknesses. The measured values match well with the results of the SEM investigation of the cross section. The PSiF-DBT/CIS layer exhibit a thickness of 60-80 nm, the PTB7/PCBM layer has a thickness of 90-110 nm, the PEDOT:PSS layer of the bottom cell has a thickness of 50-60 nm and the one of the top cell 20-30 nm. From these first results it can be concluded that tandem solar cells with PCEs of 5% should be achievable by further optimisation and loss-free series connection of the two single cells. The best tandem solar cell we obtained in our experiments so far, uses a $TiO_x$/PEDOT:PSS recombination layer and shows a power conversion efficiency of 4.1%, which is 82% of the theoretically possible value.

To go one step further, in a second series, we investigated tandem solar cells with two PSiF-DBT/CIS absorber layers to show a first example of a hybrid-hybrid tandem solar cell. As mentioned above, this approach is challenging because the absorber layers are prepared via an *in situ* method, in which thermal annealing is required for the fabrication of both absorber layers, leading to additional thermal stress for the bottom cell during the production process of the top cell. Preliminary tests on single cells have shown that a second annealing step does not significantly decrease the solar cell performance, thus, *in situ* prepared hybrid-hybrid tandem solar cells should be realisable by applying the same conversion parameters (15 min from 30 °C to 195 °C, 15 min 195 °C) for both absorber layers. So we prepared a series of

hybrid-hybrid tandem solar cells using the same interlayer combinations, tested in the first series. The IV curves of all these tandem solar cells are presented in Fig. 75 A.

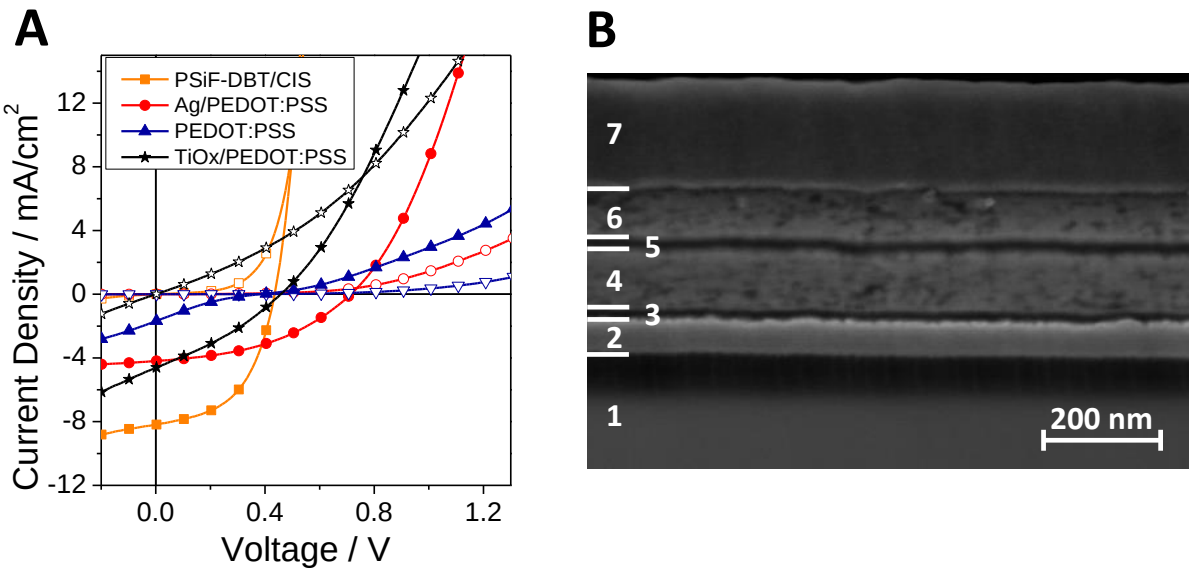


**Fig. 75 A: IV curves of hybrid-hybrid tandem cells with different interlayers; B: SEM image of the ion milled cross section of a typical hybrid-hybrid tandem solar (1: glass; 2: ITO; 3: PEDOT:PSS; 4: PSiF-DBT/CIS; 5: PEDOT:PSS; 6: PSiF-DBT/CIS; 7: Ag(2 nm, not visible)/Al).**

Although the $TiO_x$/PEDOT:PSS interlayer exhibited the best performance in the hybrid-organic tandem cell, this interlayer did not lead to properly working hybrid-hybrid tandem solar cells. The two subcells were not successfully connected in series which was revealed by the low open circuit voltage of only 0.46 V of the tandem device, which matches with the $V_{OC}$ of the PSiF-DBT single cell. Furthermore, the $I_{SC}$ exhibited a value of 4.60 mA/cm$^2$ which is only 50% of the $I_{SC}$ of the hybrid single cell and the FF decreased to a value of 0.32 leading to a PCE of only 0.7%. One possible explanation for that may be that the $TiO_x$ layer is not stable in the thin layer during the annealing step of the hybrid top cell. The pure PEDOT:PSS interlayer exhibited an even lower $V_{OC}$ of 0.38 V compared to the single cells, a drop in $I_{SC}$ to 1.68 mA/cm$^2$ and a FF of only 0.18, which stems from a S-shaped curve in the IV characteristic of the light exposed cell. Similar S-shaped curves were also already observed in the literature for tandem solar cells using only PEDOT:PSS as interlayer.[181,182]

However, with an Ag/PEDOT:PSS interlayer well working hybrid-hybrid tandem solar cells, exhibiting an increase in $V_{OC}$ up to 81% of the sum of the $V_{OC}$s of the single cells, were achieved. Fig. 5A shows the IV characteristics of the single cell in comparison with the different tandem cell approaches under 100 mW/cm$^2$ illumination. Although the $V_{OC}$s of the single cells are nearly added, the $I_{SC}$ (4.19 mA/cm$^2$) as well as FF (0.42) decreased, compared to the single cells, which led to an efficiency of the hybrid-hybrid tandem solar cell of 1.3%.

Fig. 75 B shows a SEM image of an ion milled cross section of a typical hybrid-hybrid tandem solar cell consisting of two PSiF-DBT/CIS subcells. The arrangement of the different layers, except of the several nm thick Ag-interlayers, are clearly visible in this image (glass / ITO / PEDOT:PSS / PSiF-DBT/CIS / Ag(not visible) / PEDOT:PSS / PSiF-DBT/CIS / Ag(not visible) / Al). However, the layers seem to be very homogeneous and smooth with thicknesses of 80-100 nm for the PSiF-DBT/CIS layers and 15 nm for the PEDOT:PSS layers determined from the cross section, although the first active layer has to undergo thermal treatment twice.

To improve the efficiency of *in situ* prepared hybrid-hybrid tandem solar cells it is necessary to do further research in order to find a suitable recombination layer which is not affected by the thermal treatment of the top cell and does not limit the $I_{SC}$ and FF. To further enhance the $I_{SC}$ and thus the PCE it is also necessary to use two different absorber layers so that the absorption of the tandem solar cell is extended. With this hybrid-hybrid tandem approach, it is possible to tune the overall absorption of hybrid tandem solar cells with four components, the two polymers and two different inorganic semiconductors e.g. P3HT/CdS[88], PDTPBT/PbS[112] which opens a huge playground for further research.

### 2.1.3 Conclusion

In summary, we have successfully prepared hybrid-organic as well as hybrid-hybrid tandem solar cells and we compared the effects of different recombination layers on the device performance. The solar cell characteristics indicate that the $TiO_x$/PEDOT:PSS interlayer can provide an efficient recombination region in hybrid-organic solar cells, leading to a hybrid-organic tandem cell with a $V_{OC}$ of 0.90 V, which is 91% of the sum of the subcell $V_{OC}$ values. The $I_{SC}$ seems to be limited by the single cell with the lower $I_{SC}$ value reaching a PCE of 4.1% which is an increase in device performance compared to the single cells.

In contrast to this, $TiO_x$/PEDOT:PSS is not a suitable recombination layer for the hybrid-hybrid tandem device, as here this interlayer does not lead to an increase in $V_{OC}$ compared to the single cells. The Ag/PEDOT:PSS interlayer showed the best performance in this case. As in the hybrid-organic tandem solar cell also in the hybrid-hybrid device, this interlayer exhibited the highest $V_{OC}$ but only approximately the half of the $I_{SC}$ of the single hybrid cell is maintained in the tandem structure. Nevertheless, first working hybrid-hybrid tandem solar cells were obtained, showing a power conversion efficiency of 1.3%. The $V_{OC}$ of the single cells is nearly doubled. However, the quite low $I_{SC}$ provides the necessity for further improvement of the recombination layer. The SEM pictures of the two tandem device architectures showed smooth layers indicating that in the hybrid-hybrid device the second heating step did not

significantly affect the morphology. This study opens up a new direction in research on tandem solar cells, as the presented concept of hybrid-hybrid tandem solar cells provides the potential for further enhancement of light absorption by the usage of two organic and two inorganic semiconducting materials with complementary absorption profiles in two absorber layers.

## 2.2 Additional interlayer investigation

Additional to the results published in RCS Advances, a $Cs_2CO_3$/Ag interlayer was inquired, due to the promising results $Cs_2CO_3$ achieved as an anode interlayer in P3HT/PCBM solar cells, where the power conversion efficiency could be increased from 2.3% to 3.1%.[189] This interlayer was tested in a tandem solar cell with the following device architecture: glass/ITO/PEDOT:PSS/PSiF-DBT:CIS/$Cs_2CO_3$/Ag/$V_2O_5$ /PCPDTBT:PCBM/Al. $V_2O_5$ was employed as hole collecting layer instead of PEDOT:PSS, due to the fact, that the PEDOT:PSS solution is aqueous and could therefore harm solar cell performance. For the $V_2O_5$ interlayer a method described by K. Zilberberg et al.[190] was adopted. They used a liquid based process with a vanadium-oxitriisopropoxide/isopropyl alcohol solution as a precursor, which was converted into $V_2O_5$ by storing it 1h at ambient conditions. Their method was modified by changing the coating conditions from spin coating to doctor blading, and in a first series different conversion conditions in a tandem device-type A were tested, using PSiF-DBT:CIS as bottom cell and PCPDTBT:PCBM as top cell. $V_2O_5$ interlayers prepared at ambient conditions were compared to $V_2O_5$ interlayer fabricated at inert conditions, the latter being only exposed to air for 20 s. Fig. 76 shows the IV characteristics of the different device architectures.

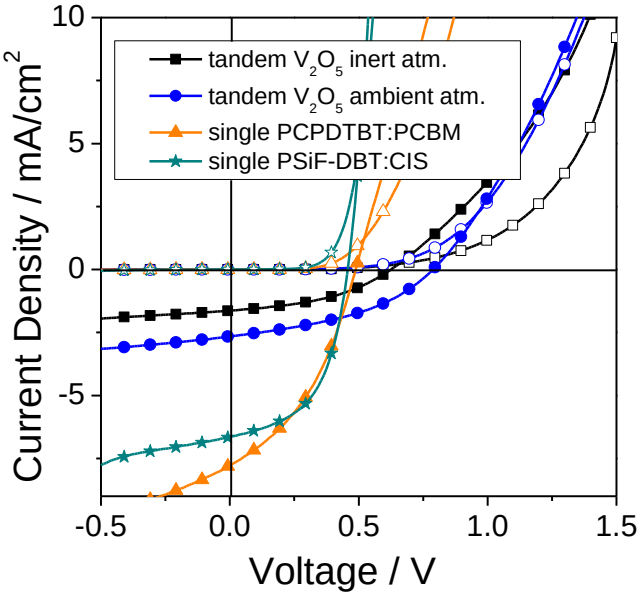


**Fig. 76: IV characteristics of the single cells in comparison to the hybrid-organic tandem cells with two different $V_2O_5$ hole conducting interlayer preparations in the dark and under 100 mW/cm$^2$ illumination.**

**Table 11: Characteristic parameters of PSiF-DBT:CIS, PCPDTBT:$PC_{61}$BM solar cells and hybrid-organic tandem solar cells, depending on $V_2O_5$ preparation methode.**

| | | $V_{OC}$ / V | $I_{SC}$ / mA/cm$^2$ | FF | Eff / % |
|---|---|---|---|---|---|
| **Single** | PSiF-DBT:CIS | 0.46 | 6.64 | 0.53 | 1.6 |
| | PCPDTBT:$PC_{61}$BM | 0.49 | 7.77 | 0.40 | 1.5 |
| **Tandem** | $V_2O_5$ inert atm. | 0.63 | 1.63 | 0.42 | 0.43 |
| | $V_2O_5$ ambient atm. | 0.79 | 2.66 | 0.41 | 0.86 |

The hybrid single solar cell (PSiF-DBT:CIS) exhibited an open circuit voltage ($V_{OC}$) of 0.46 V, a short circuit current density ($I_{SC}$) of 6.64 mA/cm$^2$ , a fill factor (FF) of 0.53 and a PCE of 1.6%. The organic single cell (PCPDTBT:$PC_{61}$BM) revealed a $V_{OC}$ of 0.49 V, a $I_{SC}$ of 7.77 mA/cm$^2$, a FF of 0.40 and a PCE of 1.5%. The obtained efficiency for the PCPDTBT/$PCB_{61}$M solar cells is lower in contrast to recently reported PCE values for PCPDTBT fullerene solar cells (3.7%, 4.62%),[191,192] but this can be explained due to the fact, that we used $PC_{61}$BM instead of $PC_{71}$BM and that we didn't use any solvent additives, which are required for these high efficiencies. Y. Gu et al[192] reported PCPDTBT/PCBM solar cells with and without different solvent additives; the solar cell without solvent additives exhibited a power conversion efficiency of 1.7%, which is quite similar to our achieved power conversion efficiency of 1.5%. The tandem device with the $V_2O_5$ hole conducting layer prepared at inert conditions showed a small increase in $V_{OC}$ of 100 mV compared to a tandem device with the $V_2O_5$ hole conducting layer prepared at ambient conditions which exhibited an increase in $V_{OC}$ of 83% of the sum of the $V_{OC}$s of the single cells.

The $I_{SC}$ of the tandem solar cell with the $V_2O_5$ interlayer prepared at inert conditions is about 60% smaller than the $I_{SC}$ of the tandem device with the $V_2O_5$ interlayer prepared at ambient conditions. This leads to an overall power conversion efficiency, which is 50% lower than the power conversion efficiency of the tandem solar cell with the $V_2O_5$ interlayer prepared at ambient conditions. The fill factor of the tandem device seems to be limited by the fill factor of the PCPDTBT:PCBM solar cell. Nevertheless both tandem devices exhibited a drop in $I_{SC}$ of over 50% compared to the PSiF-DBT:CIS single device, which is the same result achieved for Ag and TiOx/Ag interlayers, caused by the reduced transmittance of the Ag interlayer in the wavelength range of 400-800 nm.[188]

## 2.3 Attempts for the efficiency improvement in hybrid-hybrid solar cells

As mentioned above, to further enhance the $I_{SC}$ and thus the PCE it is necessary to use two different absorber layers so that the absorption of the tandem solar cell is extended. Hybrid-hybrid tandem solar cells provide the potential for further enhancement of light absorption by the usage of two organic and two inorganic semiconducting materials with complementary absorption profiles in two absorber layers. Solar cells with various inorganic acceptor materials were investigated in the first chapter of this thesis, achieving low power conversion efficiencies. Therefore, the main focus was set on finding a suitable donor polymer for CIS/polymer nanocomposite solar cells.

### 2.3.1 Investigation of suitable polymers for the top solar cell in hybrid-hybrid tandem solar cells

In order to select two different polymers with two complementary absorption spectra, the absorption of twelve polymers was measured, which is shown in Fig. 77.

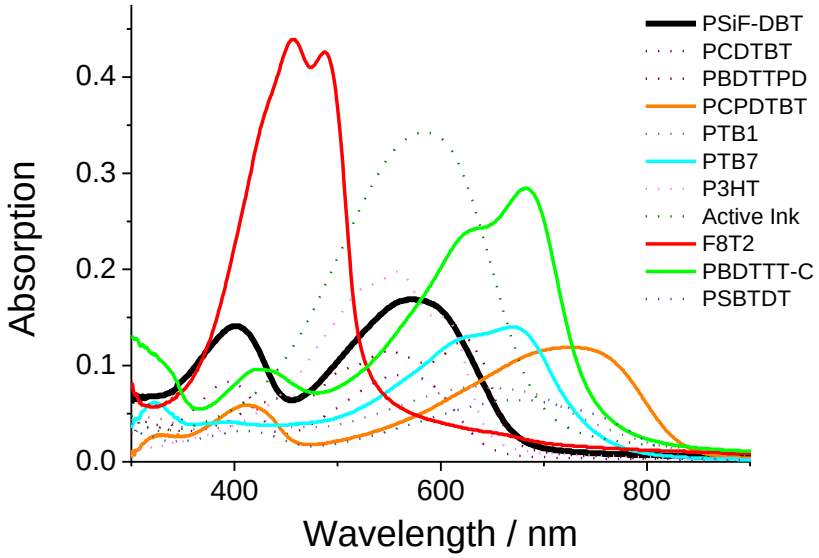


**Fig. 77: Absorption spectra of different conjugated polymers.**

Due to the fact, that the best performing hybrid solar cell prepared by our research group consists of a PSiF-DBT/CIS active layer, this solar cell was chosen as a bottom cell in most of the tandem devices. PSiF-DBT exhibits two absorption maxima, the first one reveals at 400 nm and the second one at 570 nm. Most of the measured polymers show an absorption overlap with PSiF-DBT and are therefore not suitable as active layer, for the top cell. PCDTBT for example, shows nearly the same absorption behaviour as PSiF-DBT with two absorption maxima at 394 nm and 562 nm. Other polymers, which are not suitable for the top solar cell are PBDTTPD ($\lambda_{max}$ = 624 nm), PTB1 ($\lambda_{max}$ = 639 nm), P3HT ($\lambda_{max}$ = 558 nm), Active Ink ($\lambda_{max}$ = 585 nm) and PSBTBT ($\lambda_{max}$ = 412 nm and 675 nm). Suitable polymers for our top solar cell are PCPDTBT ($\lambda_{max}$ = 411 nm and 724 nm), PTB7 ($\lambda_{max}$ = 670 nm), F8T2 ($\lambda_{max}$ =457 nm) and PBDTTT-C ($\lambda_{max}$ = 423 nm and 683 nm).

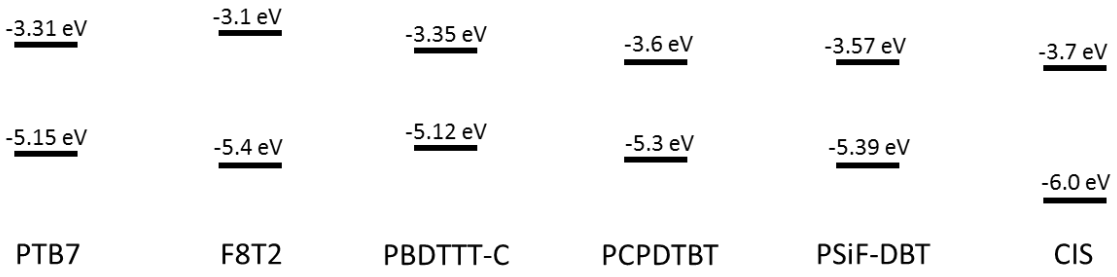


**Fig. 78: Band alignment within a polymer/CIS nanocomposite solar cell. The energy positions of the semiconductor band edge are taken from literature (PTB7[141], F8T2[193], PBDTT-C[194], PCPDTBT[191], PSiF-DBT[142], CIS[143]).**

From the energy alignment (Fig. 78) it can be seen, that all considered polymers exhibit a similar band structure to PSiF-DBT. Thus, efficient heterojunction between CIS and polymers should be formed, allowing exciton dissociation due to the sufficient large offset between HOMO and LUMO levels of the polymer and the CIS phase. The maximum open circuit voltage can be calculated due to the difference between the HOMO and LUMO levels of the polymer and the CIS phase. The maximum open circuit voltage can be obtained with F8T2:CIS (1.70 eV) and PSiF-DBT:CIS (1.66 eV) heterojunctions, followed by PCPDTBT:CIS (1.6 eV). PTB7:CIS and PBDTTT-C:CIS feature a slightly lower maximum open circuit voltage of 1.45 eV and 1.42 eV respectively. Nevertheless, usually lower open circuit voltages are achieved, because the differences between the work functions of the electrodes can also influence the $V_{OC}$.

To fabricate hybrid-hybrid solar cells with different active layers for the bottom and the top solar cell we investigated PCPDTBT:CIS and PBDTTT-C:CIS single solar cells (polymer structures are shown in Fig. 79).

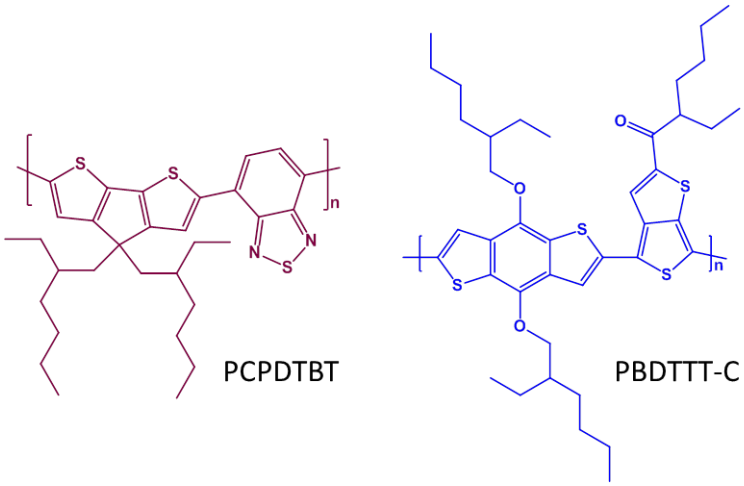


**Fig. 79: Structures of the different polymers used for the fabrication of single polymer/CIS solar cells.**

## 2.3.2 Single device testing

### *2.3.2.1 PCPDTBT : CIS*

Poly[2,6-(4,4-bis(2-ethylhexyl)-4H-cyclopenta[2,1-b;3,4-b']-dithiophene)-alt-4,7-(2,1,3-benzothiadiazole)] (PCPDTBT) is a common low band gap polymer used in organic solar cells in combination with PCBM with a power conversion efficiency of 4.6% ($V_{OC}$ = 0.62 V, $I_{SC}$ = 14.9 mA/cm$^2$, FF = 50%)[192]. It exhibits an optical band gap of 1.5 eV and can extend the spectral absorption profile into the infrared region.[195,196] With a HOMO of -5.3 eV and a LUMO of -3.75 eV the electrochemical properties are very similar to the properties of PSiF-DBT (HOMO =

-5.39, LUMO = -3.75), which leads to the assumption, that PCPDTBT:CIS solar cells can work properly.

A lot of parameters have to be considered in the investigation of a new donor material, such as polymer concentration, ratio of donor to acceptor material, stability during the thermal conversion step, thickness of the active layer, etc. In this contribution, different donor to acceptor ratios and different layer thicknesses were investigated in order to achieve working solar cells. The influence of the donor to acceptor weight ratios on the parameters $V_{OC}$, $I_{SC}$ and power conversion efficiency are shown in Fig. 80.

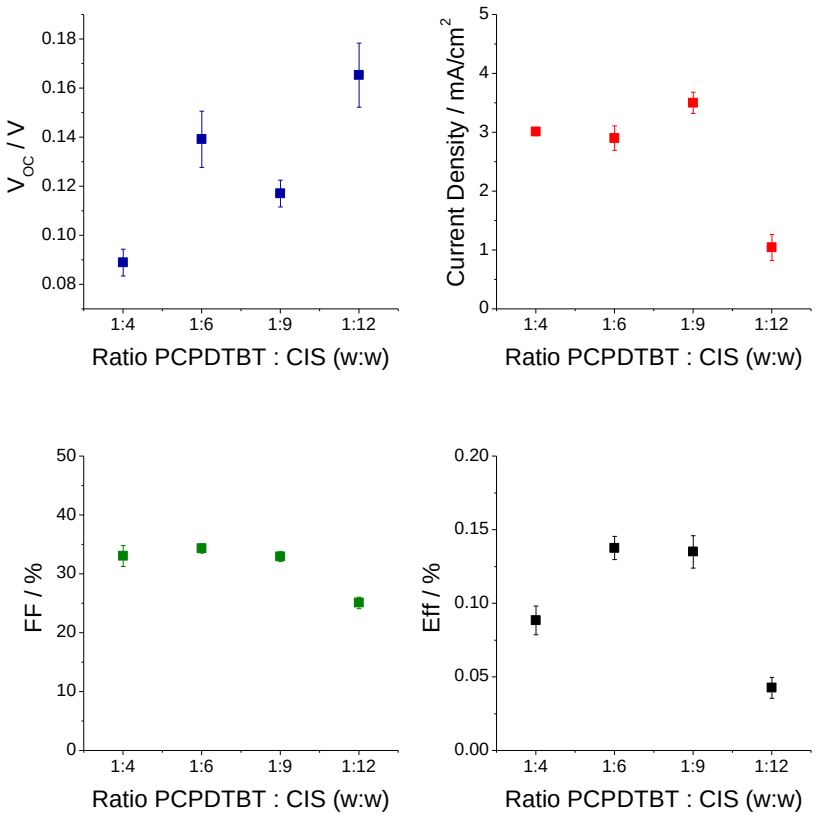


**Fig. 80: Influence of the PCPDTBT/CIS weight ratio on the parameters $I_{SC}$, $V_{OC}$, FF and efficiency of PCPDTBT/CIS hybrid solar cells (mean values of 5 best devices).**

$I_{SC}$ shows maximum values (approx. 3.65 mA/cm²) at PCPDTBT : CIS weight ratios of 1:9. The highest values for the $V_{OC}$ (173 mV) are observed at a ratio of 1:12. Fill factors are between 30 and 35% for all weight ratios, except for the solar cells with weight ratios of 1:12, which exhibit lower fill factors around 25%. This leads to a broad maximum of the solar cell efficiencies at weight ratios of 1:6 and 1:9. At these ratios low efficiencies of 0.138% are reached, while at

ratios of 1:4 and 1:12 efficiencies of only 0.09 and 0.04% are observed. Especially due to the very low open circuit voltage, the PCPDTBT : CIS nanocomposite layer is not suitable for the fabrication of tandem devices.

### *2.3.2.2 PBDTTT-C : CIS*

PBDTTT-C is a low band gap polymer with a HOMO of -5.12 eV and a LUMO of -3.35 eV[194] and a derivate of poly[4,8-bis-substituted-benzo[1,2-b:4,5-b0]dithiophene-2,6-diyl-alt-4-substituted-thieno[3, 4 b]thio-phene-2,6-diyl]. Solar cells consisting of PBDTTT-C and PCBM achieve power conversion efficiencies up to 6.3% ($V_{OC}$ = 700 mV, $I_{SC}$ = 14.7 mA/$cm_2$, FF = 64%)[197]. Thus, it is an interesting donor material for nanocomposite CIS solar cells. Solar cells with different polymer to inorganic ratios and different layer thicknesses were investigated; the power conversion parameters are shown in Fig. 81.

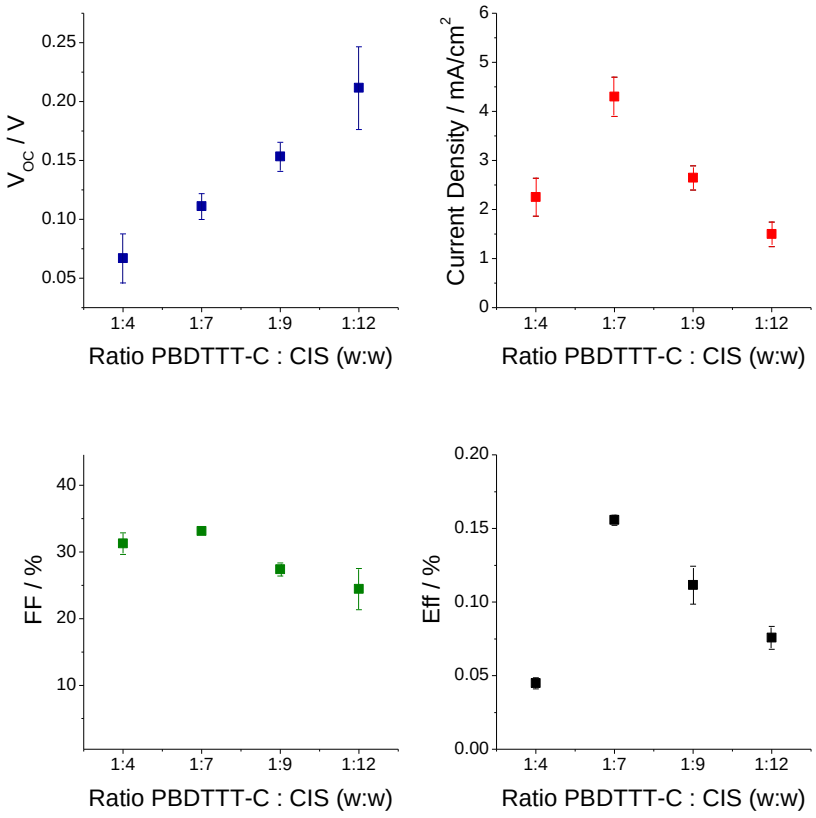


**Fig. 81: Influence of the PBDTTT-C/CIS weight ratio on the parameters $I_{SC}$, $V_{OC}$, FF and efficiency of PBDTTT-C/CIS hybrid solar cells (mean values of 5 best devices).**

The highest $I_{SC}$ of 4.62 mA/cm$^2$ was achieved at a polymer to inorganic ratio of 1:7. The solar cell with a PBDTTT-C : CIS ratio of 1:9 exhibited the highest $V_{OC}$ of 173 mV, which is still very low, compared to our standard device PSiF-DBT:CIS, which shows $V_{OC}$ values up to 0.5 V. The solar cells exhibited fill factors between 27-33% for all devices, leading to a clear maximum for power conversion efficiency of 0.16% at a donor : acceptor ratio of 1:7.

Due to the low efficiencies achieved, no tandem solar cells were fabricated containing these single cells.

## 2.4 Conclusion

In a first attempt, different recombination layers were investigated for the preparation of tandem devices. For the fabrication of *in situ* prepared hybrid-hybrid tandem solar cells, the challenge of a second annealing step of the bottom cell has to be overcome. Thus, this issue was separated from the topic of finding a suitable recombination layer, due to the fabrication of hybrid-organic solar cells. Ag/PEDOT:PSS, TiOx/Ag/PEDOT:PSS, TiOx/PEDOT:PSS, PEDOT:PSS and $Cs_2CO_3$/Ag/$V_2O_5$ were investigated in hybrid-organic tandem devices. All tandem solar cells including Ag in their recombination layer, achieved high open circuit voltages but exhibited a drastically trop in $I_{SC}$. PEDOT:PSS did not provide an efficient recombination region in tandem solar cells. The most promising results were achieved for TiOx/PEDOT:PSS interlayer which provide an efficient recombination region in hybrid-organic solar cells, leading to a hybrid-organic tandem cell with a $V_{OC}$ of 0.90 V, which is 91% of the sum of the subcell $V_{OC}$ values. Nevertheless, the TiOx/PEDOT:PSS interlayer is no suitable recombination layer for the hybrid-hybrid tandem device, as it does not lead to an increase in $V_{OC}$ compared to the single cells. First working hybrid-hybrid tandem solar cells with Ag/PEDOT:PSS interlayer were obtained, revealing a nearly doubled $V_{OC}$ of the single cells. However, the quite low $I_{SC}$ provides the necessity for further interlayer improvement. Nevertheless, the SEM picture showed smooth layers indicating that the second heating step did not significantly affect the morphology of the hybrid-hybrid tandem solar cell (Fig. 75 B). Furthermore in order to fabricate hybrid-hybrid tandem solar cells with different active layers for the bottom and the top solar cell PCPDTBT:CIS and PBDTTT-C:CIS single solar cells were investigated in the next step. Nevertheless, only poor power conversion efficiencies could be achieved. Therefore, these polymers were not used for the fabrication of hybrid-hybrid tandem solar cells.

In summary, we have successfully prepared hybrid-organic as well as hybrid-hybrid tandem solar cells and we compared the effects of different recombination layers on the device performance.

# IV Experimental

## 1 Materials

A list of the chemicals and solvents used, including their purity grade can be found in Table 12. All chemicals and solvents were purchased from Sigma Aldrich and used without any further purification.

**Table 12: Chemicals and solvents used for xanthate synthesis.**

| Chemicals / Solvents | Purity grade and Description | supplier |
|---|---|---|
| Acetone | Puriss. | Sigma Aldrich |
| Active Ink | - | Polyera |
| Antimony (III) chloride | 99% | ABCR |
| Bismuth (III) chloride | ≥98% | Sigma Aldrich |
| Carbon disulfide ($CS_2$ ) | ≥ 99.9% | Sigma Aldrich |
| Cesium carbonate | | Sigma Aldrich |
| Chlorobenzene (CB) | 99.4% | Sigma Aldrich |
| Chloroform ($CHCl_3$ ) | puriss. | Sigma Aldrich |
| Cobalt (II) chloride | ≥98% | Sigma Aldrich |
| Cu-Hep | - | Aglycon |
| Diethyl ether ($Et_2O$) | puriss., stabilized | Sigma Aldrich |
| 3,3-Dimethyl-2-butanol | 98% | Sigma Aldrich |
| 2,2-Dimethyl-3-pentanol | 97% | Sigma Aldrich |
| Dynol$^{TM}$ | 604 Surfactant | AIR Products |
| Ethanol (EtOH) | Puriss. | Sigma Aldrich |
| F8T2 | ADS2008P | ADS |
| In-Hep | - | Aglycon |
| Lead (II) acetate trihydrate | ≥99% | Sigma Aldrich |
| MEH-PPV | 541443-1G | Sigma Aldrich |
| Methanol (MeOH) | puriss. | Sigma Aldrich |
| Nickel (II) chloride | 98% | ABCR |
| PBDTTT-C | - | Solamer |
| PBDTTPD | OS0751 | One Material |
| $PC_{61}BM$ | - | Solenne |
| PCDTBT | OS0502 | One Material |
| PCPDTBT | OS0340 | One Material |
| PEDOT:PSS | - | HC Starck |
| PMMA | - | Sigma Aldrich |
| Potassium ethyl xanthate | 96 % | Sigma Aldrich |
| Potassium-tert-butoxide (t-BuOK) | purum, ≥ 97% | Sigma Aldrich |
| PSBTBT | OS1001 | One Material |
| PSiF-DBT | OS0927 | One Material |
| PTB1 | 340 | One Material |
| PTB7 | OS0007 | One Material |
| P3HT | Sepiolid P200 | Rieke |
| Tetrahydrofuran (THF) | anhydrous ≥ 99.9% | Sigma Aldrich |
| Titanium diisopropoxide bis (acetylacetonate) | 75 wt.% in isopropanol | Sigma Aldrich |
| Vanadium (V) oxyisopropoxide | - | Sigma Aldrich |

# 2 Metal xanthates as precursors for metal sulphides in solar cell applications

## 2.1 Xanthate synthesis

### 2.1.1 General procedure for potassium-xanthates:

The potassium xanthates were prepared following a procedure, described by Alex Schenk.[125] Potassium *tert*-butoxide was dissolved in THF and cooled to 0 °C under an argon flow. Afterwards 3,3-dimethyl-2-butanol for K-Hex (2,2-dimethyl-3-pentanol for K-Hep) was added slowly under stirring and after several minutes carbon disulphide was added dropwise. The reaction mixture was stirred for 5 hours before the solution was diluted with diethyl ether. The resulting solid was dried in vacuum before it was dissolved again in refluxing acetone to remove insoluble side products. The acetone phase was concentrated by rotary evaporation before the product was precipitated with diethyl ether. The yellowish-white powder was separated by filtration and dried in vacuum.

#### *2.1.1.1 Potassium(I)hexyl-xanthate: Potassium O-3,3-dimethylbutan-2-yl dithiocarbonate*

**Table 13: Weighed portion of the reactants for the synthesis of K-Hex.**

| | MW / g*mol$^{-1}$ | mass/ g | density/ g*mL$^{-1}$ | volume/ mL | mol. am./ mmol | equiv. | THF / mL |
|---|---|---|---|---|---|---|---|
| **3,3-dimethyl-3-butanol** | 116.22 | 15.00 | 0.82 | 18.3 | 146.8 | 1.10 | - |
| **$^{t}$BuOK** | 112.22 | 14.98 | - | - | 133.45 | 1.00 | 253.50 |
| **$CS_2$** | 76.14 | 11.28 | 1.27 | 8.9 | 148.13 | 1.11 | - |

Yield: 18.3 g, (76%)

$^{1}$H-NMR (300 MHz, 20 °C, acetone-$d_6$, in ppm): 5.43 - 5.36 (q, 1H, CH), 1.11 – 1.09 (d, 3H, CH$\underline{C}H_3$), 0.91 (s, 9H, C($\underline{C}H_3$)$_3$)ppm. $^{13}$C-NMR (75 MHz, 20 °C, acetone-$d_6$, in ppm): 233.65 ($CS_2O$), 84.36 (CH), 35.32 ($\underline{C}(CH_3)_3$), 26.46 (C($\underline{C}H_3$)$_3$), 14.77 (CH$\underline{C}H_3$)ppm.

IR (on Si, in cm-1): 2963, 2870, 1474, 1456, 1393, 1377, 1363, 1223, 1208, 1133, 1101, 1085, 1066, 1030, 985.

Elementary analysis for $C_7H_{13}S_2OK$: calculated: C 38.85, H 6.05, S 29.63; found: C 38.75, H 6.10, S 29.74.

#### *2.1.1.2 Potassium(I)heptyl-xanthate: Potassium O-2,2-dimethylpentan-3-yl dithiocarbonate*

**Table 14: Weighed portion of the reactants for the synthesis of K-Hep.**

| | MW / g*mol$^{-1}$ | mass / g | density / g*mL$^{-1}$ | volume / mL | mol. am./ mmol | equiv. | THF / mL |
|---|---|---|---|---|---|---|---|
| **2,2-dimethyl-3-pentanol** | 116.22 | 15.00 | 0.82 | 18.3 | 129.07 | 1.10 | - |
| **$^{t}$BuOK** | 112.22 | 13.17 | - | - | 117.33 | 1.00 | 222.93 |
| **$CS_2$** | 76.14 | 9.92 | 1.27 | 7.8 | 130.24 | 1.11 | - |

Yield: 20.2 g, (68%)

$^{1}$H-NMR (300 MHz, 20 °C, acetone-$d_6$, in ppm): 5.64-5.59 (dd, 1H, CH), 1.68-1.46 (d, 3H, $CH\underline{C}H_2$), 0.93-0.89 (s, 9H, $C(\underline{C}H_3)_3$)ppm. $^{13}$C-NMR (75 MHz, 20 °C, acetone-$d_6$, in ppm): 235.40 ($CS_2O$), 88.68 (CH), 36.19 ($\underline{C}(CH_3)_3$), 26.77($C(\underline{C}H_3)_3$), 24.11 ($\underline{C}H_2$), 11.63 ($CH_2\underline{C}H_3$)ppm.

IR (on Si, in cm$^{-1}$): 2964, 2872, 1479, 1457, 1393, 1382, 1365, 1231, 1205, 1140, 1109, 1070, 1042, 1021, 951 cm$^{-1}$.

Elementary analysis for $C_8H_{15}S_2OK$: calculated C 41.70, H 6.56, S 27.83; found: C 41.70, H 6.59, S 26.38.

### 2.1.2 General procedure for Bi(III)-xanthates

Bismuth (III) chloride was dissolved in deion. water. A solution of potassium(I)-xanthate in deion. water was added dropwise under stirring and a sticky brown solid formed immediately. After the reaction solution was stirred for 3 hours, the brown precipitate was filtered off and dried under vacuum. The residue was dissolved in chloroform and the insoluble side products were removed by filtration. After recrystallization (chloroform) orange crystals were obtained which were dried in vacuum.

#### *2.1.2.1 Bismuth(III)ethyl-xanthate: Bismuth(III) ethyl dithiocarbonate*

**Table 15: Weighed portion of the reactants for the synthesis of Bi-Et.**

| | MW / g*mol$^{-1}$ | mass / g | molar amount /mmol | equiv. | $H_2O$ / mL |
|---|---|---|---|---|---|
| **$BiCl_3$** | 315.34 | 1.00 | 3.17 | 1.0 | 30 |
| **K-Et** | 160.30 | 1.64 | 10.23 | 3.2 | 10 |

Yield: 0.76 g, (42%)

$^{1}$H NMR (300 MHz, 20°C, $CDCl_3$,δ): 4.76-4.68 (q, 2H, $CH_2$), 1.55-1.49 (t, 3H, $CH_3$) ppm. $^{13}$C NMR (75 MHz, 20 °C, $CDCl_3$, δ): 225.99 ($CS_2O$), 71.36 ($CH_2$), 13.90($CH_3$) ppm.

FT-IR (ATR in $cm^{-1}$): 2977, 1443, 1359, 1179, 1107, 1003.

Elementary analysis for $BiS_6O_3C_9H_{15}$: calculated: C 18.88, H 2.64, S 33.60; found: C 18.96, H 2.17, S 33.95.

#### 2.1.2.2 *Bismuth(III)hexyl-xanthate: Bismuth (III) O-3,3-dimethylbutan-2-yl dithiocarbonate*

**Table 16: Weighed portion of the reactants for the synthesis of Bi-Hex.**

| | MW / g*mol$^{-1}$ | mass / g | molar amount /mmol | equiv. | $H_2O$ / mL |
|---|---|---|---|---|---|
| **$BiCl_3$** | 315.34 | 3.64 | 11.6 | 1.0 | 125 |
| **K-Hex** | 216.41 | 8.00 | 37.0 | 3.2 | 40 |

Yield: 7,1 g, (83%)

$^{1}$H NMR (300 MHz, 20°C, $CDCl_3$,δ): 5.43-5.36 (dd, 1H, CH), 1.11-1.09 (d, 3H, $CHCH_3$), 0.91 (s, 9H, 3x $C(CH_3)_3$)ppm. $^{13}$C NMR (75 MHz, 20 °C, $CDCl_3$, δ): 233.65 ($CS_2O$), 84.36 (CH), 35.32 ($C(CH_3)_3$), 26.46($C(CH_3)_3$), 14.77($CH\text{-}CH_3$)ppm.

FT-IR (ATR in $cm^{-1}$):2963, 2870, 1474, 1456, 1393, 1377, 1363, 1223, 1208, 1133, 1101, 1085, 1066, 1030, 985 $cm^{-1}$.

Elementary analysis for $Bi_2S_{12}O_6C_{42}H_{78}$: calculated: C 38.85, H 6.05, S 29.63; found: C 38.75, H 6.10, S 29.74.

#### 2.1.2.3 *Bi(III)heptyl-xanthate: Bismuth(III) O-2,2-dimethylpentan-3-yl dithiocarbonate*

**Table 17: Weighed portion of the reactants for the synthesis of Bi-Hep.**

| | MW / g*mol$^{-1}$ | mass / g | molar amount /mmol | equiv. | $H_2O$ / mL |
|---|---|---|---|---|---|
| **$BiCl_3$** | 315.34 | 3.02 | 9.59 | 1.0 | 125 |
| **K-Hep** | 230.43 | 7.00 | 30.7 | 3.2 | 40 |

Yield: 6.1 g, (81%)

$^{1}$H NMR (300 MHz, 20°C, $CDCl_3$,δ): 5.64-5.59 (dd, 1H, CH), 1.68-1.46 (m, 2H, $CH_2$), 0.93-0.89 (s, 12H, $CH_3$) ppm. $^{13}$C NMR (75 MHz, 20 °C, $CDCl_3$, δ): 227.08 ($CS_2O$), 96.40 (CH), 35.90 ($\underline{C}(CH_3)_3$), 26.11 ($C(\underline{C}H_3)_3$), 23.19 ($\underline{C}H_2$), 11.07 ($CH_2\underline{C}H_3$) ppm.

FT-IR (ATR in $^{cm-1}$): 2969, 2875, 1478, 1467, 1397, 1367, 1340, 1232, 1211, 1128, 1081, 1052, 1026, 902 $cm^{-1}$.

Elementary analysis for $BiS_6O_3C_{24}H_{45}$: calculated: C 36.85, H 5.80, S 24.60; found: C 35.52, H 5.87, S 24.18.

### 2.1.3 General synthesis for Pb-xanthates

Lead (II) acetate trihydrate was dissolved in deion. water and a solution of potassium xanthate in deion. water was added dropwise under stirring. Concerning Pb-Et and Pb-Hex a white precipitate was obtained, for Pb-Hep a brown solid formed immediately. After the reaction solution was stirred for 2 hours, the precipitate was filtered off and dried under vacuum. The residue was dissolved in chloroform; insoluble side products were removed by filtration and after recrystallization with methanol white needles were obtained which were dried in vacuum. Pb-Et and Pb-Hex complexes are not stable and were not soluble in chloroform anymore after recrystallization. Therefor no further characterizations were made, except FT-IR analysis.

#### *2.1.3.1 Pb(II)ethyl-xanthate: Lead(II) ethyl dithiocarbonate*

**Table 18: Weighed portion of the reactants for the synthesis of Pb-Et.**

| | MW / g*mol$^{-1}$ | mass / g | molar amount /mmol | equiv. | $H_2O$ / mL |
|---|---|---|---|---|---|
| **$Pb(CH_3CO_2)_2$*3$H_2O$** | 379.33 | 1.00 | 2.64 | 1.0 | 10 |
| **K-Et** | 160.30 | 0.93 | 5.8 | 2.2 | 30 |

Yield = 1.1 g (93%)

FT-IR (ATR in $cm^{-1}$): 2981, 1455, 1431, 1358, 1193, 1102, 1006.

#### 2.1.3.2 *Pb(II)hexyl-xanthate: Lead(II) O-3,3-dimethylbutan-2-yl dithiocarbonate*

**Table 19: Weighed portion of the reactants for the synthesis of Pb-Hex.**

| | MW / g*mol$^{-1}$ | mass / g | molar amount /mmol | equiv. | $H_2O$ / mL |
|---|---|---|---|---|---|
| **$Pb(CH_3CO_2)_2$*3$H_2O$** | 379.33 | 1.00 | 2.64 | 1.0 | 20 |
| **K-Hex** | 216.41 | 1.26 | 5.80 | 2.2 | 60 |

Yield = 0.9 g (61%)

FT-IR (ATR in cm$^{-1}$): 2957, 2867, 1451, 1365, 1329, 1231, 1202, 1108, 1070, 1040, 1003, 870.

#### 2.1.3.3 *Pb(II)heptyl-xanthate: Lead(II) O-2,2-dimethylpentan-3-yl dithiocarbonate*

**Table 20: Weighed portion of the reactants for the synthesis of Pb-Hep.**

| | MW / g*mol$^{-1}$ | mass / g | molar amount /mmol | equiv. | $H_2O$ / mL |
|---|---|---|---|---|---|
| **$Pb(CH_3CO_2)_2$*3$H_2O$** | 379.33 | 5.00 | 13.18 | 1.0 | 170 |
| **K-Hep** | 230.43 | 6.71 | 29.00 | 2.2 | 80 |

(Yield: 2.05 g, 26%)

$^1$H NMR (300 MHz, 20°C, $CDCl_3$,δ): 5.49-5.44 (t, 1H, CH), 1.88-1.73 (m, 2H, $CH_2$), 0.98 (s, 12H, $CH_3$) ppm. $^{13}$C NMR (75 MHz, 20 °C, $CDCl_3$, δ): 229.67 ($CS_2O$), 94.24 (CH), 35.90 ($\underline{C}(CH_3)_3$), 26.31 ($C(\underline{C}H_3)_3$), 23.22 ($\underline{C}H_2CH_3$), 11.26 ($CH_2\underline{C}H_3$) ppm.

FT-IR (ATR in cm$^{-1}$): 2963, 2870, 1456, 1389, 1362, 1337, 1188, 1120, 1127, 1076, 1048, 1015, 900.

Elementary analysis for $PbS_4O_2C_{16}H_{30}$: calculated: C 32.58, H 5.13, S 21.74; found: C 32.69, H 4.87, S 22.17.

### 2.1.4 Sb(III)heptyl-xanthate: Antimony(III) O-2,2-dimethylpentan-3-yl dithiocarbonate

Antimony (III) chloride (3.00 g, 13.2 mmol, 1.0 eq) was dissolved in 120 mL of deion. water. A solution of potassium xanthate (9.70 g, 42.0 mmol, 3.2 eq) in 60 mL deion. water was added drop by drop under stirring and a sticky yellowish-orange solid was formed immediately. After

the reaction solution has stirred for 3 hours, the yellowish-orange precipitate was filtered off and dried under vacuum. The residue was dissolved in chloroform and the insoluble side products were removed by filtration. After removing the solvent via rotary evaporation, and further drying in vacuum, orange crystals were obtained (Yield: 4.37 g, 48%).

$^{1}$H NMR (300 MHz, 20°C, $CDCl_3$,δ): 5.39-5.34 (q, 1H, CH), 1.79-1.69 (m, 2H, $CH_2$), 0.96 (s, 12H, $CH_3$) ppm. $^{13}$C NMR (75 MHz, 20 °C, $CDCl_3$, δ): 224.30 ($CS_2O$), 96.88 (CH), 36.26 ($\underline{C}(CH_3)_3$), 26.39 ($C(\underline{C}H_3)_3$), 23.58 ($\underline{C}H_2CH_3$), 11.38 ($CH_2\underline{C}H_3$) ppm.

FT-IR (ATR in cm$^{-1}$): 2966, 2874, 1465, 1360, 1274, 1129, 1080, 1025, 894.

Elementary analysis for $SbS_6O_3C_{24}H_{45}$: calculated: C 41.53, H 6.54, S 27.72; found: C 41.30, H 6.99, S 28.19.

### 2.1.5 Ni(II)heptyl-xanthate: Nickel(II) O-2,2-dimethylpentan-3-yl dithiocarbonate

Nickel (II) chloride (1.00 g, 7.71 mmol, 1.0 eq) was dissolved in 60 mL of deion. water. A solution of potassium xanthate (4.09 g, 17.7 mmol, 2.3 eq) in 20 mL deion. water was added dropwise under stirring and a green solid formed immediately. After the reaction solution has stirred for 2 hours, the olive green precipitate was filtered off and dried under vacuum. The residue was dissolved in chloroform and the insoluble side products were removed by filtration and after recrystallization olive green crystals were obtained which again were dried in vacuum (Yield: 2.1 g, 62%).

$^{1}$H NMR (300 MHz, 20°C, $CDCl_3$,δ): 4.98-5.02 (q, 1H, CH), 1.69-1.74 (t, 2H, $CH_2$), 0.96 (s, 12H, $CH_3$) ppm. $^{13}$C NMR (75 MHz, 20 °C, $CDCl_3$, δ): 229.1 ($CS_2O$), 93.82 (CH), 35.73 ($\underline{C}(CH_3)_3$), 26.07 ($C(\underline{C}H_3)_3$), 22.95 ($\underline{C}H_2CH_3$), 11.10 ($CH_2\underline{C}H_3$) ppm.

FT-IR (ATR in cm$^{-1}$): 2963, 2874, 1465, 1360, 1274, 1129, 1080, 1025, 894.

Elementary analysis for $NiS_4O_2C_{16}H_{30}$: calculated: C 43.67, H 6.87, S 29.15; found: C 43.52, H 7.39, S 29.46.

### 2.1.6 Co(II)heptyl-xanthate: Cobalt(II) O-2,2-dimethylpentan-3-yl dithiocarbonate

Cobalt (II) chloride (1.04 g, 7.99 mmol, 1.0 eq) was dissolved in 30 mL of deion. water. A solution of potassium xanthate (4.23 g, 18.4 mmol, 2.3 eq) in 15 mL deion. water was added dropwise under stirring and a dark green solid formed immediately. After the reaction solution

was stirred for 2 hours, the dark green precipitate was filtered off and dried under vacuum. The reaction mixture was extracted with ethanol, filtrated with ceolite and poured into $H_2O$. The obtained dark green powder was dried in vacuum (Yield: 3.15 g, 89%).

$^1$H NMR (300 MHz, 20°C, $CDCl_3$,δ): 5.10-5.14 (t, 1H, CH), 1.66-1.74 (m, 2H, $CH_2$), 0.95 (s, 12H, $CH_3$) ppm. $^{13}$C NMR (75 MHz, 20 °C, $CDCl_3$, δ): 224.9 ($CS_2O$), 91.89 (CH), 35.86 ($\underline{C}(CH_3)_3$), 26.15 ($C(\underline{C}H_3)_3$), 23.20 ($\underline{C}H_2CH_3$), 11.30 ($CH_2\underline{C}H_3$) ppm.

FT-IR (ATR in cm$^{-1}$): 2969, 2875, 1478, 1462, 1397, 1368, 1350, 1249, 1217, 1129, 1081, 1057, 1037, 906.

Elementary analysis for $CoS_4O_2C_{16}H_{30}$: calculated: C 43.57, H 6.86, S 29.18; found: C 42.64, H 7.14, S 29.67.

## 2.2 Characterization

### 2.2.1 Elementary analysis

Elementary analyses were carried out on a Universal CHNS Elemental Analyzer Vario El III on the Institute of Inorganic Chemistry.

### 2.2.2 Nuclear magnetic resonance spectroscopy (NMR)

$^1$H NMR and $^{13}$C NMR spectra were recorded on a Bruker Ultrashield 300 MHz spectrometer. The NMR spectra were referenced to the corresponding values in literature by using solvent residual peaks ($CDCl_3$: $^1$H NMR: 7.26 ppm; $^{13}$C NMR: 77.16 ppm).

### 2.2.3 Fourier transform infrared spectroscopy (FT-IR)

FT-IR spectra were recorded on a Bruker Alpha-P instrument in transmission mode. The pure xanthates were measured as powder, whereas the PMMA/xanthate and PMMA/metal sulphide composites were measured as films on silicon wafers. Therefor the xanthates were dissolved in chloroform and drop coated on a Si-wafer. A spectral range between 4000 and 800 cm$^{-1}$ was used.

### 2.2.4 X-ray crystallography

Crystals for X-ray structure determination were obtained from a chloroform solution. All crystals suitable for single crystal X-ray diffractometry were removed from a Schlenk flask under a stream of $N_2$ and immediately covered with a layer of silicone oil. A single crystal was selected, mounted on a glass rod on a copper pin, and placed in the cold $N_2$ stream provided by

an Oxford Cryosystems cryometer. Single crystal data collection was performed on a BRUKER APEX II diffractometer with the use of Mo Kα radiation (λ= 0.71073 Å) and a CCD area detector. Empirical absorption corrections were applied using SADABS.[198,199] The structures were solved with use of either direct methods or the Patterson option in SHELXS and refined by the full-matrix least-squares procedures in SHELXL.[200] The space group assignments and structural solutions were evaluated using PLATON.[201] Non-hydrogen atoms were refined anisotropically. Hydrogen atoms were located in calculated positions corresponding to standard bond lengths and angles. Attempts to model disorder around one of the xanthate ligands and solvent of crystallization $CHCl_3$ resulted in unstable refinement.

CCDC 949783 contains the supplementary crystallographic data for compound 1. These data can be obtained free of charge from The Cambridge Crystallographic Data Centre via www.ccdc.cam.ac.uk/data_request/cif.

Crystal Data. C 43 H 78 Bi 2 Cl 4 O 6 S 12, $M$ = 1635.53, crystal size 0.20 x 0.10 x 0.10 mm, monoclinic, space group *C2/c*: $a$ = 24.5050(8) Å, $b$ = 9.0961(3) Å, $c$ = 29.5784(10) Å, $\alpha$ = 90°, $\beta$ = 105.123(2)°, $\gamma$ = 90°, $V$ = 6364.7(4) $Å^3$, $Z$ = 4, $D_c$ = 1.707 Mg $m^{-3}$, *F(000)* 3240, $\mu$ = 6.123 $mm^{-1}$, $T$ = 100(2) K, 43646 reflections ($\theta_{max}$ = 25°), 5602 unique ($R_{int}$ = 0.0261), 329 parameters, 0 restraints, *R1* (all data) = 0.0396, *wR2* (all data), = 0.0867 largest difference peak and hole: 1.716 and -1.927 e $Å^{-3}$.

## 2.3 Metal sulphides prepared from metal xanthate precursors

### 2.3.1 Standard conversion condition

For the conversion of the xanthates in their corresponding metal sulphides, usually a standard heating program was used: in 11 °C/min to 195 °C, holding this temperature for 15 min. The heating step was performed on a programmable heating plate (CAT Ingenieurbüro M. Zipperer GmbH, Germany).

### 2.3.2 Characterization

#### *2.3.2.1 Thermal gravimetric measurements*

Thermal gravimetric measurements were performed on a Netzsch Jupiter STA 449C in helium atmosphere. The heating rate was 10 °C $min^{-1}$ (from room temperature to 550 °C).

#### *2.3.2.2 High resolution mass spectra*

High resolution mass spectra (EI, 70 eV; $p_{ion\ source}$ = 1.05 . $10^{-6}$ mbar; mass range: 50–800 Da; 1 spectrum/s) were recorded on a Waters GCT Premier equipped with a direct insertion probe (temperature program of the DI: start at 40 °C, 10 °C/min to 260 °C).

#### *2.3.2.3 X-ray powder diffraction*

For X-ray powder diffraction (XRD) measurements the metal xanthates were dissolved in chloroform, drop coated onto a glass substrate at ambient condition and thermally treated on a programmable heating plate. For In- and Co-Hep furthermore samples at higher temperatures were prepared using a tube furnace (In-&Co-Hep: in 18 °C/min to 300 °C, holding this temperature for 15 min; Co-Hep: in 31 °C/min to 500 °C, holding this temperature for 15 min). For Bi-Hex also samples at lower temperatures were prepared (in 6.5 °C/min to 130 °C, holding this temperature for 15 min). Afterwards the µm thick metal sulphide layer was scraped off the glass substrate to obtain a metal sulphide powder. The XRD profiles were obtained on a Siemens D 501 diffractometer in Bragg-Brentano geometry, operated at 40 kV and 30 mA, using Cu Kα radiation (λ = 1.54178 Å) and a graphite monochromator at the secondary side.

#### *2.3.2.4 Band gap determination*

The optical band gap was acquired by optical absorption measurements. The xanthates were dissolved in chlorobenzene and were doctor bladed on a glass substrate, followed by a heat treatment using the standard conversion program. In the case of $In_2S_3$, In-Hep was dissolved in chloroform and was spin coated on a glass substrate. The optical absorption coefficient was determined by transmittance and reflectance measurements according to a method described in literature[202] using the relation

$$\alpha = \frac{1}{d} * \ln(\frac{1-R}{T})$$

with α as the absorption coefficient in $cm^{-1}$, R as the reflection coefficient, T as the transmittance coefficient and d as the layer thickness, determined with a Bruker DekTak XT surface profiler. Transmittance and reflectance measurements spectra as well as absorption spectra were recorded on a Perkin Elmer Lambda 35 equipped with an integrating sphere.

### 2.3.3 Preparation of metal sulphide/polymer nanocomposite layers

Nanocomposite layers were prepared on different substrates (for transmission electron microscopy images (TEM) NaCl substrates, for optical measurements $CaF_2$ substrates and for IR-measurements Si-wafer) by spin coating a polymer/metal-xanthate chloroform solution, followed by a thermal heating step (standard heating program). The concentration of the polymer was 5 mg/mL and the weight ratio polymer : metal sulphide was 1:5. For the preparation of the TEM samples, P3HT was used as a polymer, and the thermal heating step was performed in a tube furnace (Hereaus RO 4/25). For optical measurements and IR measurements, PMMA was used as matrix-polymer, and the conversion was accomplished on a programmable heating plate.

#### *2.3.3.1 Transmission electron microscopy (TEM)*

Transmission electron microscopy images were determined on a Tecnai F 20 microscope (FEI Company). This microscope is equipped with a Schottky emitter, an energy dispersive X-ray spectrometer and a high resolution Gatan imaging filter (HR-GIF) with an UltraScanCCD camera. TEM samples were prepared via spin coating a solution of polymer and precursor on NaCl single crystals, followed by annealing at 200 °C. Subsequent the NaCl crystal were dissolved in deion. water and the nanocomposite layer was transfered to a TEM grid.

#### *2.3.3.2 UV-vis measurements*

The samples for UV-measurements were prepared on glass substrates by doctor blading or spin coating. Absorption spectra were recorded on a UV-1800 Shimadzu UV spectrophotometer or a Perkin Elmer Lambda 35 equipped with an integrating sphere, respectively.

#### *2.3.3.3 Photoluminescence quenching*

Nanocomposite layers for PL quenching measurements were prepared on glass substrates by spin coating a polymer/metal-xanthate chloroform solution. The concentration of the polymer was 10 mg/mL and the weight ratio polymer : metal sulphide varied between 1:3 to 1:12 (w:w). The conversion was accomplished on a programmable heating plate using standard conversion conditions. PL-Quenching studies were performed on a Fluorescence Spectrophotometer F-7000 von Hitachi.

#### 2.3.3.4 Atomic force microscopy (AFM)

AFM images of the prepared nanocomposite films were performed on a Nanosuf Easyscan2 scanning probe microscope in tapping mode under ambient conditions.

### 2.3.4 Solar Cells

#### 2.3.4.1 General solar cell preparation

**Cleaning**

The etched ITO substrates (Kintec, with a sheet resistance of 10 Ω /square) were detached from the adhesive foil, which protect the ITO surface, and cleaned with water and acetone to remove contaminations. In addition, the substrates were cleaned by ultrasonic treatment in isopropyl alcohol (20 min at 50 °C/VWR ultrasonic cleaner). To activate the ITO surface, plasma etching (Diener Electronics) was performed, with oxygen as a working gas. For the plasma a constant flow of oxygen was adjusted to be 10 sccm. The plasma (100% power) was generated for three minutes to clean/etch the ITO substrates.

**PEDOT:PSS layer as hole transporting layer (optional for normal architectures)**

For normal architectures, where ITO serves as anode material, PEDOT:PSS was sandwiched between the ITO electrode and the active layer. A commercially available PEDOT:PSS solution (HC Starck Clevios PVP.Al4083), with or without dilution in deionized water (1:1 per volume) was spin-coated (2500 rpm, 300 rpm/s, 30s; CT62 spin-coater produced by Karl Suss Technique S.A.) on the plasma etched glass/ITO substrate. Subsequently the PEDOT:PSS layer was dried under inert conditions in a glove box system at 150 °C for 10 min via a heating plate.

**TiOx layer as electron transporting layer**

For the TiOx layer, used for the inverse architectures, a method of S. A. Haque[14] was adopted. Therefore a 0.1 M solution of titanium diisopropoxide bis (acetylacetonate) in chlorobenzene was used as a precursor material. 30 µL of this solution were doctor bladed at 40 °C with a speed of 10 mm/s under convenient conditions. In addition, the precursor layer was converted in a TiOx layer via a temperature step at 400 °C for 15 min using a heating plate from Schott instruments. Before coating the active layer, the TiOx layer was activated using the plasma etching process described above. For the normal architectures a method of A. J. Heeger[203] was adopted for the preparation of the TiOx layer. In this case, titanium(IV) isopropoxide was used as precursor material diluted 1:100 with methanol. After the deposition of the precursor layer

(coating parameters were the same as for the TiOx layer used in the inverse architecture), the precursor layer was converted in the TiOx layer via a temperature step (for 15 min at 90 °C on a heating plate under ambient conditions).

**Active layer**

Different solar cell architectures were investigated.

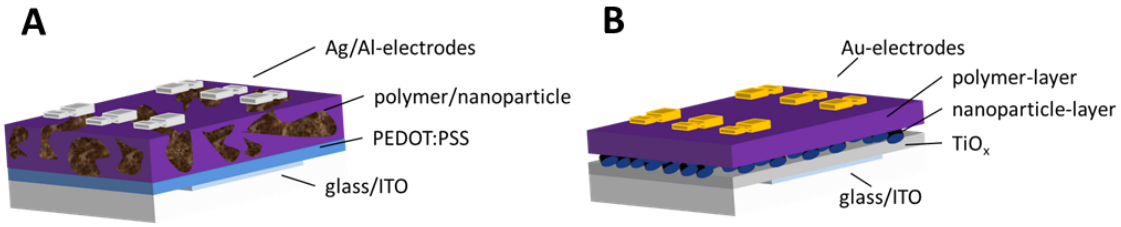


**Fig. 82: Most used solar cell architectures. A: normal bulk heterojunction; B: inverse bilayer device.**

Bulk-heterojunction (Fig. 82 A)

For the preparation of a bulk-heterojunction active layer, the polymer was dissolved in chlorobenzene and the solution stirred at least one day to obtain a homogeneous solution. Afterwards 0.5 mL of the polymer solution was added to the prepared calculated amount of xanthates. The solution was stirred for several minutes (not more than 10 min) at room temperature, in order to achieve a uniform solution. Subsequently the precursor solution was coated on the glass/ITO/(PEDOT:PSS or TiOx) substrate, using an Erichsen doctor blading machine under inert condition. To remove the chlorobenzene, the substrates were dried for 10 s at 60 °C on a heating plate of a magnetic stirrer.

Inverse bilayer (Fig. 82B)

For the preparation of inverse bilayer solar cells, the prepared xanthates were dissolved in pure chlorobenzene and the solution stirred for several minutes. Afterwards the precursor solution was coated on glass/ITO/TiOx substrate, using the same technique as for the bulk heterojunction solar cell described above. After the temperature conversion step, a polymer/chlorobenzene solution was coated on the metal sulphide layer via doctor blading, followed by a drying step at 60 °C in order to remove leftovers of chlorobenzene.

Inverse bulk heterojunction

The preparation of the inverse bulk heterojunction is nearly the same as for the inverse bilayer concept, except, that a blend of xanthate and polymer in chlorobenzene is used for the fabrication of the active layer. We fabricated inverse bulk heterojunction devices with and

without additional polymer interlayer. For the preparation of the additional polymer interlayer a polymer/chlorobenzene solution was coated on the active layer after the thermal conversion step, and dried for 15 min at 100 °C on a heating plate of a magnetic stirrer.

Conversion condition

For the decomposition of the xanthate precursors we used a tube furnace (Heraeus RO 4/25, vacuum condition or nitrogen flow) or a programmable heating plate (CAT Ingenieurbüro M.Zipperer GmbH, Germany, standing inside the glove box system). Different temperature programs for the conversion of different metal xanthates were investigated.

**Deposition of the metal back electrodes**

Back electrodes consisting of Ag (2nm)/Al (200 nm) for normal architectures and Au (100 nm) for inverse architectures were deposited via an evaporation step (at around $5*10^{-5}$ mbar), using a MED020 from Baltec, which is also equipped with a thickness measurement unit.

**IV characteristic determination**

The IV curves were determined by a Keithley 2400 SourceMeter, a custom made Lab-View software and a Dedolight DLH400D lamp. The light intensity was set to 100 mW/cm$^2$ and provides a spectrum quite similar to AM1.5G (determined using a KippZonen-CMP-11 pyranometer, no spectral mismatch was considered). The solar cells were measured using a 2.8x2.8 mm² shadow mask, in order to achieve a defined effective device area (0.0784 cm$^2$). The measurement was performed in a range of 1.5 V to -0.5 V.

#### *2.3.4.2 $Bi_2S_3$ solar cells*

Variation of the polymer : $Bi_2S_3$ ratio at 195 °C under vacuum condition

For this purpose, blends of PSiF-DBT and Bi-Hep were dissolved in chlorobenzene and doctor bladed on glass/ITO/PEDOT:PSS substrates (50 µm, 15-20 mm/s, 30 µL, 40 °C). The thermal conversion step was performed in a tube furnace under vacuum conditions (start vacuum $1.6*10^{-1}$ mbar). Finally 2 nm of Ag and 200 nm of Al were deposited via an evaporation step ($2*10^{-5}$ mbar).

**Table 21: Weighed portion of polymer and xanthates for the preparation of bulk heterojunction $Bi_2S_3$ nanocomposite solar cells under vacuum condition.**

| | PSiF-DBT | Bi-Hep | chlorobenzene |
|---|---|---|---|
| **MW / g*mol$^{-1}$** | - | 782.98 | 112.6 |
| **volume / mL** | - | - | 0.5 |
| **ratio** | | **1:2** | |
| mass / mg | 2.5 | 7.6 | - |
| concentration / mg*mL$^{-1}$ | 5 | 15.2 | - |
| **ratio** | | **1:5** | |
| mass / mg | 2.5 | 19.0 | - |
| concentration / mg*mL$^{-1}$ | 5 | 38 | - |
| **ratio** | | **1:9** | |
| mass / mg | 2.5 | 34.3 | - |
| concentration / mg*mL$^{-1}$ | 5 | 68.6 | - |
| **ratio** | | **1:12** | |
| mass / mg | 2.5 | 45.7 | - |
| concentration / mg*mL$^{-1}$ | 5 | 91.4 | - |

Variation of the polymer:$Bi_2S_3$ ratio at 200 °C under $N_2$ flow

The different PSiF-DBT : Bi-Hep blends were doctor bladed on glass/ITO/PEDOT:PSS substrates (50 µm, 15-20 mm/s, 30 µL, 40 °C), followed by a thermal conversion step at 200 °C in a tube furnace under $N_2$-flow (11 N/h at 1 bar and 20 °C; in 24 °C/min to 200 °C and holding this temperature for 15 min). Finally 2 nm of Ag and 200 nm Al were deposited on the substrate ($3*10^{-5}$ mbar).

**Table 22: Weighed portion of polymer and xanthates for the preparation of bulk heterojunction $Bi_2S_3$ nanocomposite solar cells under $N_2$-flow.**

| | PSiF-DBT | Bi-Hep | chlorobenzene |
|---|---|---|---|
| **MW / g*mol$^{-1}$** | - | 782.98 | 112.6 |
| **volume / mL** | - | - | 0.5 |
| **ratio** | | **1:5** | |
| mass / mg | 2.5 | 19.0 | - |
| concentration / mg*mL$^{-1}$ | 5 | 38 | - |
| **ratio** | | **1:9** | |
| mass / mg | 2.5 | 34.3 | - |
| concentration / mg*mL$^{-1}$ | 5 | 68.6 | - |

Inverse bilayer devices fabricated at different conversion temperatures

The glass/ITO/TiOx substrates were plasma treated, and subsequently a solution of Bi-Hex and chlorobenzene was coated on the TiOx layer via doctor blading (100 µm, 15 mm/s, 30 µL, 40 °C). After the thermal conversion (tube furnace, $N_2$-flow, temperature variation: in 6.7 °C/min to 130 °C, in 8 °C/min to 150 °C and in 11 °C/min to 195 °C) a polymer/chlorobenzene

solution was doctor bladed on the $Bi_2S_3$ layer and dried for 15 min at 100 °C on a heating plate. Finally 200 nm Au were deposited via evaporation ($3*10^{-5}$ mbar).

**Table 23: Weighed portion of polymer and xanthates for the preparation of inverse bilayer devices at different temperatures.**

| | PSiF-DBT | P3HT | Bi-Hex | chlorobenzene |
|---|---|---|---|---|
| **MW / g*mol$^{-1}$** | - | - | 740.14 | 112.6 |
| **volume / mL** | - | - | - | 0.5 |
| **mass / mg** | 2.5 | 2.5 | 60 | - |
| **concentration / mg*mL$^{-1}$** | 5 | 5 | 120 | - |

Bulk heterojunction devices with two additional interlayers

For this purpose in a first step a polymer/chlorobenzene solution was coated on glass/ITO/PEDOT:PSS substrates via doctor blading (100 µm, 20 mm/s, 30 µL, 40 °C) and was subsequently dried on a heating plate at 100 °C for 15 min. In a next step a blend of polymer and Bi-Hex in chlorobenzene with different polymer to inorganic ratios (1:3, 1:6, 1:12) was doctor bladed on the polymer layer (100 µm, 10-15 mm/s, 30 µL, 40 °C), followed by a heating step (standard conversion program). Afterwards a TiOx precursor (1:100 in methanol) was coated via doctor blading (100 µm, 10 mm/s, 30 µL, 40 °C) on the active layer, and was converted into TiOx at 90 °C for 15 min under ambient atmosphere. Finally 200 nm Al were deposited on the device via evaporation ($1*10^{-5}$ mbar). As a reference substrate a polymer/TiOx bilayer device was fabricated.

**Table 24: Weighed portion of polymer and Bi-Hex for the preparation bulk heterojunction devices with two additional interlayers.**

| | PSiF-DBT | Bi-Hex | chlorobenzene |
|---|---|---|---|
| **MW / g*mol$^{-1}$** | - | 740.14 | 112.6 |
| **volume / mL** | - | - | 0.5 |
| **ratio** | | **1:0** | |
| mass / mg | 2.5 | - | - |
| concentration / mg*mL$^{-1}$ | 5 | - | - |
| **ratio** | | **1:3** | |
| mass / mg | 2.5 | 10.8 | - |
| concentration / mg*mL$^{-1}$ | 5 | 21.6 | - |
| **ratio** | | **1:6** | |
| mass / mg | 2.5 | 21.6 | - |
| concentration / mg*mL$^{-1}$ | 5 | 43.2 | - |
| **ratio** | | **1:12** | |
| mass / mg | 2.5 | 43.2 | - |
| concentration / mg*mL$^{-1}$ | 5 | 86.4 | - |

Bulk heterojunction device; investigation of an aging process

For this purpose, a blend of PSiF-DBT and Bi-Hex was dissolved in chlorobenzene and doctor bladed on a glass/ITO/PEDOT:PSS substrate (1000 µm, 15 mm/s, 30 µL, 40 °C). The thermal conversion step was performed on a programmable heating plate in the glove box system. Finally 2 nm of Ag and 200 nm of Al were deposited via an evaporation step ($9*10^{-6}$ mbar). The device was measured directly after fabrication, after 24 h and after 48 h.

**Table 25: Weighed portion of polymer and Bi-Hex for the preparation bulk heterojunction devices for the investigation of an aging process.**

| | PSiF-DBT | Bi-Hex | chlorobenzene |
|---|---|---|---|
| **MW / g*mol$^{-1}$** | - | 740.14 | 112.6 |
| **volume / mL** | - | - | 0.5 |
| **ratio** | | **1:5** | |
| mass / mg | 2.5 | 18.0 | - |
| concentration / mg*mL$^{-1}$ | 5 | 36 | - |

### *2.3.4.3 PbS solar cells*

Bulk heterojunction device

A blend of Pb-Hep with MEH-PPV in chlorobenzene with different polymer : inorganic ratios was deposited on glass/ITO/PEDOT:PSS substrates via doctor blading (100 µm, 10-15 mm/s, 30µL, 40 °C). Afterwards, the precursor layer was converted on a programmable heating plate (standard conversion conditions). Subsequently 200 nm Al were deposited via evaporation at a reduced pressure of $1*10^{-5}$ mbar.

**Table 26: Weighed portion of MEH PPV and Pb-Hep-xanthates for the preparation bulk heterojunction with different polymer:inorganic ratios.**

| | MEH-PPV | Pb-Hep | chlorobenzene |
|---|---|---|---|
| **MW / g*mol$^{-1}$** | - | 589,87 | 112.6 |
| **volume / mL** | - | - | 0.5 |
| **ratio** | | **1:3** | |
| mass / mg | 2.5 | 18.5 | - |
| concentration / mg*mL$^{-1}$ | 5 | 37.0 | - |
| **ratio** | | **1:6** | |
| mass / mg | | 36.9 | - |
| concentration / mg*mL$^{-1}$ | | 73.8 | - |
| **ratio** | | **1:9** | |
| mass / mg | | 55.5 | - |
| concentration / mg*mL$^{-1}$ | | 111 | - |
| **ratio** | | **1:12** | |
| mass / mg | | 74.0 | - |
| concentration / mg*mL$^{-1}$ | | 148 | - |

Inverse bulk heterojunction device

The glass/ITO/TiOx substrates were plasma treated, and subsequently a blend of Pb-Hep and polymer (MEH-PPV or P3HT) in chlorobenzene with different polymer to inorganic ratios was coated on the TiOx layer via doctor blading (100 µm, 15 mm/s, 30 µL, 40 °C). Two solar cell devices were fabricated with the same ratio. After the thermal conversion (standard conversion conditions) one substrate remained without further interlayer deposition. On the other one however, an additional polymer interlayer was deposited by coating a polymer/chlorobenzene solution via doctor blading (100 µm, 30 mm/s, 30 µL, 40 °C; drying for 15 min at 100 °C on a heating plate). Finally 100 nm Au were deposited on all substrates via evaporation (reduced pressure of 1*10-5 mbar).

**Table 27: Weighed portion of MEH PPV and Pb-Hep for the preparation bulk heterojunction with different polymer:inorganic ratios.**

| | MEH-PPV bulk | Pb-Hep | MEH-PPV interlayer | chlorobenzene |
|---|---|---|---|---|
| **MW / g*mol$^{-1}$** | - | 589,87 | - | 112.6 |
| **volume / mL** | - | - | - | 0.5 |
| **ratio** | | **1:3** | | |
| mass / mg | 2.5 | 18.5 | 3.25 | - |
| concentration / mg*mL$^{-1}$ | 5 | 37.0 | 6.5 | - |
| **ratio** | | **1:6** | | |
| mass / mg | 2.5 | 36.9 | - | - |
| concentration / mg*mL$^{-1}$ | 5 | 73.8 | - | - |
| **ratio** | | **1:9** | | |
| mass / mg | 2.5 | 55.5 | - | - |
| concentration / mg*mL$^{-1}$ | 5 | 111 | - | - |
| **ratio** | | **1:12** | | |
| mass / mg | 2.5 | 74.0 | - | - |
| concentration / mg*mL$^{-1}$ | 5 | 148 | - | - |

**Table 28: Weighed portion of P3HT and Pb-Hep for the preparation bulk heterojunction with different polymer:inorganic ratios.**

| | P3HT bulk | Pb-Hep | P3HT interlayer | chlorobenzene |
|---|---|---|---|---|
| **MW / g*mol$^{-1}$** | - | 589,87 | - | 112.6 |
| **volume / mL** | - | - | - | 0.5 |
| **ratio** | | **1:3** | | |
| mass / mg | 2.5 | 18.5 | 3.25 | - |
| concentration / mg*mL$^{-1}$ | 5 | 37.0 | 6.5 | - |
| **ratio** | | **1:6** | | |
| mass / mg | 2.5 | 36.9 | | - |
| concentration / mg*mL$^{-1}$ | 5 | 73.8 | | - |

### *2.3.4.4 $Sb_2S_3$ solar cells*

Bulk heterojunction P3HT/$Sb_2S_3$ solar cells with different polymer to inorganic ratios

For the preparation of bulk heterojunction P3HT/$Sb_2S_3$ devices, a blend of P3HT and Sb-Hep in chlorobenzene with different polymer to inorganic ratios was doctor bladed on glass/ITO/PEDOT:PSS devices (100µm, 30µL, 40 °C) after filtration. The coating speed was varied between 5 mm/s to 15 mm/s in an attempt to achieve similar layer thicknesses independent from the polymer to inorganic ratios. Afterwards, the precursor layer was converted on a programmable heating plate (standard conversion condition). Subsequently 200 nm Al were deposited via evaporation at a reduced pressure of $1*10^{-5}$ mbar.

**Table 29: Weighed portion of polymer and Sb-Hep for the preparation bulk heterojunction devices.**

| | **P3HT** | **Sb-Hep** | **chlorobenzene** |
|---|---|---|---|
| **MW / g*mol$^{-1}$** | - | 695.76 | 112.6 |
| **volume / mL** | - | - | 0.5 |
| **ratio** | | **1:5** | |
| mass / mg | 2.5 | 25.6 | - |
| concentration / mg*mL$^{-1}$ | 5 | 51.2 | - |
| **ratio** | | **1:8** | |
| mass / mg | 2.5 | 41.0 | - |
| concentration / mg*mL$^{-1}$ | 5 | 82 | - |
| **ratio** | | **1:11** | |
| mass / mg | 2.5 | 56.3 | - |
| concentration / mg*mL$^{-1}$ | 5 | 112.6 | - |
| **ratio** | | **1:15** | |
| mass / mg | 2.5 | 76.8 | - |
| concentration / mg*mL$^{-1}$ | 5 | 153.6 | - |

Inverse bilayer P3HT/$Sb_2S_3$ devices

For this purpose, glass/ITO/TiOx devices were plasma treated and subsequently a filtered solution of Sb-Hep in chlorobenzene was doctor bladed on the devices (100 µm, 7.5-20 mm/s, 30 µL, 40 °C). Afterwards, the precursor layer was converted on a programmable heating plate (standard conversion condition). After cooling, a P3HT layer was doctor bladed on the $Sb_2S_3$ layer, followed by a drying step on a heating plate for 15 min at 100 °C. Subsequently 100 nm Au were deposited via evaporation at a reduced pressure of $5*10^{-6}$ mbar.

**Table 30: Weighed portion of polymer and Sb-Hep for the preparation of inverse bilayer devices.**

| | P3HT | Sb-Hep | chlorobenzene |
|---|---|---|---|
| **MW / g*mol$^{-1}$** | - | 695.76 | 112.6 |
| **volume / mL** | - | - | 0.5 |
| **mass / mg** | 2.5 | 60 | - |
| **concentration / mg*mL$^{-1}$** | 5 | 120 | - |

#### *2.3.4.5 $In_2S_3$ solar cells*

Bulk-heterojunction devices

For the preparation of bulk heterojunction PSiF-DBT/$In_2S_3$ devices, a blend of polymer and In-Hep in chlorobenzene with different polymer to inorganic ratios was doctor bladed on glass/ITO/PEDOT:PSS devices (100µm, 30µL, 40 °C). The coating speed was varied between 7.5 mm/s to 20 mm/s in an attempt to achieve similar layer thicknesses independent from the polymer to inorganic ratios. Afterwards, the precursor layer was converted on a programmable heating plate using different temperature programs (in 9.5 °C/min to 175 °C, in 10 °C/min to 185 °C, in 11 °C/min to 195 °C and in 12 °C/ min to 205 °C, holding these temperature for 15 min). Subsequently 2 nm Ag and 200 nm Al were deposited via evaporation at a reduced pressure of 9*10$^{-6}$ mbar.

**Table 31: Weighed portion of polymer and In-Hep for the preparation of bulk heterojunction devices.**

| | PSiF-DBT | In-Hep | chlorobenzene |
|---|---|---|---|
| **MW / g*mol$^{-1}$** | | 688.82 | 112.6 |
| **volume / mL** | | | 0.5 |
| **ratio** | | **1:3** | |
| mass / mg | 2.5 | 15.9 | - |
| concentration / mg*mL$^{-1}$ | 5 | 31.8 | - |
| **ratio** | | **1:4** | |
| mass / mg | 2.5 | 21.1 | - |
| concentration / mg*mL$^{-1}$ | 5 | 42.2 | - |
| **ratio** | | **1:5** | |
| mass / mg | 2.5 | 26.4 | - |
| concentration / mg*mL$^{-1}$ | 5 | 52.8 | - |
| **ratio** | | **1:6** | |
| mass / mg | 2.5 | 31.7 | - |
| concentration / mg*mL$^{-1}$ | 5 | 63.4 | - |
| **ratio** | | **1:7** | |
| mass / mg | 2.5 | 37.0 | - |
| concentration / mg*mL$^{-1}$ | 5 | 74 | - |
| **ratio** | | **1:9** | |
| mass / mg | 2.5 | 47.6 | - |
| concentration / mg*mL$^{-1}$ | 5 | 95.2 | - |
| **ratio** | | **1:12** | |
| mass / mg | 2.5 | 63.4 | - |
| concentration / mg*mL$^{-1}$ | 5 | 126.8 | - |

# 3 Tandem solar cells

## 3.1 Characterization and measurement

### 3.1.1 PCE-values

PCE values were determined from IV curves recorded using a Keithley 2400 SourceMeter a custom made Lab-View software and a Dedolight DLH400D lamp. The light intensity was set to 100 mW/cm$^2$ providing a spectrum quite similar to AM1.5G (determined using a KippZonen-CMP-11 pyranometer, no spectral mismatch was considered). The effective device area (0.004 cm$^2$) was defined by 2x2 mm$^2$ shadow masks applied to the solar cells during the measurements of the IV curves.

### 3.1.2 EQE-measurements

EQE spectra were obtained from a MuLTImode 4 monochromator equipped with a xenon lamp (AMKO) and a Keithley 2400 SourceMeter.

### 3.1.3 UV-vis measurements

Absorption spectra were specified with a Shimadzu UV-1800 spectrophotometer and with a Perkin Elmer UV/VIS spectrometer Lambda 35 equipped with an integrated sphere.

### 3.1.4 Scanning electron microscope (SEM)

SEM analyses were conducted on a Zeiss Ultra 55 and the cross section for this characterization was realized by ion polishing using a Gaton Ilion+.

### 3.1.5 Profilometer

Layer thicknesses were determined on a Bruker DekTak XT surface profiler.

## 3.2 Device fabrication

### 3.2.1 Tandem solar cells

<u>Investigation of Ag/PEDOT:PSS, TiOx/Ag/PEDOT:PSS, TiOx/PEDOT:PSS, PEDOT:PSS interlayers</u>

The precursor for the hybrid layer, consisting of a copper and indium xanthate mixture with PSiF-DBT, was deposited by doctor blading (100 µm, 10 mm/s, 30 µL, 40 °C), followed by a thermal conversion step on a programmable heating plate (standard program). As

recombination layers Ag/PEDOT:PSS, TiOx/PEDOT:PSS and pure PEDOT:PSS were investigated. The metallic interlayers (4 nm) were deposited inside a glovebox system by evaporation at a base pressure of $8*10^{-6}$ mbar. The second PEDOT:PSS layer was prepared by doctor blading (100 µm, 15 mm/s, 50 mL) of a PEDOT:PSS : isopropanol solution (1:5 V:V) at a temperature of 60 °C and were dried under vacuum for 10 min. The PTB7:$PC_{61}BM$ layer was prepared by doctor blading a mixture of chlorobenzene/1,8-diiodoctane (97:3% by volume)[168] solution on top of the PEDOT:PSS layer (100 µm, 20 mm/s, 30 µL, 40 °C). 180 nm thick Al electrodes for the hybrid-organic tandem devices and 2 nm Ag and 200 nm Al for the hybrid-hybrid devices were subsequently thermally evaporated inside a glovebox system. For the comparison single junction solar cells were also fabricated with the device structure ITO/PEDOT:PSS/PSiF-DBT:CIS/TiOx/Ag for the hybrid cell and ITO/PEDOT:PSS/PTB7:$PC_{61}BM$/Al for the organic cell.

**Table 32: Weighed portion of PSiF-DBT, Cu-Hep, In-Hep, PTB7 and PCBM for the fabrication of bulk heterojunction single and tandem solar cells.**

| | PSiF-DBT | Cu-Hep | In-Hep | PTB7 | $PC_{61}BM$ | chlorobenzene |
|---|---|---|---|---|---|---|
| **MW / g*mol$^{-1}$** | | 254.9 | 688.7 | | | 112.6 |
| **volume / mL** | | | | | | 0.5 |
| **ratio** | | **1:9** | | **1:1.5** | | |
| mass / mg | 2.5 | 16.1 | 73.9 | 5 | 15 | - |
| concentration / mg*mL$^{-1}$ | 5 | 32.2 | 147.8 | 10 | 30 | - |

Investigation of $C_2CO_3$/Ag/$V_2O_5$ interlayers in PSiF-DBT:CIS/PCPDTBT:$PC_{61}BM$ tandem solar cells

For the preparation of the bottom solar cell a blend of PSiF-DBT, Cu-Hep-and In-Hep was dissolved in chlorobenzene and doctor bladed on glass/ITO/PEDOT:PSS substrates (100 µm, 7.5 mm/s, 30 µL, 40 °C). Subsequently the precursor layer was converted via a thermal conversion step at standard conversion conditions. The $Cs_2CO_3$/Ag interlayer was deposited on the bottom solar cell via evaporation ($1*10^{-5}$ mbar; 2 nm $Cs_2CO_3$ were evaporated at a rate of 0.1-0.2 Å/s, 3nm Ag were evaporated with a rate of 0.1 Å/s). The precursor for the $V_2O_5$ (vanadium(V)oxytriisopropoxide) interlayer was deposited via doctor blading (100µm, 25 mm/s, 30 µL, 40 °C) under ambient conditions and under inert conditions in a glove box system (this device was exposed to air for 20 s) respectively. The devices were dried for 30 s on a 60 °C heating plate in the glove box. For the preparation of the top solar cell a blend of PCPDTBT and $PC_{61}BM$ was dissolved in chlorobenzene and deposited via doctor blading (100 µm, 10 mm/s, 30 µL, 40 °C) on the bottom solar cell. Subsequently 200 nm Al were deposited via evaporation ($1*10^{-5}$ mbar).

For the preparation of the PSiF-DBT:CIS reference solar cell a blend of PSiF-DBT, Cu-Hep and In-Hep was dissolved in chlorobenzene and doctor bladed on a glass/ITO/PEDOT:PSS substrate (100 µm, 10 mm/s, 30 µL, 40 °C). Afterwards the precursor layer was converted at a standard conversion conditions. Finally 2 nm $C_2CO_3$ and 200 nm Al were deposited on the devices via evaporation ($9*10^{-6}$ mbar).

For the preparation of the PCPDTBT:$PC_{61}BM$ reference solar cell a blend of PCPDTBT and $PC_{61}BM$ was dissolved in chlorobenzene and deposited on a glass/ITO/PEDOT:PSS device via doctor blading (100 µm, 10 mm/s, 30 µL, 40 °C). Subsequently 200 nm Al were deposited on the device via evaporation at a reduced pressure of $1*10^{-5}$ mbar.

**Table 33: Weighed portion of polymers, xanthates and PCBM for the fabrication of bulk heterojunction single and tandem solar cells.**

| | PSiF-DBT | Cu-Hep | In-Hep | PCPDTBT | $PC_{61}BM$ | chlorobenzene |
|---|---|---|---|---|---|---|
| **MW / g*mol$^{-1}$** | | 254.9 | 688.7 | | | 112.6 |
| **volume / mL** | | | | | | 0.5 |
| **ratio** | | **1:9** | | **1:8** | | |
| mass / mg | 2.5 | 16.1 | 73.9 | 2.5 | 20 | - |
| concentration / mg*mL$^{-1}$ | 5 | 32.2 | 147.8 | 5 | 40 | - |

### 3.2.2 Single solar cells

PCPDTBT:CIS bulk heterojunction solar cells with different polymer to inorganic ratio

For this purpose, a blend of PCDTBT, Cu-Hep and In-Hep was dissolved in chlorobenzene. Subsequently it was doctor bladed on glass/ITO/PEDOT:PSS devices (100 µm, 10 & 15 mm/s, 30 µL, 40 °C), followed by a thermal conversion step (standard program). Afterwards 2 nm of Ag (0.1 Å/s) and 200 nm of Al were deposited on the devices via evaporation ($6*10^{-6}$ and $7*10^{-6}$ respectively).

**Table 34: Weighed portion of PCDTBT and xanthates for the fabrication of bulk heterojunction solar cells.**

| | PCDTBT | Cu-Hep | In-Hep | chlorobenzene |
|---|---|---|---|---|
| **MW / g*mol$^{-1}$** | | 254.9 | 688.7 | 112.6 |
| **Volume / mL** | | | | 0.5 |
| **ratio** | | **1:4** | | |
| mass / mg | 2.5 | 7.1 | 32.8 | - |
| concentration / mg*mL$^{-1}$ | 5 | 14.2 | 65.6 | - |
| **ratio** | | **1:6** | | |
| mass / mg | 2.5 | 10.7 | 49.3 | - |
| concentration / mg*mL$^{-1}$ | 5 | 21.4 | 98.6 | - |
| **ratio** | | **1:9** | | |
| mass / mg | 2.5 | 16.1 | 73.9 | - |
| concentration / mg*mL$^{-1}$ | 5 | 32.2 | 147.8 | - |
| **ratio** | | **1:12** | | |
| mass / mg | 2.5 | 21.4 | 98.5 | - |
| concentration / mg*mL$^{-1}$ | 5 | 42.8 | 197 | - |

PBDTTT-C:CIS bulk heterojunction solar cells with different polymer to inorganic ratios

A blend of PBDTTT-C, Cu-Hep and In-Hep was dissolved in chlorobenzene and subsequently doctor bladed on glass/ITO/PEDOT:PSS devices (100 µm, 10 & 15 mm/s, 30 µL, 40 °C). Afterwards the precursor layer was converted via the standard thermal conversion program. Finally 2 nm of Ag (0.1 Å/s) and 200 nm of Al were deposited on the devices via evaporation ($9*10^{-6}$ mbar and $7*10^{-6}$ mbar respectively).

**Table 35: Weighed portion of PBDTTT-C and xanthates for the fabrication of bulk heterojunction solar cells.**

| | PBDTTT-C | Cu-Hep | In-Hep | chlorobenzene |
|---|---|---|---|---|
| **MW / g*mol$^{-1}$** | | 254.9 | 688.7 | 112.6 |
| **Volume / mL** | | | | 0.5 |
| **ratio** | | **1:4** | | |
| mass / mg | 2.5 | 7.1 | 32.8 | - |
| concentration / mg*mL$^{-1}$ | 5 | 14.2 | 65.6 | - |
| **ratio** | | **1:6** | | |
| mass / mg | 2.5 | 10.7 | 49.3 | - |
| concentration / mg*mL$^{-1}$ | 5 | 21.4 | 98.6 | - |
| **ratio** | | **1:9** | | |
| mass / mg | 2.5 | 16.1 | 73.9 | - |
| concentration / mg*mL$^{-1}$ | 5 | 32.2 | 147.8 | - |
| **ratio** | | **1:12** | | |
| mass / mg | 2.5 | 21.4 | 98.5 | - |
| concentration / mg*mL$^{-1}$ | 5 | 42.8 | 197 | - |

# V Summary and Outlook

Nanocomposite solar cells are an interesting alternative to organic solar cells, due to the fact, that the semiconductor nanoparticles can contribute to the overall absorption. Nevertheless, their overall power efficiency cannot compete with organic solar cells so far.

This work deals with two concepts to improve the power conversion efficiencies of nanocomposite solar cells. One approach in order to get rid of isolating capping ligands is the investigation of the *in situ* prepared nanoparticles via xanthate precursors. The second approach to enhance the efficiency is the fabrication of tandem solar cells.

Nanocomposite solar cells using xanthate precursors have already been published in literature. T. Rath et al.[15] used Cu-Hep and In-Hep for the fabrication of PSiF-DBT/CIS solar cells, achieving efficiencies up to 2.8%. Furthermore, S. A. Haque et al. used Cd-Et xanthates in addition with a pyridine ligand and Sb-Et for the preparation of P3HT/CdS[88] and P3HT/$Sb_2S_3$[89] solar cells, with a power conversion efficiencie of 2% and 1.3% respectively. Thus, the first part of this work is focused on the synthesis and characterization of metal xanthates suitable as precursors for metal sulphides. One requirement is their high solubility in apolar solvents, due to the fact, that conjugated polymers are usually only soluble in these solvents. According to A. Fischereder[108] copper and indium xanthates with 2,2-dimethylpentan-3-yl and 3,3-dimethylbutan-2-yl side chains are very promising candidates for this purpose. Thus, Bi-, Pb-, Sb-, Co-and Ni xanthates with the respective side chains were synthesised with high purity according to NMR, FT-IR and elementary analysis. For Bi-Hex a crystal structure was obtained revealing a dimeric structure. Furthermore, the thermal conversion was investigated by thermal gravimetric analysis and high resolution mass spectroscopy. All xanthates decompose at moderate temperatures between 130 °C and 175 °C which is important concerning their application in nanocrystal-polymer solar cells, as their formation takes place in the presence of the conjugated polymers. High temperatures could harm the structure and the optoelectronic properties of these polymers leading to poorer power conversion efficiencies in solar cells. Mass spectroscopy revealed that all analysed xanthates do not only decompose, but also partly evaporate. This is important information concerning the fabrication of nanocomposite layers if the conversion is carried out under vacuum conditions. To investigate which crystal phase of the metal sulphides is formed, XRD measurements were performed. In the case of $Bi_2S_3$, PbS, $Sb_2S_3$ and $In_2S_3$ only one crystal phase was formed, whereas Ni and Co-sulphides appeared in more than one phase, and hence were not further investigated. The size of the nanoparticles was determined using Sherrer formula. The smallest nanoparticles were

obtained for $In_2S_3$ with 16 nm (at a conversion temperature of 300 °C), followed by $Bi_2S_3$ with nanoparticles around 27 nm (195 °C). $Sb_2S_3$ nanoparticles have a size of around 44 nm, while PbS nanoparticles with a size of around 50 nm are the largest once. The band gaps of $Bi_2S_3$ (1.62 eV), $Sb_2S_3$ (2.1 eV) and $In_2S_3$ (2.4 eV) were determined, exhibiting similar values reported in literature.

To check the suitability of the metal sulphides as acceptor materials for solar cell preparation, and to investigate if charge transfer occurs in these nanoparticle/polymer active layers, photoluminescence quenching measurements were performed with different polymers which are commonly used in organic photovoltaics. All polymers were efficiently quenched after introduction of the different nanoparticles.

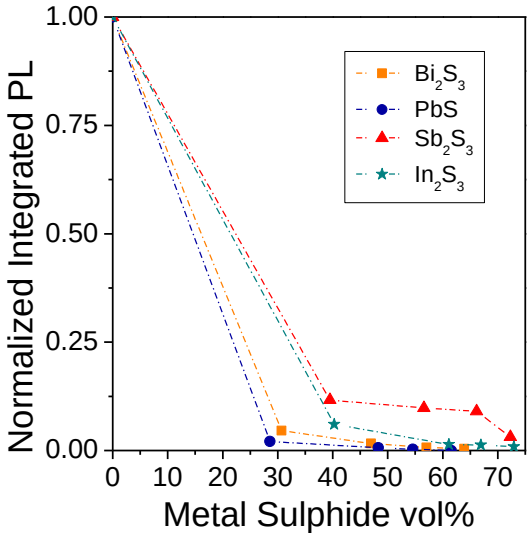


**Fig. 83: Comparison of the normailzed integrated PL of PSiF-DBT/metal sulphide nanocomposites.**

Fig. 83 shows a comparison of the normalized integrated PL of the PSiF-DBT/metal sulphide nanocomposites. It was discovered, that the PSiF-DBT is quenched most effectively by PbS nanoparticles, followed by $Bi_2S_3$. Nevertheless, all four metal sulphides should be suitable as acceptor material in polymer (PSiF-DBT) / nanoparticle solar cells.

TEM pictures were recorded of $Bi_2S_3$ nanoparticles, which show, that nanorods are formed in the polymer matrx. The formation via a ligand free *in situ* process in the solid state is a highly interesting result, as it was not possible before to realize nanorod structures via ligand free *in situ* processes.

Finally solar cells with $Bi_2S_3$, $Sb_2S_3$, PbS and $In_2S_3$ as acceptor materials were produced. In order to improve the power conversion efficiency of the single devices a series of parameters was

tested: different conjugated polymers, various precursor compositions, diverse coating speeds, conversion at different temperatures, various device architectures and the incorporation of interlayers.

In the case of $Bi_2S_3$ polymer solar cells, the only working devices were obtained at a conversion temperature of 130 °C. At this temperature some $Bi_2S_3$ nanoparticles have already been built, but there is also some leftover xanthate. Thus, solar cells fabricated at 130 °C will probably never exhibit high efficiencies due to the impurities of the acceptor phase. Solar cells fabricated at higher temperatures were shorted and no diode characteristics could be observed. To prevent short circuits in the solar cells hole as well as electron transport layers were introduced to the solar cell architecture. Nevertheless, also with this improved geometry, no working solar cells could be achieved. Until now, the origin of the shorted behaviour of the solar cells remained unclear and for the clarification of this issue further research is necessary.

Regarding PbS/polymer solar cells, only working inverse bilayer devices and inverse bulk heterojunction devices with an additional polymer interlayer could be realized. Thus, power conversion efficiencies up to 0.04% were obtained. Further device optimization is necessary including decreasing the surface roughness in order to achieve nanocomposite solar cells with higher power conversion efficiency.

Sb-Hep seems to be not stable and was therefore only poorly soluble in apolar solvents after one week after synthesis. Thus, the polymer precursor blend had to be filtered before coating of the active layer. Therefore, no reasonable results could be obtained for bulk heterojunction solar cells. Thus, inverse bilayer devices were investigated, exhibiting power conversion efficiencies of up to 0.1%. To achieve higher efficiencies, Sb-xanthates with different side chains should be investigated.

The most promising results were achieved with $In_2S_3$ as acceptor material in nanocomposite solar cells. Different polymer to inorganic ratios at different conversion temperatures were investigated. The highest efficiency of 0.3% could be achieved for a polymer to inorganic ratio of 1:6 at a conversion temperature of 185 °C.

**Table 36: Comparison of the characteristic device parameters of the best performing devices.**

| | | $V_{OC}$ / V | $I_{SC}$ / mA/cm$^2$ | FF | Eff. / % |
|---|---|---|---|---|---|
| PbS/P3HT | inverse bulk heterojunction | 0.26 | 0.5 | 0.33 | 0.04 |
| $Sb_2S_3$/P3HT | inverse bilayer | 0.29 | 1.3 | 0.29 | 0.11 |
| $In_2S_3$/PSiF-DBT | bulk heterojunction | 0.23 | 3.2 | 0.42 | 0.31 |

In Table 36 the characteristic device parameters of the different metal sulphide solar cells are compared.

The second part of this thesis is focused on the preparation of polymer/nanoparticle hybrid tandem solar cells.

In the first step, different recombination layers were inquired.

For the fabrication of *in situ* prepared hybrid-hybrid tandem solar cells, the challenge of a second annealing step of the bottom cell has to be overcome (Fig. 84). Thus, this issue was separated from the topic of finding a suitable recombination layer, due to the fabrication of hybrid-organic tandem solar cells.

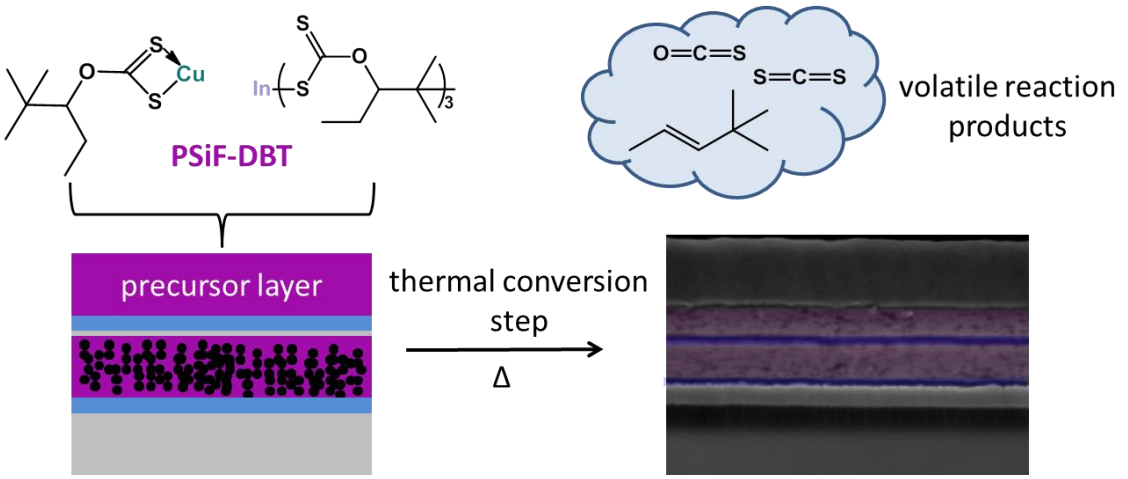


**Fig. 84: Schematic demonstration of the fabrication of a hybrid-hybrid tandem solar cell.**

The Ag/PEDOT:PSS, TiOx/Ag/PEDOT:PSS, TiOx/PEDOT:PSS and PEDOT:PSS interlayers were investigated using following device architectures: glass/ITO/PEDOT:PSS/PSiF-DBT:CIS/IL/PEDOT:PSS/PTB7:PCBM/Al, glass/ITO/PEDOT:PSS/PTB7:PCBM/IL/PEDOT:PSS/PTB7:PCBM/Al and glass/ITO/PEDOT:PSS/PSiF-DBT:CIS/IL/PEDOT:PSS/PSiF-DBT:CIS/AgAl. IL is used in this context as abbreviation for the interlayer.

All tandem solar cells with Ag or Ag/TiOx as recombination layer, exhibited high $V_{OC}$s, but a drastically trop in $I_{SC}$. PEDOT:PSS did not provide an efficient recombination region in tandem solar cells. The most promising results were achieved for TiOx/PEDOT:PSS interlayer which provide an efficient recombination region in hybrid-organic solar cells, leading to a hybrid-organic tandem cell with a $V_{OC}$ of 0.90 V, which is 91% of the sum of the subcell $V_{OC}$ values. The $I_{SC}$ seems to be limited by the single cell with the lower $I_{SC}$ value reaching a PCE of 4.1% which is an increase in device performance compared to the single cells. Nevertheless, the

TiOx/PEDOT:PSS interlayer is no suitable recombination layer for the hybrid-hybrid tandem device, as it does not lead to an increase in $V_{OC}$ compared to the single cells.

First working hybrid-hybrid tandem solar cells with Ag/PEDOT:PSS interlayer were obtained, revealing a nearly doubled $V_{OC}$ of the single cells. However, the quite low $I_{SC}$ provides the necessity for further interlayer improvement. Nevertheless, the SEM picture showed smooth layers indicating that the second heating step did not significantly affect the morphology of the hybrid-hybrid tandem solar cell (Fig. 84).

The $Cs_2CO_3$/Ag/$V_2O_5$ was tested in devices using following architecture: glass/ITO/PEDOT:PSS/PSiF-DBT:CIS/$Cs_2CO_3$/Ag/$V_2O_5$/PCPDTBT:PCBM/Al. Furthermore two different preparation conditions (inert and ambient) were investigated for the $V_2O_5$ interlayer. Tandem devices with $V_2O_5$ interlayers prepared at ambient conditions revealed significantly higher $V_{OC}$s than tandem devices, with $V_2O_5$ interlayers prepared at inert conditions. The hybrid-organic tandem solar cell as well as the organic-organic tandem solar cell using $Cs_2CO_3$/Ag/$V_2O_5$ as interlayer exhibited nearly doubled $V_{OC}$ but only the half of the $I_{SC}$ compared to the single cells, as it was discovered before for tandem solar cells using Ag/PEDOT:PSS and TiOx/Ag/PEDOT:PSS as interlayer.

To fabricate hybrid-hybrid tandem solar cells with different active layers for the bottom and the top solar cell PCPDTBT:CIS and PBDTTT-C:CIS single solar cells were investigated in the next step. Different polymer to inorganic ratios and different layer thicknesses were tested, leading to poor power conversion efficiencies of 0.14% for PCPDTBT:CIS and 0.16% for PBDTTT-C:CIS single devices. Due to the low efficiencies of the hybrid solar cells consisting of PCPDTBT or PBDTTT-C and CIS, these polymers were not used for the fabrication of hybrid-hybrid tandem solar cells.

This study starts a new direction in research on *in situ* prepared nanocomposite solar cells. The presented concept of new precursors for metal sulphides in the combination with the hybrid-hybrid tandem solar cells provides the potential for further enhancement of light absorption. This can be achieved by the usage of two inorganic semiconducting materials with complementary absorption profiles in two absorber layers, as for example polymer/CIS as bottom active layer and polymer/ NIR-absorbing PbS[112] as top active layer. Nevertheless, further improvements of the single solar cells, as well as the detection of a suitable recombination layer for the tandem approach are necessary to make nanocomposite solar cell competitive to organic solar cells. An efficiency improvement of the single cells may be achieved by testing of various solvent additives, the usage of new solvent mixtures and the

investigation of a different temperature program, in order to affect the morphology of the nanocomposite and to minimize the surface roughness. Consequently further experiments have to be performed, to exhibit the hole potential of these *in situ* prepared nanocomposite solar cells.

# VI Appendix

## 1 List of abbreviations

| | |
|---|---|
| **a-Si** | amorphous silicon |
| **CB** | conduction band |
| **CIGS** | copper indium gallium diselenide |
| **CIS(e)** | copper indium diselenide |
| **CV** | cyclic voltammetry |
| **CZTS** | copper zinc tin sulphide |
| **DSSCs** | dye sensitized solar cells |
| **$E_g$** | band gap |
| **$E_{ff}$** | efficiency |
| **Et** | ethyl dithiocarbonate |
| **EQE** | external quantum efficiency |
| **FF** | fill factor |
| **FT-IR** | fourier transformation spectroscopy |
| **F8T2** | poly[(9,9-dioctylfluorenyl-2,7-diyl)-*co*-bithiophene] |
| **Hep** | o-2,2-dimethylpentane-3-yl dithiocarbonate |
| **Hex** | o-3,3-dimethylbutan-2-yl dithiocarbonate |
| **HOMO** | highest occupied molecular orbital |
| **HRMS** | high resolution mass spectroscopy |
| **$I_{sc}$** | short circuit current |
| **ITO** | indium tin oxide |
| **LUMO** | lowest unoccupied orbital |
| **MEH-PPV** | poly[2-methoxy-5-(2-ethylhexyloxy)-1,4-phenylenevinylene] |
| **NMR** | nuclear magnetic resonance spectroscopy |
| **PBDTTPD** | poly(di(2-ethylhexyloxy) benzo[1,2- *b* :4,5- *b* ′ ]dithiophene- *co* octylthieno[3,4-*c* ]pyrrole-4,6-dione) |
| **PCBM** | [6,6]-phenyl C61 butric acid methyl ester |
| **PCDTBT** | poly[*N*-9′-hepta-decanyl-2,7-carbazole-alt-5,5-(4′,7′-di-2-thienyl-2′,1′,3′-benzothiadiazole)] |
| **PCE** | power conversion efficiency |
| **PCPDTBT** | poly[2,6-(4,4-bis-(2-ethylhexyl)-4H-cyclopenta[2,1-b;3,4-b0]dithiophene)-alt-4,7-(2,1,3-benzothiadia- zole)] |
| **PDF** | powder diffraction file |
| **PDTPBT** | poly(2,6-( N -(1-octylnonyl)dithieno[3,2-b :20,30- d ]pyrrole)- alt -4,7-(2,1,3-benzothiadiazole)) |
| **PEDOT:PSS** | poly(3,4-ethylenedioxythiophene) poly(styrenesulfonate) |

| | |
|---|---|
| **PL** | photoluminescence |
| **$P_{max}$** | maximum power output |
| **PMMA** | poly(methylmethacrylate) |
| **PSBTBT** | poly[(4,4'-bis(2-ethylhexyl)dithieno[3,2-*b*:2',3'-*d*]silole)-2,6-diyl-alt-(2,1,3-benzothiadiazole)-4,7-diyl] |
| **PSiF-DBT** | poly[(2,7-silafluorene)-alt-(4,7-di-2-thienyl-2,1,3-benzothiadiazole |
| **PTB7** | poly({4,8-bis[(2-ethylhexyl)oxy]benzo[1,2-b:4,5-b']dithiophene-2,6-diyl}{3-fluoro-2-[(2-ethylhexyl)carbonyl]thieno [3,4-b]thiophenediyl}) |
| **P3HT** | poly(3-hexylthiophene-2,5-diyl) |
| **SAED** | electron diffraction image |
| **TEM** | transmission electron microscopy |
| **TOPO** | trioctylphosphine oxide |
| **VB** | valence band |
| **$V_{OC}$** | open circuit voltage |
| **XRD** | X-ray diffraction |

# 2 List of tables

# 3 List of figures

# 4 List of publications

*Publications which are relevant for this thesis:*

**Papers**

**2013**

V. Kaltenhauser, T. Rath, W. Haas, A. Torvisco-Gomez, B. Friedel, B. Kunert, R. Saf, F. Hofer, G. Trimmel: Bismuth sulphide/polymer nanocomposites from a highly soluble bismuth xanthate precursor, submitted.

V. Kaltenhauser, T. Rath, M. Edler, A. Reichmann, G. Trimmel: Exploring polymer/nanoparticle hybrid solar cells in tandem architecture*; RSC Adv*. **2013**, DOI: 10.1039/C3RA43842B.

T. Rath, V. Kaltenhauser, W. Haas, A. Reichmann, F. Hofer, G. Trimmel: Solution-processed small molecule/copper indium sulfide hybrid solar cells; *Sol. Energy Mater. & Sol. Cells* **2013**, *114*, 38–42.

**Posters**

**2013**

V. Kaltenhauser, M. Edler, T. Rath, A. Reichmann, W. Haas, F. Hofer, G. Trimmel: Nanocomposite tandem solar cells; MRS 2013 San Francisco.

**2012**

T. Rath, M. Edler, W. Haas, S. Moscher, A. Pein, V. Kaltenhauser, S. Dunst, M. Arar, C. Fradler, R. Saf, R. Trattnig, M. Jäger, M. Postl, M. Seidl, N. Bansal, S. A. Haque, F. Hofer, E. List, G. Trimmel: A Direct In Situ-Preparation Route for Organic-Inorganic Hybrid Solar Cells Based on Metal Sulfides and Conjugated Polymers; Plastic Electronics 2012 Dresden.

M. Arar, A. Pein, W. Haas, V. Kaltenhauser, C. Fradler, S. Dunst, F. Hofer, K. Norrman, F. C. Krebs, T. Rath, G. Trimmel: Fill Factor Enhancement for PSiF-DBT/CIS Solar Cells through Silver-modified Aluminum Electrodes; Plastic Electronics 2012 Dresden.

T. Rath, M. Arar, A. Pein, C. Fradler, V. Kaltenhauser, M. Edler, S. Moscher, R. Trattnig, E. List, W. Haas, S. Dunst, F. Hofer, G. Trimmel: Copper Indium Sulphide / Polymer Nanocomposite Solar Cells; 27th European PV Solar Energy Conference and Exhibition 2012 Frankfurt.

T. Rath, M. Edler, W. Haas, S. Moscher, R. Trattnig, M. Jäger, A. Pein, V. Kaltenhauser, S. Dunst, M. Arar, C. Fradler, R. Saf, M. Postl, M. Seidl, N. Bansal, S. A. Haque, F. Hofer, E. List, G.

Trimmel: Polymer / copper indium sulphide hybrid solar cells; EMRS Spring Meeting 2012 Straßburg.

**2011**

S. Dunst, S. Nestl, A. Pein, S. Moscher, V. Kaltenhauser, T. Rath, G. Trimmel: Influence of electrode materials and different interlayers on the stability of nanocomposite solar cells; ISOS-4 2011 Denver.

G. Trimmel, V. Kaltenhauser, S. Dunst, T. Rath, S. Moscher, A. Pein, W. Haas, F. Hofer: Influence of Different Interlayers on the Performance of Nanocomposite Solar Cells; 26th European Photovoltaic Solar Energy Conference and Exhibition (26th EU PVSEC) 2011 Hamburg.

V. Kaltenhauser, T. Rath, S. Dunst, S. Moscher, A. Pein, W. Haas, F. Hofer, G. Trimmel, G.: Influence of different interlayers on the performance of nanocomposite solar cells; EMRS Spring Meeting 2011 Nizza.

### Oral Presentation

**2012**

T. Rath, M. Arar, A. Pein, C. Fradler, V. Kaltenhauser, M. Edler, S. Moscher, R. Trattnig, E. List, W. Haas, S. Dunst, F. Hofer, G. Trimmel: Copper Indium Sulphide / Polymer Nanocomposite Solar Cells; 27th European PV Solar Energy Conference and Exhibition Frankfurt.

## *Further publications:*

### Papers

**2013**

A. Kelly, V. Kaltenhauser, I. Mühlbacher, K. Rametsteiner, H. Kren, C. Slugovc, F. Stelzer, F. Wiesbrock: Poly(2-Oxazoline)-Derived Contact Biocides: Contributions to the Understanding of Antimicrobial Activity; *Macromol. Biosci*. **2013**, *13* 116-125.

**2012**

F. Wiesbrock, A. Kelly, K. Rametsteiner, V. Kaltenhauser, F. Stelzer, Microwave-Assisted Syntheses and Applications of Poly(2-Oxazoline)-Derived Contact Biocides.; *Polymer Preprint.* **2012**, *53*, 321-322.

## Posters

### 2012

A. Kelly, V. Kaltenhauser, F. Stelzer, F. Wiesbrock: Microwave-Assisted Synthesis of Poly(2-Oxazoline)-Derived Contact Biocides; Microwave & Flow Chemistry Conference 2012 Lanzarote.

### 2010

V. Kaltenhauser, E. Kreutzwiesner, C. Slugovc, F. Stelzer, F. Wiesbrock: New Potential Antimicrobial Compounds; Austrian-Slovenian Polymer Meeting ASPM 2010. Leoben.

## Oral presentations

### 2013

A. Kelly, V. Kaltenhauser, F. Stelzer, F. Wiesbrock: Surface Equipment with Poly(2-oxazoline)-Based Contact Biocides; Advanced Polymers via Macromolecular Engineering (APME)2013 Durham

F. Wiesbrock, A. Kelly, V. Kaltenhauser, I. Mühlbacher: Poly(Ethylene Imine)-Derived Contact Biocides: Fabrication of Antimicrobially Active Surfaces; Austrian-Slovenian Polymer Meeting (ASPM) 2013 Bled.

F. Wiesbrock, A. Kelly, V. Kaltenhauser: Microwave-Assisted Synthesis of Contact Biocides; Microwave & Flow Chemistry 2013 Napa CA.

### 2012

F. Wiesbrock, A. Kelly, K. Rametsteiner, V. Kaltenhauser, F. Stelzer: Microwave-Assisted Synthesis and Applications of Poly(2-Oxazoline)-Derived Contact Biocides; ACS Spring meeting 2012 San Diego CA.

A. Kelly, V. Kaltenhauser, F. Stelzer, F. Wiesbrock: Microwave-Assisted Synthesis of Poly(2-Oxazoline)-Derived Contact Biocides (Poster Highlight); Microwave & Flow Chemistry Conference 2012 Lanzarote.

### 2011

F. Wiesbrock, A. Kelly, V. Kaltenhauser, F. Stelzer: Novel Poly(2-Oxazoline)-Derived Contact Biocides; Advanced Polymers Through macromolecular Engineering 2011 Cappadocia.

J. Kienberger, A. Dunst, E. Kreutzwiesner, N. Noormofidi, V. Kaltenhauser, A. Kelly, F. Wiesbrock, C. Slugovc, F. Stelzer: Battle against bacteria – biocide polyolefin compounds; Advances in Polymer Science and Technology (APST) 2011 Linz.

F. Wiesbrock, A. Kelly, V. Kaltenhauser, K. Rametsteiner, F. Stelzer: Microwave-Assisted Fabrication of Novel Polymer Contact Biocides; 14. Österreichische Chemietage 2011 Linz.

## Patents

### 2011

F. Wiesbrock, F. Stelzer, C. Slugovc, N. Noormofidi, V. Kaltenhauser, E. Kreutzwiesner, K. Rametsteiner: Use of Contact Biocides Based on Poly(2-Substuituted) Oxazolines. WO2012/149591.

# 5 Curiculum Vitae

*Personal Details*

| | |
|---|---|
| Name | Verena Kaltenhauser |
| Address | Ginzkeygasse 1, 8045 Graz |
| Mail | kaltenhauser@tugraz.at |
| Date of birt | 21.03.1987 |
| Citizenship | Austria |

*Education and Qualifications*

| | |
|---|---|
| 1993-1997 | Elementary school in Andritz, Graz |
| 1997-2005 | Secondary school in BG/BRG Kirchengasse, Graz |
| 2005-2010 | Graz University of Technology – Technical Chemistry |
| 2009-2010 | Diploma Thesis: Potential new antimicrobial compounds |
| 2010-2013 | PhD thesis at Graz University of Technology (PhD supervisor: Assoc. Prof. DI Dr. Gregor Trimmel) |

# 6 Bibliography

[1] www.bu.edu: The Climate Crisis, Breaking the Fossil Fuel Habit.

[2] J. Weickert, R. B. Dunbar, H. C. Hesse, W. Wiedemann, L. Schmidt-Mende *Adv. Mater.* **2011**, *23*, 1810-1828.

[3] M. Graetzel *Nature* **2001**, *414*, 338-344.

[4] M. A. Green *Physica E* **2002**, *14*, 65-70.

[5] M. A. Green, K. Emery, Y. Hishikawa, W. Warta, E. D. Dunlop *Prog. Photovolt.: Res. Appl.* **2013**, *21*, 1-11.

[6] M. P. Suryawanshi, G. L. Agawane, S. M. Bhosale, S. W. Shin, P. S. Patil, J. H. Kim, A. V. Moholkar *Mater. Tech.* **2013**, *28*, 98-109.

[7] M. Graetzel *Inorg. Chem.* **2005**, *44*, 6841-6851.

[8] S. Günes, H. Neugebauer, N. S. Sariciftci *Chem. Rev.* **2007**, *107*, 1324-1338.

[9] E. Martínez-Ferrero, J. Albero, E. Palomares *J. Phys. Chem. Lett.* **2010**, *1*, 3039-3045.

[10] F. Gao, Y. Wang, D. Shi, J. Zhang, M. K. Wang, X. Y. Jing, R. Humphry-Baker, P. Wang, S. M. Zakeeruddin, M. Graetzel *J. Am. Chem. Soc.* **2008**, *130*, 10720-10728.

[11] G. Li, R. Zhu, Y. Yang *Nat. Photon.* **2012**, *6*, 153-161.

[12] M. A. Green, K. Emery, Y. Hishikawa, W. Warta, E. D. Dunlop *Prog. Photovolt: Res. Appl.* **2012,** *20*, 606-614.

[13] T. Rath, G. Trimmel *Hybrid Mater.* **2013***, 1*, 15-36.

[14] H. C. Leventis, S.P. King, A. Sudlow, M.S.Hill, K.C. Molloy, S.A. Haque *Nano. Lett*. **2010**, *10*, 1253-1258.

[15] T. Rath, M. Edler, W. Haas, A. Fischereder, S. Moscher, A. Schenk, R. Trattnig, M. Sezen, G. Mauthner, A. Pein, D. Meischler, K. Bartl, R. Saf, N. Bansal, S.A. Haque, F. Hofer, E.J.W. List, G. Trimmel *Adv. Energy Mater*. **2011**, *1*, 1046-1050.

[16] L. Persano, A. Composeo, F. Di Benedetto, R. Stabile, A. M. Laera, E. Piscopiello, L. Tapfer, D. Pisignano *Adv. Mater*. **2012**, *24*, 5320-5326.

[17] C. De Mello Donegá *Chem. Soc. Rev*. **2011**, *40*, 1512-1546.

[18] R. Pardo, M. Zayat, D. Levy *Chem. Soc. Rev*. **2011**, *40*, 672-687.

[19] B. Lebeau, S. Brasselet, J. Zyss, C. Sanchez *Chem. Mater*. **1997**, *9*, 1012-1020.

[20] T.-P. Nguyen *Surf. Coating Technol*. **2011**, *206*, 742-752.

[21] C. Sanchez, B. Lebeau, F. Chaput, J.-P. Boilot *Adv. Mater*. **2003**, *15*, 1969-1994.

[22] T. Xu, Q. Qiao *Energ. Environ. Sci*. **2011**, *4*, 2700-2720.

[23] L. E. Brus *J. Chem. Phys*. **1984**, *80*, 4403-4409.

[24] V. Coropceanu, J. Cornil, D. A. da Silva Filho, Y. Olivier, R. Silbey, J.-L. Brédas *Chem. Rev*. **2007**, *107*, 926-952.

[25] Y. Zhou, M. Eck, M. Krüger *Energ. Environ. Sci.* **2010**, *3*, 1851-1864.

[26] N. C. Greenham, X. Peng, A. P. Alivisatos *Phys. Rev. B* **1996**, *54*, 17628-17637.

[27] S. Ren, L. Y. Chang, S.-K. Lim, J. Zhao, M. Smith, N. Zhao, V. Bulovic, M. Bawendi, S. Gradečak *Nano. Lett*. **2011**, *11*, 3998-4002.

[28] K. F. Jeltsch, M. Schädel, J.-B. Bonekamp, P. Niyamakom, F. Rauscher, H. W. A. Lademann, I. Dumsch, S. Allrad, U. Scherf, K. Meerholz *Adv. Funct. Mater* **2012**, *22*, 397-404.

[29] R. Zhou, Y. Zheng, L. Qian, Y. Yang, P. H. Holloway, J. Xue *Nanoscale*, **2012**, *4*, 3507-3514.

[30] R. Zhou, R. Stalder, D. Xie, W. Cao, Y. Zheng, Y. Yang, M. Plaisant, P.H. Holloway, K.S. Schanze, J.R. Reynolds, J. Xue *ACS Nano* **2013**, *7*, 4846-4854.

[31] Z. Chen, H. Zhang, X. Du, X. Cheng, X. Chen, Y. Jiang, B. Yang, *Energy Environ. Sci*. **2013**, *6*, 1597-1603.

[32] S.-S. Sun, N. S. Sariciftci: *Organic Photovoltaics, Mechanisms, Materials and Devices*, **2005**, Taylor & francis Group, p. 218.

[33] B. R. Saunders *J. Coll. Interf. Sci*. **2012**, *369*, 1-15.

[34] B. R. Saunders, M. L. Turner *Adv. Coll. Interf. Sci.* **2008**, *138*, 1-23.

[35] M. Wright, A. Uddin *Sol. Energ. Mater. Sol. Cell.* **2012**, *107*, 87-111.

[36] A. J. Moulé, L. Chang, C. Thambidurai, R. Vidu, P. Stroeve *J. Mater. Chem*. **2012**, *22*, 2351-2368.

[37] B. J. Schwartz *Annu. Rev. Phys. Chem.* **2003**, *54*, 141-172.

[38] G. Gustafsson, Y. Cao, G. M. Treacy, F. Flaveter, N. Colinari, A. J. Heeger *Nature* **1992**, *357*, 477-479.

[39] J. H. Burroughes, D. D. C. Bradley, A. R. Brown, R. N. Marks, K. Mackay *Nature* **1990**, *347*, 539-541.

[40] C. J. Brabec, N. S. Sariciftci, J. C. Hummelen *Adv. Funct. Mater*. **2001**, *11*, 15-26.

[41] H. E. A. Huitema, G. H. Gelinck, P. H. van der Putten, K. E. Kuijk, C. M. Hart *Nature* **2001**, *414*, 599.

[42] E. M. Galand, Y. G. Kim, J. K. Mwaura, A. G. Jones, T. D. McCarley, V. Shrotriya *Macromol.* **2006**, *39*, 9132-9142.

[43] D. Mulbacher, M. C. Scharber, M. Morana, Z. Zhu, D. Waller, R. Gaudiana *J. Adv. Mater*. **2006**, *18*, 2884-2889.

[44] A. J. Ferguson, N. Kopidakis, S. E. Shaheen, G. Rumbles *J. Phys. Chem. C* **2008**, *112*, 9865-9871.

[45] X. J. Wang, E. Perzon, J. L. Delgado, P. de la Cruz, F. L. Zhang, F. Langa, M. Andersson, O. Inganas *Appl. Phys. Lett*. **2004**, *85*, 5081-5083.

[46] L. M. Campos, A. Tontcheva, S. Gunes, G. Sonmez, H. Neugebauer, N. S. Sariciftci, F. Wudl *Chem. Mater*. **2005**, *17*, 4031-4033.

[47] F. Zhang, W. Mammo, L. M. Andersson, S. Admassie, M. R. Andersson, O. Inganas *Adv. Mater.* **2006**, *18*, 2169-2173.

[48] J. Y. Kim, K. Lee, N. E. Coates, D. Moses, T. Q. Nguyen, M. Dante, A. J. Heeger *Science* **2007**, *317*, 222-225.

[49] E. Havinga, W. ten Hoeven, H. Wynberg *Polym. Bull.* **1992**, *29*, 119-126.

[50] E. Havinga, W. ten Hoeven, H. Wynberg *Synth. Met*. **1993**, *55*, 299-306.

[51] M. Jayakannan, P. A. Van Hal, R. A. J. Janssen *J. Polym. Sci. A: Polym. Chem.* **2001**, *40*, 251−261.

[52] S. A. Jenekhe, L. Lu, M. M. Alam *Macromol.* **2001**, *34*, 7315−7324.

[53] X. Guo, M. D. Watson *Macromol.* **2011**, *44*, 6711−6716.

[54] E. Wang, Z. Ma, Z. Zhang, K. Vandewal, P. Henriksson, O. Inganäs, F. Zhang, M. R. Andersson *J. Am. Chem. Soc*. **2011**, *133*,14244−14247.

[55] B. Burkhart, P. Khlyabich, T. Canak, T. LaJoie, B. C. Thompson *Macromol.* **2011**, *44*, 1242−1246.

[56] G. L. Gibson, T. M. McCormick, D. S. Seferos *J. Am. Chem. Soc*. **2012**, *134*, 539-547.

[57] G. Öktem, A. Balan, D. Baran, L. Toppare *Chem. Commun*. **2011**, *47*, 3933.

[58] C. Shen, Y. Rubin, F. Wudl *Angew. Chem*. **2004**, *116*, 1524− 1528.

[59] A. W. Hains, Z. Liang, M. A. Woodhouse, B. A. Gregg *Chem. Rev*. **2010**, *110*, 6689−6735.

[60] P. M. Beaujuge, J. Subbiah, K. R. Choudhury, S. Ellinger, T. D. McCarley, F. So, J. R. Reynolds *Chem. Mater*. **2010**, *22*, 2093−2106.

[61] J. Boucle, S. Chyla, M. S. P. Schaffer, J. R. Durrant, D. D. C. Bradley, J. Nelson *Adv. Funct. Mater.* **2008**, *18*, 622-633.

[62] W. J. E. Beek, M. M. Wienk, R. A. Janssen *Adv. Mater*. **2004**, *16*, 1009-1013.

[63] W. J. E. Beek, M. M. Wienk, R. A. Janssen *Adv. Funct. Mater*. **2006**, *16*, 1112-1116.

[64] W. U. Huynh, J. J. Dittmer, A. P. Alivisatos *Science* **2002**, *295*, 2425-2427.

[65] D. Qi, M. Fischbein, M. Drndic, S. Šelmic *Appl. Phys. Lett*. **2005**, *86*, 093103.

[66] K. R. Chodhury, Y. Sahoo, T. Y. Ohulchanskyy, P. N. Prasad *Appl. Phys. Lett*. **2005**, *87*, 073110.

[67] B. Sun, H. J. Snaith, A. S. Dhoot, S. Westenhoff, N. C. Greenham *J. Appl. Phys*. **2005**, *97*, 014914.

[68] T.-W. F. Chang, S. Musikhin, L. Bakueva, L. Levina, M. A. Hines, P. W. Cyr, E. H. Sargent *Appl. Phys. Lett.* **2004**, *84*, 4295-4297.

[69] Y. Zhou, F. S. Riehle, Y. Yuan, H.-F. Schlerermacher, M. Niggemann, G. A. Urban, M. Krüger *Appl. Phys. Lett*. **2010**, *96*, 013304-013303.

[70] J. Seo, W. J. Kim, S. J. Kim, K.-S. Lee, A. N. Cartwright, P. N. Prasad *Appl. Phys. Lett*. **2009**, *94*, 133302.

[71] T. Antoun, R. Brayner, S. Al Terary, F. Fiévet, M. Chehimi, A. Yassar *Eur. J. Inorg. Chem*. **2007**, *46*, 1275-1284.

[72] L. Locklin, D. Patton, S. Deng, A. Baba, M. Millan, R. C. Advincula *Chem. Mater*. **2004**, *16*, 5187-5193.

[73] P. A. van Hal, M. M. Wienk, J. M. Kroon, W. J. H. Verhees, L. H. Sloof, W. J. H. van Gennip, P. Jonkheijm, R. A. J. Janssen *Adv. Mater*. **2003**, *15*, 118-121.

[74] V. Barlier, V. Bounor-Legare, G. Boiteux, D. Leonard, J. Davenas *Mater. Chem. Phys*. **2009**, *115*, 429-433.

[75] W. J. E. Beek, L. H. Sloof, M. M. Wienk, J. M. Kroon, R. A. J. Janssen *Adv. Funct. Mater*. **2005**, *15*, 1703-1707.

[76] A. A. R. Watt, P. Meredith, J. D. Riches, S. Atkinson, H. Rubinsztein-Dunlop Curr. *Appl. Phys.* **2004**, *4*, 320-322.

[77] P. Sonar, K. P. Sreenivasan, T. Maddanimath, K. Vijayamohanan *Mater. Res. Bull*. **2006**, *41*, 198-208.

[78] E. Maier, A. Fischereder, W. Haas, G. Mauthner, J. Albering, T. Rath, F. Hofer, E. J. W. List, G. Trimmel *Thin Solid Films* **2011**, *519*, 4201-4206.

[79] E. Maier, T. Rath, W. Haas, O. Werzer, R. Saf, F. Hofer, D. Meissner, O. Volobujeva, S. Bereznev, S. Mellikov, H. Amenitsch, R. Resel, G. Trimmel *Sol. Energ. Mater. Sol. Cell.* **2011**, *95*, 1354-1361.

[80] N. Wolf, D. M. Roundhill *Polyhedron* **1994**, *13*, 2801-2808.

[81] X. H. Jiang, W. G. Zhang, Y. Zhong, S. L. Wang *Molecules* **2002**, *7*, 549-553.

[82] S. S. Garje, V. K. Jain *Coord. Chem. Rev* **2003**, *236*, 35-56.

[83] L. Tschugaeff *Berichte Der Deutschen Chemischen Gesellschaft* **1899**, *32*, 3332-3335.

[84] Y. Wu, C. Wadia, W. L. Ma, B. Sadtler, A. P. Alivisatos *Nano. Lett*. **2008**, *8,* 2551-2555.

[85] T. L. Li, Y. L. Lee, H.S. Teng *J. Mater. Chem*. **2011**, *21*, 5089-5098.

[86] M. J. Bierman, S. Jin *Energ. Environ. Sci.* **2009**, *2*, 1050-1059.

[87] C.-H. Lai, M.-Y. Lu, L.-J. Chen *J. Mater. Chem.* **2012**, *22*, 19-30.

[88] S. Dowland, T. Lutz, A. Ward, S. P. King, A.Sudlow, M. S. Hill, K. C. Molloy, S. A. Haque *Adv. Mater.* **2011**, *23*, 2739-2744.

[89] N. Bansal, F.T.F. O'Mahony, T. Lutz, S.A. Haque *Adv. Energy Mater*. **2013**, DOI: 10.1002/aenm.201300017.

[90] C. Deibel, V. Dyakonov *Rep. Prog. Phys*. **2010**, *73*, 096401.

[91] M. Al-Ibrahim, O. Ambacher, S. Sensfuss, G. Gobsch *Appl. Phys. Lett.* **2005**, *86*, 201120-201123.

[92] Y. Kim, S. A. Choulis, J. Nelson, D. D. C. Bradley, S. Cook, J. R. Durrant *Appl. Phys. Lett*. **2005**, *86*, 063502-063503.

[93] G. Li, Y. Yao, H. Yang, V. Shrotriya, G. Yang, Y. Yang *Adv. Funct. Mater*. **2007**, *17*, 1636-1644.

[94] D. J. D. Moet, M. Lenes, J. D. Kotlarski, S. C. Veenstra, J. Sweelssen, M. M. Koetse, B. de Boer, P. W. M. Blom *Org. Electron***. 2009**, *10*, 1275-1281.

[95] C. Müller, E. Wang, L. M. Andersson, K. Tvingstedt, Y. Zhou, M. R. Andersson, O. Inganas *Adv. Funct. Mater.* **2010**, *20*, 2124-2131.

[96] M. K. Siddiki, J. Li, D. Galipeau, Q. Qiao *Energ. Environ. Sci*. **2010**, *3*, 867-883.

[97] S. Shockley, H. J. Queissner *J. Appl. Phys*. **1961**, *32*, 510-519.

[98] T. Ameri, G. Dennler, C. Lungenschmied, C. J. Brabec *Energ. Environ. Sci*. **2009**, *2*, 347-363.

[99] A. De Vos *J. Phys. D: Appl. Phys*. **1980**, *13*, 839-846.

[100] S. Sista, Z. Hong, L-M. Chen, Y. Yang, *Energ. Environ. Sci*. **2011**, *4*, 1606-1620.

[101] C. Zhang, S. W. Tong, C. Jiang, E. T. Kang, D. S. H. Chan, C. Zhu *Appl. Phys. Lett*. **2008**, *92*, 083310.

[102] N. Pradhan, B. Katz, S. Efrima *J. Phys. Chem. B* **2003**, *107*, 13843 – 13854.

[103] K. Xu, W. Ding *Mater. Lett.* **2008**, *62*, 4437-4439

[104] D. P. Dutta, G. Sharma, S. Ghoshal, N.P. Kushwah, V.K. Jain *J. Nanosci. Nanotech*. **2006**, *6*, 235-240

[105] M. Tejos, B.G. Rolon, R. del Rio, G. Cabello *Mater. Sci. Semicond. Process*. **2008**, *11*, 94-99

[106] A. González – Roura, J. Casas, A. Liberia *Lipids* **2002***, 37*, 401 – 406.

[107] P. S. Nair, T. Radhakrishnan, N. Revaprasadu, G. Kolawole, P. O´Brien *J. Mater. Chem*. **2002**, *12*, 2722-2725.

[108] A. Fischereder, Ph.D. Thesis, TU Graz, Graz, 2011.

[109] Y.Li, Y. Zhang, Y. Lei, P. Li, H. Jia, H. Hou, Z. Zheng *Mater.Sci. Eng.B* **2012**, *177*, 1764-1768.

[110] Z. Wang, S. Qu, X. Zeng, J. Liu, F. Tan, L. Jin, Z. Wang *Appl. Surf. Sci.* **2010**, *257*, 423–428.

[111] J. A. Chang, J. H. Rhee, S. H. Im, Y. H. Lee, H.-j. Kim, S. I. Seok, M. K. Nazeeruddin, M. Gratzel *Nano Lett*. **2010**, *10*, 2609-2612.

[112] J. Seo, M. J. Cho, D. Lee, A. N. Cartwright, P. N. Prasad *Adv. Mater*. **2011**, *23*, 3984-3988.

[113] E. J. D. Klem, C. W. Gregory, G. B. Cunningham, S. Hall, D. S. Temple, J. S. Lewis *Appl. Phys. Lett*. **2012**, *100*, 173109.

[114] D. Noureldine, T. Shoker, M. Musamehb, T. H. Ghaddar *J. Mater. Chem*. **2012**, *22*, 862–869.

[115] K. Anuar, Z. Zulkarnain, N. Saravanan, A. Zuriyatina, R. Sharin *Mater. Sci*. **2004**, *10*,

1320-1392.

[116] Z. Yu, J. Du, S. Guo , J. Zhang , Y. Matsumoto *Thin Solid Films* **2002**, *415*, 173–176.

[117] A.U. Ubale, A.N. Bargal *Mater. Res. Bull.* **2011**, *46*, 1000–1010

[118] D. Barreca, A. Gasparotto, C. Maragno, R. Seraglia, E. Tondello, A. Venzo, V. Krishnan, H. Bertagnolli *Appl. Organometal. Chem*. **2005**, *19*, 59-67.

[119] M. R. Hunt, A. G. Krüger, L. Smith, G. Winter *Aust. J. Chem*. **1971**, *24*, 53-57.

[120] L. H. Little, G. W. Poling, J. Leja Can. *J. Chem*. **1961**, *29*, 745-754.

[121] M. L. Shankaranarayana, C. C. Patel *Can. J. Chem*. **1961**, *39*, 1633-1637.

[122] A. J. Vreugdenhil, S. H. R. Brienne, I. S. Butler, J. A. Finch, R. D. Markwell *Spectrochim. Acta Part A* **1997**, 2139-2151.

[123] U. Agarwala, R.P.B. Lakshimi *Inorg. Chim. Acta* **1968**, *2*, 337-339.

[124] L. H. Wee, L. C. Sing, E. R. T. Tiekink "*Synthesis and characterisation of antimony thiolates*" National University of Singapore, Singapore.

[125] A. Schenk, Diploma Thesis, TU Graz, Graz, **2011**.

[126] N.A. Khwaja, T.J. Cardwell, R.J. Magee *Anal. Chim.Acta* **1973**, *64*, 9-17.

[127] C. L. Raston, A. H. White *J. Chem. Soc. Dalton Trans*. **1976**, 791-794.

[128] M. R. Snow, E. R. T. Tiekink *Aust. J. Chem*. **1987**, *40*, 743-750.

[129] Y. Li, Y. Zhang, Y. Lei, P. Li, H. Jia, H. Hou, Z. Zheng *Mater. Sci. Eng. B* **2012**, http://dx.doi.org/10.1016/j.mseb.2012.08.16

[130] J. Liu, E. N. Kadnikova, Y. Liu, M. D. McGehee, J. M. J. Frechet *J. Am. Chem. Soc.* **2004**, *126*, 9486-7.

[131] K. M. Coakley, M. D. McGehee *Apll. Phys. Lett.* **2003**, *83*, 3380.

[132] L. Baeten, B. Conings, H.-G. Boyen, J. D'Haen, A. Hardy, M. D'Olieslaeger, J. V. Manca, M. K. Van Bael *Adv.Mater* **2011**, *23*, 2802-5.

[133] M. Y. Versavel, J. A. Haber *Thin Solid Films* **2007**, *515*, 7171-7176.

[134] Z. R. Geng, M. X. Wang, G. H. Yue, P. X. Yan *J. Christ. Growth* **2008**, *310*, 341-344.

[135] A. M. Salem, M. S. Selim *J. Phys. D: Appl. Phys*. **2001**, *34*, 12–17.

[136] M. Lajnef, H. Ezzaouia *J. Open Appl. Phys*. **2009**, *2*, 23-26.

[137] G.-Y. Liu, L.-Y. Xu, F. Zhou, Y. Zhang, H. Li, Y. F. Xu and J. M. Lu *Phys. Chem. Chem. Phys*. **2013**, *15*, 11554-11558.

[138] A. K. Rath, M. Bernechea, L. Martinez and G. Konstantatos *Adv. Mater*. **2011**, *23*, 3712-3717.

[139] L. Martínez, A. Stavrinadis, S. Higuchi, S. L. Diedenhofen, M. Bernechea, K. Tajima, G. Konstantatos *Phys. Chem. Chem. Phys*. **2013**, *15*, 5482-5487.

[140] A. Guchhait, A. K. Rath, A. J. Pal *Sol. Energ. Mater. Sol. Cell.* **2011**, *95*, 651-656.

[141] B. Y. Liang, Z. Xu, J. Xia, S.-T. Tsai, Y. Wu, G. Li, C. Ray, L. Yu *Adv. Mater.* **2010**, *22*, E135-E138.

[142] E. Wang, L. Wang, L. Lan, . Luo, W. Zhuang *Appl. Phys. Lett*. **2008**, *92*, 033307.

[143] E. Arici, N. S. Saricifci, D. Meissner *Adv. Funct. Mater*. **2003**, *13*, 165-171.

[144] J.-H. Kim, J. H. Park, J. H. Lee, J. S. Kim, M. Sim, C. Shima, K. Cho *J. Mater. Chem.* **2010**, 20, 7398-7405.

[145] V. Kaltenhauser, T. Rath, M. Edler, A. Reicmann, G. Trimmel *RCS. Adv*. **2013**, DOI: 10.1039/C3RA4382B.

[146] J. Tang, A. P. Alivisatos *Nano Lett*. **2006**, *6*, 2701-2706.

[147] Q. Han, J. Chen, X. Yang, L. Lu, X. Wang *J. Phys. Chem. C* **2007**, *111*, 14072-14077.

[148] W. Lou, M. Chen, X. Wang, W. Liu *Chem. Mater*. **2007**, *19*, 872-878.

[149] H.-C. Liao, M.-C. Wu, M.-H. Jao, C.-M. Chuang, Y.-F. Chen and W.-F. Su *Cryst. Eng. Comm.* **2012**, *14*, 3645-3652.

[150] S. A. McDonald, G. Konstantos, S. Zhang, P. W. Cyr, E. L. D. Klem, L. Levina, E. H. Sargent *Nature Mater*. **2005***, 4*, 138-142.

[151] S. M. Sze: "*Physics of Semiconductor Devices"* Wiley Interscience, New York, **1981**.

[152] I. Moreels, K. Lambert, D. Smeets, D. D. Muynck, T. Nollet, J. C. Martins, F. Vanhaecke, A. Vantomme, C. Delerue, G. Allan, Z. Hens *ACS Nano* **2009**, *3*, 3023-3030.

[153] A. Guchhait, A. K. Rath, A. J. Pal *Appl. Phys. Lett*. **2010**, *96*, 073505.

[154] K. M. Noone, N. C. Anderson, N. E. Horwitz, A. M. Munro, A. P. Kulkarni, D. S. Ginger *ACS Nano* **2009**, *2,* 1345-1352.

[155] S. A. McDonald, P. W. Cyr, L. Levina, E. H. Sargent *Appl. Phys. Lett*. **2004***, 85*, 2089-2091.

[156] S. Günes, K. P. Fritz, H. Neugebauer, N. S. Sariciftci, S. Kumar, G. D. Scholes *Sol. Energ. Mater. Sol. Cell.* **2007**, *91*, 420-423.

[157] S.-J. Moon, Y. Itzhaik, J.-H. Yum, S. M. Zakeeruddin, G. Hodes, M. Grätzel *J. Phys. Chem. Lett.* **2010**, *1*, 1524-1527.

[158] J. A. Chang, S. H. Im, Y. H. Lee, H.-J. Kim, C.-S. Lin, J. H. Heo, S. I. Seok *Nano. Lett*. **2012**, *12*, 1863-1867.

[159] T. Lutz, A. MacLachlan, A.Sudlow, J. Nelson, M. S. Hill, K. C. Molloy, S. A. Haque *Phys. Chem. Chem. Phys.* **2012**, *14*, 16192-16196.

[160] P. P. Boix, G. Larramona, A. Jacob, B. Delatouche, I. Mora-Ser, J. Bisquert *J. Phys. Chem. C* **2011**, dx.doi.org/10.1021/jp210002c.

[161] T. Rath, B. Kunert, R. Resel, G. Fritz-Popovski, R. Saf, G. Trimmel *Inorg. Chem*. **2008**, *47*, 3014-3022.

[162] J. L. Shay, B. Tell *Surf. Sci.* **1973**, *37*, 748-762.

[163] R. H. Bube, W. H. McCaroll *J. Phys. Chem. Solids* **1959**, *10*, 333-335.

[164] D. Hariskos, S. Spiering, M. Powalla *Thin Solid Films* **2005,** *480*, 99-109.

[165] H. Jia, W. He, X. Chen, Y. Lei, Z. Zheng *J. Mater. Chem*. **2011**, *21*, 12824-12828.

[166] J. Gilot, M. M. Wienk, R. A. J. Janssen *Adv. Energ. Mater*. **2010**, *22*, E67-E71.

[167] T. T. Larsen-Olsen, E. Bundgaard, K. O. Sylvester-Hvid, F. C. Krebs *Org. Electron.* **2011**, *12*, 364-371.

[168] Z. He, C. Zhong, S. Su, M. Xu, H. Wu, Y. Cao *Nat. Photon.* **2012**, *6*, 591-595.

[169] Press release – Heliatek, http://www.heliatek.com/newscenter/latest_news/neuer-weltrekord-fur-organische-solarzellen-heliatek-behauptet-sich-mit-12-zelleffizienz-als-technologiefuhrer/?lang=en, accessed on March 25, 2013.

[170] R. Zhou, J. Xue *Chem. Phys. Chem*. **2012**, *13*, 2471-3480.

[171] L. Zhao, Z. Lin *Adv. Mater*. **2012**, *24*, 4353-4368.

[172] S. D. Oosterhout, M. M. Wienk, S. S. van Bavel, R. Thiedmann, L. J. A. Koster, J. Gilot, J. Loos, V. Schmidt, R. A. J. Janssen *Nat. Mater*. **2009**, *8*, 818-824.

[173] Y. Zhou, M. Eck, C. Men, F. Rauscher, P. Niyamakom, S. Yilmaz, I. Dumsch, S. Allard, U. Scherf, M. Krüger *Sol. Energ. Mater. Sol. Cell.* **2011**, *95*, 3227-3232.

[174] S. Dayal, N. Kopidakis, D. C. Olson, D. S. Ginley, G. Rumbles *Nano Lett*. **2010**, *10*, 239-242.

[175] L. X. Reynolds, T. Lutz, S. Dowland, A. MacLachlan, S. King, S. A. Haque *Nanoscale* **2012**, *4*, 1561-1564.

[176] T. Rath, V. Kaltenhauser, W. Haas A. Reichmann, F. Hofer, G. Trimmel *Sol. Energ. Mater. Sol. Cell.* **2013**, *114*, 38-42.

[177] M. Arar, A. Pein, W. Haas, F. Hofer, K. Norrman, F. C. Krebs, T. Rath, G. Trimmel *J. Phys. Chem. C* **2012**, *116*, 19191-19196.

[178] S. D. Oosterhout, M. M. Wienk, M. Al-Hashimi, M. Heeney, R. A. J. Janssen *J. Phys. Chem.* **2011***, 115*, 18901-18908.

[179] A. Yakimov, S. R. Forrest *Appl. Phys. Lett.* **2002**, *80*, 1667-1669.

[180] M. Hiramoto, M. Suezaki, M. Yokoyama *Chem. Lett.* **1990**, *19*, 327-330.

[181] J. H. Seo, D.-H. Kim, S.-H. Kwon, M. Song, M.-S. Choi, S. Y. Ryu, H. W. Lee, Y. C. Park, J.-D. Kwon, K.-S. Nam, Y. Jeong, J.-W. Kang, C. S. Kim *Adv. Mater.* **2012**, *24*, 4523-4527.

[182] D. W. Zhao, X. W. Sun, C. Y. Jiang, A. K. K. Kyaw, G. Q. Lo, D. L. Kwong *Appl. Phys. Lett.***2009***, 93*, 083305.

[183] T. Kim, J. H. Jeon, S. Han, D.-K. Lee, H. Kim, W. Lee, K. Kim *Appl. Phys. Lett*. **2011**, *98*, 183503.

[184] J. Sakai, K. Kawano, T. Yamanari *Sol. Energ. Mater. Sol. Cell.* **2010**, *94*, 376-380.

[185] J. Gilot, M. M. Wienk, R. J. Janssen *Appl. Phys. Lett.* **2007**, *90*, 143512.

[186] M. Polak, Ph.D. Thesis, Ernst-Moritz-Arndt University Greifswald, **2009.**

[187] B. Kasemo, J. Lausmaa *J. Biomed. Mater.* **1988**, *22*, 145-158.

[188] F.-C. Chen, C.-H. Lin *J. Phys. D: Appl. Phys.* **2010**, *43*, 025104.

[189] F.-C.Chen, J.-L. Wu, S. S. Yang, K.-H. Hsieh, W.-C. Chen *J. Appl. Phys*. **2008**, *103*, 103721.

[190] K. Zilberberg, S. Trost, H. Schmidt , T. Riedl *Adv. Energ. Mater***. 2011**, *1*, 377–381

[191] J. Kettle, H. Waters, M. Horie, S.-W. Chang *J. Phys. D: Appl. Phys*. **2012**, *45*, 125102.

[192] Y. Gu , C. Wang, T. P. Russell *Adv. Energ. Mater*. **2012**, *2*, 683–690.

[193] X. W. Xu, E.W. Zhu, L.Y. Bian, Z. X. Wang, J. Wang, Z. L. Zhuo, J. Wang, F. J. Zhang, W. H. Tang *Chin Sci Bull*. **2012**, *57*, 970-975.

[194] H.-Y. Chen, J. Hou, S. Zhang, Y. Liang, G. Yang, Y. Yang, L. Yu, Y. Wu, G. Li *Nat. Photon*.**2009**, *3*, 649-653.

[195] J. Peet, J.Y. Kim, N.E. Coates, W.L. Ma, D. Moses, A.J. Heeger, G.C. Bazan *Nat. Mater*. **2007**, *6,* 497–500.

[196] C. Soci, I.W. Hwang, D. Moses, Z. Zhu, D. Waller, R. Gaudiana, C.J. Brabec, A.J. Heeger, *Adv.Funct. Mater.* 2007, *17*, 632–636.

[197] J. Hou, H.-Y. Chen, S. Zhang, R. I. Chen, Y. Yang, Y. Wu, G. Li *J. Am. Chem. Soc.* **2009**, *131*, 15886-15887.

[198] R.H. Blessing *Acta Crystallogr. A* **1995**, *51*, 33–38.

[199] G.M. Sheldrick *SADABS, Version 2.10*, Siemens Area Detector Correction, Universitaet Goettingen, Germany; **2003**.

[200] G. M. Sheldrick SHELXTL, Version 6.1, Bruker AXS, Inc., Madison, WI ; **2002**.

[201] A.L. Spek *J. Appl. Crystallogr*. **2003**, *36*, 7.

[202]N. Khemiri, F. Chaffar Akkari, M. Kanzari, B. Rezig *Phys.Stat.Sol. (a)* **2008**, *205*, 1952-1956.

[203] S. Cho, K. Lee, A. J. Heeger Adv. Mater. 2009, 21, 1941-1944.